STUDIES ON LASER ASSISTED MACHINING OF GELCAST FUSED SILICA CERAMIC COMPOSITES

Submitted in partial fulfillment of the requirements

for the award of the degree of

Doctor of Philosophy

by

PUNUGUPATI GURABVAIAH

Roll No: 714123

Department of Mechanical Engineering
NATIONAL INSTITUTE OF TECHNOLOGY
WARANGAL – 506004
Telangana State, INDIA.
December – 2019

STUDIES ON LASER ASSISTED MACHINING OF GELCAST FUSED SILICA CERAMIC COMPOSITES

Submitted in partial fulfilment of the requirements

for the award of the degree of

Doctor of Philosophy

by

PUNUGUPATI GURABVAIAH

Roll No: 714123

Supervisor:

Dr. P. Subhash Chandra Bose

Associate Professor

Department of Mechanical Engineering
NATIONAL INSTITUTE OF TECHNOLOGY
WARANGAL – 506004
Telangana State, INDIA.
December – 2019

THESIS APPROVAL FOR Ph.D.

This thesis entitled **"Studies on Laser Assisted Machining of Gelcast Fused Silica Ceramic Composites"** by **Mr. Punugupati Gurabvaiah** is approved for the degree of Doctor of Philosophy.

Examiners

_____

_____

_____

Supervisor

Dr. P. Subhash Chandra Bose

Associate Professor,
Mechanical Engineering Department,
NIT Warangal

Chairman

Prof. R. Narasimha Rao

Head, Mechanical Engineering Department, NIT Warangal

NATIONAL INSTITUTE OF TECHNOLOGY

WARANGAL – 506 004, Telangana State, INDIA

CERTIFICATE

This is to certify the thesis entitled **"Studies on Laser Assisted Machining of Gelcast Fused Silica Ceramic Composites"** submitted by **Mr. Punugupati Gurabvaiah**, Roll No. 714123, to **National Institute of Technology, Warangal** in partial fulfilment of the requirements for the award of the degree of **Doctor of Philosophy in Mechanical Engineering** is a record of bonafide research work carried out by him under my supervision and guidance. This work has not been submitted elsewhere for the award of any degree.

Place: Warangal.
Date:

Dr. P. Subhash Chandra Bose
(Supervisor)
Associate Professor,
Department of Mechanical Engineering,
National Institute of Technology,
Warangal, Telangana State.

NATIONAL INSTITUTE OF TECHNOLOGY

WARANGAL – 506 004, Telangana State, INDIA

DECLARATION

This is to certify that the work presented in the thesis entitled "**Studies on Laser Assisted Machining of Gelcast Fused Silica Ceramic Composites**", is a bonafide work done by me under the supervision of **Dr. P. Subhash Chandra Bose**, Associate Professor, Department of Mechanical Engineering, NIT Warangal, India and has not been submitted for the award of any degree to any other University or Institute.

I declare that this written submission represents my ideas in my own words and where ever others ideas or words are included have been adequately cited and referenced with the original sources. I also declare that I have adhered to all principles of academic honesty and integrity and have not misrepresented or fabricated or falsified any idea/data/fact/source in my submission. I understand that any violation of the above will cause for disciplinary action by the institute and can also evoke penal action from the sources which have thus not been properly cited or from whom proper permission has not been taken when needed.

Place: Warangal.
Date:

Punugupati Gurabvaiah
Roll No. 714123

Dedicated to

My Parents

and

My family members

ACKNOWLEDGEMENTS

I would like to express my sincere gratitude and profound indebtedness to **Dr. P. Subhash Chandra Bose**, Associate Professor of Mechanical Engineering Department, National Institute of Technology, Warangal for giving me an opportunity to carry out doctoral work under his esteemed supervision. This work is a reflection of his thoughts, ideas and concepts. Dr. P. Subhash Chandra Bose looks at things in the right perspective, and it has truly been a learning experience working with him. I owe a lot to him for making me a part of the continuity of the profession.

I extend my sincere gratitude to **Prof. N. V. Ramana Rao,** Director, National Institute of Technology Warangal, India for providing the necessary facilities and encouragement throughout my work.

I am thankful to **Prof. R. Narasimha Rao**, Head, Department of Mechanical Engineering, NIT Warangal and other faculty members for their encouragement and support extended during this period.

It's my great opportunity to express my deepest gratitude to the Departmental Scrutiny Committee members, **Dr. N. Selvaraj**, Professor and **Dr. R. Narasimha Rao**, Professor, Department of Mechanical Engineering, and **Dr. G. Brahma Raju**, Assistant Professor, Department of Metallurgical and Materials Engineering for their adeptness and many discussions during the research period.

I am grateful to **Prof. C. S. P. Rao,** Director, National Institute of Technology Andhra Pradesh, for his constant support and motivation to carry out my research work.

I am thankful to **Dr. G. Raghavendra**, Assistant Professor, Department of Mechanical Engineering, NIT Warangal for his encouragement and support extended during this period.

I am grateful to **Dr. M. Raja Vishwanathan,** Assistant Professor and Head-Department of Humanities & Social Science, NIT Warangal, for his constant support.

I express my sincere thanks to my co-scholars **Pagidi Madhukar, C. Naresh, K. Rakesh, M. Vinod Babu, D. Purusottama Rao, K. Mahesh, D. Sashidhar, M. Sekhar** and seniors **T. Gopala Rao, Kishore Kumar Kandi and T. Nagaveni,** NIT Warangal and my friend **M. Lokesh** for their support and help in completion of this thesis.

I would like to extend my heartfelt thanks to **Mr. B. Rangilal, Mr. G. Ilaiah** and **K. Raju** technical staff of Production Engineering Lab and **Mr. M. V. Vijay Kumar** Office staff of Mechanical Engineering Department, NIT Warangal for their constant help and encouragement.

A special debt of deep gratitude to my parents and family members for their unceasing sacrifices, endeavors and encouragement.

Finally, I would also like to acknowledge the help given by all the persons who have directly or indirectly supported the work.

Punugupati Gurabvaiah

Research Publications

International Journals

1. Gurabvaiah Punugupati, P. S. C. Bose, G. Raghavendra, C. S. P. Rao, "Response Surface Modeling and Optimization of Gelcast Fused Silica Micro Hybrid Ceramic Composites" Silicon (2019). https://doi.org/10.1007/s12633-019-00247-w. (SCI)
2. Gurabvaiah Punugupati, P. S. C. Bose, G. Raghavendra, C. S. P. Rao, S. Ojha "Erosion Behavior of Gelcast Fused Silica Ceramic Composites" Silicon (2019), https://doi.org/10.1007/s12633-019-00184-8. (SCI)
3. Gurabvaiah Punugupati, P. S. C. Bose, G. Raghavendra, C. S. P. Rao, "Influence of Solid Loading and Ratio of Monomers on Mechanical and Dielectric Properties of Hybrid Ceramic Composites" Silicon (2018), https://doi.org/10.1007/s12633-018-0061-4. (SCI)
4. Gurabvaiah Punugupati, Kishore Kumar Kandi, P. S. C. Bose, C. S. P. Rao, "Modeling and optimization of wear characteristics of gelcast fused silica ceramic composites using RSM", Materials Today: Proceedings 5 (2018), Pages 6946-6953. (Scopus)
5. Gurabvaiah Punugupati, Kishore Kumar Kandi, P. S. C. Bose and C. S. P. Rao, "Laser assisted machining: a state of art review", Materials Science and Engineering 149 (2016) 012014. (Scopus)

International Conferences

1. Gurabvaiah Punugupati, Kishore Kumar Kandi, P. S. C. Bose, C. S. P. Rao, "Process modeling of gelcast Si_3N_4 ceramics using multi gene genetic programming", Materials Today: Proceedings, Volume 4, Issue 2, Part A (2017), Pages 1900-1909.

ABSTRACT

Structural ceramics have interesting mechanical, thermal, chemical and dielectric properties, which suggest great potential for structural applications even at high temperatures. These are also used in electronic applications like insulators, semiconductors, conductors and magnets due to their electrical and magnetic properties. Advanced structural ceramics have been progressively used in aerospace, automobile industries, defence, biomedical, construction, nuclear industries, chemical, petrochemical and oil/gas industries due to their excellent properties. The usage of fused silica in such applications largely depends on the ability to reliably and economically mass produce complex and complicated shaped components. This is a challenge for the ceramic industry using traditional fabrication techniques. Moreover, forming complex shaped parts by machining and grinding of final sintered parts is seldom viable as it is very expensive. Advanced ceramic fabrication techniques such as colloidal direct casting offer a way to produce complex shapes. This study builds upon the gelcasting near net shape casting method by successfully developing a new slutty formulation and processing technique. Among the fabrication techniques for ceramic composites, gelcasting has recently attracted much attention as being a versatile, low cost and environmental friendly process. Defence organizations such as DRDL, ARCI etc. have been working with ceramic radomes used in missiles. During interaction with experts from these prominent R&D Institutions, it is found that radomes are importing from foreign countries like Germany and Russia. Cost of each radome is approximately Rs. 30-40 lakh. Even though manufacturing knowledge transfer is also restricted during these purchases.

Fused Silica ceramics possess low thermal expansion, high chemical resistance, excellent optical qualities, low dielectric constant, low loss tangent and chemical properties. With exceptional physical and chemical properties, fused silica has various applications such as antenna windows, optical devices, heat shields, high power lasers, precision instruments, semiconductor manufacturing, aerospace applications and these applications continuously increasing. For machining efficiently these high precision elements, it is exceptionally difficult using conventional metal cutting methods because of higher cutting force and excessive tool wear which leads to a lower material removal rate and high cost. Laser assisted machining is effective method for improving the machinability of difficult to machine material like ceramics. Fabrication and machining of ceramic composites and development of regression models are very much essential for user industries like aerospace and defence.

Based on the thorough literature survey, gap is identified and formulated the problem on fabrication and characterization of fused silica based composites using gelcasting technique by varying precursor amounts, solid loading, monomers and its contents and to identify the best suitable material for wave transparent materials. Silicon nitride (Si_3N_4), Boron nitride (BN) and Alumina (Al_2O_3) added to fused silica (SiO_2) to enhance flexural strength keeping porosity and dielectric constant in range. Effect of various parameters of gelcasting on mechanical and dielectric properties are studied on these SiO_2 based ceramic composites. New ceramic materials SiO_2–Si_3N_4–BN and SiO_2–Si_3N_4–Al_2O_3 fabricated for wave transparent applications which have excellent properties. The full factorial approach used for the evaluation of properties of ceramics. RSM and DOE approach is used for the modeling and optimization of the ceramic composites.

The detailed experimental plan involving number of experiments for gelcasting of SiO_2–Si_3N_4–BN and SiO_2–Si_3N_4–Al_2O_3 ceramic composites was designed using Design Expert 9.0 software. A face centered composite design with 6 center points have been used in the experimental plan. The levels of the input parameters are solid loading (SiO_2, Si_3N_4, BN and Al_2O_3 content), monomer content and monomer ratio were fixed based on literature. SiO_2–Si_3N_4–BN and SiO_2–Si_3N_4–Al_2O_3 ceramic composites were fabricated by gelcasting process by varying solid loading, monomer content and monomer ratio. The sintering temperature was kept constant at 1250 ^oC for fabrication of ceramics. Properties like flexural strength, porosity and dielectric constant are planned to evaluate as per the experimental plan.

The author has fabricated porous SiO_2–Si_3N_4–BN and SiO_2–Si_3N_4–Al_2O_3 ceramic composites by gelcasting by varying solid loading, monomer content and monomer ratio and evaluated flexural strength, porosity and dielectric constant. The regression models for the analysis of flexural strength, porosity and dielectric constant are developed and the influence of input variables on these responses is studied. The optimum process parameters for maximum flexural strength, maximum porosity and minimum dielectric constant were evaluated with the help of RSM coupled with desirability function to optimize multiple responses. The predicted values for responses such as flexural strength, porosity and dielectric constant obtained from mathematical models are compared with experimental values for SiO_2–Si_3N_4–BN and SiO_2–Si_3N_4–Al_2O_3 ceramics.

Erosion test was performed on ceramics which get optimal properties for three types of ceramics pure fused silica, SiO_2–Si_3N_4–BN and SiO_2–Si_3N_4–Al_2O_3. Different impingement angles (30^o, 45^o, 60^o and 90^o) and three impact velocities (86 m/s, 101 m/s and 148 m/s) were chosen to examine the behavior of erosion on gelcasted ceramics using SiO_2 particles as erodent. The maximum rate of erosion is obtained at normal impingement angle (90^o), which shows the brittle nature of ceramics. The impact velocity and angle of impingement have an appreciable effect on erosion rate. Resistance to erosive wear is found to have improved with the inclusion of reinforcements in the fused silica ceramics. The erosion rates of different ceramics are compared. Ceramic composite with a combination SiO_2–Si_3N_4–Al_2O_3 shows the highest resistance to wear. The surface roughness and morphology of the eroded surfaces have also been studied.

Among the ceramics, SiO_2–Si_3N_4–Al_2O_3 ceramic composite has better properties. Hence, it is considered for the machining with Laser Assisted Machining (LAM). A face centered central composite design of 6 center points has been used in the experimental plan. The levels of input parameters rotational speed, feed, depth of cut and laser power were set based on literature and trail experiments. Machining conducted on SiO_2–Si_3N_4–Al_2O_3 ceramic with varying rotational speed, feed, depth of cut and laser power as per RSM and DOE basis and evaluated surface roughness and material removal temperature. Regression models for the analysis of responses such as surface roughness and material removal temperature are developed and the influence of input variables on these responses is studied. Optimum process parameters for minimum surface roughness and minimum material removal temperature were studied using RSM coupled with desirability function to optimize multiple responses. The actual experimental values for both responses compared with predicted regression models. Surface roughness of SiO_2–Si_3N_4–Al_2O_3 ceramic is improved with laser assisted machining.

CONTENTS

LIST OF TABLES

LIST OF FIGURES

ABBREVIATIONS

APS	Ammonium persulphate
TEMED	Tetramethylethylenediamine
DE	Dielectric constant
FS	Flexural strength
HAS	Hydrolysis Assisted Solidification
MAM	Methacrylamide
MBAM	*N*,*N'*-Methylenebisacrylamide
MC	Monomers content
Por.	Porosity
PEG	Polyethylene glycol
SL	Solid loading
MR	Ratio of monomers
SEM	Scanning electron microscopy
TEMED	*N*,*N*,*N'*,*N'*- Tetramethylethylenediamine
XRD	X-Ray Diffractometer
S	Rotational Speed
F	Feed
DOC	Depth of cut
P	Power
SR	Surface Roughness
MRT	Material removal temperature

NOMENCLATURE

η	Viscosity
τ	Shear stress
γ	Shear rate
F	Fracture load
L	Length of support span
b	Width of the sample
h	Height
BD	Bulk Density
AP	Apparent porosity
W_1	Dry Weight
W_3	Soaked Weight
W_2	Suspended weight
ρ	Density
ε	Dielectric constant
c	Capacitance
d	Thickness of the specimen
A	Area of the cross-sectional surface
L_0	Length of the sample after sintering
L	Length of the sample after sintering

CHAPTER I

INTRODUCTION

1.1. Introduction to ceramics

A ceramic material is an inorganic compound consisting of a metal (or semimetal) and one or more non-metals. The word ceramic derives from the Greek keramos meaning potter's clay or parts made from fired clay. Ceramics have been used since the dawn of civilization and have played a vital role in the evolution and improvement of human life. Ceramic materials are inorganic compounds at higher temperature and are classified as conventional ceramics or traditional, made of clay based ceramics and advanced ceramics, made of synthetic materials have specific structural and functional properties. Ceramics can be defined as "solid materials, which demonstrate exceptionally strong ionic bonding and in few cases covalent bonding." A somewhat simple definition is (Kingery) "the art and science of making and using solid articles, which have as their essential component and are composed in large part of inorganic nonmetallic materials."

Conventional ceramic materials are expanding at a slower pace and some of them even tend to decrease i.e refractory materials. Bricks for buildings, dishes and coffee cups are some of the notable ceramics. The trend for the structural ceramics is expanding continuously. These ceramics are oxides (SiO_2, Al_2O_3, TiO_2, ZrO_2) and nitrides (Si_3N_4, BN, AlN), carbides (B_4C, SiC) and borides. However, these ceramics were used in advanced structural applications (Groover, 2007).

Ceramics possess many useful properties like wear resistance, stiffness, high hardness, high elastic modulus, chemical inertness, corrosion resistance, low thermal expansion co efficient, good optical qualities and high strength retention at higher temperatures. Ceramic materials have application in various areas of industries including aerospace, high speed machining, materials fabrication, chemical industries, high power nuclear reactors, power production and transportation etc. Silicon nitride based ceramics are used as ball bearings, automobile engine parts, radomes and cutting inserts. There exist clear demand for ceramics as they can operate at temperatures greater than 1500 ^oC; such areas include re-entry nozzles in rockets or re-entry hypersonic space crafts. One of the main applications that have attracted

great attention is ball bearings. The ceramic balls used in hybrid bearings along with steel races are used in turbo pumps of space craft main engine. The friction and tribological characteristics of structural ceramics such as SiC, zirconia, alumina and silicon nitride are exceptional (Barsoum and Barsoum, 2002). The ceramic material selection for particular applications is presented in Figure 1.1.

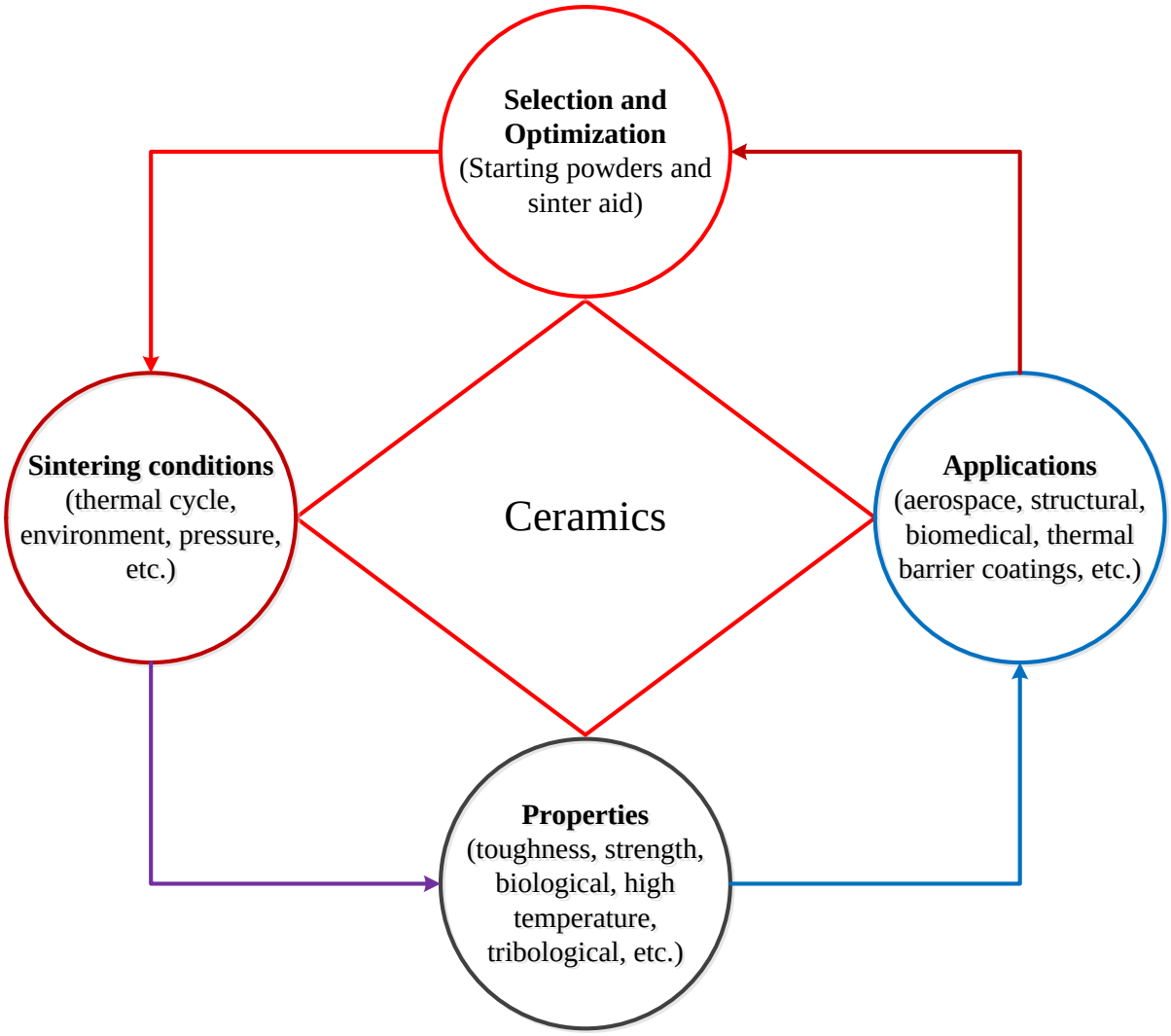

Figure 1.1. Ceramic materials selection

In spite of so many important applications, the main limitation of ceramics for structural and non-structural use is their substandard fracture toughness. Past decades, it has been observed that an optimal blend of higher toughness with strength and hardness is needed for maximum benefits to user in terms of present and upcoming applications including in the sector of aerospace and biomaterials. To overcome these shortcomings, the development of

ceramics with optimum combinations of mechanical, electrical and thermal properties is a major concern in ceramic industry.

1. 2. Ceramic composites

"A composite is a structural material that contains two or more constituents that are combined at a macroscopic level and are not soluble in each other." A composite in engineering sense, is a material that has been physically presented to from one single bulk without physical blending to form a homogeneous material (Attili and RamaKrishna, 2015). Monolithic ceramics, especially these with enhanced toughness and strength, have been emphasized in various industries and research labs. In fact, monolithic ceramics are not suitable for all kinds of structural and biomedical applications.

The main advantage of a composite material compared with other material is the blend of various properties that are superior to conventional base materials. The main objective of reinforcement is to improve properties like hardness, toughness, thermal shock resistance, thermal expansion co efficient, thermal conductivity and electrical conductivity of composites. The addition of these properties makes composites attractive materials for many industrial applications. These are many important parameters that determine the phase distribution and their functionality in the ceramic based system. Fabrication technique plays a major role in sintered ceramic properties. Secondary phase of ceramics have a lot of advantages, and such phases are able to produce considerable structural changes and alter properties of monolithic materials. Apart from the advantages, some principal drawbacks include brittleness, expensive processing, difficulty in manufacture complex shapes, development of thermal stresses due to differential thermal expansion coefficients of medium and reinforcement.

1.2.1 Advantages

Ceramics have many advantages such as high strength at elevated temperatures, high elastic modulus, good corrosion and wear resistance, low density, low co efficient of friction, good chemical inertness, resistance to catastrophic failure and high stiffness.

1.2.2 Applications

The major applications of ceramic composites are in aerospace, defence, gas turbines, turbine blades, cutting tools, wear components, heat exchangers, bio ceramics, coatings etc. Ceramic radomes are using in missiles and rockets.

1.3. Radome

The antenna housing, namely (Radome) is one of the most significant parts of the guided missile radar. A radome is a weatherproof, structural enclosure that guards a microwave or radar antenna and is fabricated by a material that receives electromagnetic signal from the antenna. This is done because it controls the aerodynamic performance of the missile, determines the accuracy with which the missile is guided to the target, and is resistant to thermal and mechanical loads on a missile during manoeuvres. The main function of a radome is to protect an antenna from environmental destructions i.e. from wind, snow, ice and freezing temperatures to rain, sun and even lightning. The Radome materials are compelled to work in severe environments with lightweight, low dielectric constant, low tangential loss, high flexural strength to withstand handling, aerodynamic and thermal stresses, high thermal shock resistance, minimal moisture absorption, high rain erosion and high modulus of elasticity to maintain the thin walls of the radomes due to buckling. The demands of radome and its basic material have become essential as the speed and manoeuvrability of missiles have amplified. Figure 1.2 shows the image of the sintered and machined $Si_4Al_2O_2N_6$ radome.

Figure 1. 2. Image of sintered and machined β-SiAlON radome (Ganesh, 2011)

Various types of missiles moving at speeds in the range of 5 to 12 Mach number and the surface temperature of the radome may reach up to 2000 ^{o}C with mechanical loads up to 10 tons (Ganesh, 2011and Suzdaltsev, 2015). Radomes are typically made of dielectric materials that are illustrated by a dielectric constant, tangent loss factor and other electrical factors. Several configurations are used to reduce radomes Radio frequency reflections. The configuration for a specific application depends on the operating frequency and mechanical constraints. Ceramic radomes are typically attached to the front part of rockets. Research is being carried out for manufacturing ceramic radomes for high-speed missiles.

1. 4. Near net shape techniques

Near net shape manufacturing can be classified into dry shaping techniques such as uniaxial pressing, isostatic pressing, wet colloidal shaping methods like slip casting, tape casting, gelcasting and plastic shaping process such as injection molding, extrusion etc., as shown in Figure 1.3. Dry shaping technique needs a reasonably dry feed and usually contains ceramic powder with < 5v/v% binder.

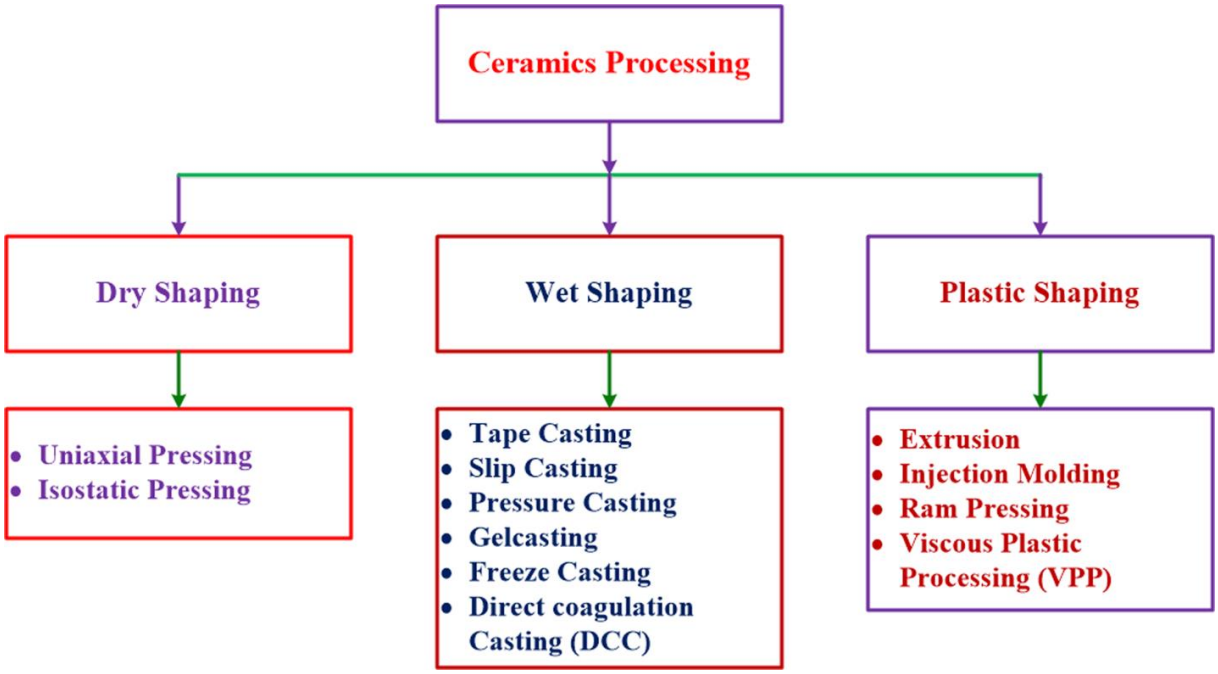

Figure 1. 3. Classification of Ceramic Processing

The reliability of ceramic dry processing is restricted by flaws caused by agglomerates. This problem can be avoided by wet processing techniques. Generally, wet colloidal processes are restricted, in the case of complex workpieces with altogether thick and

thin cross-sections because of the density gradients in a green body. The wet processing techniques offer an opportunity of breaking agglomerates but create other problems in the starting powders, for instance, differential sedimentation as a result of particle size distribution. There are various methods to get rid of this problem, for instance, the use of flocculated sludge or frozen systems (Rice, 2002). The disadvantages of this method are that coagulated and flocculated systems with more open structures and lower densities lead to green bodies that higher sintering temperatures require to reach theoretical density. Further details are discussed in the following sections with respect to dry and wet forming techniques. Ceramic processing has continuously improved and new methods are initiated constantly.

1.4.1 Direct coagulation Casting (DCC)

Direct coagulation casting (DCC) is the solidification process for aqueous slurries introduced by a group of scientists from ETH Zurich, SF (1920). DCC method is a unique near net shape method of homogeneous suspension of particles with high solid loading on the green ceramic body. The basic principle of DCC process is that a coagulated stable suspension which is poured into a non-porous mold to use a time-delayed chemical reaction in the suspension results in a destabilization and a dense, homogeneous green body. Consolidation of the high dense suspension is controlled by a coagulant to increase the pH to isoelectric point (IEP) of the suspension and/or to move the ion concentration in the suspension where it is used. Such species double-layer repulsive forces minimize compression or collapse of the double-layer.

This process results in high green density and homogeneous microstructures. At high solids concentrates in the liquids to solid transition and through drying, non-linear shrinkage occurs for green body and after the sintering step, exact sizes of the component can be expected. DCC is particularly suitable for the production of complex parts with large and small cross sections in the same part (Graule et al., 1995 and Graule et al., 1994).

1.4.2 Slip Casting

Slip casting is an appropriate and reliable technology for production of dense and uniform ceramics (Moreno et al., 1991 and Tari et al., 1998). In fact, this shaping method improves the packaging structure of ceramic particles in the green body with low porosity and a fine distribution of pore size to a large extent. Slip casting is essential to attain thick slurry

of highly deflocculated powder with a high volume fraction. For this purpose, a large repulsive force between the ceramic particles can be attained with modification in surface characteristics of the powder. By the way, the repulsion force is greater than the force of attraction. This is attained by electrostatic repulsion, which arises from overlapping of the electric double layers (ζ- potential) or from steric hindrance, resulting from adsorbed molecules of the solvent or dispersant type (Hotza and Greil, 1995). Through specific control of the above said factors, ceramics with high density and a homogeneous microstructure could be produced. Slip casting is an appropriate method to achieve homogeneous microstructure and high green density materials, permitting the production of complex shaped components.

1.4.3 Pressure Casting

The improved and extended form of slip casting is pressure casting. This forming technique uses some pressure or stress to improve casting rates and also uses vacuum to improve fluid infiltration in the mold. For example, by three to six fold for a thickness of ˜1 cm, increase in green density and decrease in dry shrinkage is 2 to 4 folds. Pressure castings are now widely used in sanitary ware industry, microwave drying of components and molds and the automation of process has decreased both process energy and process time i.e 2-3 days to 9-10 hours. The mold life is increased by changing polymer to plastic molds. The components produced from pressure casting can be used in high performance application area like turbine and piston engines. This is because of increment in part reliability by the reduction of process flaws. The Si_3N_4 engine rotors with a thickness more than 50 mm and more complex cross section were also produced but it has a casting time of approximately 3.50 hours (Rice, 2002).

1.4.4 Freeze Casting

Freeze casting was developed as a near net shape wet processing technique, which gives dense ceramic component with fine replica of the mould shape (Sofie and Dogan, 2001). The first person to work on this method was Fukasawa who discovered potential of the porous ceramics and considerable efforts were then placed (Fukasawa and Ando, 2001). Freezing is a simple technique for the production of complex ceramics or porous molding polymer parts (Fukasawa et al., 2001). In this method, ceramic suspension is poured into a mold and frozen. Temporarily, the solvent freezing acts as a binder to hold the workpiece for

removal. Thereafter, component is directed to freeze drying to sublimate the solvent in vacuum. The limitations of drying and shrinkage that can cause cracks and deformation during normal drying are avoided. Subsequent to drying, the samples are sintered to produce a high strength and stiff porous material with the required porosity. The result is a component with a complex porous microstructure and is often generated during freezing (Kang et al., 1999). It is possible to impose a preferential orientation for porosity by controlling the growth direction of ice crystals in the final component.

1.4.5 Hydrolysis Assisted Solidification (HAS)

Hydrolysis-assisted solidification (HAS) is an innovative technique for net-shaping green ceramic components from aqueous ceramic suspensions in nonporous molds. This method utilizes thermally initiated and/or accelerated hydrolysis of aluminium nitride (AlN) powder, which was mixed into ceramic suspensions. This method is a kind of cross between the curing of the cement parts and offer of gelation by certain advantages. The method is based on thermal and thermally activated aluminum nitride (AlN) ceramic bonded suspensions with high concentration. During the hydrolysis of AlN, water is absorbed. The solid loading is increased because the water is bound to metal hydroxide and ammonia is formed, which increases the pH of the slurry (the pH value is shifted towards the isoelectric point (IEP) of alumina). The two means, consumption of water and pH change can be used for the solidification of a ceramic aqueous suspension in a matrix. In addition, aluminum hydroxide would get a reaction product further away from the hydrolysis of AlN gels; the heating will further aid the solidification process and increase the green strength of the molded body. The advantages of this method are outstanding rheological properties, high solidification rate and a high density. Disadvantages include limited duration and temperature stability.

$$AlN + 3H_2O = Al(OH)_3 + NH_3 \quad (1.1)$$

$$NH_3 + H_2O = NH_4OH \quad (1.2)$$

$$AlO(OH) + H_2O = Al(OH)_3 \quad (1.3)$$

From the reactions (1.1), water is consumed throughout the hydrolysis of AlN powder, (1.2) ammonia is produced and (1.3) AlN particles are suspended to form aluminum hydroxides. The first reaction increases the solid loading and the second has a significant

impact on the pH value of the slurry, electro kinetics and thus affects its rheological properties. Resolution of AlN ceramic particles can affect the ionic and precipitation phases formed by the reaction can lead to increased solid surface area or a change in the rheological properties of the liquid medium. It was clear that all of these reactions can alter the rheological properties of the ceramic slurry significantly and therefore the involvement of each effect in this study was investigated (Rak, 2000 and Kosmac et al., 1997).

1.4.6 Tape Casting

Tape casting is near net shape process employed for mass fabrication of ceramic substrates and multilayer structures (Rak, 2000 and Hotza and Greil, 1995). A suspension comprising ceramic powder in a solvent with the mixing of dispersing agents, binders and plasticizers is poured into a fixed or movable surface. The cast strip having a typical thickness of the order of 100 to 300 μm is dried followed by sintering to acquire a required form. Different types of non-aqueous organic solvents like alcohols, ketones or hydrocarbons are generally used to produce highly concentrated suspensions exhibiting repeated rheological properties and drying behavior depending on the ceramic powder composition.

These days, the ecological and healthiness features of the tape casting method have attracted particular attention. As a result, in the literature, the formulation of suspension appeared with water as solvent in place of organic liquids. The starting suspension for tape casting generally includes mixture of ceramic powder depending on the phase, solvents, additives (antifoam agent, dispersant, surfactant, etc.), binder, and one or more plasticizers. In order to obtain complete dissolution of the hydrocolloid, the suspension is heated to a particular temperature. After degassing, the suspension is poured with a doctor blade on a support film. The properties of the organic binder enable its use in easy-to-use tapes. In next steps, the tape is removed from the carrier sheet, followed by drying, heat treatment, to remove the organic compounds from the green body, and sintering process. If necessary, further shaping, calendering or rolling between drying and calcining may take place (Nahass et al., 1992).

1.4.7 Gelcasting

Gelcasting technique was developed for hard metals in the metals and ceramics division of Oak Ridge National Laboratory (ORNL), Oak Ridge USA. The processes are

further expanded for ceramic materials by mixing polymer chemistry, slip processing and represent minimal departure from conventional ceramic fabrication by Janney and Omatete (Rahaman, 2017, Young et al., 1991, Ornatete et al., 1997 and Janney et al., 1998). The common principle in this technique is that the ceramic particles suspended are surrounded by a 3-dimensional network of cross linked polymers (Figure 1.4). To obtain higher solid loading, typically a dispersant is applied which affects the particles in ceramic slurry to disperse by means of an electric double layer or steric stabilization. Shrinkage of ceramics can be reduced during sintering process and density of the same improved by high solid loading. The free radical reactions leads to the formation of micro gels of monomer and cross linker inside the suspension, which eventually combine to form a macro gel network. The gel network formed inside the suspension holds the particles together collectively to mold a high dense green sample which is de-moldable and takes the shape of mold cavity. Molds of different metals or plastic materials that are non-porous can be used for this process.

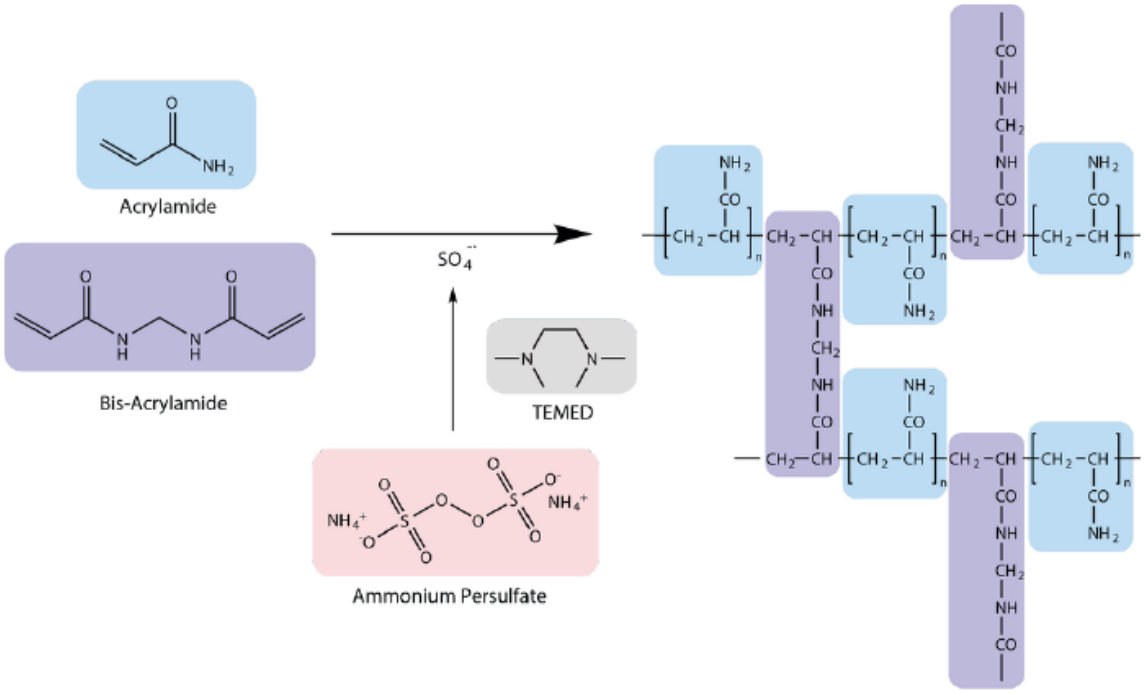

Figure 1.4. Schematics of gel formations

In this technique, dense slurry is achieved by mixing ceramic powder and monomers to the solvent. After the ceramic suspension is poured into mold to get the desired shape and during heating, in-situ polymerization takes place to form a gel network to bind the ceramic particles collectively in a hard green body. The first gel monomer used was acrylamide (AM)

(Young et al., 1991). However, industries are not interested to use this process because AM is neurotoxin. AM was replaced by a less toxic monomer methacrylamide (MAM). An initiator and a catalyst are added to the mixed slurry to start and accelerate the polymerization. The slurry was then poured into a non-porous mold. The liquid surrounding the ceramic particles will be permanently gelled by polymerization and get the shape of the mold. The parts shaped are then removed from the mold and dried in controlled humidity conditions to minimize warping and cracking. In gelcasting technique, drying time for green bodies is normally more, otherwise cracking and warping may takes place. The green sample can then undergo standard binder burnout and sintering to get denser samples.

Ceramic industries use AM and MAM polymer materials sparsely in gelcasting process because of their toxic nature. Therefore, various alternative techniques of gelcasting have been investigated. Researches have concentrated on developing gelcasting technique which are eco-friendly and non-hazardous by studying different binder systems which gel or polymerize through chemical reaction process (Morissette and Lewis, 2000, Cai et al., 2003, Huha et al., 2000 and Zhou et al., 2000) or a thermal process (cooling or heating) (Li et al., 2014).

In recent years, researchers have worked on natural, nontoxic and inexpensive materials as binders. They include gelatin (Chen et al., 1999, Colonetti et al., 2018, Sanches et al, 2015, Hammel et al., 2017 and Lombardi et al., 2009), agarose (Santacruz et al., 2005, Zhang and Feng, 2010 and Adolfssonw, 2006), agar (Tulliani et al,. 2013 and Olhero et al., 2000), curdlan (Xu et al., 2015), egg white (He et al., 2011), rice husk (Nayak and Bera, 2012), glutinous rice flour (Wan et al., 2014), starch (Chandradass et al., 2009) and nontoxic cellulose ethers (Li et al., 2008). These naturally obtained binders were not suitable to meet the requirements of industrial processing. High green strength components produced using gelcasting were the main advantage, developed at Oak Ridge using AM or MAM as binders. The main drawback with neutral gelling agents used for gelcasting referred above is that commonly generate green strength components have low reliability and consistency.

In this research study gelcasting process was selected because it is a forming technique which has been presented to fabricate high green strength parts. Different direct casting processes are presented in Table 1.1.

Table 1.1. Benefits and drawbacks of different wet fabrication techniques

S. No.	Fabrication techniques	Benefits	Drawbacks
1	Gelcasting (polymer)	Great green strength and established process	Toxicity problems, costly reagents
2	Gelcasting (natural additives)	Safe eco-friendly, water based technique	Low green strength
3	Freeze casting	Water based method, unique sublimation technique	Low green strength
4	Aqueous injection moulding	Fast, eco-friendly	Size limitation, high viscosity
5	Centrifugal slip Casting	One step process for filters	Additional equipment Required
6	Direct coagulation casting	No size and wall thickness Issues, high green density	Poor green strength, costly additives
7	Electrophoretic casting	Suitable for functionally graded composites and coatings	Sensitive to current Parameters
8	Hydrolysis assisted Solidification	Fast, high green density	Gaseous product formation, Poor green Strength
9	Pressure slip casting	Fast, eco-friendly	Drying, additional equipment needed
10	Temperature induced forming	Simple	Heat transfer, Gaseous product formation

Gelcasting has various advantages over conventional ceramic forming techniques like near net shape forming, less amounts of organic monomers, high green strength, high sintered density and homogeneity, where high strength makes ease of machinability. This process is more cost effective by using non-porous glass, metal or plastic molds which are reusable. Gelcasting process is a prominent technique for fabrication of complex shapes like turbine

parts, radomes, gears etc. Comparisons of different ceramic forming techniques are presented in Table 1.2.

Table 1.2. Comparisons of different ceramic forming techniques [Guo, 2011]

Property	**Gelcating**	**Slip Casting**	**Injection Molding**	**Pressure Casting**
Molding Time	5-60 minutes	1-10 hours	10-60 seconds	10 minutes-5 hours
Strength (Dried)	Very high	Less	---	Less
Mold Materials	Metal, glass, polymer, wax	Plaster	Metal	Porous plastic
Binder Burnout	2-3 hours	2-3 hours	7 days	2-3 hours
Maximum Part Dimension	> 1 meter	> 1 meter	About 30 cm, 1 dimension must =< 1cm	About 1 meter
Molding Defects	Minimum	Minimum	Significant	Minimum
Warpage During Drying/Binder Burnout	Minimum l	Minimum	Possibly be severe	Minimum
Thick/Thin Sections	Both are ok	Thick section requires more casting time	Issues with binder removal for thick section	Thick section requires more casting time

1. 5. Applications of gelcasting

Gelcasting is most similar to conventional slurry forming operations like slip casting and spray casting. Moreover, it is a water based technique. The main difference of gelcasting

process with most of the traditional ceramic manufacturing techniques is solid loading. Gelcasting process requires high solid loading (50-60 vol%) in comparison to that which is typically used in slip casting and spray drying (25-40 vol%). Due to the presence of high solid loading, the green strength of the samples was more. Highly complex shaped components such as turbine blades with highly uniform properties were fabricated by an efficient gelcasting method. Gelcasting process was also used to manufacture sinter near net shape parts in tool steel, nickel based super alloys, aluminium alloys and stainless steel (Janney et al., 1998).

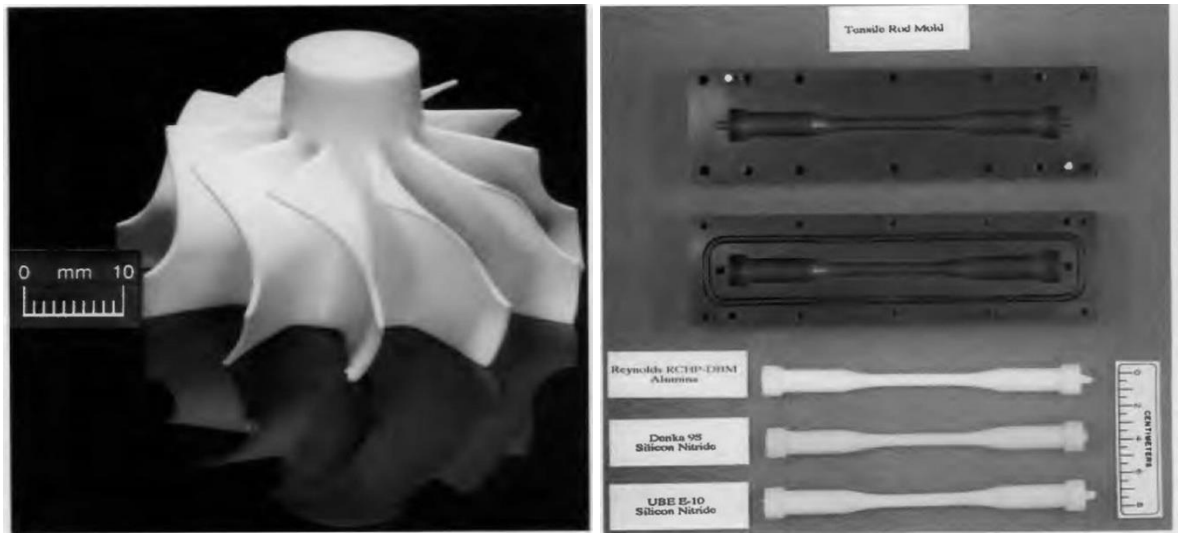

(a) (b)

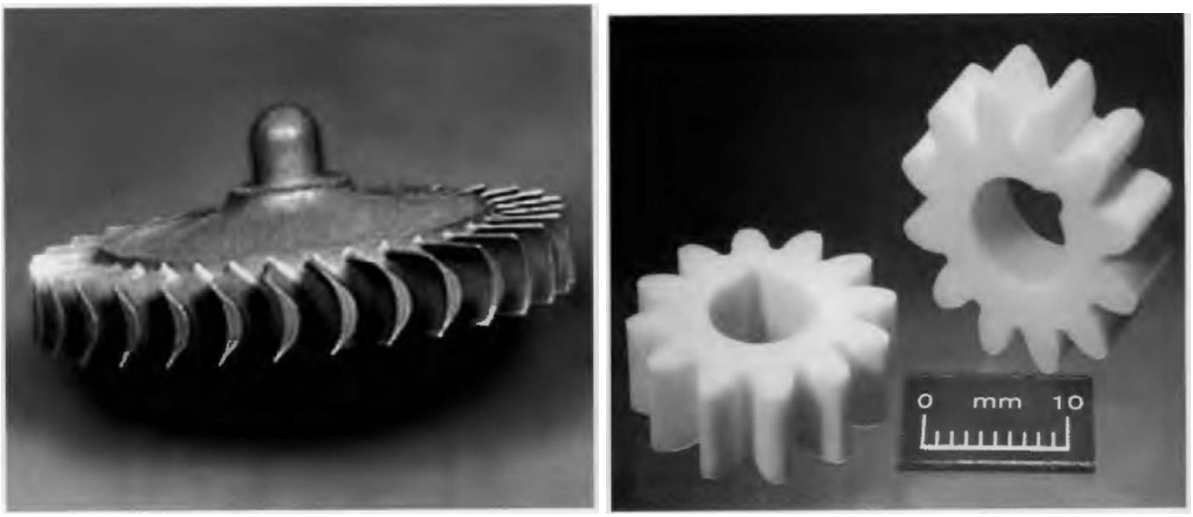

(c) (d)

Figure 1.5. Complex parts produced by gelcasting (a) alumina turbocharger rotor (b) silicon nitride tensile test bars (c) alumina gears (d) silicon nitride turbine wheel.

About a decade ago, it was researched and found that gelcasting could be used in industrial production. Silicon nitride was used as the material for the blade and vane of turbine rotor, as presented in Figure 1.5 (a). The density of blade with gel casting was uniform while the density of blade slip casting was varied. Silicon nitride tensile test bars and alumina gears are presented in figure 1.5 (b) and figure 1.5 (c) respectively. Figure 1.5 (d) shows a silicon nitride turbine wheel which was fabricated for commercial aircraft and use in on-board engines in military. This type of turbine was usually fabricated by injection molding and slip casting. Compared to these two forming techniques, gel casting can provide higher percentage of defect-free products.

1.6. Rheology of ceramic slurry for gelcasting process

For acceptable properties of the final product and for good strength of the blank, there is the need to comply with proper content of ceramic powder in the slurry. This content should be at least 50 vol%. The more we have ceramic powder in the slurry, the more we increase the viscosity of the suspension. However, it is important that the concentration of powder does not reach such boundaries; the suspension will be so viscous that it would be impossible to pour it into the mold. Conversely, high content of ceramic particles reduces shrinkage and deformation of the blank during drying, while increasing the final density after sintering.

1.7. Monomers

The most commonly used monomers in gelcasting are acrylamides such as methacrylamide (MAM), methylenebisacrylamide (MBAM) and hydroxymethyl acrylamide (HMAM) with initiator and catalyst as ammonium persulfate (APS) and tetramethylethylenediamine (TEMED) respectively. The existence of oxygen impulsively stops radical polymerization by a peroxide group at the end of the polymer chain. In this work, the use of methacrylamide and methylenebisacrylamide as a gel forming agent in gelcasting of fused silica and fused silica based ceramic composites was examined. Research on the use of low toxic monomers seems ecologically promising and is a better choice for applications for gelcasting complex shaped ceramics.

1.8. Solvents

The most commonly used solvent is water. It has low viscosity. After addition of suitable ceramic powder and dispersant into water, it produces a highly liquid suspension. This is probably one of the biggest advantages of using water as a solvent. Another advantage is the ease of drying water, and optionally prevention of subsistence problems associated with the environment when disposing of residues of organic solutions. In the case of using an organic solvent, taking into account other properties is necessary. These include not only the low pressure saturated steam at a temperature of cross linking but also relatively low viscosity. Among these solvents, we can include phthalate esters, petroleum solvents with high boiling point, dibasic esters, and long chain alcohols.

In addition, attention was paid to the selection of the dispersant, it must be such that it is suitable for combination of solvent and monomers. Monomers act as dispersant and interact with the system ceramic powder-solvent-monomer. Additionally, the dispersant may react negatively to the initiator system-monomer, which may lead to the acceleration or deceleration of the polymerization process. Most commonly used initiator for polymerization is ammonium persulfate (APS). Most commonly used catalyst is Tetramethylethylenediamine (TEMED).

1.9. Drying, Binder burnt-out and sintering

Drying is done to avoid ceramic blank not only in cracking but also the deformation of the whole possible reaction components caused due to shrinkage. Studies have shown that the humidity of the environment in which the drying takes place, is one of the most important parameters to achieve the best results. Therefore it is recommended to dry the ceramic preform at a relative humidity in the contact time of the particles. Then it is already possible to increase the drying speed. It is performed by either increasing the temperature or by reducing relative humidity. It brings us to smaller risk cracks. The big advantage of the method of gel casting is a small amount of polymer remaining in the ceramic blank for the drying process. Removal of binders is guaranteed only at temperatures of 700 ^{o}C. The temperature of the binder removal is greatly dependent on their type and composition. After removal of organic components, the body holds the ceramic particles together due to the

influence of secondary Van der Waals forces. The compaction of the ceramic body occurs during subsequent sintering.

1.10. Properties required for a Radomes

The properties required for radomes are flexural strength, porosity, dielectric constant and dielectric loss tangent. These properties are measured using various equipment and are presented in Chapter-3.

1.10.1 Flexural strength

Flexural strength (modulus of rupture) is defined as "the ability of material to with stand bending forces applied perpendicular to its longitudinal axis". Three point bending test was adopted to measure the flexural strength. Figure 1.6 shows the load configuration for a beam in three-point bending test. Three point bending test was conducted according to ASTM (C1161–94) standard. The flexural strength of the sintered test specimen was measured with a universal testing machine with a span length of 30 mm and crosshead speed of 0.5 mm/min.

The flexural strength was calculated using Eq. (1.4).

$$\sigma_f = \frac{3FL}{2bh^2} \tag{1.4}$$

Where

σ_f = Flexural strength (MPa), F = Fracture load (N), L = Length between outer supports (mm). b = Specimen width (mm), h = Specimen height (mm).

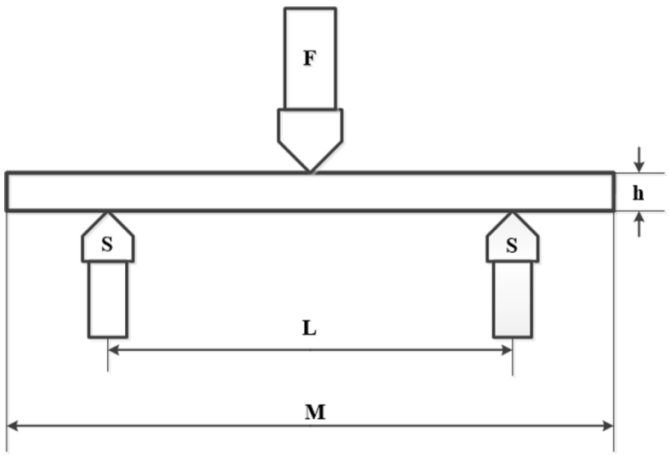

Figure 1.6. Load configuration for a beam in three point bending

In figure, where F = applied load, L = support span, h = specimen height, M= specimen length and S = fixed support

1.10.2 Apparent porosity

Bulk density is defined as "the ratio of mass to volume that contains the cavities in a porous material". The bulk density and apparent porosity are given in Eq. 1.5 and 1.6 respectively.

$$Bulk\ density = \frac{w_1}{w_3 - w_2} \tag{1.5}$$

Apparent porosity is defined as "the ratio of open pore volume to total volume".

$$Apparent\ porosity = \frac{w_3 - w_1}{w_3 - w_2} \times 100 \tag{1.6}$$

Where

w_1 = Dry weight of the sample, w_2 = Suspended weight of the sample, w_3 = Saturated weight the sample.

Bulk density and apparent porosity were measured by Archimedes principle as per ASTM C373-88 (2006). Archimedes principle states that "when an object is partially or fully immersed in a fluid it experiences an upward force that is equal to the weight of the fluid displaced by it".

1.10.3 Dielectric constant and loss tangent

Dielectric properties are also an important aspect of performance factor for wave transparent applications. Dielectric constant is defined as "a quantity measuring the ability of a substance to store electrical energy in an electric field". Dielectric constant can be calculated using Eq. (1.7) by measuring capacitance.

$$K = \varepsilon_r' = \frac{c \times d}{A} = \frac{\varepsilon_0}{\varepsilon} \tag{1.7}$$

Where K=dielectric constant, ε_r'= relative permittivity, c= capacitance, d= thickness of the specimen, A= area of cross sectional surface, ε= permittivity of the medium, ε_0= permittivity of free space or vacuum

Loss tangent is defined as "the ratio of energy loss to the relative permittivity" in Eq. 1.8.

$$\tan \delta = \frac{\varepsilon_r''}{\varepsilon_r'} \quad (1.8)$$

Where tan δ= loss tangent, ε_r''= energy loss

Loss tangent qualifies a dielectric material's inherent dissipation of electromagnetic energy.

1.10.4 Thermal Conductivity

The purpose of thermal conductivity of ceramic materials is vital to a number of industrial applications. The thermal conductivity of gelcast materials is exaggerated by a number of phases present, the pore size and distribution, the monomer content, the sintering temperature, the solid charge, etc. Above the Debye temperature the photon-photon contact by lattice vibration of the array is the main process for the conduction of heat in ceramics, and is estimated using Eq. 1.9.

$$k = \frac{1}{3} \times c \times \nu \times \lambda \quad (1.9)$$

Where k = thermal conductivity, c= specific heat of the sample, ν = elastic wave velocity or mean velocity and λ= mean free path among interactions.

1.10.5 Air Erosion Wear

Solid particle erosion (SPE) is illustrated as the ejection of material by the continuous impact of tiny erodent particles. The erosion phenomenon is useful under certain circumstances as in sand impacting and peak velocity abrasive water jet cutting but becomes a worrying factor when dealing with equipment like jet turbines, fluidized bed combustion system, pipe lines and valves carrying particulate matter, cyclone generators, gas turbines, burner parts and cutting tools (Curkovic et al., 2011, Choi et al., 2003, Wang et al., 2013 and Liu and Sun 2010). The directions of motion of solid particles contained in fluid (gaseous or liquid) medium can be accelerated or decelerated by fluid. SPE can be considered as abrasive erosion when the impact angle is between 0^o to 30^o and when impact erosion occurs for an impact angle between 60^o to 90^o.

Material loss happens by plastic misshapening or potentially brittle crack, contingent upon the material being dissolved or under working factors. Ductile materials experience

material loss from plastic distortion in which the material is evacuated by the dislodging or cutting activity of the disintegrating molecule. In brittle material, then again, the material is evacuated by the arrangement and convergence of cracks because of which grain discharge from outside the target material happens. Erosion in materials is based on many parameters like structure and characteristics of materials, exposure states, physical and chemical properties of erodent particles; which are interrelated (Murugesh and Scattergood, 1991, Srinivasan and Scattergood, 1988, Shipway and Hutchings, 1996, Zhou and Bahadur, 1991, S. Lathabai and Pender, 1995, Xiong et al., 1997, Hussainova, 2001, Celotta et al., 2007 and Hussainova, 2003).

1.11. Laser Assisted Machining (LAM)

Machinability is used to describe how easily a material can be cut to the required shape (surface finish and tolerance) with respect to the tooling and machining processes involved. In a machining operation tool life, metal removal rate, component forces and power consumption, surface finish generated and surface integrity of the machined component as well as the shape of the chips can all be used to measure machinability. The use of high strength materials like titanium alloys, nickel alloys, and tool steels, in industry is increasing (Germain et al., 2011). They are still being researched and developed to meet the increasing requirement of higher strength and heat resistance, especially in aerospace industry (Dutta and Indranil, 2013 and Sun et al., 2013). The machinability of these advanced materials is typical due to the high temperature and pressure at the cutting zone and tool. Properties such as low thermal conductivity, high cutting forces and cutting temperatures make the materials difficult to machine. This introduced a new processing method called thermal assisted machining (TAM). Thermal assisted machining includes gas torch, induction and furnace preheating method, plasma assisted machining, and laser assisted machining (Jeon et al., 2013).

The difficult-to-cut materials have good characteristics, but they are difficult to machine using conventional machines because of their physical and chemical characteristics such as brittleness (Kim et al., 2013). Laser assisted machining is a new and innovative technique for machining the hard-to-wear materials. Laser is used as a heat source with the beam focused on the un-machined section of the work piece to soften the material directly in front of the cutting tool. The addition of heat softens the surface layer of the material, so that ductile deformation rather than brittle deformation occurs during cutting (Armitage et al.,

2006). Most important advantage of laser assisted machining is its ability to produce much better workpiece surface quality than the conventional machining, together with larger material removal rates and moderate tool wear (Chang and Kuo, 2007). LAM is gaining popularity for the high laser beam intensity at low mean beam power, good focusing characteristics due to very small pulse duration, small kerf widths and narrow heat effected zones, high productivity, reduced process, eco-friendliness, low manufacturing cost and better surface finish (Kuar et al., 2006). Schematic diagram of LAM setup is shown in Figure 1.7.

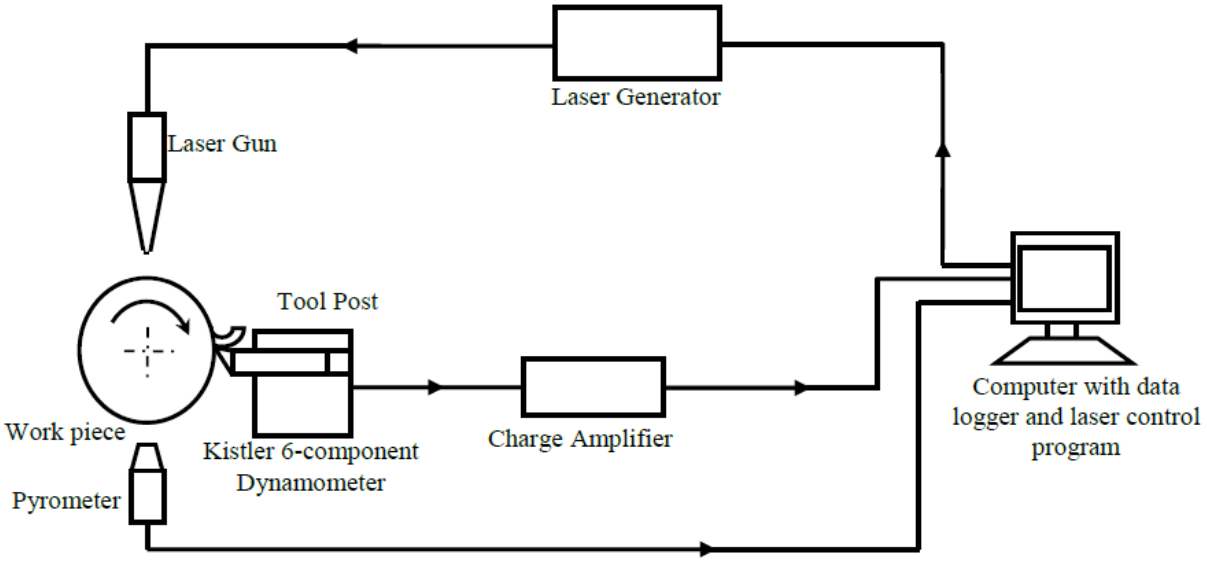

Figure 1.7. Schematic diagram of LAM setup

1.12. Hard-to-cut material

In recent years, the use of difficult-to-cut materials has increased the development of automobile, aerospace, shipbuilding and semiconductor industries, as they have much better high temperature strength, durability and corrosiveness than general metal (Melkote et al., 2009, Rozzi et al., 2000 and Mun, 2010). Difficult-to-cut materials include titanium alloy (Ti-6Al-4V alloy) (Dandekar, 2010), nickel-based superalloy (Inconel 718 alloy) (Anderson et al., 2006), compacted graphite iron (Skvarenina and Shin, 2006), mullite (Rebro et al., 2002), Si_3N_4 ceramic (Lei et al., 2000 and Kim et al., 2011), Waspaloy (Ding and Shin 2013), A359 aluminum matrix (Dandekar and Shin, 2013), AZ91 magnesium (Rashid et al., 2013), stainless steel P550 (Anderson and Shin, 2006) and hardened AISI D2 steel (Dumitrescu et al., 2006).

1.12.1 Titanium alloys

Titanium alloys are interesting materials in numerous engineering fields like engines, aerospace, vehicles, biomedical, nuclear and gas turbines etc., which is predominantly due to their properties such as high yield stress, high strength to weight ratio, high toughness, high wear resistance, high creep, high corrosion resistivity, ability to retain high strength at high temperature and fine biocompatibility (Shokrani et al., 2012 and Sun et al., 2009). Titanium alloys are categorized as difficult-to-machine materials because of low elastic modulus, high chemical affinity and low thermal conductivity (Bermingham et al., 2011). The life of the cutting tools is reduced when machining Titanium alloys.

1.12.2 Nickel based alloys

The Nickel based alloys like Inconel, Hastelloy, Nimonic, Waspaloy and Udimet, etc. have advantages over Titanium alloys which make them attractive for aerospace, gas turbine and nuclear industries because of their broad range of operational temperature at extreme conditions. Nickel based alloys poses properties such as superior hot strength, hardness, high temperature resistance, high resistance to creep and corrosion, high thermal fatigue resistivity, high erosion resistivity, resistance to thermal shock and high melting temperature. The cutting temperatures and the forces produced while machining are very high because of high strength of the nickel alloys. Drastic increase in cutting temperature leads to excessive tool wear and low surface quality of the machined part. In addition, the hardness of nickel alloys increases with increase in the temperature below 650 ^{o}C. Machining of Nickel based alloys are associated with low cutting speeds, bad surface finish, short tool life and high machining costs which make them difficult to machine materials (Shokrani et al., 2012).

1.12.3 Ceramics

Advanced engineering structural ceramics such as mullite, silicon nitride, alumina, zirconia and reaction bonded silicon nitride (RBSN) have been increasingly used for production of components like valves, rotors, bearings, roller followers, cutting tools and artificial hip joints because of their properties such as high temperature strength, low density, higher wear and corrosion resistance. Due to high brittleness and hardness, machining of ceramics is very difficult. Diamond grinding is one of the machining processes to get precision parts used in industries (Lei et al., 2001 and Shokrani et al., 2012). Alumina and

zirconia experience thermal fracture, while mullite and Si_3N_4 undergo plastic deformation at sufficiently high work piece temperatures, resulting in improved tool wear and surface roughness when oxyacetylene flame is used as heat source (Rebro et al., 2002). LAM of Si_3N_4 provides significant advantages over conventional machining (Sun et al., 2009).

1.12.4 Ferrous alloys

Iron based hard to cut alloys are classified as low carbon ductile steels, stainless steels and hardened steels used in aerospace, automotive, chemical and food processing industries. The problem in machining low carbon steels, especially AISI 1008 is that it produces continuous curled chips which can scratch machined surface, jam the automatic machine tool and causes machine down. Low carbon steels tend to adhere and produce built up edge (BUE) on the cutting tool which may affect the cutting forces, tool life and surface finish of the machined part. Low thermal conductivity, high heat capacity and high strength made the stainless steels difficult to cut materials. Hard machining is when the steels have hardness beyond 45HRC (Shokrani et al., 2012).

1.12. 5 Composites

Composites are usually inhomogeneous and anisotropic in nature due to the presence of tough and flexible reinforcement fibres or whiskers in a brittle matrix. Surface quality issues happen because of fibre pullout, delamination, uncut fibres, high dimensional deviation, and high surface roughness. The severe tool wear caused by hard abrasive particles like SiC, Al_2O_3 etc. present in the composite are harder than WC tools (Shokrani et al., 2012). Metal matrix composites have high strength to weight ratio, high stiffness, and good damage resistance over a wide range of operating conditions, which are useful for structural applications (Dandekar and Shin, 2010). Though the composites exhibit good performance, their poor machinability leads to severe tool wear, less machining efficiency and difficulty in getting good surface quality (Wang et al., 2002). Different heating methods used in thermal assisted machining are represented in Table 1.3.

Table 1.3. Heating techniques used in TAM (Jeon and Lee, 2012).

Heat source	Advantage	Disadvantage
Electricity	Simple equipment, Uniform heat distribution	Difficult to accurate control
Induction coil	Ease in use, high capacity preheating	Difficult on high concentration preheating, limited tool movement
Gas flame	Less initial investment cost	Difficult on high concentration preheating
Plasma	High degree of heat concentration, no need for electrical conduction	Difficult to precise control
Laser	High degree of heat concentration, Easy control of heat source	Costly equipment, Absorption rate different per material

1.13. Design of Experiments

At least one process parameter or factors are deliberately altered in an experiment in order to study result of changes on at least one response of variable. The Design of Experiment (DOE) is an efficient methodology for scheduling tests, with the goal that the information obtained can be analyzed to yield legitimate as well as objective conclusions (Kim, 2008).

DOE starts with finding the objectives of an experimental trail and selecting the operational factors for the experimental study. It will explain a complete experimental procedure in advance for performing the experiments. Appropriate experimental plans minimize the measure of data that can be acquired for a given measure of experimental attempt (Telford, 2007).

Methods for design of Experiments:

1. Complete randomized design.
2. Designs Randomized blocks.
3. Design of full factorial.
4. Design of fractional factorial.
5. Design Response surface method.

1.13.1 Response surface Methodology (RSM)

RSM is one of the statistical modeling methods that can be applied to get the relation between input variables and output. RSM is widely used in engineering problems and the industrial world to know the effect of process parameters on the outputs. RSM comprises observational methods committed to the advancement of connection existing between the procedure parameters of an investigation and the deliberate reactions, helpful for creating, enhancing and streamlining the procedure by directing low quantities of tests (Li et al., 2013 and Sktani et al., 2018). RSM is utilized to decide the factor levels that will at the same time fulfil an arrangement of wanted detail and to decide the ideal blend of components that yield a coveted reaction and depict that the reaction is close to the ideal. It is similar to determining how a particular output is influenced by the alterations in the level of the parts over the foreordained levels of interest and to attain a quantitative appreciation of the system (Baradeswaran et al., 2014).

The general quadratic equation is represented by Eq. 1.10.

$$Y = \beta_0 + \sum_{i=1}^{n} \beta_i x_i + \sum_{i=1}^{n} \beta_{ii} x_i^2 + \sum_{i<j}^{n} \beta_{ij} x_i x_j + \varepsilon \quad (1.10)$$

Where

Y= response (dependent variable).

β_0=constant coefficient.

β_i, β_{ii}, β_{ij}= regression coefficients for linear, quadratic and interaction effects respectively.

n= number of process parameters.

x_i, x_j= factors (independent variables).

ε= standard error.

The quality of the generated mathematical models is obtained by the coefficient of determination (R-square) while ANOVA (analysis of variance) is applied to determine the statistical significance of the model.

1.13.2 Central Composite Design (CCD)

The most generally used and known response surface design is central composite design (CCD). These are implemented enormously in developing quadratic polynomial mathematical models. CCD represented in Figure 1.8 has three types of design points.

1. Two level factorial or fractional factorial design points.
2. Axial points (sometimes called “star” points).
3. Center points.

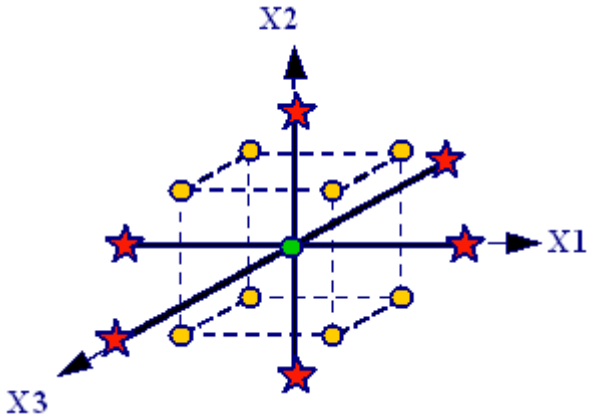

Figure 1.8. Center composite design

1.13.2.1 Factorial points

Two level factorial part of the design contains all feasible combinations of -1 and +1 levels of the factors. Four design points are obtained for two factor problem. The design points are: (-1, +1) (-1, -1) (+1, -1) (+1, +1)

1.13.2.2 Star or Axial points

The star points consist of factors set to zero, midpoint except one factor which has value + or –α. For a two factor case the star points are: (-α, 0) (+α, 0) (0, -α) (0 +α)

The ‘α’ value is determined in each design for both blocks i.e. rotatability and orthogonality. The engineer can select between this data set or choose a different one. Generally the value is always set to the rotatable value. Another location for the star points is at the face of the cube segment on the design. This is generally named face centered central composite design.

1.13.2.3 Center points

Center points as the name implies, are points with all levels set to coded level 0, with midpoint of each factor range being (0, 0). Center points are generally iterated 4-6 times to obtain a better estimate of pure error (experimental error). For example, with 2 factors the design will be generated with 5 center points by default.

On the other side, the major setback of RSM is to fit the data to a quadratic polynomial. It can't be said that all systems containing curvature are well accommodated by the quadratic polynomial (Rao, 2011). Hence, trail experiments are required to obtain the range of independent input parameters.

1.13.3 Multi objective optimization

The multi objective optimization was conducted on gelcasting process followed by mathematical modeling and analysis. Desirability is an objective function D, introduced by Myers and Montgomery and its desirable value (d_i) ranges from 0 to 1, least to most desirable, respectively. Desirability function empowers adjusting among every single test reaction with extra advantages such that the outcomes can be plotted. It has advantage over other multi model advancement procedures like linear programming. Any process that deals with identifying ideal working conditions to accomplish the best item quality for a specific application. On account of different strife destinations and communication impact of the procedures, a preferred manufacturing strategy is needed as far as finding the ideal procedures factors and creating vigorous modern applications is concerned.

The desirability function was utilized to change every reaction (yi) into a solitary allure that shifts over the range $0 \leq d_i \leq 1$, where $d_i=1$ when an objective fulfills the reaction necessity and $d_i=0$ when the objective is outside the acknowledged area. If the objective is minimized, then desirability function was chosen to limit the response in Eq. 1.11, while the objective is maximized, desirability from most extreme and the better one was chosen utilizing Eq. 1.12:

$$d = \begin{cases} 1, & y < T \\ \left(\frac{(U-y)}{(U-T)}\right)^r & T \leq y \leq U \\ 0 & y > U \end{cases} \quad (1.11)$$

Where, U is the upper limit, T is the target, and r is the desirability weight.

$$d = \begin{cases} 1, & y < L \\ \left(\frac{(y-L)}{(T-L)}\right)^r & L \leq y \leq T \\ 0 & L > T \end{cases} \quad (1.12)$$

Where, L is the lower limit, T is the target, y is response and r is the desirability weight.

Once every reaction is changed, the individual desirabilities are then consolidated into a solitary reaction utilizing the general attractive quality capacity, which gives worldwide ideal of the multi-reaction streamlining, as communicated in Eq. 1.13. The factor settings with the most noteworthy worldwide attractive quality are chosen to be ideal settings.

$$d = \begin{bmatrix} (\prod_{i=1}^{n} d_{i1})^{1/n} \\ (\prod_{i=1}^{n} d_{i2})^{1/n} \\ (\prod_{i=1}^{n} d_{i3})^{1/n} \end{bmatrix} \quad (1.13)$$

Where, D is the overall desirability, n is the total number of experimental responses and d_1, d_2, d_3 . . . d_n are single desirability function for each response (Mia, 2018, Mohamed et al., 2016 and ChittaranjanDas, 2016).

1.4 Organization of the thesis

The structure of the thesis is as follows

Chapter 1 presents a brief introduction to the ceramic materials and their applications. Different types of near net shaping methods, especially wet processing techniques are discussed. This chapter also discussed the gelcasting procedure in detail. This chapter also gives an overview of the characterization and erosion testing of the ceramics. This chapter briefly introduces the concept of laser assisted machining. This chapter also presents the development of regression models and multi response optimization using response surface methodology. This chapter also gives an overview of the content of this thesis.

Chapter 2 focused on literature review, which consists of six sections. In the first section, review of wave transparent materials using different processing techniques was discussed. The second section analyzed the influence of reinforcements like Si_3N_4, BN and other additives which affect the properties of SiO_2 based ceramics. In the third section, analysis of solid particle erosion studies of different materials and effect of various process variables on erosion rate are discussed. In the fourth section, laser assisted machining of ceramics, titanium based alloys, nickel based alloys, metal matrix composites and ferrous alloys are explored. Review of modeling and multi objective optimization is presented in the fifth section. Finally, in the sixth section, gaps in literature are identified and analyzed. Research objectives are projected and a work plan is developed to attain research objectives.

Chapter 3 summarizes the description of materials and equipment utilized to measure the performance characteristics. Experimental setup used in this work is described in this chapter. This chapter also provides details of sample processing and their characterization for different fused silica based composites. It identifies experimentally the appropriate ceramic slurry system and processing routes of porous SiO_2–Si_3N_4–BN and SiO_2–Si_3N_4–Al_2O_3 ceramic composites using gelcasting method, measurement and analysis of methods for related properties. This chapter also discusses the methodology used for conducting both gelcasting and laser assisted machining.

Chapter 4 deals with the characterization of porous SiO_2–Si_3N_4–BN and SiO_2–Si_3N_4–Al_2O_3 ceramic composites by varying monomer content, the ratio of monomers and solid loading. The results of mechanical and dielectric constant of the sintered SiO_2–Si_3N_4–BN and SiO_2–Si_3N_4–Al_2O_3 ceramic composites are presented. This chapter also discussed the development of regression models for SiO_2–Si_3N_4–BN and SiO_2–Si_3N_4–Al_2O_3 ceramic composites and also the effect of process parameters on responses. The optimal process parameters are obtained using RSM coupled with desirability function.

Chapter 5 presents the solid particle erosion studies of SiO_2, SiO_2–Si_3N_4–BN and SiO_2–Si_3N_4–Al_2O_3 ceramics with SiO2 particles as erodent. This chapter discusses the effect of various impingement angle and impact velocities on erosion rate. It also discusses the influence of acute and normal impingement angles on surface roughness and morphology of the SiO_2, SiO_2–Si_3N_4–BN and SiO_2–Si_3N_4–Al_2O_3 ceramics at with higher impact velocity.

Chapter 6 deals with laser assisted machining of SiO_2–Si_3N_4–Al_2O_3 ceramic composite performed using the experimental plan obtained by RSM with a face centered central composite 6 points at the center. It studies the influence of process parameters on responses by developing regression models. This chapter also presents multi response optimization of laser assisted machining of SiO_2–Si_3N_4–Al_2O_3 ceramic composite. The responses are simultaneously optimized and the optimal levels of the process parameters are determined. Finally, the main findings and conclusions of this investigation are summarized in Chapter 7. Also, at the end, a few suggestions for future work on the related topics have been enumerated.

Summary

This chapter presents a brief introduction to the ceramic materials and their applications. Different types of near net shaping methods, especially wet processing techniques are discussed. This chapter also discussed the gelcasting procedure in detail. This chapter also gives an overview of the characterization and erosion testing of the ceramics. This chapter briefly introduces the concept of laser assisted machining. It also presents the development of regression models and multi response optimization using response surface methodology. The chapter also gives an overview of the content of this thesis.

CHAPTER 2

LITERATURE REVIEW

2.1. Introduction

In the current scenario, ceramic composites are widely used in engineering applications, especially in aerospace where aircraft parts are fabricated using gelcasting. The necessity of using gelcasting is due to its simple in nature and its capability to process complicated shapes used in many industries. Hence, studies on gelcasting technique are attaining popularity now-a-days. Laser assisted machining (LAM) is gaining importance due to its ability to machine difficult to cut materials. Now a days LAM is used to machine different types of super alloys such as nickel based and titanium based alloys as well as structural ceramics, ferrous alloys, metal matrix composites, etc. A thorough literature review is presented in this chapter dealing with designing wave transparent materials using different fabrication techniques and laser assisted machining of difficult to cut materials.

2.2. Wave Transparent Materials

A brief review of the state-of-art papers published related to various materials used for wave transparent applications is presented in this section.

Yang et al., (2016) fabricated porous silicon nitride wave transparent ceramics through gelcasting and pressureless sintering. It investigated porous silicon nitride sintered at 1650 ^{o}C for 3 hours with 3 wt% of sintering additives (Y_2O_3/Al_2O_3). They obtained a porosity of 39.28%, flexural strength of 146 MPa, fracture toughness of 1.44 MPa. $m^{1/2}$ and dielectric constant of 4.03 at a frequency of 14 GHz .

Zou et al., (2013) fabricated wave transparent porous silicon nitride ceramics using gelcasting and gas pressure sintering. The influence of solid loading on microstructure, mechanical and dielectric properties was studied. Solid loading has an appreciable effect on porosity, flexural strength and dielectric properties. As solid loading increases from 30 to 45 vol%, porosity decreased from 57.6 to 36.4%, flexural strength enhanced from 108.3 to 235.1 MPa, dielectric constant increased from 2.63 to 3.68 and loss tangent increased from 0.00285 to 0.00356.

Wang et al., (2013) produced porous BN/Si_3N_4 ceramics through gelcasting. Polymethylmethacrylate microsphere (PMMA) was selected as pore forming agent. The influence of PMMA on microstructure, phase composition, mechanical and dielectric properties of porous ceramics was examined. It is observed that addition of 10 wt% of PMMA enhances flexural strength to 71.6±4.5 MPa and dielectric constant to 3.35.

Duan et al., (2012) fabricated silica fiber reinforced silica and boron nitride based composites (SiO_{2f}/SiO_2-BN) using sol gel technique and urea route. The influence of oxidation treatment on the structure, mechanical and dielectric properties of composites was studied. The oxidation treatment at 450 ^oC of the composite resulted in a density 1.81 g/cm^3, flexural strength 113.9 MPa and elastic modulus 36.5 GPa. The composite exhibits exceptional dielectric properties with dielectric constant and loss tangent of 3.22 and 0.0039 respectively.

Duan et al., (2012) et al manufactured porous Si_3N_4 ceramics with varying amounts of $CaHPO_4$ as an additive using gelcasting. Influence of $CaHPO_4$ can enhance the sintering capability and phase change from α-Si_3N_4 to β–Si_3N_4. The results show that flexural strength, elastic modulus, fracture toughness reach 365.1 MPa, 107.9 GPa and 3.82 MPa. $m^{1/2}$ respectively at 15 wt% of $CaHPO_4$. The dielectric constant increases (α-Si_3N_4=5.6, β-Si_3N_4=7.9) with the addition of $CaHPO_4$.

Wang et al., (2012) prepared porous BN/Si_3N_4 composite ceramics with varying proportions of BN content using gelcasting. Addition of BN content, mechanical properties of BN/Si_3N_4 were partly reduced, but dielectric properties and thermal shock resistance improved. Pure Si_3N_4 ceramics possess porosity of 48.1%, flexural strength of 128 MPa, dielectric constant of 4.1 and critical temperature difference of 395 ^oC. By the addition of 10 wt% of BN to Si_3N_4, porosity, flexural strength, dielectric constant and critical temperature difference reached 49.4%, 106.6 MPa, 3.8 and 445 ^oC respectively.

Wang et al., (2010) et al fabricated wave transparent materials used in high supersonic and hypersonic speed applications with silicon nitride powders using low mold pressure (10 MPa) and pressureless sintering. The obtained flexural strength, porosity, dielectric constant and dielectric loss were in the range of 57-176 MPa, 45-60%, 2.35-3.39 and 0.0016-0.0035 respectively.

Li et al., (2010) prepared porous silicon nitride ceramics with Y_2O_3 as sintering additive and naphthalene powder as pore forming agent by gas pressure sintering. Porosity of the sintered Si_3N_4 ceramic went from 40-54% when Y_2O_3 amount increased from 3 to 15 wt% and sintering temperature increased from 1700 to 1850 ^oC. The flexural strength of the porous ceramic reached 226 MPa.

Yu et al., (2009) fabricated high performance porous Si_3N_4 ceramics using gelcasting. The effect of monomer content and monomer ratio on the preparation of porous Si_3N_4 was studied. It was found that monomer content and monomer ratio had great influence on mechanical and physical properties of porous Si_3N_4 ceramics. The flexural strength and porosity of Si_3N_4 ceramics are above 130 MPa and 50% respectively as the pore size is less than 1 μm.

Yu et al., (2008) fabricated Al borate whisker reinforced Al phosphate composites with normal pressure sintering. The crystallization of Al phosphate was reduced and mechanical properties of aluminum borate whisker reinforced aluminum phosphate composite were enhanced by aluminum borate whisker. The flexural strength of ceramic composite reached 215.3 MPa with 30 vol% aluminum borate whisker sintered at 1050 ^oC for 1 hour. Dielectric constant and loss tangent of the composites were 4.23 and 0.0024 at 10 GHz.

Ganesh et al., (2008) emphasized the characteristics of differently prepared β–$Si_4Al_2O_2N_6$ ceramics. Dense β-$Si_4Al_2O_2N_6$ ceramics were obtained from α–Al_2O_3, α–Si_3N_4, Y_2O_3 and AlN powders sintering at 1675 ^oC for 4 hours, with green bodies consolidated by a conventional dry powder processing and an aqueous gelcasting technique.

Zhou et al., (2001) prepared Si_3N_4 ceramics using a processing strategy which includes (i) coating of silicon nitride powder with sintering aid. (ii) Oxidation of the coating. (iii) Cold isostatic pressing. (iv) Gelcasting of green samples. (v) Gas pressure sintering. This processing strategy improves the flexural strength and Weibull modulus of silicon nitride ceramics to 944.7±29.5 MPa and 33.9 respectively.

Glide et al., (1997) prepared a silicon oxynitride (SiON) nanocomposite by calcination of α–Si_3N_4 ceramic powder at 1700 ^oC in open environment. The sintering was conducted in nitrogen atmosphere at a temperature greater than 1800 ^oC. The dielectric constant is obtained 4.78 at room temperature and 0.0025 at 1000 ^oC. Table 2.1 shows the overview of materials used for Radome fabrication.

Table 2.1. Overview of materials used for Radome fabrication.

S. No.	Author	Year	Material	Processing Technique	Flexural strength (Mpa)	Dielectric constant (ε)	Loss tangent (tan δ)
1	Xuejin Yang et al	2016	Si_3N_4	Gelcasting and pressureless sintering	146	4.03	–
2	Chunrong Zou et al	2013	Si_3N_4	Gelcasting and gas pressure sintering	235.1	3.68	0.00356
3	Shengjin Wang et al	2013	BN/Si_3N_4	Gelcasting	71.6	3.35	–
4	Li Duan et al	2012	SiO_{2f}/SiO_2–BN	Sol gel method	113.9	3.22	0.0039
5	Xiaoming Duan et al	2012	Si_3N_4	Gelcasting	365.1	7.9	–
6	Shengjin Wang et al	2012	BN/Si_3N_4	Gelcasting	106.6	3.8	–
7	Hongjie Wang et al	2010	Si_3N_4	Low molding pressure and pressureless sintering	176	3.39	0.0035
8	Yong Li et al	2010	Si_3N_4	Gas pressure sintering	226	–	–
9	Juanli Yu et al	2009	Si_3N_4	Gelcasting	130	–	–

10	Lu ZhenYu et al	2008	Aluminum borate whisker reinforced aluminum phosphate	Normal pressure sintering	215.3	4.23	0.0024
11	Ibram Ganesh et al	2008	β–$Si_4Al_2O_2N_6$	Gelcasting	226	7.22	–
12	Longjie Zhou et al	2001	Si_3N_4	Process strategy	944.7	–	–
13	Gary Glide et al	1997	Si_2N_2O	Calcination	–	4.78	0.0014

2.3. Fused silica (SiO_2) ceramics

Wan et al., (2014) examined the gelcasting process prepared using a monomer NN-dimethylacrylamide (DMAA) as a gel system. Influence of solid loading on rheological properties of slurries, properties of green samples and sintered ceramics were investigated. The maximum solid loading of 65 vol% was achieved by gelcasting process. It was found that the highest flexural strength of 15.4 MPa for green bodies and 67.4 MPa for sintered bodies was obtained at the solid loading of 64 vol% and 66 vol% respectively. Dielectric constant of 3.27 and dielectric loss (1 MHz) of 7.82 $\times 10^{-4}$ were achieved at solid loading of 64 vol%.

Wan et al., (2014) examined the effect of sintering temperature on microstructure, mechanical, dielectric properties and thermal shock resistance of fused silica ceramics fabricated by gelcasting using low toxicity 2-hydroxyethyl methacrylate and toxic acrylamide system. Fused silica ceramics sintered at 1275 ^{o}C have maximum flexural strength of 81.32 MPa but higher co efficient of linear expansion (2.56×10^{-6}/k at 800 ^{o}C). It was found that fused silica ceramics have excellent flexural strength of 67.43 MPa, residual strength of (after thermal shock) 65.45 MPa, dielectric constant of 3.34 and lowest dielectric loss of 1.20×10^{-3} (@1 MHz) at sintering temperature of 1250 ^{o}C .

Wan et al., (2014) studied the effect of natural glutinous rice flour (GRF) as binder on density and flexural strength. The GRF based aqueous system was found to behave exceptionally well in gelcasting process. Flexural strength of green bodies at 3 wt% of GRF was found to be 11.87 MPa. The sintered bulk density and flexural strength of ceramics were 1.72 g/cm^3 and 47.02 MPa respectively.

Wan et al., (2013) investigated the effect of non-toxic and water soluble monomer NN-dimethylacrylamide (DMAA) as a gelling agent in gelcasting fused silica. The selected dispersant is acrylic acid-2-acrylamide-2-methypropane sulphonic acid co polymer (AA-AMPS) which is used to make high vol% solid loadings and low viscous slurries. Zeta potential, pH, dispersant dosage, solid loading and milling time have been investigated to fabricate optimum gelcasting slurries. It was reported that optimum conditions were pH of 4.8, dispersant dosage of 0.1–0.2 wt% and milling time of 5 hrs. Bending strength of the fused silica green samples was reached up to 20.16 MPa with 3.14% polymer. Bulk density and

flexural strength of sintered fused silica obtained was 1.975 g/cm^3 and 81.36 MPa respectively with the introduction of nano-meter silica which is a sintering booster.

Manivannan et al., (2013) studied the effect of solid loading in aqueous gelcasting of fused silica ceramics with colloidal silica as binder. The optimum solid loading of 73 vol% and viscosity of 0.70 Pa.s was found suitable for gelcasting system. The maximum flexural strength was 9 MPa for green body and 60 MPa for sintered body; density of 88% for green body with 2.2% dry shrinkage and 95% theoretical for sintered body with 4.3% drying shrinkage. The physical and mechanical properties of fused silica were improved due to the filling of nano-silica particles in the interstitial position of green body.

Mao et al., (2006) reported the fabrication of porous silica ceramics using starch consolidation casting technique. Ball milled starch with different proportions were mixed to the slurry. Flexural strength of sintered specimens varied from 10 MPa to 20 MPa, and low dielectric constant varied from 2 to 2.4 corresponding porosity varies from 42-56%.

Zhang et al., (2006) studied the fabrication of high strength ceramic green parts using gelcasting with 2-hydroxyethyl methacrylate (HEMA), a toxicity gel. The HEMA based aqueous systems was found to perform as well as AM based systems in terms of properties of gelcasting suspensions, cast green parts and densified components.

2.4. SiO_2-Si_3N_4 ceramic composites

Lin et al., (2016) studied the effect of temperature and atmosphere on microstructure and properties of Siliconoxynitride (Si_2N_2O) which was radomes material with multilayer structures, prepared by two step sintering method. Results reported that the decomposition of Si_2N_2O is the reason for multilayer formation. The flexural strength of material decreased after it decomposed at 1600–1700 ^oC while decomposition which occurred at 1800 ^oC strengthened the ceramic bodies. It is found that flexural strength ranges from 210–236 MPa, dielectric constant <4.8 and loss tangent (tan δ) <0.0044.

Zou et al., (2012) fabricated porous Si_3N_4 ceramics with high porosity using gelcasting, a near net shape technique. Different proportions of amorphous silica were added to porous Si_3N_4 frames by repeating the sol gel infiltration and sintering process. Improvement in density and formation of well distributed micro pores with both uniform pore

size and smooth pore wall was observed in sol gel process. The flexural strength and fracture toughness increased from 92.6 MPa and 1.05 MPa. $m^{1/2}$ to 148.1 MPa 1.70 MPa. $m^{1/2}$ respectively and porosity decreased from 49.3% to 22%; as SiO_2 content was added from 0 to 25.9 vol%. The dielectric constant increased from 2.65 to 3.61, but dielectric loss did not change much (3.23×10^{-3} to 3.84×10^{-3}).

Ganesh et al., (2010) fabricated dense β–SiAlON–SiO_2 varying SiO_2 20, 40, 60 and 80 wt% from β–$Si_4Al_2O_2N_6$ and fused silica at sintering temperature 1500-1700 ^oC for 3-4 hours. Powder mixture containing 60 wt% β–$Si_4Al_2O_2N_6$ and 40 wt% fused SiO_2 was consolidated followed by a neat net shape process based on hydrolysis induced aqueous gelcasting (GCHAS). The ceramics exhibited a flexural strength of 140 MPa, Young's modulus of 214 GPa, co efficient of thermal expansion of $3.5\times10^{-6}/^oC$, hardness of 1390 kg/mm^2, fracture toughness of 4.2 $MPa.m^{1/2}$, dielectric constant of 5.896 and tan δ of 0.002 at sintering temperature of 1750 ^oC for 3 hours.

Jia et al., (2003) investigated the mechanical properties under ambient and elevated temperature of two types of hot pressed fused silica ceramic composites, SiO_2+5 vol% Si_3N_4 and SiO_2+5vol% Si_3N_4+10vol%. The ambient strength and fracture toughness improved by the addition of Si_3N_4. By the addition of chopped carbon fibers, fracture toughness suddenly increased from 1.22 to 2.4 MPa. $m^{1/2}$. The strength of two composites reached maximum at 1000 ^oC i.e. 168.9 and 130.6 MPa which were 77% and 77.4% higher than their atmospheric strength respectively. Table 2.2 shows overview of fabrication of SiO_2 and Si_3N_4–SiO_2 ceramic composites.

2.5. SiO_2–BN ceramic composites

Jia et al., (2011) fabricated boron nitride reinforced fused silica matrix composites using cold isostatic pressing (CIP) and gelcasting methods. Two types of fused SiO_2 powders with various particle sizes 5.82 μm and 3.24 μm in d50 were used. Gelcasting technique shows exceptional performance in terms of thermal stability, sinterability and mechanical properties over CIP. The flexural strength, fracture toughness and Young's modulus reached highest values of 101.5±4.3 MPa, 1.57±0.04 MPa. $m^{1/2}$ and 61.3 GPa respectively.

Zhai et al., (2007) prepared BN–SiO_2 composite ceramics using hot pressing of hexagonal boron nitride (h–BN) powder and SiO_2 sol. The mechanical properties were studied

by varying SiO_2 content from 10 wt% to 40 wt%. The maximum flexural strength and fracture toughness was found to be 180.30 MPa and 3.20 MPa. $m^{1/2}$ respectively. The dielectric constant and loss tangent were found to be 2.5-2.8 and 10^{-3} respectively at an electromagnetic frequency range 1 MHz to 2 GHz.

Wen et al., (2000) studied the effect of the content of BN on mechanical properties, when added to fused silica matrix by hot pressing process. The sinterability and thermal shock resistance of BN content increased but ablation surface temperature was reduced due to presence of fused SiO_2. The maximum bending strength of 246 MPa and fracture toughness of 2.87 MPa. $m^{1/2}$ were obtained at 60 vol% BN, which are 5.2 and 6 times greater than the monolithic fused silica SiO_2 respectively.

2.6. SiO_2–Si_3N_4–BN ceramic composites

Dong et al., (2012) fabricated porous Si_3N_4/SiO_2/BN ceramic composite using dry pressing and pressureless sintering at a temperature of 1750 ^oC under nitrogen environment. High strength and low dielectric constant were observed in porous ceramic composites. The effect of born nitride content on microstructure, porosity, mechanical and dielectric properties of porous ceramic composites were evaluated. The fabricated porous ceramics possess porosity in the range of 29% to 48% at different proportions of BN content. The flexural strength of ceramic composite ranged from 78-215 MPa and dielectric constant lay between 3.9 and 5 at 1 MHz frequency.

Long et al., (2012) prepared porous Si_3N_4 ceramics incorporated with hexagonal boron nitride (h-BN) and SiO_2 nano particles using pressureless sintering at relatively low temperature in which stearic acid was used as pore forming agent. The effect of reinforcements BN and SiO_2 nanoparticles on mechanical properties and thermal shock resistance of porous Si_3N_4 ceramics were evaluated. The porous ceramic composites obtained possess good thermal shock resistance of 800 ^oC, high flexural strength (130 MPa) and high porosity.

Weiru et al., (2008) fabricated Si–B–O–N microwave transparent ceramic composites using gas pressure sintering (GPS). The influence of BN and SiO_2 nano particle amount on the mechanical and dielectric properties of the ceramic composite was examined. The flexural strength of composite varied from 74.7 MPa to 174.83 MPa, the dielectric constant varied from 3.5 MPa to 4.2 and loss tangent varies from 0.5×10^{-3} to 4.5×10^{-3}.

Jiang et al., (2007) fabricated 2.5D SiO_{2f}–Si_3N_4–BN composites for high temperature application through preceramic polymer impregnation pyrolysis (PIP) technique with repeated infiltration of hybrid precursor and pyrolysis at high temperature in ammonia environment. PIP method is a fast way to prepare dense composite due to the low viscosity, good wettability and higher yield of hybrid ceramic polymers. The flexural strength, dielectric constant, loss tangent and surface recession rate obtained are 101.8 MPa, 3.4, 6×10^{-3} and 0.038 mm/sec respectively.

Jiang et al., (2007) fabricated SiO_{2f}/Si_3N_4–BN composites using repeated infiltration of hybrid preceramic precursor and pyrolysis at high temperature in ammonia environment. Moisture behavior of SiO_{2f}/Si_3N_4–BN composite and influence of moisture on mechanical properties and microstructure were examined. Flexural strength can be adjusted and a maximum value of 161.7 MPa attained by controlling moderate relative humidity. Table 2.3 shows overview of fabrication of BN-SiO_2 and SiO_2-Si_3N_4-BN ceramic composites.

2.7. SiO_2 and other reinforcement ceramic composites

Wan et al., (2016) examined the influence of a small quantity of alumina (Al_2O_3) on mechanical strength, thermal shock resistance, room temperature and high room temperature dielectric and ultra high temperature ablation properties of fused SiO_2 ceramics fabricated by gelcasting. Addition of 0.5 wt% of Al_2O_3 enhances flexural strength to 79.9 MPa and thermal shock residual strength to 82 MPa. Prominently, the addition of Al_2O_3 did not reduce the outstanding ambient temperature or high temperature dielectric properties of fused SiO_2 ceramics. The dielectric constant of 3.54 and dielectric loss of 3.03×10^{-3} was obtained after addition of 0.5 wt% of Al_2O_3 to the fused silica.

Wan et al., (2016) fabricated fused silica ceramics adding zirconia (ZrO_2) through gelcasting. The influence of ZrO_2 inclusion on the mechanical strength, thermal shock resistance, microstructure, ambient temperature and high temperature dielectric properties of fused SiO_2 ceramics was examined. The flexural strength reaches 97.6 MPa by the addition of 10 wt% ZrO_2. Prominently, ZrO_2 seems to have a small effect on exceptional high temperature dielectric properties of fused SiO_2 ceramic parts. The dielectric constant of 4.63 and dielectric loss of 1.55×10^{-3} was observed after the inclusion of 10 wt% ZrO2 to the 3.03×10^{-3}. Table 2.4 shows overview of fabrication of SiO_2 and other reinforcement ceramic composites.

Table 2. 2. Overview of fabrication of SiO_2 and Si_3N_4–SiO_2 ceramic composites

S. No.	Authors	Year	Fabrication Technique	Material	Flexural Strength (MPa)	Dielectric constant (ε)	Loss tangent (Tan δ)
1	Wei. Wan et al	2014	Gelcasting	Fused Silica	47.02	–	–
2	Wei. Wan et al	2014	Gelcasting	Fused Silica	67.4	3.27	7.52×10^{-4}
3	Wei. Wan et al	2014	Gelcasting	Fused Silica	81.32	3.34	1.20×10^{-3}
4	Wei. Wan et al	2013	Gelcasting	Fused Silica	81.36		
5	R. Manivannan et al	2013	Gelcasting	Fused Silica	60	–	–
6	MAO Xiao-Jian et al	2006	Starch consolidation casting	Silica	20	2.1	–
7	Yu Zhang and Yi-Bing Cheng	2006	Gelcasting	Fused Silica	30	–	–
				Si_3N_4–SiO_2			
1	Shaojie Lin et al	2016	Uniaxial + isostatic pressing	Si_3N_4–SiO_2	236	4.8	0.0044
2	Chunrong Zou	2012	Gelcasting	Si_3N_4–SiO_2	148.1	3.61	3.84×10^{-3}
3	Ibram Ganesh and Govindan Sundararajan	2010	Gelcasting	B-SiAlON–SiO_2	140	5.896	0.002
4	Xiangming Li et al	2009	Sol gel infiltration	Si_3N_4–SiO_2	120	3.80	3.11×10^{-3}
5	D.C. Jia et al	2002	Hot pressing	SiO_2+5 vol% Si_3N_4	168.9	–	–

Table 2.3. Overview of fabrication of BN-SiO_2 and SiO_2-Si_3N_4-BN ceramic composites

S. No.	Authors	Year	Fabrication Technique	Material	Flexural Strength (MPa)	Dielectric constant (ε)	Loss tangent (Tan δ)
1	Ming Du et al	2011	Hot pressing	BNNPs/SiO_2	120.2	–	–
2	Dechang Jia et al	2011	Gelcasting	BNp/SiO_2	101.5	–	–
3	Huazhang et al	2007	Hot pressing	BN–SiO_2	180.30	2.8	0.001
4	G. Wen et al	2000	Hot pressing	BN–SiO_2	240	–	–
				SiO_2-Si_3N_4-BN			
1	Wei Dong et al	2012	Dry pressing	Si_3N_4–SiO_2–BN	215	5	–
2	Na-Na Long et al	2012	Pressureless sintering	BN–SiO_2–Si_3N_4	130	–	–
3	J. C. Han et al	2010	Partial sintering	Si_3N_4–BN–SiO_2	60	2.67	–
4	Zhang Weiru	2008	Gas pressure sintering	Si_3N_4–BN–SiO_2	174.83	4.2	4.5×10^{-3}
5	Young Gang Jiang et al	2007	Preceramic polymer impregnation pyrolysis (PIP)	2.5DSiO_{2f}/Si_3N_4–BN	101.8	3.4	6×10^{-3}
6	Y. G. Jiang et al	2007	Hybrid preceramic precursor and pyrolysis	SiO_{2f}/Si_3N_4–BN	161.7	–	–

Table 2.4. Overview of fabrication of SiO_2 and other reinforcement ceramic composites

S. No.	Authors	Year	Fabrication Technique	Material	Flexural Strength (MPa)	Dielectric constant (ε)	Loss tangent (Tan δ)
1	Wei Wan et al	2016	Gelcasting	Fused silica+0.5 wt% Al_2O_3	79.9	3.54	3.03×10^{-3}
2	Wei Wan et al	2016	Gelcasting	Fused silica+ Zirconia	97.6	4.63	1.55×10^{-3}

2.8. Laser Assisted Machining (LAM)

Laser assisted machining was first introduced in 1970 and has since been proven by many studies as an effective method for improving the machinability of difficult to machine materials such as nickel based alloys, titanium alloys and hardened steels. LAM is based on laser as a heat source where the beam is focused on the un-machined area of workpiece; the heated material is consequently removed in chips by cutting tool. This means that the previously heated material is removed.

2.8.1. Laser Assisted Machining of Ceramics

Lie et al., (2001) evaluated the LAM of silicon nitride. The performance parameters like tool wear, metal removal mechanism, surface integrity and subsurface damage were measured at different input parameters such as preheating time and laser power. The tool life improved with LAM compared to conventional machining. The predominant mode of tool wear was adhesion which could be minimized by maintaining the cutting zone temperature which makes easy material removal. The grinding thickness is more than the thickness of layer of work piece affected by LAM (2 to 4 μm). There is no possibility of subsurface cracks on machined surface and the degradation of material strength in LAM.

Rebro et al., (2002) presented the evaluation of laser-assisted machining (LAM) of pressureless sintered mullite ceramics. A wide range of operating conditions were set from input parameters like laser power, beam diameter, laser tool distance, feed rate, cutting speed and depth of cut to get optimum performance measures such as cutting forces, specific cutting energy, metal removal temperature and surface temperature. The laser power in the range 170 W to 190 W enables the decrease in specific cutting forces, considerable amount of improvement in the tool life and work piece surface properties. To reduce thermal cracks, the depth of cut should be approximately 0.75 mm. To maintain adequate temperature gradients and avoid thermal fracture, the feeds range from 0.012 to 0.016 mm/rev provided there is sufficient laser energy absorption. Thermal fracture of the work piece is due to the induced excessive temperature gradients caused by higher feed rates.

Chang et al., (2007) studied laser-assisted machining experiments on aluminum oxide (Al_2O_3) ceramic materials under various operating conditions like rotational speed, feed, depth of cut and laser pulsed frequency. The performance measures are surface roughness and

material removal rate. Higher rotational speeds are required to get good surface roughness. The material removal temperature exceeds 850 ^{o}C means that laser power provides sufficient energy for the work piece to reach glass transition temperature and easily machined.

Pfefferkorn et al., (2004) investigated the LAM of magnesia partially stabilized zirconia (PSZ) to determine the effect of heating on performance measures such as cutting energy, tool wear, metal removal mechanism and surface integrity using polycrystalline cubic boron nitride (PCBN) cutting tool. The specific cutting energy reduced from 6.6 to 2.6 J/mm^3 and tool life increased from 3 to 120 minutes by enhancing the material removal temperature from 530 to 1210 ^{o}C. The specific cutting energy reduced with an increase in feed even though there is considerable decrement in the material removal temperature. The optimum range of material removal temperature for this matrix is approximately 900 to 1100 ^{o}C. Table 2.5 shows overview of laser assisted machining of ceramics.

2.8.2. Laser Assisted Machining of Titanium alloys

Dandekar et al., (2010) used Laser assisted machining (LAM) and Hybrid machining to improve the tool life and material removal rate. The input parameters for the two processes were tool material and material removal temperature, the output parameters measured are cutting force, specific cutting energy, surface roughness, microstructure and tool wear. The tool life improved by a factor 1.7 using LAM for cutting speeds below 107 m/min compared with conventional machining, while tool life increased by 2 times by hybrid machining for cutting speed below 150 m/min, at a metal removal temperature of 250 ^{o}C. The tool life of the K68 tool material for the same machining conditions for dry, laser assisted and hybrid machining were 28.62 min, 48.78 min and 55.10 min respectively.

Bermingham et al., (2012) characterized the tool life and wear mechanism for uncoated carbide tools using thermally assisted machining (TAM). This process reduces the component of cutting forces up to 30% by preheating the work piece to 350 ^{o}C. The tool life is improved only up to 7%, which is insignificant compared to the over 235% improvement that occurs when coolants are used for same cutting conditions.

Rashid et al., (2012) studied the effect of laser beam on cutting force and cutting temperatures inspected over a range of feed rates and cutting speeds. The cutting forces were reduced by 15% over a total range of cutting speeds and feed rates. The optimum feed rates

for industrial application to get maximum advantage with laser power of 1200 W were between 0.15 mm/rev to 0.25 mm/rev. Below a feed of 0.15 mm/rev, there was insignificant reduction in cutting energy, whereas above 0.25 mm/rev, the tool wear developed rapidly. While machining of titanium alloy with a laser power of 1200 W, the optimum cutting speed range was 25 m/min to 100 m/min. Above 100 m/min, the tool wear was maximum and below 25 m/min, excessive heat energy caused chip tool welding which spoiled the surface integrity of the machined surface. The temperature range should be 1050 ^{o}C to 1250 ^{o}C to achieve the significant reduction in cutting forces while machining Titanium alloys with the assistance of laser power.

Rashid et al., (2012) again stated that a laser power range of 1200 W to 1600 W would be productive in reducing the cutting forces during LAM with cutting speeds between 25 m/min and 125 m/min.

2.8.3. Laser Assisted Machining of Nickel based alloys

Anderson et al., (2006) evaluated the machinability of Inconel 718 under varying conditions such as feed and depth of cut by examining tool wear, cutting forces, surface roughness, and specific cutting energy. The specific cutting energy reduces by 25%, the improvement in the surface roughness by a factor of 2–3 and there is a 200–300% increase in ceramic tool life over conventional machining while the material removal temperature increases from ambient temperature to 650 ^{o}C. The surface roughness changes from 1.7 μm in conventional machining to 0.9 μm during LAM at 540 ^{o}C. The cost for machining 1 m length of Inconel 718 decreases 50% from conventional ceramic machining and 66% from conventional carbide machining at 3 m/sec.

Attia et al., (2010) studied the high speed machinability of super alloy Inconel 718 under Laser assisted and dry conditions. The tests were conducted for cutting speeds up to 500 m/min and feeds up to 0.5 mm/rev, using ceramic cutting tool (SiAlON) with Nd: YAG laser power. Under the optimum cutting conditions the surface finish improved by more than 25%, material removal rate increased by approximately 800% and there is a significant reduction in the cutting forces compared to conventional machining.

Germain et al., (2010) presented laser assisted machining of Inconel 718 (NiCr19FeNb at 46 HRc) with carbide and ceramic insert. LAM significantly reduced cutting forces by

approximately 40%, independent of the cutting tool insert. The tool life of the carbide insert in LAM was low compared to conventional machining whereas the tool life of the ceramic inserts in LAM improved by 25% than in conventional machining.

Ding and Shin, (2013) investigated the machinability of Waspaloy under varying conditions of metal removal temperature, cutting speed and feed by examining tool wear, cutting forces, and surface finish. The metal removal temperature range was 300 to 400 ^{o}C for machining Waspaloy with WG–300 tools to get optimum cutting force, tool wear and surface finish. The tool life improved by 50% while machining with LAM compared to conventional machining. The decrease in cutting forces and specific cutting energy was 20% when metal removal temperature increased to 400 ^{o}C. The cutting forces for conventional machining and LAM were 205 N and 164 N respectively for the same machining conditions. Table 2.6 shows overview of laser assisted machining of Titanium and Nickel based super alloys.

2.8.4. Laser Assisted Machining of Composites

Dandekar and Shin, (2010), used LAM for the improvement of tool life and metal removal with minimum surface damage. Performance parameters like specific cutting energy, cutting forces, subsurface damage, surface roughness and tool wear were measured by changing the material removal temperature. LAM reduces the surface roughness, specific cutting energy, tool wear, and fiber pullout compared with conventional machining. A temperature of 300 ^{o}C was set as the optimum metal removal temperature at a feed of 0.02 mm/rev, a depth of cut of 0.5 mm and a speed of 30 m/min. At this condition LAM provides a 65% reduction in surface roughness, specific cutting energy and tool wear compared to conventional machining under the same cutting conditions. Also, LAM shows an increment in the machinability of high volume fraction, long fiber metal matrix composite (MMC) through improved material removal rate (MRR), better surface finish, increased tool life, and reduced damage.

Wang et al., (2002) presented the LAM of aluminum matrix composite (Al_2O_3 p/Al). The process parameters were cutting speed, feed rate and depth of cut, the performance measures were tool wear, cutting force and tool life. LAM improves tool life, reduces tool wear and increases wear resistance of the machined component. LAM also reduces the cutting forces from 30 to 50%.

Dandekar and Shin, (2013), studied the machining of a particle reinforced metal matrix composite (A359 aluminum matrix composite reinforced with 20% by volume fraction silicon carbide particles) using LAM. The responses involved cutting forces, specific cutting energy, surface roughness, subsurface damage and tool wear at different material removal temperature. A temperature of 300 ^{o}C was set as the optimum metal removal temperature at feed of 0.1 mm/rev, a depth of cut of 0.76 mm and a speed of 150 m/min with carbide tooling. The surface roughness and specific cutting energy reduced by 27% and 12% respectively using LAM compared to conventional machining at the same cutting conditions. The effective tool life is improved by a factor 1.7–2.35 over conventional machining based on cutting speed when the surface roughness is 2 μm. Cutting force, tool wear and surface roughness are reduced using LAM at all cutting speeds (50-200 m/min) than conventional machining. Table 2.7 shows overview of laser assisted machining of metal matrix composites.

2.8.5. Laser Assisted Machining of Ferrous alloys

Dumitrescu et al., (2006) demonstrated LAM of fully hardened AISI D2 tool steel using a high power diode laser (HPDL) in orthogonal and longitudinal turning processes. LAM removes the catastrophic fracture of the carbide cutting tools, suppresses machining chatter and saw tooth chip formation, reduces the thrust component of cutting force and increase the tool life almost 100% compared to the conventional machining. HPDL system is best suited for milling applications rather than turning because of power density limitation.

Skvarenina et al., (2006) evaluated the machinability of compacted graphite iron (CGI) whose structure yields high strength, makes it difficult to machine. By varying the feed, depth of cut and material removal temperature, cutting forces, specific cutting energy, tool wear and surface roughness were evaluated. The tool life improved by 60% at a feed of 0.15 mm/rev, cutting speed of 1.7 m/sec (for conventional machining 19.2 min and for LAM 30.3 min) and metal removal temperature of 400 ^{o}C compared to conventional machining at a feed of 0.1 mm/rev. Surface roughness increased by 5% compared to conventional machining at a feed of 0.150 mm/rev. For conventional machining, surface roughness was 2.35 μm and for LAM it was 2.24 μm. LAM also reduces the cost approximately by 20% machining of an engine cylinder liner.

Masood et al., (2011) studied the LAM of hard to cut material, high chromium white cast iron. Laser power has a significant effect on cutting force, hardness, temperature, surface profile and cutting chips. The heat penetration increases as the distance between the laser spot and cutting tool increases, and it also increases when laser power increases. LAM reduces the cutting forces and feed forces to a maximum extent of 24% and 22% respectively.

Ding and Shin, (2010), investigated the laser assisted machining of AISI 4130 shaft by changing the operating conditions such as metal removal temperature, heating, cutting speed and feed rate. The cutting force and the specific cutting energy were reduced by 20% at a metal removal temperature above 200 ^{o}C compared to conventional hard turning process. The surface roughness in conventional machining is 1.6 μm whereas in LAM it is in the range of 0.2-0.4 μm at the similar machining conditions. The hardness of the component after LAM is typically from 47 to 48.5 HRC which is close to the hardness of conventional machining. LAM produces about 150 MPa more compressive surface axial residual stress than conventional machining. Table 2.8 shows overview of laser assisted machining of ferrous alloys

Table 2.5. Overview of laser assisted machining of ceramics

S. No.	Authors	Year	Workpiece material	Tool Material	Type of Laser	Cutting force	Surface roughness	Tool Wear	Material removal rate
1	Jong-Do Kim et al	2011	Si_3N_4	CBN	2.5 KW HPDL	Reduced	–	improved	–
2	Chih-Wei Chang & Chun-Pao Kuo	2007	Al_2O_3	CBN	Nd:YAG pulsed wave	–	Reduced	–	improved
3	Frank E Pfefferkorn et al	2004	Magnesia partially stabilized zirconia	PCBN	1.5 KW CO_2	Specific cutting energy reduced by 2.5 times	Reduced	Tool life improved up to 121 minutes	–
4	Patrick A. Rebro et al	2002	Mullite	Uncoated carbide tool	1.5 KW CO_2	40% reduced	Reduced	improved	–
5	S. Lei eta al	2001	Si_3N_4	PCBN	1.5 KW CO_2	Reduced	Improved	improved	improved

Table 2.6. Overview of laser assisted machining of Titanium and Nickel based super alloys

S. No.	Authors	Year	Workpiece material	Tool Material	Type of Laser	Cutting force	Surface roughness	Tool Wear	Material removal rate
Titanium based super alloys									
1	R. A. Rashid et al	2012	Ti–6Cr–5Mo–5V–4Al	Uncoated WC	Nd:YAG	reduced by 15%	–	–	–
2	Chinmaya R. Dandekar et al	2010	Ti–Al–4V	Uncoated WC/Co	1.5 KW CO_2	–	–	1.7 times improvement in tool life	–
Nickel based super alloys									
1	Hongtao Ding& Yung C. Shin	2012	Waspaloy	Ceramic	1.5 KW CO_2	20% reduction in specific cutting energy	2–3 times improvement	50% improvement in tool life	–
2	H. Attia et al	2010	Inconel 718	Ceramic (SiAlON)	Nd:YAG	Reduced	25% reduced	–	8 times increased
3	G. Germain et al	2008	Inconel 718	Carbide/ Ceramic	ROFIN YAG	40% reduction in specific cutting energy	–	–	–
4	Mark Anderson et al	2006	Inconel 718	Carbide/ Ceramic	CO_2	reduced by 25%	2-3 times reduced	200-300% improvement in tool life	–

Table 2.7. Overview of laser assisted machining of metal matrix composites

S. No.	Authors	Year	Workpiece material	Tool Material	Type of Laser	Cutting force	Surface roughness	Tool Wear	Material removal rate
1	Chinmaya R. Dandekar & Yung C. Shin	2013	SiC–Al MMC	Carbide	1.5 KW CO_2	12% reduction in specific cutting energy	35% reduced	1.7-2.35 improvement in tool life	–
2	Chinmaya R. Dandekar & Yung C. Shin	2010	(Al–2% Cu/ Al_2O_3) MMC	PCD	1.5 KW CO_2	65% reduced	65% reduced	57% improvement in tool life	increased
3	Stuart Barnes et al	2003	Al/SiC MMC	HSS	Direct diode laser	Reduced	–	reduced	–
4	Y Wang et al	2002	Al_2O_3 particle reinforced Al MMC	Carbide	YAG	reduced by 30-50%	improved	reduced by 20-30%	–

Table 2.8. Overview of laser assisted machining of ferrous alloys

S. No.	Authors	Year	Workpiece material	Tool Material	Type of Laser	Cutting force	Surface roughness	Tool Wear	Material removal rate
1	S. H. Masood et al	2011	White cast iron	CBN	2.5 KW Nd:YAG	Reduced by 24%	–	–	–
2	Hongtao Ding& Yung C. Shin	2009	Compacted graphite iron	uncoated carbide	1.5 KW CO_2	–	5% improvement	60% improvement in tool life	–
3	P. Dumitrescu et al	2006	AISI D2 tool steel	TiN coated carbide	HPDL	Reduced	–	100% improvement in tool life	–
4	S. Skvarenina & Y. C. Shin et al	2005	hardened steel	PCBN	CO_2 & Nd:YAG	20% reduction in specific cutting energy	–	–	–

2.9. Solid Particle Erosion (SPE)

The erosion behavior of brittle materials such as alumina ceramics, cermets were examined earlier and it was observed that erosion is determined by the properties of both erodent and target material. Curkovic et al., (2011) experimentally examined the influence of hardness, shape of erodent and impingement angle on erosion of high purity alumina ceramics with two types of erodents viz. SiC and SiO_2. It was found that hard and angular SiC particles had huge impact compared to delicate and rounded SiO_2 particles. Higher rate of erosion was observed at normal impingement angle for both types of erodents.

Choi et al., (2013) evaluated erosion characteristics of silicon nitride (Si_3N_4) ceramics. It has been observed that the erosion loss of ceramics depends on the grain size rather than hardness and fracture toughness (mechanical properties).

Liu et al., (2010) emphasized that erosion behavior is impacted by impingement angle, impact velocity of erodent particles (SiC), phase ratio and relative density of boron carbide (B_4C) ceramic composites, fabricated using uniaxial hot pressing.

Sharma et al., (2014) experimentally investigated the influence of impingement angle with alumina and SiC as erodents on erosion characteristics of SiC–WC composites.

Amrithan et al., (2010) experimentally found the influence of particle size, impact velocity and impingement angle of erodent particles on the erosion behavior of biomorphic Si/SiC ceramic composites. It also found that erosion loss is very high when the impact angle is 90^o compared to the lower angles of incidence.

Zhang et al., (2000) examined the rate of erosion of alumina ceramics and found that it is enhanced by the impact velocity of particles. The erosion rate for dry and wet erosion was obtained for different particle velocities and fluxes; it was 37 m/s and 50 g/cm^2 sec for airborne erosion and 16.5 m/s and 120 g/ cm^2 sec for slurry jet erosion. It is also observed that huge variation in erosion rates were found related to acute angles and normal impact.

Gopi et al., (2008) developed erosive wear models on the basis of experimental data which successfully validated most cited models in the literature. Erosion rate increases with increase in particle velocity for dry-impact erosion. A power law exponent which varies from 2.82 to 2.92 is obtained for the velocity of particle. Erosion increases with sine of the angle of

impact, with exponent ranging from 2.31 to 2.35 for dry-impact and 1.45 to 1.48 for slurry-impact respectively.

Renjo et al., (2015) experimentally found erosion behavior and surface finish of slip cast Al_2O_3-ZrO_2 ceramics with dry silica sand as erodent.

2.10. Response Surface Methodology (RSM)

Li et al., (2013) successfully implemented RSM to a process of fabrication of calcia partially stabilized zirconia (CaO–PSZ). They studied the optimization of pressureless sintering process by applying RSM. Two regression models were generated using RSM in terms of holding time, sintering temperature and heating rate as process variables to illustrate the relative density and bending strength as responses. They also determined the optimum process conditions for maximum relative density and bending strength by examining contour plots and analysis of variance.

Sktani et al., (2018) successfully implemented design of experiments (DOE) through RSM involving central composite design (CCD). To optimize the process, the input variables included addition between CaO and $CaCO_3$, sintering temperature and soaking time. Regression models were developed for responses and their accuracy checked using variance analysis. They also studied the effect of process variables on response and found sintering temperature was the most influential.

Xiangli et al., (2008) successfully used RSM to optimize the fabrication conditions that influence the performance of Polydimethylsiloxane (PDMS) ceramic composite membranes. The regression models between process parameters and responses were developed using RSM. The input variables included polymer concentration, cross link agent concentration and dip coating time and responses permeation flux and selectivity of composite membrane. It is observed that polymer concentration is the most significant parameter which affects the response.

Li et al., (2013) successfully implemented RSM to a process of fabrication of magnesia partially stabilized zirconia (Mg–PSZ). They studied the optimization of pressureless sintering process by applying RSM. Two regression models were generated using RSM in terms of holding time, sintering temperature and heating rate as process variables to

illustrate the relative density and bending strength as responses. They also determined the optimum process conditions for maximum relative density and bending strength by examining contour plots and analysis of variance.

2.11. Gap Analysis

After a thorough literature review, the following research Gaps were identified.

- Limited literature is available for the fabrication of wave transparent ceramic materials with suitable properties required for radomes.
- A lot of work has been carried out for the processing of silicon nitride based ceramics to obtain the required properties for radomes.
- There is not much work on the combination of fused silica base and gelcasting for the improvement of properties of ceramic composites.
- Limited literature is available on process modeling and optimization of fused silica ceramic composites.
- Not enough literature is available on laser assisted machining of ceramic composites (Si_3N_4, Al_2O_3, Mullite, Zirconia etc)
- There is not much work available on laser assisted machining of fused silica ceramic composites.

2.12. Research Problem and objectives of the present work

Structural ceramics have interesting mechanical, thermal, chemical and dielectric properties, which suggest great potential for structural applications even at high temperatures. These are also used in electronic applications like insulators, semiconductors, conductors and magnets due to their electrical and magnetic properties. Advanced structural ceramics have been progressively used in aerospace, automobile industries, defence, biomedical, construction, nuclear industries, chemical, petrochemical and oil/gas industries due to their excellent properties. The usage of fused silica in such applications largely depends on the ability to reliably and economically mass produce complex and complicated shaped components. This is a challenge for the ceramic industry using traditional fabrication techniques. Moreover, forming complex shaped parts by machining and grinding of final sintered parts is seldom viable as it is very expensive. For machining efficiently these high

precision elements, it is exceptionally difficult using conventional metal cutting methods because of higher cutting force and excessive tool wear which leads to a lower material removal rate and high cost. Laser assisted machining effective method for improving the machinability of difficult to machine material like ceramics.

2.13. Research objectives

The main objectives of this study are to fabricate wave transparent ceramics with ceramic materials SiO_2, Si_3N_4, BN and Al_2O_3 with best of the properties for flexural strength, dielectric constant and also to machine ceramics using laser assisted machining. The objectives being proposed in this study are:

- Fabrication of SiO_2–Si_3N_4–BN and SiO_2–Si_3N_4–Al_2O_3 ceramic composites using Gelcasting technique and evaluation of mechanical and dielectric properties.
- To identify the best combination of ceramic materials varying solid loading (SL), monomer content (MC) and monomer ratio (MR) on gelcasting of SiO_2 ceramic composites.
- To develop regression models for the analysis of responses such as flexural strength, porosity and dielectric constant and to study the effect of process parameters on the responses and also to evaluate the optimum process parameters for maximum flexural strength, maximum porosity and minimum dielectric constant using RSM coupled with desirability function to optimize multiple responses.
- To evaluate the erosion characteristics of ceramic composites with different angles of impingement and impact velocities.
- To develop regression models for the analysis of responses such as surface roughness and material removal temperature and to study the effect of process parameters like rotational speed, feed, depth of cut and laser power on the responses in laser assisted machining of ceramic composite and also to evaluate the optimum process parameters for minimum surface roughness and minimum material removal temperature using RSM coupled with desirability function to optimize multiple responses.

2.14. Work plan

Experiments were conducted to effectively fabricate fused silica ceramic composites suitable for wave transparent application and laser assisted machining. The detailed work plan is schematically presented in Figure 2.1.

Figure 2.1. Work plan

2.15. Expected outcomes

The expected outcome of the current study presented is as follows.

- Fabricated fused silica ceramic composites would be useful for aerospace industry for manufacturing of radomes through a near net shape technique called gelcasting.
- The user industry can predict flexural strength, porosity and minimization of dielectric constant and their conflicting influence on manufactured parts through regression models being developed. Optimum process parameters may lead to better flexural strength and minimum dielectric constant.
- Solid particle erosion tests are significant in prediction of type of materials without prior knowledge of given materials. The user industries are highly benefitted through this technique.
- The generated machining data would be useful for aerospace industry for surface roughness and material removal temperature and industry may take essential precautions while laser assisted machining of fused silica ceramic composites and then cut down wastages such as scrap and rework and in turn lead to cost reduction.
- The user industry can predict surface roughness and material removal temperature and their adverse effect on machined components through regression models being developed. Optimum process parameters may lead to better surface roughness low and material removal temperature.

Summary

A thorough literature review is presented in this chapter dealing with designing wave transparent materials using different processing techniques. The analysis of the influence of process parameters on mechanical and dielectric properties in the gelcasting process is also discussed. The analysis of the effect of process parameters on surface roughness and material removal temperature in laser assisted machining is also carried out. Finally, literature gaps are identified and analyzed. Research objectives are projected and a work plan is developed to attain research objectives. This research work has been investigated for the influence of solid loading, monomer content and monomer ratio on ceramic composite properties and to explore the possibility of a new composite material for near net shaped ceramic part with enhanced properties for a wave transparent application. Hence, a problem related to gelcasting of SiO_2–Si_3N_4–BN and SiO_2–Si_3N_4–Al_2O_3 ceramic composites is formulated to develop porous SiO_2 based ceramic composites. This research work also has been investigated the influence of rotational speed, feed, depth of cut and laser power on surface roughness and material removal temperature.

CHAPTER 3

MATERIALS AND METHODS FOR FABRICATION OF CERAMIC SAMPLES

3.1. Introduction

This chapter reports the details of the materials and different types of equipment used for the fabrication of ceramics. The chapter discusses techniques to fabricate samples for phase and micro structural analysis. This chapter also emphasizes the details of sample processing and their characterization for different fused silica based composites. It identifies experimentally the appropriate ceramic slurry system and processing routes of porous SiO_2–Si_3N_4–BN and SiO_2–Si_3N_4–Al_2O_3 ceramic composites using gelcasting method, as well as measurement and analysis methods for related properties. The challenges in fabricating each ceramic composite are discussed and solutions provided through preliminary studies.

3.2. Materials Used

3.2.1 Fused Silica

Fused silica ceramics have high resistance to corrosion, good thermal shock resistance (withstand shock resistance greater than twenty thermal cycles between room temperature and 1000 °C), very low coefficient of thermal expansion (0.54×10^{-6}/ ^{o}C, 25–800 °C), low ε (3–4 from 25 to 1000 °C), low dielectric loss (~0.0004), less weight loss rate (0.0025 mg/s at 2500 °C) and excellent insulating property (resistivity = 1015 Ωm at room temperature). These characteristics make fused SiO_2 potential material for antenna windows in aerospace, electronics, metal and polysilicon industries (Mishra et al., 2010 and Wan et al., 2013). Table 3.1 shows the various ceramic materials and other additives used in the present work along with the properties and details of suppliers.

Table 3.1. Base materials used for the preparation of ceramic composites

S. No.	Material	Function	Average particle size	Density (g/cm^3)	Supplier details
1	Fused silica powder (SiO_2)	Ceramic Powder	1-5 µm	2.2	M/S Ants Ceramics Pvt Ltd, Thane- India
2	Silicon Nitride (Si_3N_4)	Ceramic Powder	1-5 µm	3.44	M/S Ube Industries, Japan
3	Boron nitride (BN)	Ceramic Powder			Alfa Aesar- USA
4	Alumina (Al_2O_3)	Ceramic Powder	50-200 µm	3.98	Alfa Aesar- USA
5	Methacrylamide CH_2-$C(CH_3)CONH_2$	Monomer		1.235	Sigma Aldrich Chemie- Germany
6	N N'-Methabisacrylamide (MBAM) ($C_7H_{10}N_2O_2$)	Cross linker		1.24	Sigma Aldrich Chemie, Germany
7	Darvan 821A	Dispersant		1.25	Vanderbilt Minerals LLC-USA
8	Polyethelene glycol 400 (PEG-400) $H(OCH_2CH_2)nOH$	Surfactant		1.126	Sigma Aldrich Chemie- Germany
9	Tetramethylethylenediamine-(TEMED) $C_6H_{16}N_2$	Catalyst		1.982	Sigma Aldrich Chemie- Germany
10	Ammonium persulfate (APS) $H_8N_2O_8S_2$	Initiator		0.775	Alfa Aesar- USA
11	Diluted Nitric acid (HNO_3) and Sodium hydroxide (NaOH)	pH adjustment			S. D. fine chemicals, India

3.3. Slurry preparation

Slurry based systems are considered an effective means to fill molds and obtain high green strength parts and therefore sintered parts. To attain this goal, the characterization of ceramic materials and addition of additives to homogeneous ceramic slurry is important. When ceramic materials, dispersants, monomers and other additives do not have the appropriate characteristics, it is difficult to get optimum properties. The objective of the experimental study was to examine various suspension systems of SiO_2 ceramic and an optimal composition for the manufacture of near net shape ceramic components.

A premix solution was prepared by mixing Methacrylamide (MAM) and N, N'-Methylenebisacrylamide (MBAM) in distilled water with a dispersant. Ceramic powders and additives were added to premix solution maintaining the proper solid loading of the suspensions. In order to break down agglomerates and to achieve good homogeneity, the suspensions were mixed in magnetic stirrer. Hydrochloric acid and ammonia were used to adjust pH value and the values were measured using pH meter. The resultant suspension was deaired for 5-10 min using dessicator connected to a vacuum pump and an initiator (10 wt% aqueous solution of ammonium persulfate, APS) and a catalyst (tetramethylethylenediamine, TEMED) was introduced into it. Immediately, the suspension was cast into a nonporous mold and dried under controlled humidity in an oven. The samples were binder burnt out and sintered in N_2 atmosphere, followed by natural cooling in High temperature Muffle furnace.

3.3.1. Slurry Mixing

Figure 3.1 (a) Magnetic stirrer (b) pH meter

A magnetic stirrer (REMI 5 MLH) (Figure 3.1 a) is used for mixing the suspension to produce a stable and homogenous dispersion of ceramic powders. A DC (PMDC) motor gives high torque and retains speed constant in the magnetic stirrer even in case of variation in volume or viscosity. The magnetic stirrer's specifications are presented in Table 3.2. The pH value of all the suspensions is measured by pH meter as shown in Figure 3.1 (b).

Table 3.2: Specifications of the Magnetic stirrer

Specification	Value
Power	500 W
Maximum stirring quantity	5 litres
Motor rating	10W
Speed range	100-1500 rpm
Display resolution	1 rpm
Heating power	500W
Temperature Range	Up to 340°C maximum

3.3.2. Deairing

The suspension used in gelcasting process must be flowable in nature. The air trapped in the suspension leaves pores in the molded parts, which reduces mechanical properties and leads to defects. Thus, Deairing was carried out before casting. Excessive deairing can lead to solvent loss by evaporation and influence the properties of the suspension. After intimate mixing with a magnetic stirrer, the suspension undergoes deairing for 20 min before gelation takes place. Deairing is done using a desiccator which is connected to a vacuum pump as shown in Figure 3.2.

Figure 3.2. Dessicator

3.3.3. Casting and Gelation reaction

Initiator and catalyst were added to the suspension before casting. The slurry was then cast into moulds as shown in Figure 3.3 and gelled for about 20 min after casting. This allows retaining a reasonable amount of time (10 min) at ambient temperature after adding initiator and catalyst to the suspension for deairing and molding filling. This prevents premature gelation, which destroys the usefulness of the slurry. After gelation, a few samples were cut in green state.

Figure 3.3. Moulds

3.3.4. Drying

In gelcasting process, the green sample was produced without removal of the liquid phase of the suspension after polymer gel reaction. In other words, the wet gelcasted bodies contain almost as much water as the initial suspension. This water must be removed by a consequent drying phase, which is most important in the gelcasting process. The gelled wet body was detached from the mold after gelation. Drying should be carried out under controlled temperature and humidity conditions using Controlled Humidity Oven (Thermospectrum Instruments Pvt. Ltd, India), presented in Figure 3.4. Gelcast green bodies were first dried under high moisture: 90% RH and 40 °C in the ambient chamber to remove 40% to 50% water content. From there, humidity was reduced to 30% relative humidity, and the temperature was increases to 90 ^{o}C to accelerate drying process. Specifications of humidity oven are given in Table 3.3.

Table 3.3. Specifications of Controlled-Humidity Oven

Specification	Value
Temperature range	10 to 90°C
Humidity range	25 to 95% RH
Accuracy	±0.1°C or ±2% RH
Resolution	0.1 °C or 1% RH
Controller	PID control Microprocessor
Temperature sensor	PT – 100
RH sensor	Direct capacitance type

Figure 3.4. Controlled-Humidity Oven

3.3.5. Binder burnout and sintering

Subsequent to drying, the samples were dealt with in a traditional way. The organic monomer (MAM & MBAM) content is only approximately 5-15 wt% of the silicon nitride powder. The binder was removed in a separate step or taken out immediately in a sintering furnace. The samples were sintered in a High-Temperature Tube Furnace (Bionics Scientific Technologies, New Delhi) (Figure 3.5) connected to an N_2 cylinder for gas purging. The specifications of the furnace are given in Table 3.4. The Sintering atmosphere was N_2 gas.

The heating and cooling cycles were regulated by means of PID controller in the furnace. The cooling phase was done naturally inside the furnace.

Table 3.4. Specifications of High-Temperature Muffle Furnace

Model	BST/MF/1800
Maximum Temperature	1800°C
Working Temperature	1700°C
Heating Element	($MoSi_2$) Molybdenum di Silicide
Temperature Accuracy	+/- 1°C
Temperature Controller	PID controller
External Chamber Construction	304 Grade Stainless Steel
Internal Chamber Construction	Ceramic Refractory Chamber of size 200×200×100 mm^3
Power Supply	220 / 440 Volts

Figure 3.5. High-Temperature Muffle Furnace

3.4. Property Characterization

3.4.1. Relative density and porosity measurement

The density of all samples was measured using Archimedes principle. First, the weight of the dry sample (W_1) was measured by means of weighing balance (accuracy of 0.1 mg), before it was immersed in water in vacuum for 5 min. After that the suspended weight of the sample (W_2) was measured. Finally, wet weight of the sample was measured (W_3) after removing it from water and covering with a tissue paper for 1 min to remove residue of water on the surface. This method was repeated to ensure reliability of weighing. Then porosity and bulk density was calculated using measured values as described in ASTM Standard C914 – 09 using equations 3.1, 3.2 and 3.3.

$$True\ volume\ of\ the\ sample\ = \frac{W_1 - W_2}{\rho_w} \quad (3.1)$$

$$Bulk\ density\ of\ the\ sample = \frac{W_1 \rho_w}{W_3 - W_2} \quad (3.2)$$

$$Open\ porosity\ = \frac{W_3 - W_1}{W_3 - W_2} \quad (3.3)$$

Where, W_3 is saturated weight of the sample, W_2 is suspended weight of the sample and W_1 is dry weight of the sample.

3.4.2. Mechanical properties

3.4.2.1. Preparation of samples for mechanical testing

For mechanical testing, the large gelcasted sintered samples were cut by Diamond saw (Figure 3.6) into rectangular bars of dimensions 3mm x 4mm x 40mm and re-machined until they met fineness requirement. High-speed diamond cut-off saw preparing samples for three point bending test is very tiresome and difficult. A few samples broke at some point during the cutting into small test samples. However, at the end, an adequate number of test samples were acquired. The cut samples were then ground and polished using 240, 600, 800 and 1200 grits SiC paper simultaneously to obtain a plain surface on the sample.

Table 3.5. Specifications of Diamond cut off saw

Power	Voltage: 110 V AC 50/60 Hz
Motor and spindle	Speed range from 400 to 3250 pm
Cutting blade	Impregnated diamond blade of 4” (101.6 mm) diameter × 0.014” (0.35 mm) thickness × 0.5” (12.7 mm) arbor
Transformer	300 W AC to AC transformer (Dual change 220/240 V to 110/120 V)

Figure 3. 6: High-speed diamond cut-off saw

3.4.2.2. Flexural strength measurement

The gelcasted samples were cut into small bars of sizes 3x4x45 mm according to ASTMC1161-94 for a three point bending test according to ASTM (C1161-94) standard. For the flexural strength of sintered test, the specimen was measured using universal testing machine (Dak systems, Bangalore) (Figure 3.7) with a load cell of 1 kN. The span length and crosshead speed were 20 mm and 0.05 mm/min respectively. All corners and edges of the samples were beveled with SiC abrasive paper, to avoid stress concentration.

Table 3. 6. Universal Testing Machine Specifications

Capacity in KN	50
Clearance between columns in mm	1000
Load cells in KN	10, 5, 2.5, 1, 0.5, 0.25, 0.1, 0.05, 0.01, 0.005
Maximum crosshead Travel in mm	1100
Maximum speed at capacity in mm/min	500

Testing speed Range in mm/min	0.001 to 1000
Capacity at Maximum speed in KN	5
Jog speed in mm/min	0.001 to 1000
Return speed in mm/min	0.001 to 750

Figure 3.7. Universal Testing Machine

3.4.3. Dielectric constant

Figure 3.8. Impedance Analyzer set up

The dielectric constant (ε) is described as "the ratio of amount of capacitance of a capacitor packed with a dielectric material to amount of capacitance of identical capacitor

measured in vacuum as a dielectric means". The dielectric constant depends on the frequency and range of optical frequency. Electronic polarization is the main determinant because of orientation of polarizations and cannot react to this time scale. Therefore, ε depends strongly on chemical structure and density [128]. The dielectric constant of gelcasted sintered ceramic > 1 mm thickness was measured by an impedance analyzer (MTZ-35, Biologic Sciences Instruments Pvt. Ltd., France), as presented in Figure 3.8, in the frequency range of 50 Hz to 35 MHz.

3.4.4. X-ray Diffraction

Analytical method used to characterize the ceramic powders and sintered samples was X-ray diffraction (XRD). The diffraction patterns were measured using X-ray Diffractometer (Panalytical X'Pert powder, Netherlands), shown in Figure 3.9.

Figure 3.9. XRD Machine

The purity of the phases was determined by X-ray diffraction with a Cu Ka-radiation operating at 10-15 kV and 20 mA. All measurements were performed using a 0.020 progressive scan in 2- regime recording from 10 to 800 for 30 minutes. Comparison of identified patterns with the X'Pert high-score software patterns was made by ICDD (International Centre for Diffraction Data) data files.

3.4.5. Scanning Electron Microscopy (SEM) observations

The morphology of as received ceramic powders and microstructure of gelcasted specimens were examined by Scanning Electron Microscope (VEGA3, Tescan, Czech Republic) as presented in Figure 3.10. All samples were sputtered using an Au/Pd for a minimum of 50 seconds target to ensure high conductivity during the electron microscopy and secured to an SEM stub using carbon tape prior to imaging. Operating voltage used in SEM was between 10-20 kv.

Figure 3.10. Scanning electron Microscopy machine

3.4.6. Electronic Analytical Precision Balance

An Electronic Analytical Precision Balance (Afcoset, ER-120A, India) shown in Figure 3.11 was used to measure the weights of samples for measuring the bulk density and apparent porosity. The specifications Electronic Analytical Precision Balance are given in Table 3.7.

Figure 3.11. Electronic Analytical Precision Balance

Table 3.7. Specifications of Electronic Analytical Precision Balance

Maximum Capacity	120 g
Readability	0.1 mg
Repeatability	0.1 mg (Standard Deviation) maximum capacity
Non-linearity	±0.1 mg (10 g change), ±0.2 g (0-maximum capacity)
Sensitivity drift	±2 ppm/^{o}C
Stabilization time	5 sec (Approximately)
Operating Temperature	5-40 ^{o}C
Pan diameter	85 mm (3.35”)
Weighing chamber (L× B ×H)	178 mm × 154 mm × 186 mm
External dimensions (L× B ×H)	195 mm × 411 mm × 266 mm
Weight	11 kg
AC input	220, 240 V AC (50 Hz) 11 VA

3.4.7. Erosion Wear Testing

Fused silica ceramic composite specimens were polished to obtain fine surface finish. Then, samples were cleaned ultrasonically in alcohol and dried at 100 ± 5 °C for 2 to 4 h. Erosive wear experiment was performed at room temperature on erosion test rig as per ASTM G76 standard. The outline sketch of the erosion test is presented in Fig. 3.12.

Figure 3.12. Erosion test rig

Table 3.8. Specifications of erosion test rig

Fluid	Air
Temperature	Ambient
Pressure	6 bar maximum
Velocity	Up to 300 m/s maximum
Nozzle	Tungsten carbide
Particle Temperature	Ambient
Feed rate	0.5 to 10 gm/min continuously variable
Specimen size	25 mm x 25 mm maximum, Thickness 3-5 mm maximum.
Specimen Heating Temperature	400 ^{0}C
Nozzle Size	1.5 mm
Specimen adjustment	in X,Y,Z and tilt of specimen from 0-90^0 (continuously variable)
Double disc arrangement for particle velocity measurement.	

The erosion test rig contains air compressor, a conveyor belt type particle feeder which controls the amount of sand particles and air mixing and acceleration chamber. The compressed air provides necessary pressure to the chosen range of silica sand which is pumped constantly by a conveyor belt feeder into the mixing chamber. This pressurized air then passes through a convergent brass nozzle with internal diameter of 3 mm. The specimen is impinged by erodent particles at various angles which can be controlled by a swivel head and an adjustable sample holder. The specifications of the erosion test rig are presented in Table 3.8.

3.5. Laser Assisted Machining (LAM) setup

The setup of LAM is shown in Figure 3.13. The setup consists of a CNC lathe with a dynamometer, for measuring the cutting forces induced on the tool. These cutting forces are amplified using a charge amplifier. A temperature gun was used to measure the temperature of the workpiece during machining operation. Laser power was generated by a laser generator required for machining and the laser was discharged through a laser gun on to the work piece. All these were controlled by a computer controller. YBD152 CVD coated (medium thick

Al_2O_3 + thick TiCN) carbide cutting insert was used for machining. The size of the workpiece used for machining was 100 mm long and 30 mm diameter. The specifications of LAM are presented in Table 3.9.

Figure 3.13: Schematic diagram of LAM setup

Table 3.9: Specifications of LAM

1. CNC Lathe

Specifications	Size
i) Swing Over Bed	300 mm
ii) Swing Over cross slide	150 mm
iii) Distance between centres	600 mm
iv) Spindle Nose	A2-4
v) Range of spindle speed	300-3000 rpm
vi) X travel	150 mm
vii) Z travel	500 mm
viii) X axis rapid feed	5000 mm/min
ix) Z axis rapid feed	5000 mm/min
x) X axis Cutting feed rate	0-1000 mm/min
xi) Z axis Cutting feed rate	0-1000 mm/min

xii) Tool post	Quick change tool post with 8 different tools should facilitate maintop of dynometer
xiii) Tool Shank	20 x20 mm
xiv) Spindle Motor	7.5 kW/10 HP
xv) X axis Servo Motor	1.5 KW
xvi) Z axis servo Motor	1.5 KW
xvii) Coolant	Automatic
xviii) Lubrication	Automatic
xix) Controller	Industrial controller with absolute encoder
xx)Programming	Standard G & M code programming & specific command to operate & control frequency & intensity of laser source.
xxi) Power	3 phase,415V,50Hz

2. Laser Unit Comprising of

(a) Laser head

i) Max. Average Power at Laser (W)	600
ii) Typical Power at Work piece (W)	500
iii) Max. Power consumption (kW)	4
iv) Pulse Repetition Rate Frequency (Hz)	2 to 50Khz
v) Pulse to Pulse Stability(Power stability)	± 3%
vi) Prealigned optics fibre with	
1) Standard Fiber Diameter (μm)	600
2) Standard Fiber Lengths (m)	5m
vii) Power	Single phase20-240v,50Hz

(b) Chiller/cooler

i) Cooling Water requirements @ 15°C input	4μ/min
ii) Cooling Requirement (kW)	5
iii) Max. Pressure Drop (bar min.)	2
iv) Ambient Temperature (°C)	5 – 40

(c) Laser Operated Software

i) Laser operating Software like Laser View or any other suitable software
ii) Complete cycle programming triggered by a single command
iii) Intel processor computer with 18inch monitor.

3. Laser Type**:** Nd: YAG Laser fiber optic 600W Pulsed Laser

3.5.1. Surface roughness measurement

The measurements of average surface roughness (Ra) were made with Taylor Hobson Surtronic S-100 Series Surface Roughness Tester shown in the Figure 3.14. The instrument directly gives the value in digital format. Designed for shop floor, industrial and inspection room applications, the S-100 series offers a versatile solution for all surface finish measurement requirements. Ideal for a wide range of industries including precision bearings, automotive and aerospace engineering, the S-100 series has key attributes that are most important for quality control in today's precision industries.

Figure 3.14. Talylor Hobson surface roughness tester

3.5.2. Temperature Measurement

The instrument shown in Figure 3.15 is known as Infrared thermometer and is used for temperature measure at the cutting zone during machining.

Figure 3.15 Infrared Temperature Gun

This is a laser thermometer used to diagnose, inspect and check any temperature from a distance point i.e. non-contact point. The instrument has an internal memory to save up to 100 measurements. It is compatible with thermocouple K probe. Infrared thermometer is used to measure the surface temperature of an object. Its optic lens catches the energy emitted and reflected by the object. This energy is collected and focused onto a detector. This information is displayed as temperature. The laser pointer is used only to aim at the target.

3.6. Processing of SiO_2–Si_3N_4–BN ceramics

3.6.1 Experimental design

As discussed in the literature review, a large number of variables are involved in the gelcasting process and virtually all the variables affect the performance characteristics, and considering all of them for steady will result in unmanageable data. Therefore, only major and important control processes parameters such as solid loading, monomer content and ratio of monomers were considered in the study. Experimental design comprises determining the factors, their levels and performance characteristics and lastly type of design. The samples prepared using the process parameters are shown in Table 3.10.

Table 3.10. Process parameters and their levels

S. No.	Parameter	Levels		
1	Solid Loading (%)	48	50	52
2	Monomer content (wt %)	5	10	15
3	Monomer ratio (MAM:MBAM)	10:1- Kept constant		
4	Silicon nitride (Si_3N_4)	5% - Kept constant		
5	Boron nitride (BN)	1% - Kept constant		

3.6.2 Experimental procedure

Figure 3.16 shows the fabrication process for the preparation of fused silica ceramics.

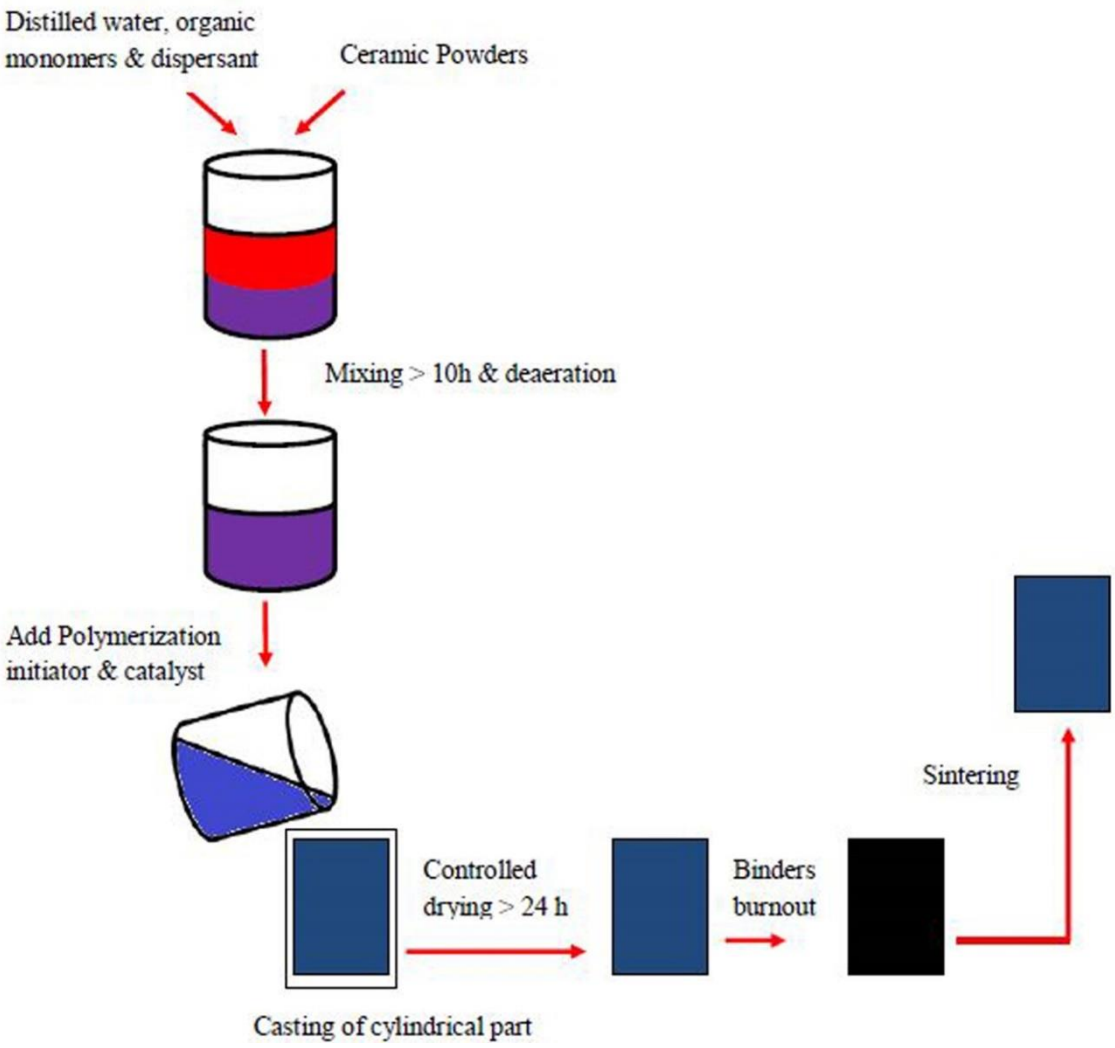

Figure 3.16. Flow chart of gelcasting

The ceramic samples were prepared at different sloid loadings, monomer ratios and at constant monomer content. Initially the premix solution was prepared by adding dispersant Darvan 821A (1 wt% monomer content), PEG (surfactant), monomers MAM and MBAM (wt% of fused silica) in distilled water. The solution was stirred with a magnetic stirrer. The premix solution was added with solid loading of required vol% of SiO_2, Si_3N_4 and BN and stirred for more than 6 h. The entrapped air in the slurry was removed for 10–15 min using deaerator and then initiator APS (1 wt% of monomer content) while TEMED was added to initiate polymerization and solidification. Later, the slurry was poured into a glass mold and after polymerization, the green samples were demolded. The green bodies were dried under controlled humidity conditions for 24 h. The binders were burnt at 600 °C in a high temperature muffle furnace for 1 hour at a heating rate of 2 °C/min. The sintering process for ceramic samples was conducted in nitrogen atmosphere at 1250 °C with a heating rate of 4 °C/min. The ceramic bodies were prepared at different solid loadings of 48%, 50%, 52%, different monomer contents 5, 10 and 15 wt% and constant monomer ratio 10:1.

3.6.3 Characterization

The bulk densities of sintered ceramic samples were determined by Archimedes displacement method. Pattern behavior was observed for the received powder using X-Ray diffractometer (PAnalytical Xpert powder, Netherlands). Scanning Electron Microscope (VEGA 3LMU. TESCAN, Czech Republic) was used to detect the morphologies of raw powders and sintered gelcast samples. In order to determine flexural strength of the samples, the three point bending test at room temperature was carried out following the ASTM D-143 (1996) standard on the specimen with dimensions of 40mm×4mm×3 mm at a crosshead speed of 0.5 mm/min on an Electronic Universal Testing Machine (Dak Systems, India. The loss tangent and dielectric constant are measured using an impedance analyzer (MTZ-35, Biologic Science Instruments, France) in the frequency range of 0.1~35 MHz.

The full factorial design and central composite design with 6 center points are used and represented in Table 3.11 and Table 3.12 respectively.

Table 3.11. Characterization of SiO_2–Si_3N_4–BN ceramic composite

S. No	Sol. Loading (%)	Monomer content (wt %)	Flexural Strength (MPa)	Porosity (%)	Dielectric constant (@30 MHz)
1	48	5	46.7	38.9	4.86
2	48	10	70.84	32.93	5.73
3	48	15	67.5	40.01	4.26
4	50	5	61.02	34.93	5.18
5	50	10	84.92	29.81	5.98
6	50	15	81.57	36.19	4.97
7	52	5	68.71	31.27	5.95
8	52	10	98.27	26.37	6.47
9	52	15	94.85	32.93	6.05

Table 3.12. Experimental design and test data

S. No.	Sol. Loading (vol%)	Monomer content (wt%)	Flexural strength (Mpa)	Porosity (%)	Dielectric constant (@30 MHz)
1	48	5	46.7	38.9	4.86
2	50	15	81.57	36.19	4.97
3	52	5	68.71	31.27	5.95
4	48	15	67.5	40.01	4.26
5	48	10	70.84	32.93	5.73
6	50	5	61.02	34.93	5.18
7	50	10	84.92	29.81	5.98
8	52	10	98.27	26.37	6.47
9	50	10	84.92	29.81	5.98
10	50	10	84.92	29.81	5.98
11	50	10	84.92	29.81	5.98
12	50	10	84.92	29.81	5.98
13	52	15	94.85	32.93	6.05

3.7. Processing of SiO_2–Si_3N_4–Al_2O_3 ceramics

3.7.1 Experimental design

As discussed in the literature review, a large number of variables are involved in the gelcasting process and virtually all these variables affect performance characteristics, considering all of them for steady will result in unmanageable work. Therefore, only major and important control processes parameters such as solid loading, monomer content and ratio of monomers were considered in this study. Experimental design comprises of determining the factors, their levels and performance characteristics on which the factors influences and lastly type of design. The samples prepared using the process parameters are shown in the Table 3.13.

Table 3.13. Process parameters and their levels

S. No	Parameter	Levels		
1	Solid Loading (%)	48	50	52
2	Monomer content (wt %)	5	10	15
3	Monomer ratio	5:1	10:1	15:1
4	Silicon nitride (Si_3N_4)	5% - Kept constant		
5	Alumina (Al_2O_3)	1% - Kept constant		

3.7.2 Experimental procedure

The ceramic samples were prepared at different sloid loadings, monomer ratios and at constant monomer content. Initially the premix solution was prepared by adding dispersant Darvan 821A (1 wt% monomer content), PEG (surfactant), monomers MAM and MBAM (wt% of fused silica) in distilled water. The solution was stirred with a magnetic stirrer. The premix solution was added with solid loading of required vol% of SiO_2, Si_3N_4 and Al_2O_3 and stirred for more than 6 h. The entrapped air in the slurry was removed for 10–15 min using deaerator and then initiator APS (1 wt% of monomer content) while TEMED was added to initiate polymerization and solidification. Later, the slurry was poured into a glass mold and after polymerization the green samples were demolded. The green bodies were dried under controlled humidity conditions for 24 h. The binders were burnt at 600 °C in a high

temperature muffle furnace for 1 h at a heating rate of 2 °C/min. The sintering process for ceramic samples was conducted in the nitrogen atmosphere at 1250 °C with a heating rate of 4 °C/min. The ceramic bodies were prepared at different solid loadings of 48%, 50%, 52%, monomer contents 5, 10 and 15 wt% and monomer ratio 5:1, 10:1 and 15:1.

3.7.3 Characterization

The bulk densities of sintered ceramic samples were determined by Archimedes displacement method. Pattern behavior was observed for the received powder using X-Ray diffractometer (PAnalytical Xpert powder, Netherlands). Scanning Electron Microscope (VEGA 3LMU. TESCAN, Czech Republic) was used to detect the morphologies of raw powders and sintered gelcast samples. In order to determine flexural strength of the samples, the three point bending test at room temperature was carried out following ASTM D-143 (1996) standard on the specimen with dimensions of 40mm×4mm×3 mm at a crosshead speed of 0.5 mm/min on an Electronic Universal Testing Machine (Dak Systems, India. The loss tangent and dielectric constant were measured using an impedance analyzer (MTZ-35, Biologic Science Instruments, France) in the frequency range of 0.1~35 MHz.

The full factorial design and central composite design with 6 center points were used and are represented in Table 3.14 and Table 3.15 respectively.

Table 3.14. Characterization of SiO_2–Si_3N_4–Al_2O_3 ceramic composite

S. No.	Solid loading (vol %)	Ratio of monomers	Monomer content (wt%)	Flexural Strength (MPa)	Porosity (%)	Dielectric constant
1	48	5:1	5	56.9	34.1	5.2
2	48	5:1	10	63.15	33.03	5.57
3	48	5:1	15	62.81	36.5	4.64
4	48	10:1	5	60.12	35.7	5.01
5	48	10:1	10	65.23	34.544	5.485
6	48	10:1	15	64.45	37.76	4.712
7	48	15:1	5	54.12	37.544	4.47
8	48	15:1	10	64.34	34.296	5.11
9	48	15:1	15	63.41	38.1	4.02

10	50	5:1	5	68.27	33.36	5.75
11	50	5:1	10	73.15	32.08	5.957
12	50	5:1	15	70.12	37.04	5.01
13	50	10:1	5	76.13	35.4	6.01
14	50	10:1	10	78.67	31.72	6.17
15	50	10:1	15	75.38	35.23	5.782
16	50	15:1	5	70.12	36.74	4.62
17	50	15:1	10	72.12	33.92	5.366
18	50	15:1	15	65.4	37.4	4.75
19	52	5:1	5	78.22	32.443	6.02
20	52	5:1	10	92.66	30.63	6.45
21	52	5:1	15	85.26	34.124	5.15
22	52	10:1	5	80.78	32.1	6.25
23	52	10:1	10	95.12	28.5	6.782
24	52	10:1	15	87.26	33.5	5.91
25	52	15:1	5	79.01	34.5	4.788
26	52	15:1	10	88.59	32.1	5.791
27	52	15:1	15	83.13	35.5	4.892

Table 3.15. Experimental design and test data

Run	Solid loading (vol %): A	Ratio of monomers: B	Monomer content (wt %): C	Flexural Strength (MPa)	Porosity (%)	Dielectric Constant (30 MHz)
1	50	10	15	75.38	34.95	5.782
2	52	15	5	87.2	35.5	4.788
3	52	5	15	85.2	34.124	5.15
4	50	15	10	74.12	35.92	5.366
5	48	15	5	48.12	37.544	4.47
6	52	10	10	95.12	28.5	6.982
7	50	10	10	80.63	31.72	6.57
8	50	5	10	73.15	32.08	5.957

9	50	10	5	77.13	33.4	6.01
10	50	10	10	80.92	32.01	6.45
11	50	10	10	80.63	31.72	6.57
12	48	5	15	60.81	36.5	4.64
13	48	5	5	50.9	35.12	5.2
14	52	15	15	80.13	36.5	4.792
15	48	15	15	63.41	38.1	4.02
16	48	10	10	67.23	34.544	6.485
17	50	10	10	81.03	31.93	6.32
18	50	10	10	80.75	30.02	6.86
19	50	10	10	79.36	31.09	6.06
20	52	5	5	76.22	33.433	6.02

3.8. Laser Assisted Machining

Laser assisted machining was conducted on SiO_2–Si_3N_4–Al_2O_3 ceramic composite by varying rotational speed, feed, depth of cut and laser power. The responses such as surface roughness and material removal temperature were measured. A central composite face centered design with 6 center points was considered from RSM for experimental design. Experimental design of process variables and their levels are presented in Table 3.16.

Table 3.16. Experimental design of process variables and their levels

Symbol	Factors	Levels		
		-1	0	1
A	Rotational Speed (RPM)	400	500	600
B	Feed (mm/rev)	0.025	0.050	0.075
C	Depth of cut (mm)	0.1	0.2	0.3
D	Power (W)	400	500	600

Experimental design and test data is shown in Table 3.17.

Table 3.17. Experimental design and test data

S. No.	Rotational Speed (RPM)	Feed (mm/rev)	Depth of cut (mm)	Power (W)	Surface Roughness (µm)	Material Removal Temperature (^{o}C)
1	500	0.05	0.2	500	2.13	647.4
2	600	0.075	0.1	400	1.46	433.2
3	400	0.05	0.2	500	2.17	648.5
4	400	0.075	0.1	400	1.3	452.2
5	500	0.05	0.2	500	2.13	647.4
6	600	0.025	0.1	400	1.74	434.2
7	500	0.05	0.2	500	2.13	647.4
8	500	0.05	0.2	500	2.13	647.5
9	400	0.025	0.3	400	1.35	444.3
10	600	0.025	0.3	400	1.76	468.3
11	600	0.075	0.1	600	1.51	801.7
12	400	0.075	0.3	400	1.95	476.4
13	400	0.075	0.3	600	1.61	813.9
14	500	0.05	0.2	500	2.13	647.4
15	600	0.025	0.3	600	1.91	824.6
16	500	0.05	0.3	500	2.1	679.6
17	500	0.05	0.2	600	2.04	802.04
18	600	0.05	0.2	500	2.03	677.2
19	400	0.025	0.1	600	1.54	804.7
20	400	0.075	0.1	600	1.57	798.67
21	600	0.025	0.1	600	1.54	790.3
22	500	0.05	0.2	500	2.13	648.21
23	600	0.075	0.3	600	2.61	820.4
24	500	0.05	0.1	500	2	637.25
25	400	0.025	0.1	400	1.1	434.9
26	500	0.025	0.2	500	1.96	644.92
27	500	0.075	0.2	500	2.2	649.2
28	600	0.075	0.3	400	1.98	456.9
29	400	0.025	0.3	600	1.77	817.3
30	500	0.05	0.2	400	1.8	637.31

Summary

In this chapter, the details of materials used for fabrication of porous SiO_2 based SiO_2–Si_3N_4–BN and SiO_2–Si_3N_4–Al_2O_3 ceramic composites are presented. The various equipment used for slurry preparation with their specifications are presented in this chapter. This chapter also presents details of equipment used in this work for property characterization, namely mechanical properties, dielectric properties, XRD analysis, and SEM analysis. This chapter also brought into focus equipment used in this work for machining of ceramics using laser assisted machining.

It identifies experimentally the processing routes of porous SiO_2–Si_3N_4–BN and SiO_2–Si_3N_4–Al_2O_3 ceramic composites using gelcasting method. The levels of input factors such as solid loading, monomer content and ratio of monomers were fixed. The experiments are planned based on full factorial and RSM approach.

The input parameters required for solid erosion wear were fixed. The levels of input factors such as rotational speed, feed, depth of cut and laser power in laser assisted machining were also fixed. The experiments were planned based on RSM and DOE with face centered central composite design with 6 centre points approach.

CHAPTER 4

CHARACTERIZATION AND PROCESS OPTIMIZATION OF CERAMIC COMPOSITES

4.1. Introduction

This Chapter deals initially with the characterization of SiO_2, Si_3N_4, BN and Al_2O_3 raw materials. The chapter also discusses the mechanical and dielectric characterization of ceramic composites. The results of flexural strength, porosity and dielectric constant of sintered SiO_2–Si_3N_4–BN and SiO_2–Si_3N_4–Al_2O_3 ceramic composites are presented. This chapter also details the modeling of SiO_2–Si_3N_4–BN and SiO_2–Si_3N_4–Al_2O_3 ceramic composites under varying conditions of solid loading, monomer content and monomer ratio. The effect of input variables on the responses such as flexural strength, porosity and dielectric constant is studied. The optimal process variables for maximum flexural strength, maximum porosity and minimum dielectric constant have been investigated using RSM coupled with desirability approach to optimize multiple responses. The predicted values for responses such as flexural strength, porosity and dielectric constant obtained from mathematical models are compared with experimental values for SiO_2–Si_3N_4–BN and SiO_2–Si_3N_4–Al_2O_3 was also presented in this chapter.

4.2. Characterization of Raw Materials

4.2.1. Characterization of SiO_2 powder

Pattern behavior was observed for the received powder using X-Ray diffractometer (PAnalytical Xpert powder, Netherlands). Scanning Electron Microscope (VEGA 3LMU, TESCAN, Czech Republic) was used to detect the morphologies of raw powders. Figure 4.1 shows the SEM image of fused silica ceramic powder (M/S Ants Ceramics Pvt Ltd, Thane-India). The fused silica particles are randomly distributed with different sizes and with an average particle size of 1–5 μm. Figure 4.2 shows the XRD image of fused silica obtained in powder form. In crystalline materials, atoms are periodically arranged but in amorphous materials atoms are randomly arranged. Thus, x-ray light incident in a crystal plane on atoms

then it scattered in a particular direction and gives high intensity narrow peaks but in the case of amorphous materials, when x-ray light is incident on atoms in a plane, it is scattered in random directions due to random orientation of atoms and gives a broad peak or background hump.

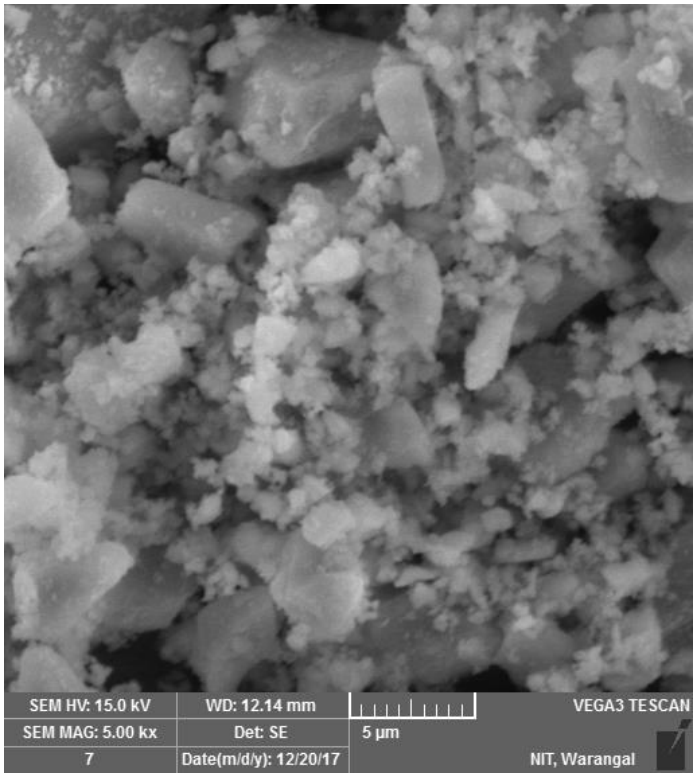

Figure 4.1. SEM image of Fused silica powder

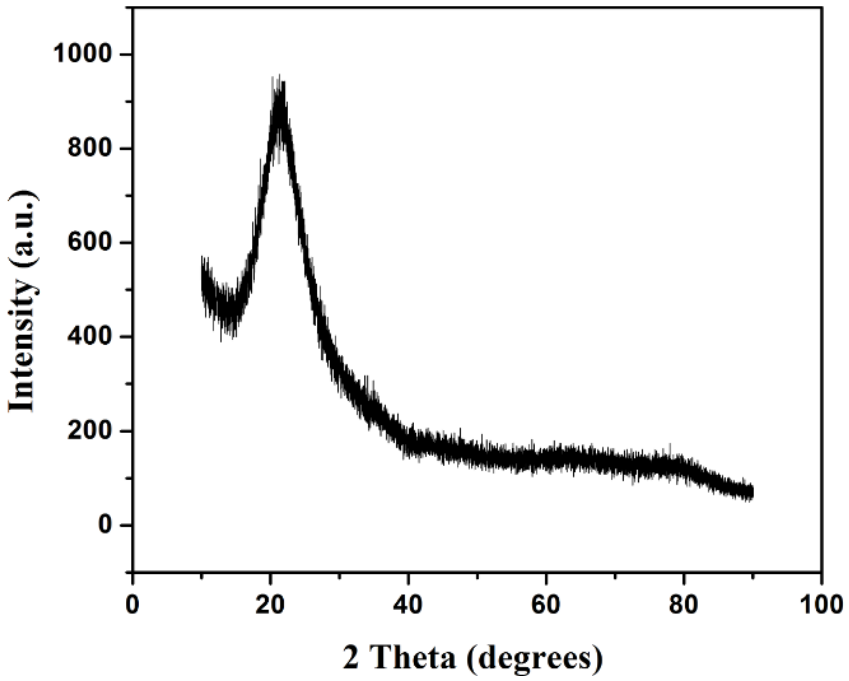

Figure 4.2. XRD pattern of Fused silica powder

4.2.2. Characterization of Si_3N_4 powder

Figure 4.3 shows the distribution of particles of Si_3N_4 (Ube Industries, Japan). It can be seen that the powders have irregular morphology with an average particle size of 1–5 μm. Figure 4.4 shows the X Ray diffraction analysis results of silicon nitride powder. Comparing X-ray diffraction patterns with JCPDS standards (No.98-005-9091), the diffraction peaks can be indexed as particles of Si_3N_4, which is consistent with manufacturer's data. The secondary phase was found.

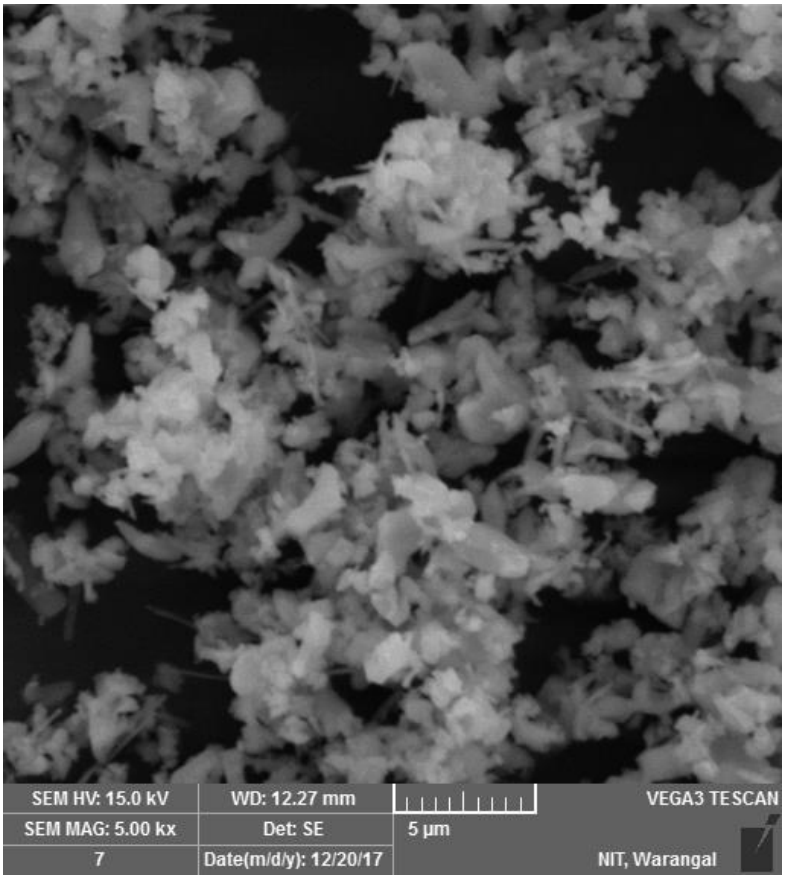

Figure 4.3. SEM image of Si_3N_4 powder

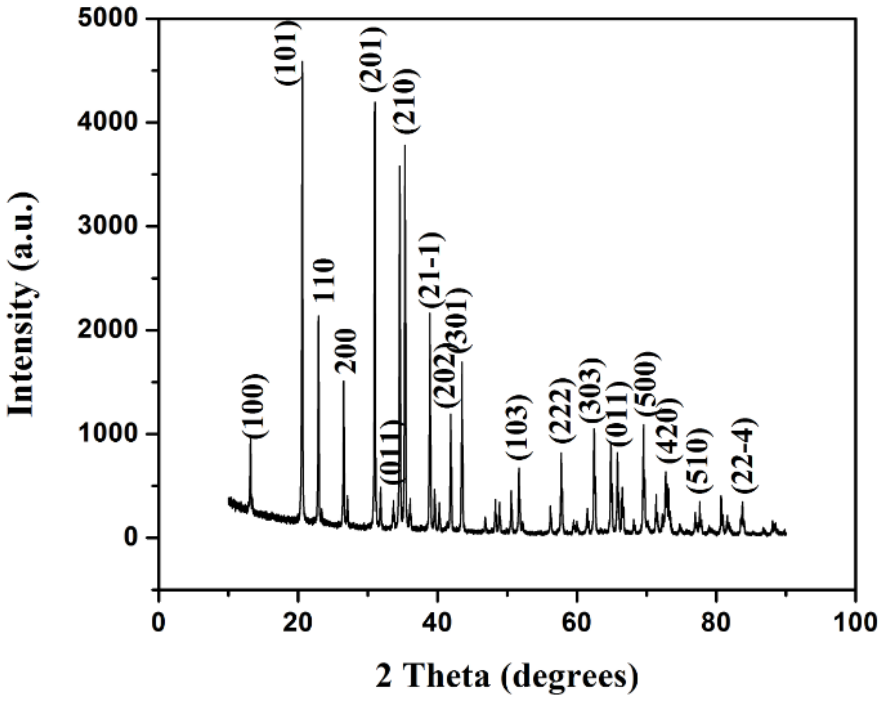

Figure 4.4. XRD pattern of Si_3N_4 powder

4.2.3. Characterization of BN powder

SEM micrograph of the as received BN ceramic powder (Alfa Aesar- USA) used in this study is shown in Figure 4.5.

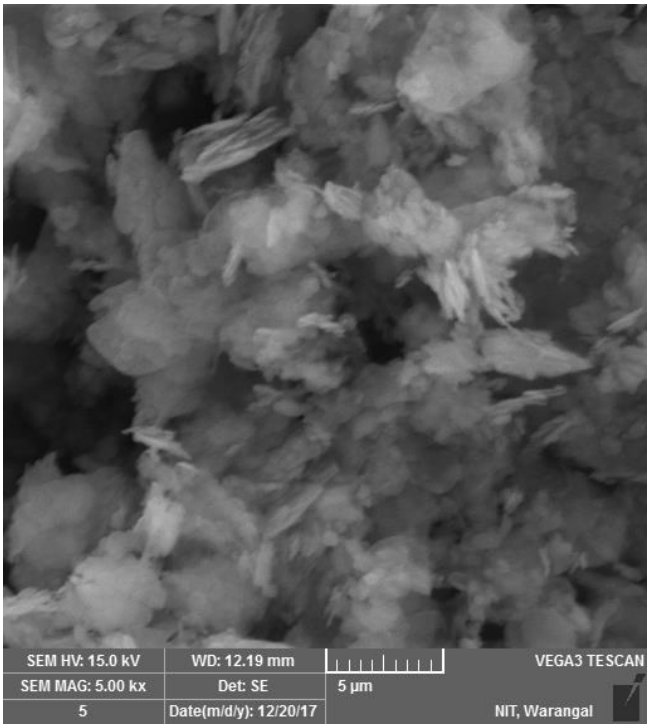

Figure 4.5. SEM image of BN powder

The X-ray diffraction pattern of the as-received BN ceramic powder is shown in Figure 4.6. By comparing XRD pattern with JCPDS standards, the diffraction peaks can be indexed as pure BN, as noted on the data sheet received from Alfa Aesar- USA.

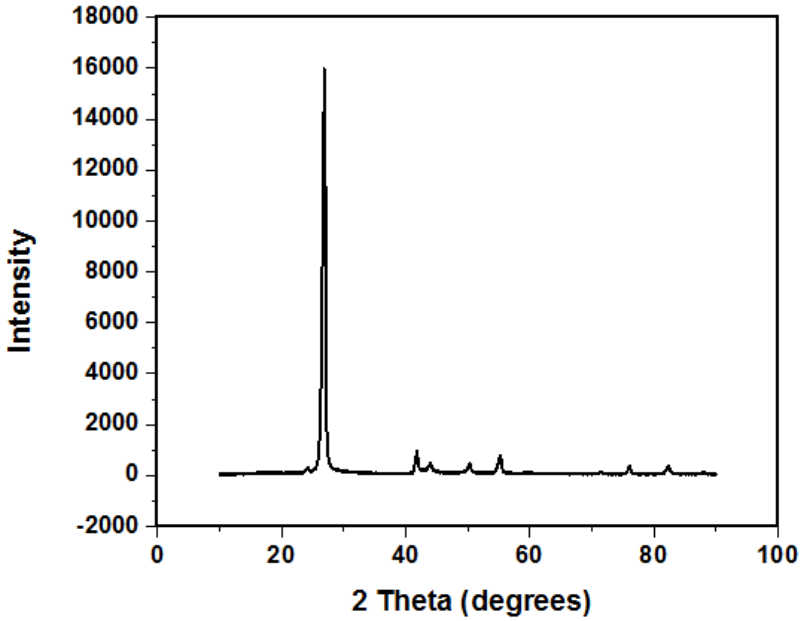

Figure 4.6. XRD pattern of BN powder

4.2.4. Characterization of Al_2O_3 powder

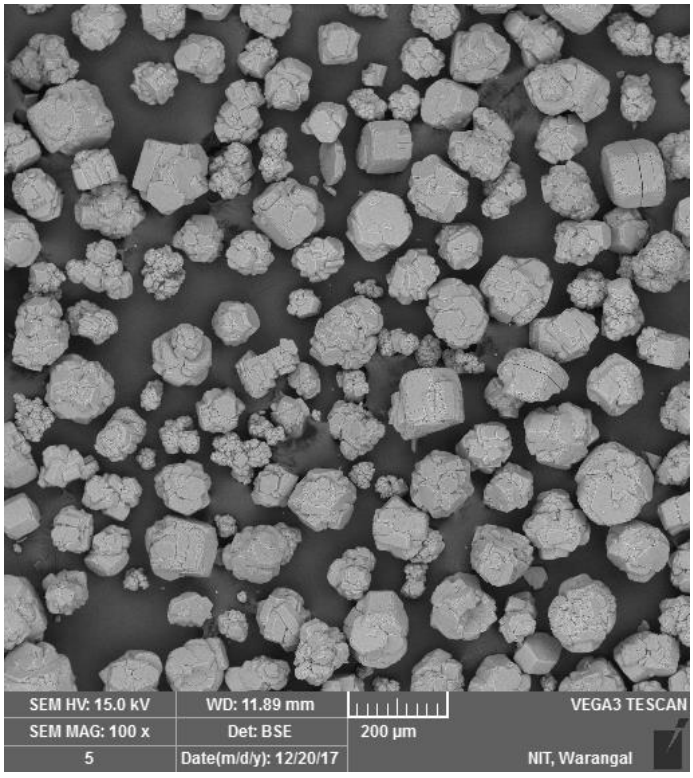

Figure 4.7. SEM image of Al_2O_3 powder

SEM micrograph of as received Al_2O_3 ceramic powder (Alfa Aesar- USA) used in this study is shown in Figure 4.7. The particles are randomly distributed in different sizes with average particle size of 50–200 μm. The X-ray diffraction pattern of as-received Al_2O_3 ceramic powder is shown in Figure 4.8. By comparing XRD pattern with JCPDS standards, the diffraction peaks can be indexed as pure Al_2O_3, as noted on the data sheet received from Alfa Aesar- USA.

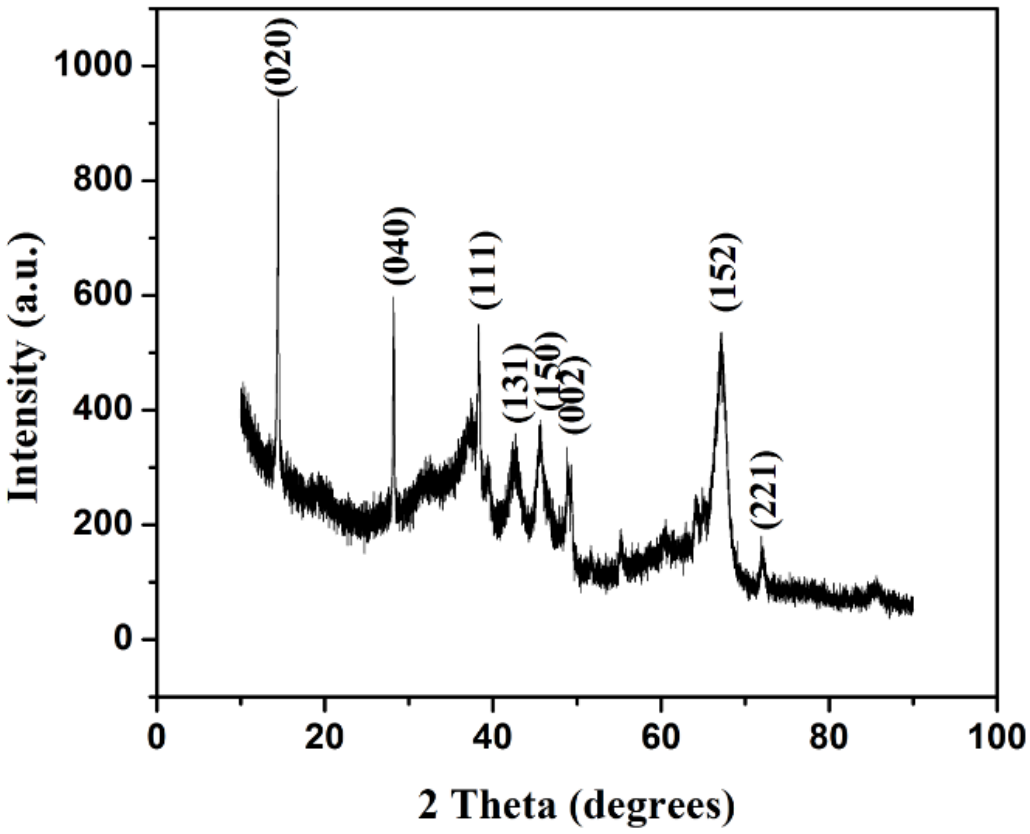

Figure 4.8. XRD pattern of Al_2O_3 powder

4.3. Physical phenomenon of gelcasting

Figure 4.9 shows the mechanism of polymerization of acrylamide (AM) and methylenebisacrylamide (MBAM) using ammonium persulfate (APS) and Tetramethylethylenediamine (TEMED) as polymerization initiator and catalyst, respectively. The free-radical reaction leads to the formation of micro-gels of monomer and cross-linker inside the suspension, which eventually combine to form a macro-gel network. The gel network formed inside the suspension holds the particles together collectively (Figure 4.10) to mold a dense green body that is demoldable and takes the form of the mold cavity. During

heating in-situ polymerization takes place to form a gel network to hold the ceramic particles collectively into a hard green body (Ranjith Kumar et al., 2007).

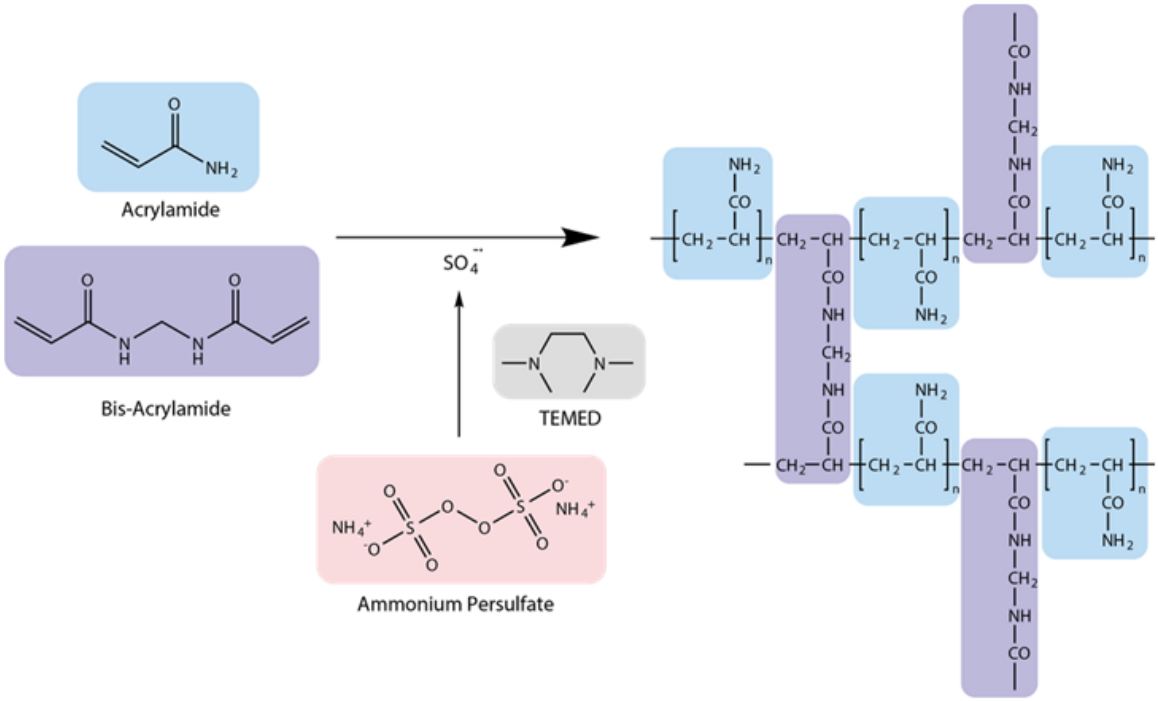

Figure 4.9. Mechanism of acrylamide polymerization

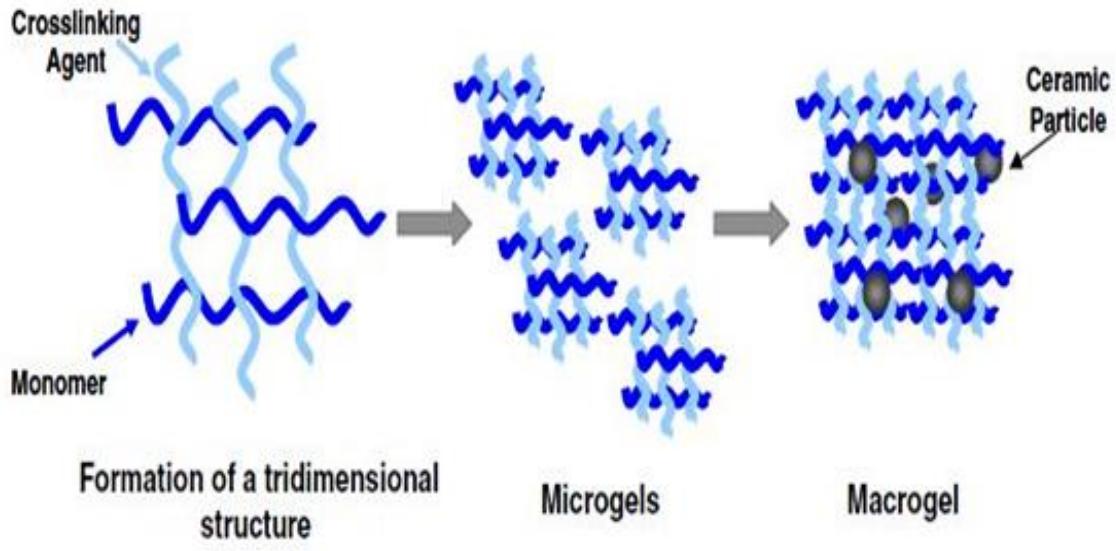

Figure 4.10. Schematic of the gel formation

4.4. Characterization of SiO_2–Si_3N_4–BN ceramic composite

The outstanding properties of fused silica material suggest that these ceramic materials are excellent for the preparation of radomes and electromagnetic wave transparent windows. Fused silica ceramics have low thermal expansion, high chemical resistance, low dielectric constant, low loss tangent and excellent optical qualities (Mishra et al., 2010 and Wan et al., 2013). But fused silica ceramics possess low mechanical strength which limits the needs of advanced re-entry vehicles, especially hypersonic space crafts. To overcome the shortfall, now a days fused silica is used by the addition of different ceramic materials (Wan et al., 2014 and Du et al., 2010). Advanced structural ceramic composites possess excellent characteristics like high strength, better reliability and lower environmental effect. The structural strength of fused silica ceramics was very poor for application in areas of advanced reentry vehicles, especially hypersonic space crafts. To meet the requirements of aerospace applications, the strength of the fused silica ceramic needs to be improved. Silicon nitride ceramics possesses excellent mechanical properties like high fracture toughness, high strength, and high chemical resistance, high thermal shock resistance, and then they show great promise in engineering applications (Yu et al., 2009). Boron nitride is a ceramic which possess excellent thermal shock resistance, chemical inertness, low thermal expansion, good dielectric properties and high electrical resistance.

4.4.1. Mechanical characterization

4.4.1.1 Flexural strength

The influence of monomer content on flexural strength at various solid loadings was observed in Figure 4.11. The warped surfaces were removed from the samples to conduct three point bending test. From the results it was found that flexural strength enhances with solid loading because the density of sintered ceramic sample increases and the space between the particles decreases resulting in low shrinkage. Also flexural strength increases as the monomer content increases and reaches an optimal point and then decreases. The flexural strength of the sintered bodies is affected by the pores formed during organic binder burnout. If the monomer content is low, the flexural strength of green samples remains low as 3-dimesnsional network is very coarse resulting in non-uniform distribution of fused silica particles, which affects flexural strength.

From the results it is observed that there was an increase in solid loading from 48% to 50% with the strength increasing from 46.7 MPa to 61.05 MPa at 5 wt% monomer content. At 10 wt% monomer content, the strength increases from 70.84 MPa to 84.92 MPa when there is an increase in solid loading from 48% to 50%. As the solid loading increases from 48% to 50%, the strength increases from 67.5 MPa to 81.57 MPa at 15 wt% monomer content. The same sequence was observed for the remaining solid loadings. Flexural strength increases from 46.7 MPa to 70.84 MPa when the monomer content increases from 5 to 10 wt% and the strength decreases from 70.84 MPa to 67.5 MPa when monomer ratio increases from 10 to 15 wt% showing an optimum value at 10 wt% at solid loading of 48%. The same sequence is followed for the remaining solid loadings. The maximum flexural strength is obtained by a combination of SiO_2–Si_3N_4–BN is 98.27 MPa at a monomer content 10 wt%, monomer ratio of 10:1 and solid loading of 52%. The 3-dimesnsional network structures are compact at optimum monomer ratio and when distribution of fused silica particles is uniform.

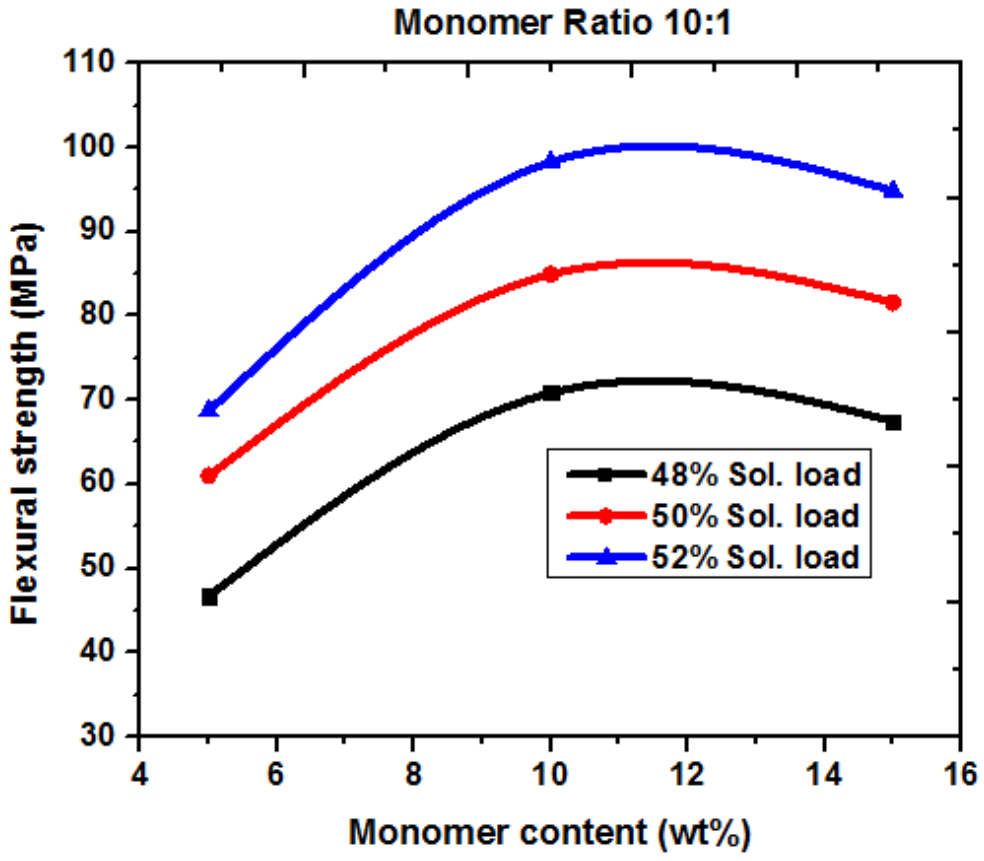

Figure 4.11. Effect of monomer content on flexural strength at different solid loadings

4.4.1.2 Porosity

The effect of the ratio of monomers on porosity at different solid loadings is shown in Figure 4.12. The porosity of the sintered ceramics decreases with increment in solid loading because the density of the sample increases. The porosity decreases up to a certain limit and then increases with increase in monomer content a at constant monomer ratio. From the results, it is found that with an increase in solid loading from 48% to 50%, porosity decreases from 38.9% to 34.93% at 5 wt% monomer content. At 10 wt% monomer content, porosity decreases from 32.93% to 29.81% when the solid loading increases from 48% to 50%. As the solid loading increases from 48% to 50% porosity decreases from 40.01% to 36.19% at 15 wt% monomer content. The same sequence is observed for the remaining solid loadings. Wei Wan et al., (2014) also observed the same pattern with solid loadings. Porosity decreases from 38.9% to 32.93% when the monomer content increases from 5 to 10 wt% and porosity increases from 32.93% to 40.01% when the monomer content increases from 10 to 15 wt% showing an optimum value at 10 wt% at solid loading of 48%. The same sequence is followed for the remaining solid loadings. The minimum porosity obtained by the combination of SiO_2–Si_3N_4–BN is 26.37% at a monomer ratio of 10:1, 10 wt% monomer content and solid loading of 52%.

The monomer and cross linking agent can form macro molecular network to hold the ceramic particles together and furthermore it can assume an important role in the making of the pores during the fabrication of ceramic composites. The increased solid content could obviously decrease the porosity of the resultant porous material. Increase in the solid content decreases pore size. The increase of crosslinking agent makes the crosslink density of cross-linked polymer gels in green body increase, the distribution of ceramics particles very uniform, the drying shrinkage smaller, and thus increases the porosity of sintering body increases (Yu et al., 2009).

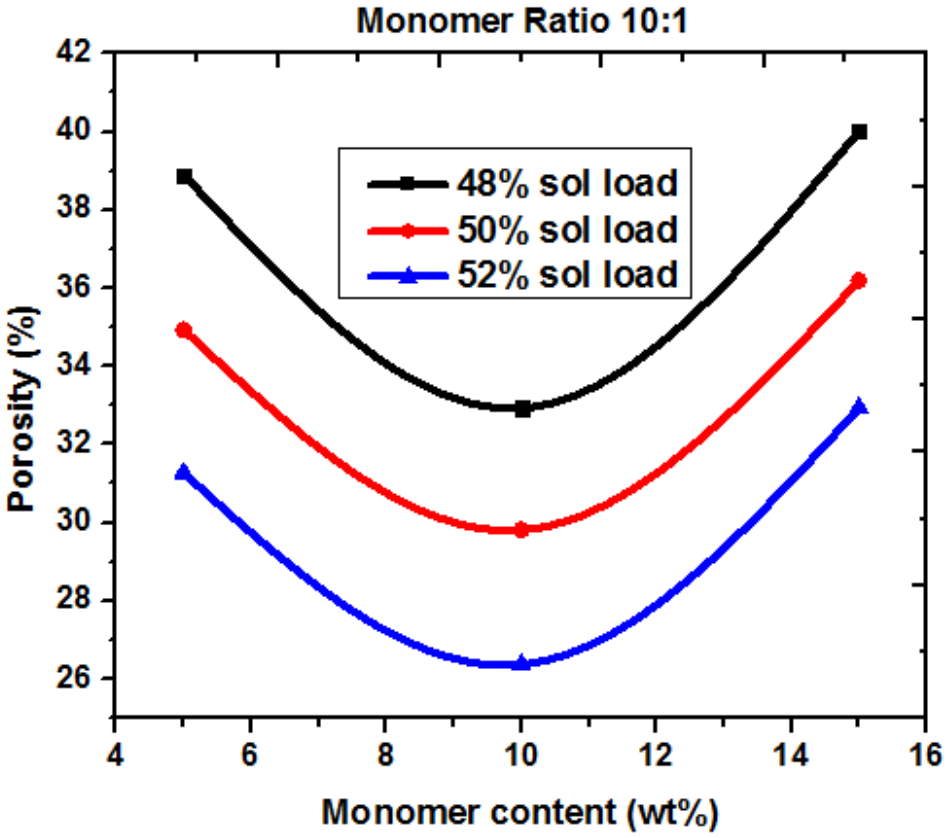

Figure 4.12. Effect of monomer content on porosity at different solid loadings

4.4.2. Dielectric constant

Figure 4.13 shows the effect of monomer content on dielectric constant at different solid loadings. The dielectric properties of SiO_2–Si_3N_4–BN ceramic composites depend heavily on porosity. From the results it is observed that there was an increment in solid loading from 48% to 50% with dielectric constant increasing from 4.86 to 5.18 at 5 wt% monomer content. At 10 wt% monomer content, the dielectric constant increases from 5.73 to 5.98 when there is an increment in solid loading from 48% to 50%. As the solid loading increases from 48% to 50%, the dielectric constant increases from 4.26 to 4.97 % at 15 wt% monomer content. The same sequence is observed for the remaining solid loadings where the dielectric constant increases from 4.86 to 5.73 when the monomer content increases from 5 to 10 wt% and the dielectric constant decreases from 5.73 to 4.26 when monomer ratio increases from 10 to 15 wt% showing an optimum value at 10 wt% at solid loading of 48%. The same sequence is followed for the remaining solid loadings. The minimum dielectric constant is obtained by a combination of SiO_2–Si_3N_4–BN is 4.26 at a monomer content 15 wt%, monomer ratio of 10:1 and solid loading of 48%.

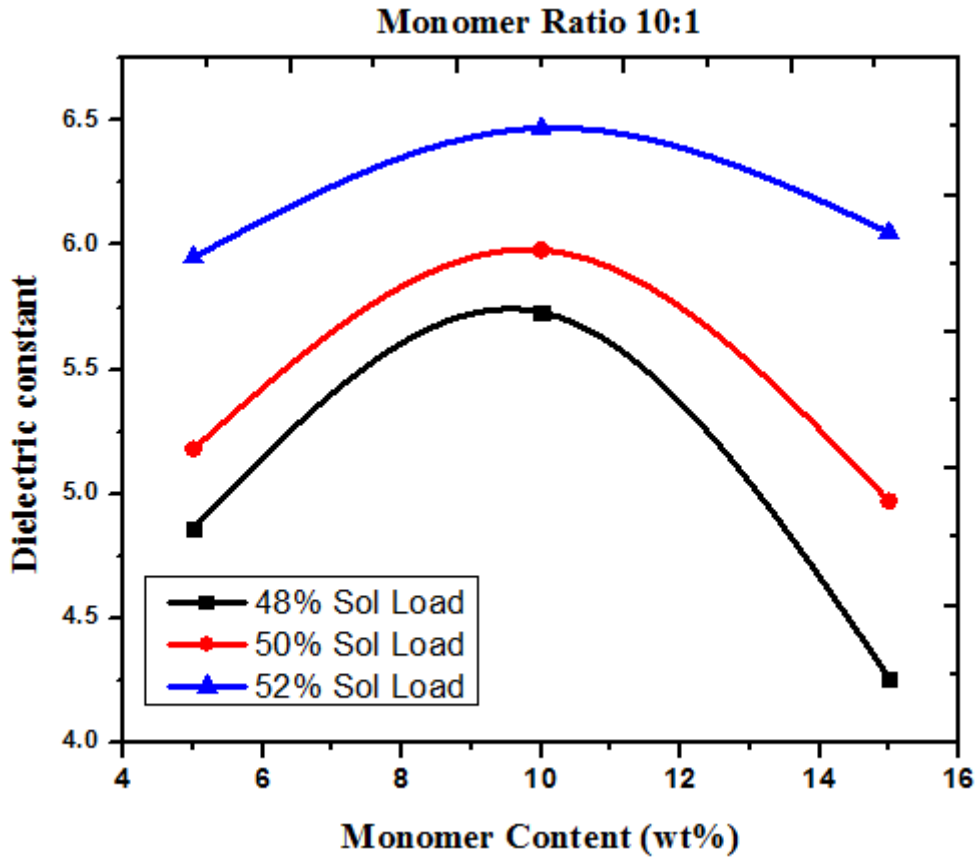

Figure 4.13. Effect of monomer content on dielectric constant at different solid loadings

4.5. Characterization of SiO_2–Si_3N_4–Al_2O_3 ceramic composite

The outstanding properties of fused silica material suggest that these ceramic materials are excellent for the preparation of radomes and electromagnetic wave transparent windows. Fused silica ceramics have low thermal expansion, high chemical resistance, low dielectric constant, low loss tangent and excellent optical qualities. But fused silica ceramics possess low mechanical strength which limits the needs of advanced re-entry vehicles, especially hypersonic space crafts. To overcome the shortfall, now a days fused silica is used by the addition of different ceramic materials. Alumina is a typical additive to silica-based ceramic production and glasses. Alumina keeps the vehicle of soluble particles through the silica structure that are vital for cristobalite arrangement. Alumina does not specifically influence the crystallization temperature of cristobalite, which is kept up at roughly 1200 °C, yet alumina can expand the crystallization rate in small concentrations (Wilson et al., 2011).

4.5.1. Mechanical characterization

4.5.1.1 Flexural strength

The influence of monomer content on flexural strength at various solid loadings and monomer ratios was observed in Figures 4.14, 4.15 and 4.16 respectively.

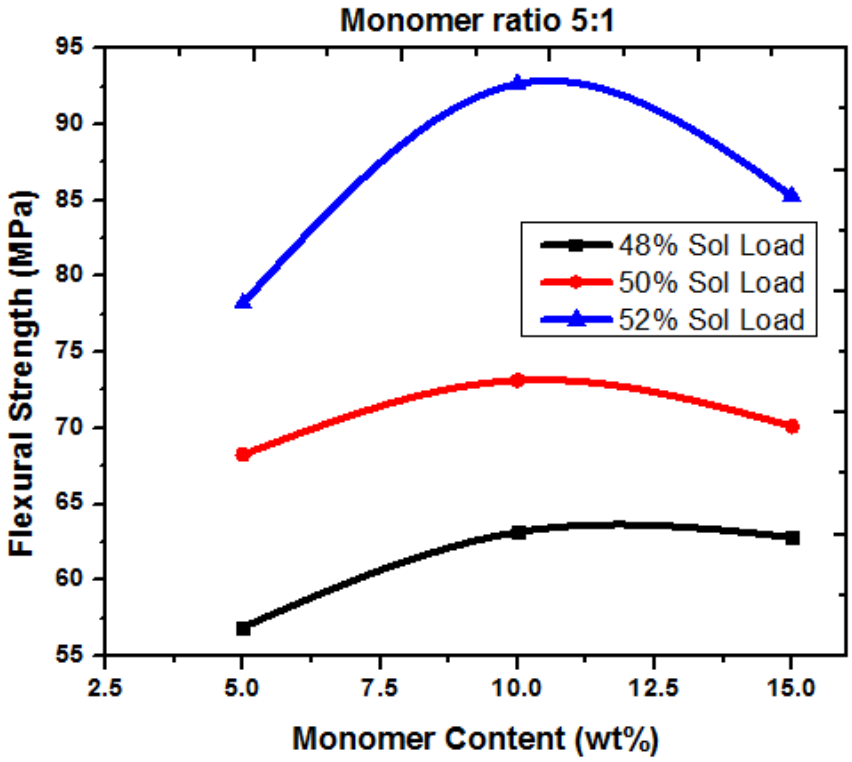

Figure 4.14. Effect of monomer content on flexural strength at different solid loadings at monomer ratio 5:1

From the results it is observed that there was an increment in solid loading from 48% to 50% with the strength increasing from 60.12 MPa to 76.13 MPa at 5 wt% monomer content. At 10 wt% monomer content, the strength increases from 65.23 MPa to 78.67 MPa when there is an increment in solid loading from 48% to 50%. As the solid loading increases from 48% to 50%, the strength increases from 64.45 MPa to 75.38 MPa at 15 wt% monomer content. The same sequence is observed for the remaining solid loadings. Flexural strength increases from 60.12 MPa to 65.23 MPa when the monomer content increases from 5 to 10 wt% and the strength decreases from 65.23 MPa to 64.45 MPa when monomer ratio increases from 10 to 15 wt% showing an optimum value at 10 wt% at solid loading of 48%. The same sequence is followed for the remaining solid loadings. The maximum flexural strength is obtained by a combination of SiO_2–Si_3N_4–Al_2O_3 is 95.12 MPa at a monomer content of 10 wt%, monomer ratio of 10:1 and solid loading of 52%. The 3-dimensional network structures

are compact at optimum monomer ratio and when distribution of fused silica particles was uniform.

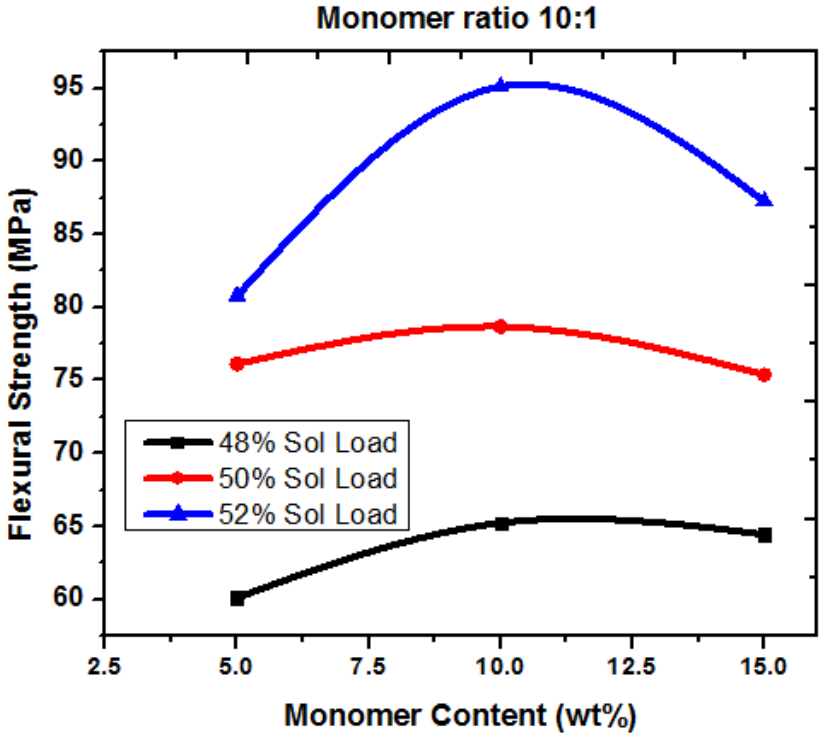

Figure 4.15. Effect of monomer content on flexural strength at different solid loadings at monomer ratio 10:1

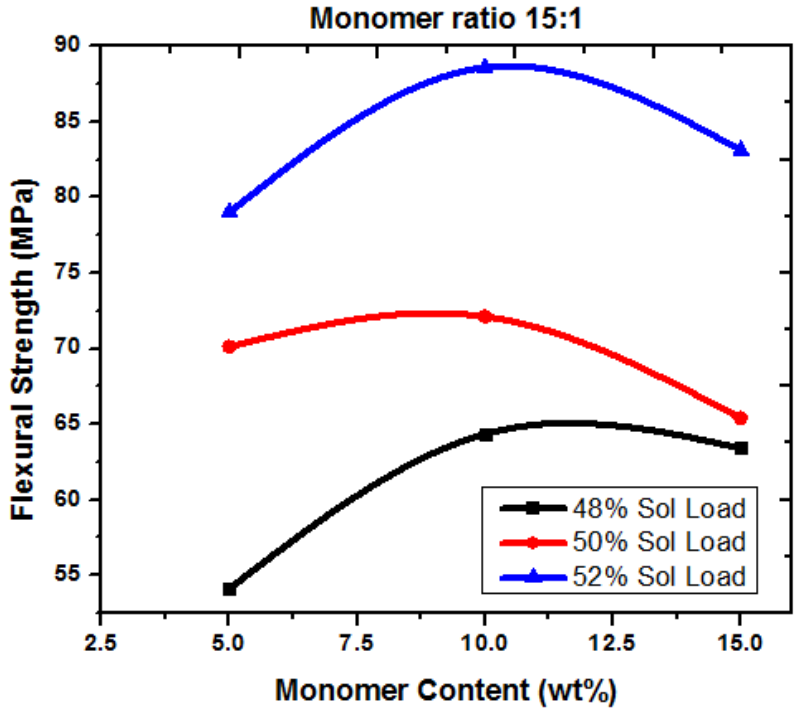

Figure 4.16. Effect of monomer content on flexural strength at different solid loadings at monomer ratio 15:1

4.5.1.2 Porosity

The influence of monomer content on porosity at various solid loadings and monomer ratios was observed in Figures 4.17, 4.18 and 4.19 respectively. The porosity of the sintered ceramics decreases with increment in solid loading because the density of the sample increases. The porosity decreases up to a certain limit and then increases with increase in monomer content at a constant monomer ratio. From the results it is found that with an increment in solid loading from 48% to 50%, the porosity decreases from 35.7% to 35.4% at 5 wt% monomer content. At 10 wt% monomer content, the porosity decreases from 34.54% to 31.72% when the solid loading increases from 48% to 50%. As the solid loading increases from 48% to 50%, porosity decreases from 37.76% to 35.23% at 15 wt% monomer content. The same sequence is observed for the remaining solid loadings. Wan et al., (2014) also observed the same pattern with solid loadings. The porosity decreases from 35.7% to 34.54% when the monomer content increases from 5 to 10 wt% and porosity increases from 34.54% to 37.76% when the monomer content increases from 10 to 15 wt% showing an optimum value at 10 wt% at solid loading of 48%.

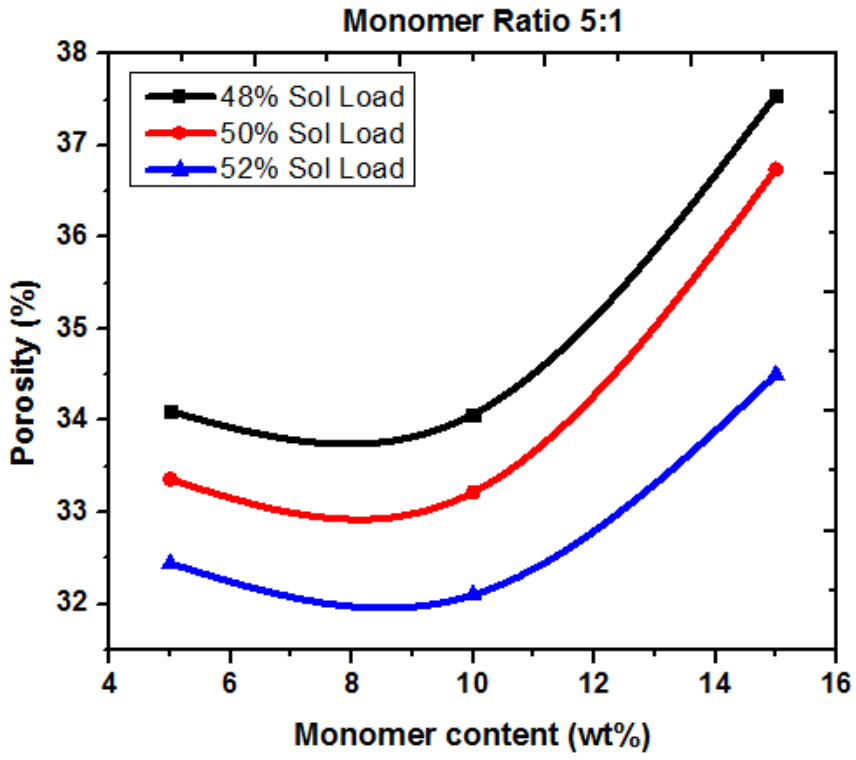

Figure 4.17. Effect of monomer content on porosity at different solid loadings at monomer ratio 5:1

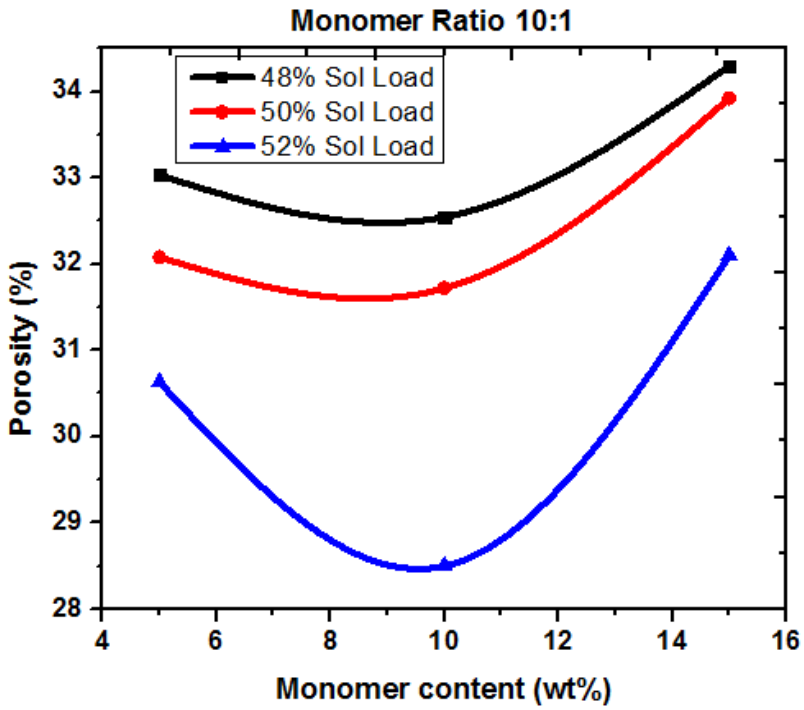

Figure 4.18. Effect of monomer content on porosity at different solid loadings at monomer ratio 10:1

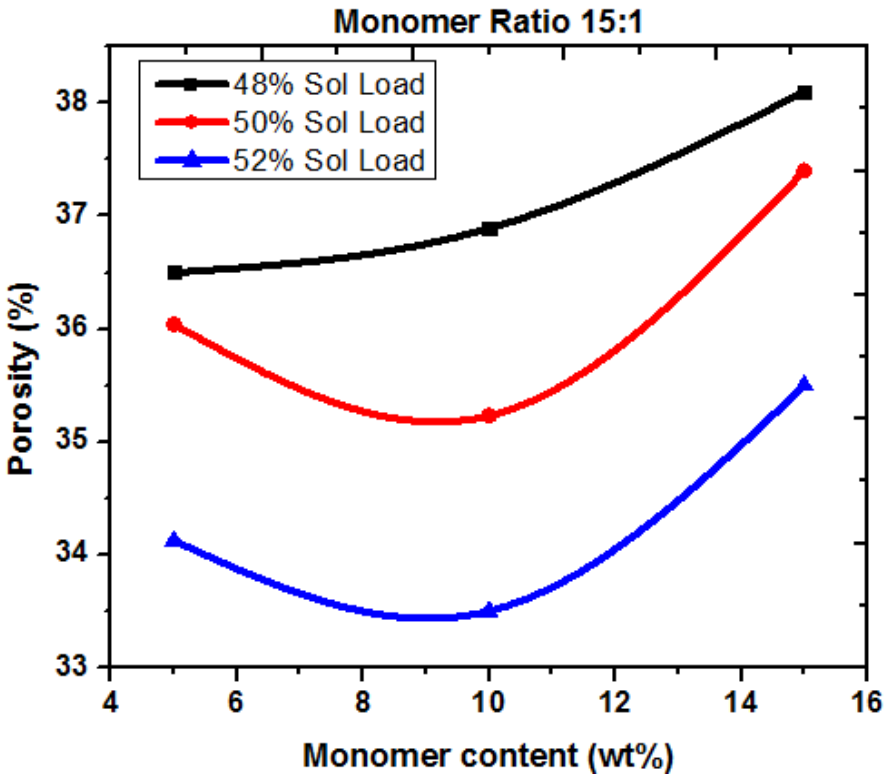

Figure 4.19. Effect of monomer content on porosity at different solid loadings at monomer ratio 15:1

The same sequence was followed for the remaining solid loadings. The minimum porosity obtained by the combination of SiO_2–Si_3N_4–Al_2O_3 is 28.37% at a monomer ratio of 10:1, 10 wt% monomer content and solid loading of 52%.

4.5.2. Dielectric constant

The influence of monomer content on porosity at various solid loadings and monomer ratios was presented in Figures 4.20, 4.21 and 4.22 respectively. The dielectric properties of SiO_2-Si_3N_4-Al_2O_3 ceramic composites depend heavily on porosity. From the results it is observed that there was an increment in solid loading from 48% to 50% with the dielectric constant increasing from 5.01 to 6.01 at 5 wt% monomer content. At 10 wt% monomer content, the dielectric constant increases from 5.485 to 6.14 when there is an increment in solid loading from 48% to 50%. As the solid loading increases from 48% to 50%, the dielectric constant changes from 4.712 to 5.782 % at 15 wt% monomer content.

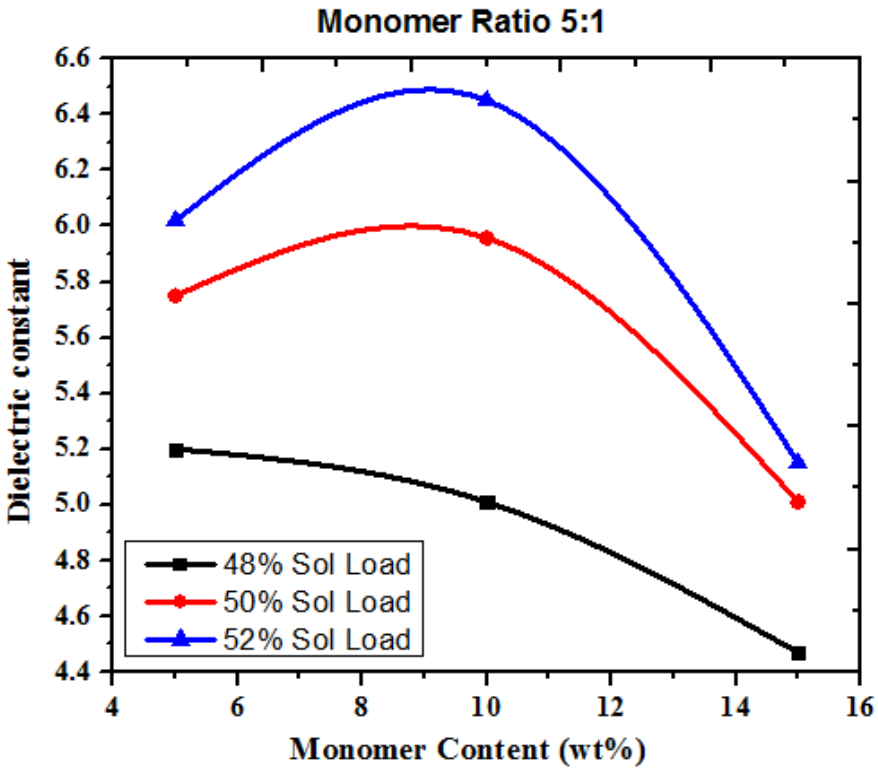

Figure 4.20. Effect of monomer content on dielectric constant at different solid loadings at monomer ratio 5:1

The same sequence was observed for the remaining solid loadings. Dielectric constant increases from 5.01 to 5.485 when the monomer content increases from 5 to 10 wt% and the dielectric constant decreases from 5.485 to 4.71 when monomer ratio increases from 10 to 15

wt% showing an optimum value at 10 wt% at solid loading of 48%. The same sequence is followed for the remaining solid loadings. The minimum dielectric constant is obtained by a combination of SiO_2–Si_3N_4–Al_2O_3 is 4.02 at a monomer content 15 wt%, monomer ratio of 15:1 and solid loading of 48%.

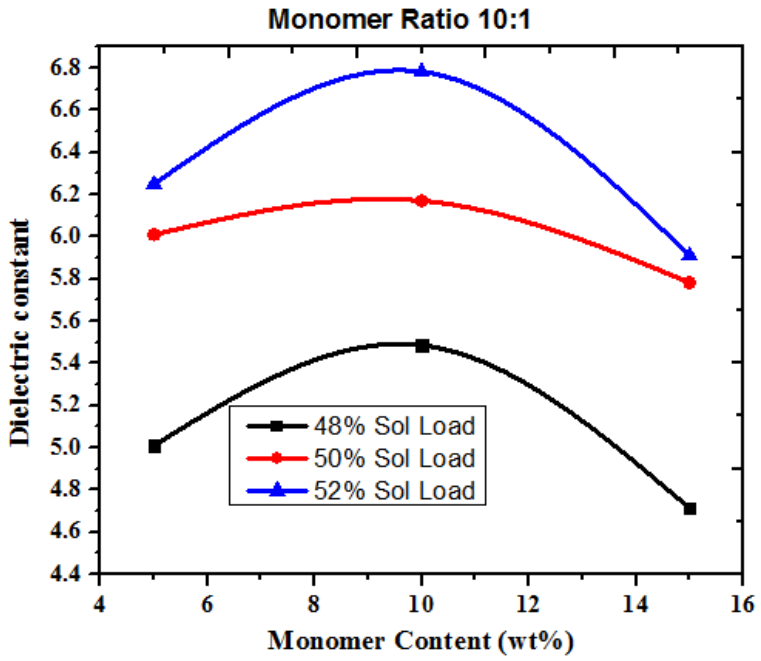

Figure 4.21. Effect of monomer content on dielectric constant at different solid loadings at monomer ratio 10:1

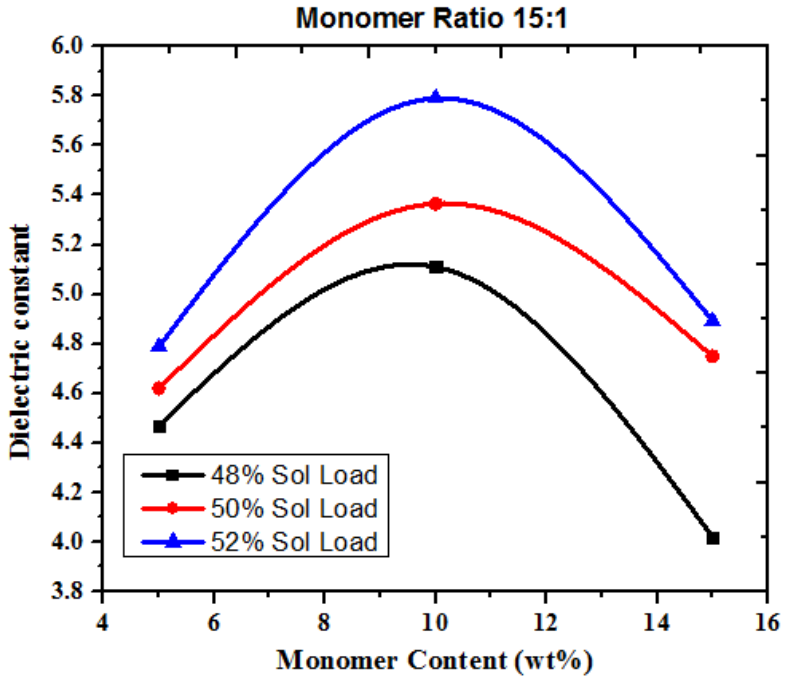

Figure 4.22. Effect of monomer content on dielectric constant at different solid loadings at monomer ratio 15:1

4.6. Process modeling and optimization of SiO_2–Si_3N_4–BN ceramic Composite

RSM is a statistical and numerical technique that is utilized for the design and optimization of engineering problems. It is mainly used to find an approximate mathematical model for estimating the future response and to find the process parameters that optimize the predicted model (Xiangli et al., 2008). The aim of the current analysis is to find the optimum settings of interaction effects of the input process parameters (SL, MR and MC) that result in optimum responses for flexural strength, porosity and dielectric constant. Consequently RSM was decided for the present exploratory examination since it is perfect and a reasonable outline of multivariable measurable techniques. Analysis of Variance (ANOVA) is used for recommended and balanced models. The F-values were utilized to test the statistical immensity of recommended and changed models for ANOVA. It looks at the probability of partitioning the variety in trial information into parts. Every one of the terms in the condition was figured and organized, in an ANOVA table. There are parts of parameters which were proposed to assess the nature of the scientific models and how ably they suit exploratory information like coefficient of determination (R^2), adjusted coefficient of determination (Adj. R^2), coefficient of variation (C.V.), adequate precision and lack of fit (LOF) (Li et al., 2013). The experimental design and test data is shown in Table 4.1.

Table 4.1. Experimental design and test data

S. No.	Sol. Loading (vol%)	Monomer content (wt%)	Flexural strength (Mpa)	Porosity (%)	Dielectric constant
1	48	5	46.7	38.9	4.86
2	50	15	81.57	36.19	4.97
3	52	5	68.71	31.27	5.95
4	48	15	67.5	40.01	4.26
5	48	10	70.84	32.93	5.73
6	50	5	61.02	34.93	5.18
7	50	10	84.92	29.81	5.98
8	52	10	98.27	26.37	6.47
9	50	10	84.92	29.81	5.98
10	50	10	84.92	29.81	5.98

11	50	10	84.92	29.81	5.98
12	50	10	84.92	29.81	5.98
13	52	15	94.85	32.93	6.05

4.6.1. Modeling of flexural strength

ANOVA for response surface model of flexural strength is shown in Table 4.2.

Table 4.2 ANOVA for response surface model of flexural strength

Source	Sum of Squares	Df	Mean Square	F Value	p-value Prob > F	
Model	2455.91	5	491.182	498.729	< 0.0001	significant
A-Solid loading	982.784	1	982.784	997.885	< 0.0001	
B-Monomer content	759.15	1	759.15	770.815	< 0.0001	
AB	7.1289	1	7.1289	7.23844	<0.0311	
A^2	3.24725	1	3.24725	3.29715	0.1123	
B^2	568.287	1	568.287	577.019	< 0.0001	
Residual	6.89407	7	0.98487			
Lack of Fit	6.89407	3	2.29802			
Pure Error	0	4	0			
Cor Total	2462.8	12				

R-Squared: 0.997, Adj R-Squared=0.995, Pred R-Squared=0.973, Adequate Precision: 73.94, C.V.: 1.272

From ANOVA it is observed that A, B, AB and B^2 are significant model terms. The regression model developed for flexural strength is given in Eq. 4.1.

$$Flexural\ strength\ (MPa) = 85.1255 + 12.798 \times A + 11.2483 \times B + 1.335 \times A \times B - 1.084 \times A^2 - 14.344 \times B^2 \quad (4.1)$$

It is essential to know that the obtained model gives an adequate approximation to the actual system. Model acceptability can be ensured by drawing diagnostic figures like predicted versus experimental. Figure 4.23 represents the difference between experimentally measured values and predicted values for flexural strength. The measured values were found relatively close to the straight line. The graphs backed by Adj. R^2 values for three responses

were 0.995 which is close to 1 indicating a better compliance between observed and predicted values.

Figures 4.24 and 4.25 shows the single factor effect and Figure 4.26 shows the interaction effect on flexural strength. It is observed that with increase in SL, there is enhancement in the density of fused silica ceramic composites which is favorable for increase in flexural strength. However, the maximum flexural strength is obtained at 52%.

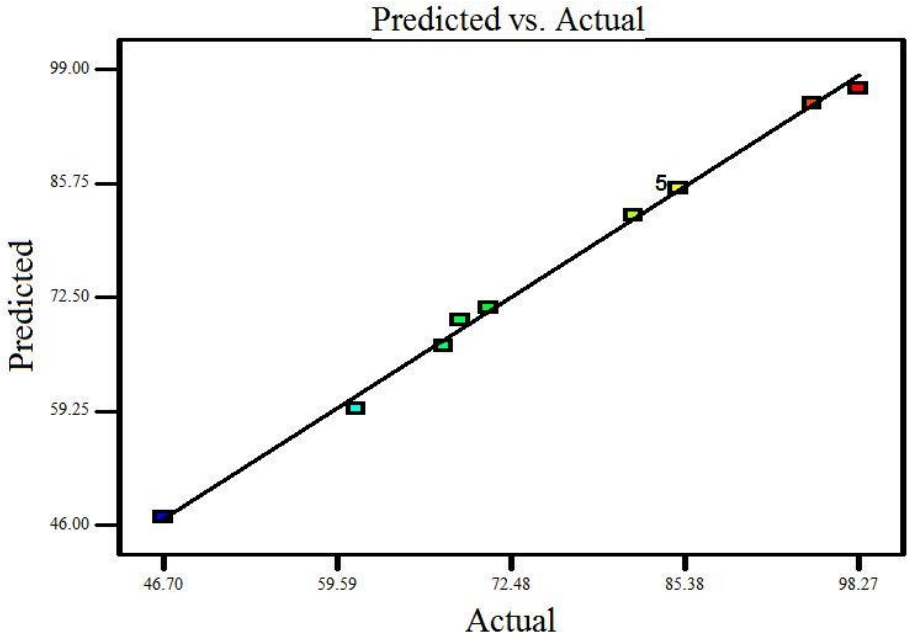

Figure 4.23. Predicted versus actual for flexural strength

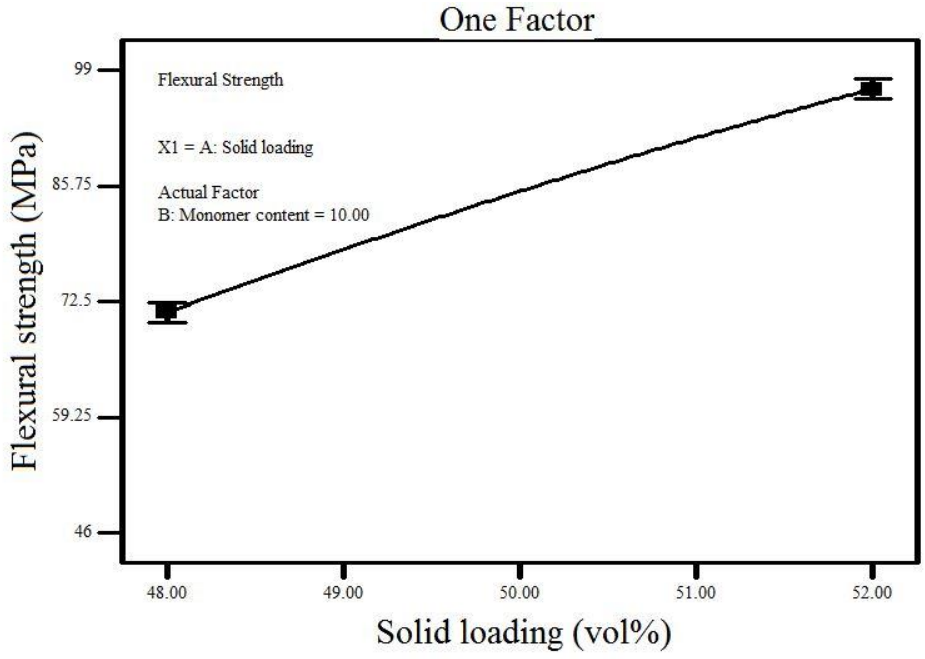

Figure 4.24. Effect of solid loading on flexural strength

The organic binder burnout plays a vital role in pore formations which affects flexural strength of the sintered ceramics. If the MR is low, the flexural strength of dried samples remains low as the 3-dimesnsional network is too coarse that results in non-uniform distribution of SiO_2 particles that influence decrease in flexural strength. Maximum flexural strength is obtained at 52 vol% SL, 10:1 MR and 10 wt% MC.

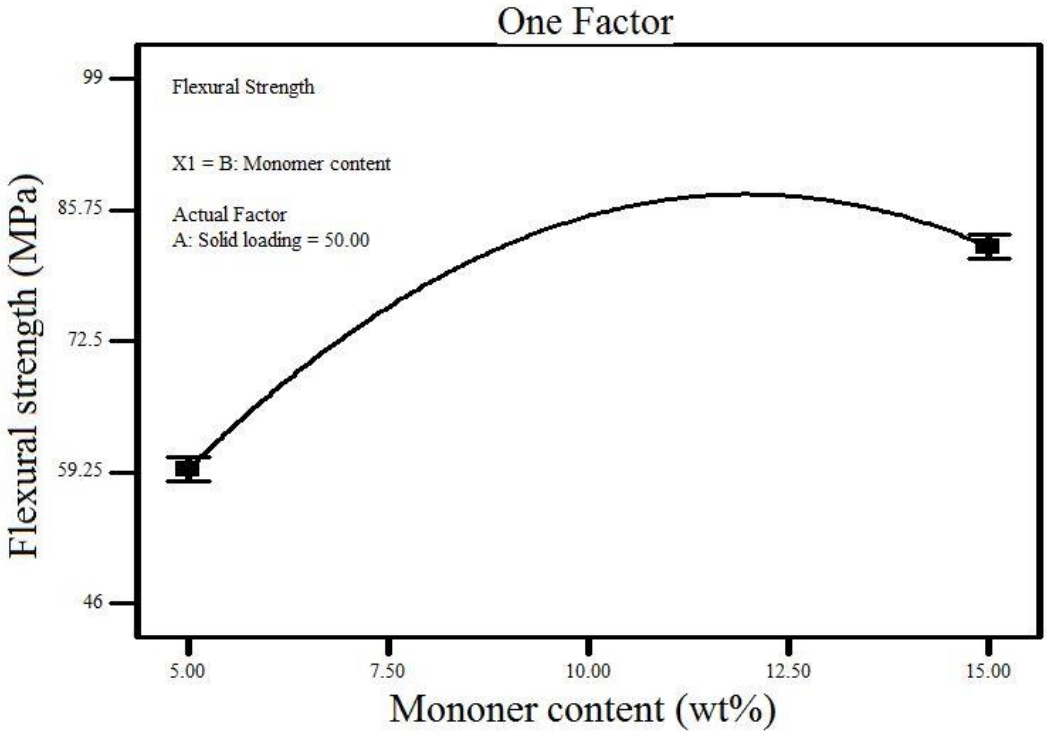

Figure 4.25. Effect of monomer content on flexural strength

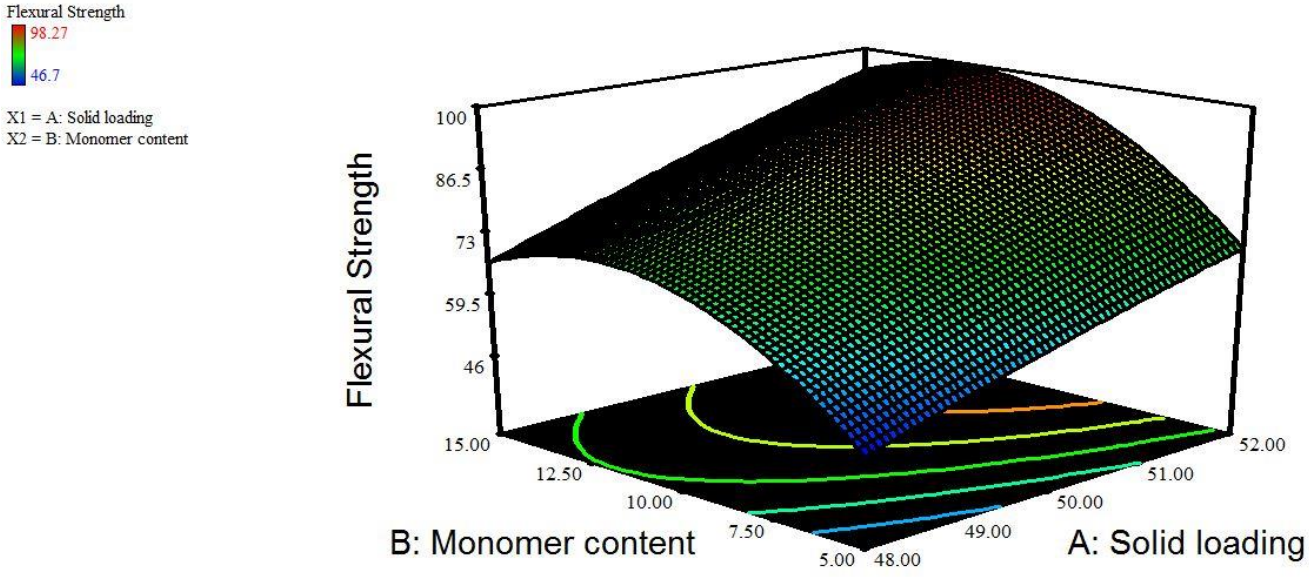

Figure 4.26. Effect of monomer content and solid loading on flexural strength

4.6.2. Modeling of porosity

ANOVA for response surface model of porosity is shown in Table 4.3.

Table 4.3 ANOVA for response surface model of porosity

Source	Sum of Squares	df	Mean Square	F Value	p-value Prob > F	
Model	192.4172	6	32.0695	1859.31	< 0.0001	significant
A-Solid loading	21.5168	1	21.5168	1247.489	< 0.0001	
B-Monomer content	2.706817	1	2.70682	156.9343	< 0.0001	
AB	0.210675	1	0.21068	12.2144	0.0129	
A^2	0.001366	1	0.00137	0.079212	0.7878	
B^2	97.19554	1	97.1955	5635.15	< 0.0001	
AB^2	0.075625	1	0.07563	4.384545	0.0812	
Residual	0.103489	6	0.01725			
Lack of Fit	0.103489	2	0.05174			
Pure Error	0	4	0			
Cor Total	192.5207	12				

R-Squared: 0.999, Adj R-Squared=0.998, Pred R-Squared=0.987, Adequate Precision: 139.29, C.V.: 0.404

From ANOVA it was observed that A, B, AB and B^2 are significant model terms. The regression model developed for porosity is given in Eq. 4.2.

$$Porosity\ (\%) = 29.758 - 3.28 \times A + 0.672 \times B + 0.1375 \times A \times B + 0.022 \times A^2 + 5.9322 \times B^2 - 0.3975 \times A \times B^2 \quad (4.2)$$

It is essential to know that the obtained model gives adequate approximation to the actual system. Model acceptability can be ensured by drawing diagnostic figures like predicted versus experimental. Figure 4.27 represents the difference between experimentally measured values and predicted values for porosity. The measured values were found relatively close to the straight line. The graphs backed by Adj. R^2 values for three responses were 0.998 which is near 1 indicating better compliance between observed and predicted values. Figure 4.28 and 4.29 shows the single factor effect and Figure 4.30 shows the interaction effect on porosity.

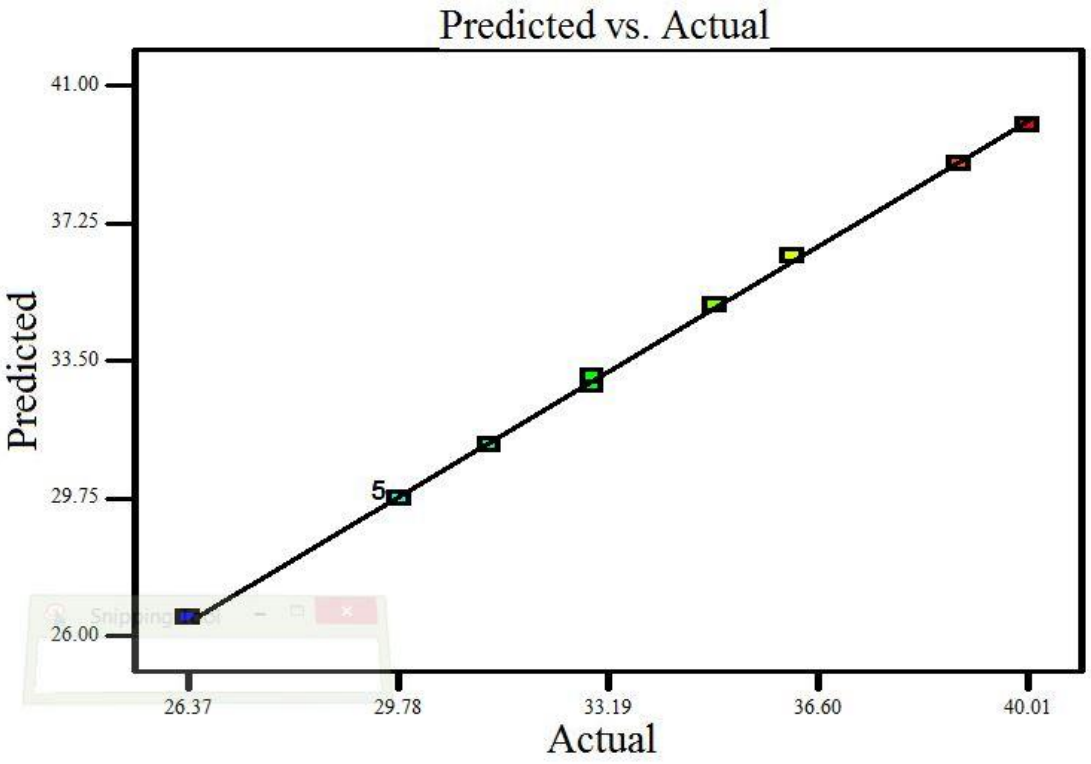

Figure 4.27. Predicted versus actual for porosity

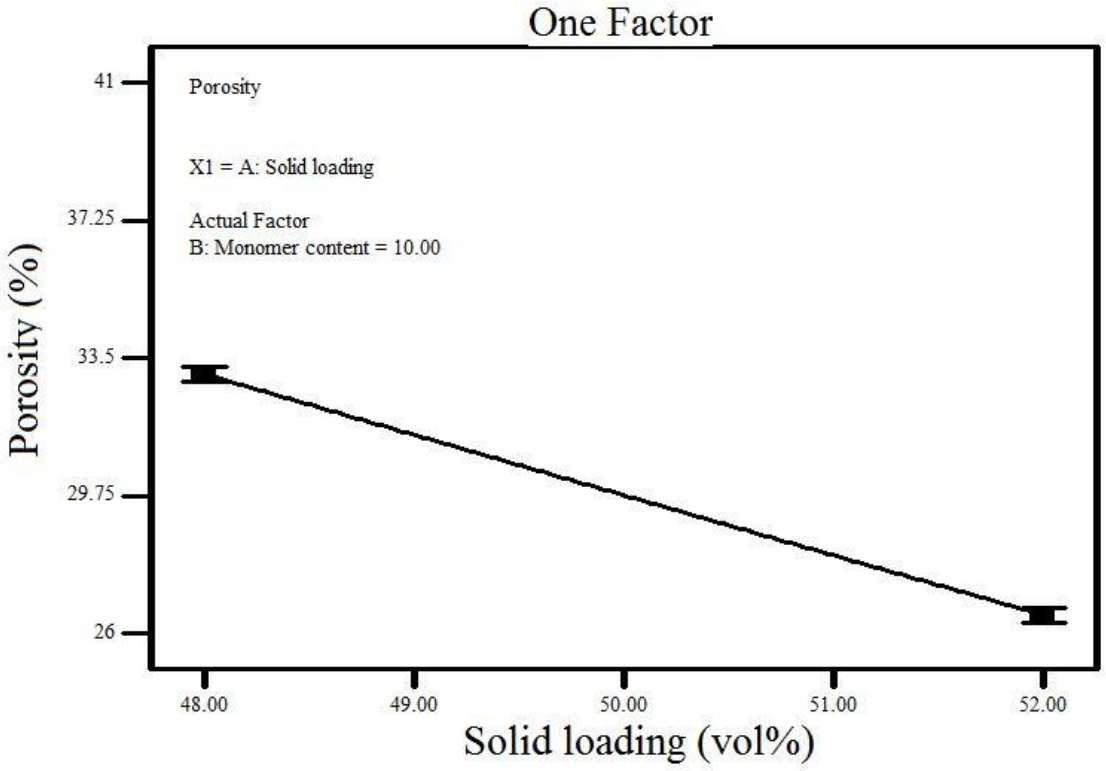

Figure 4.28. Effect of solid loading on porosity

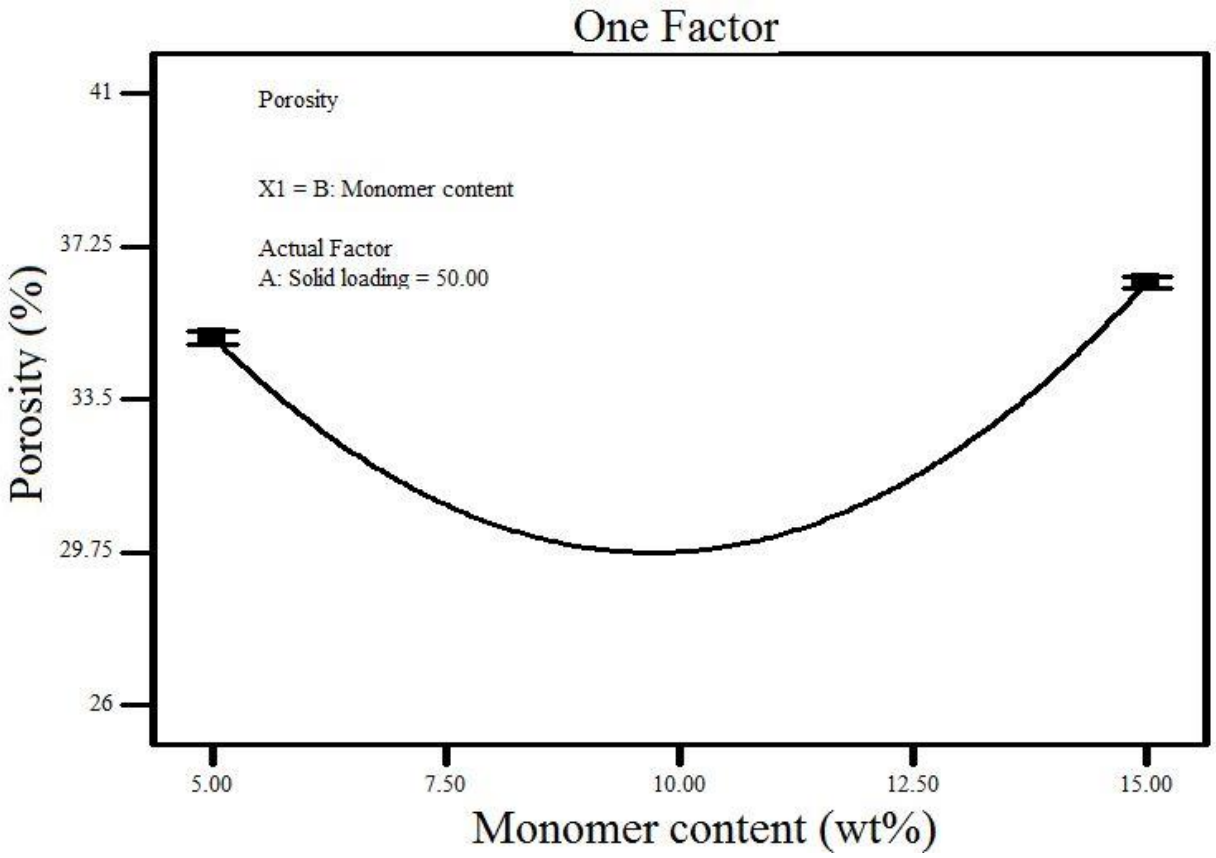

Figure 4.29. Effect of monomer content on porosity

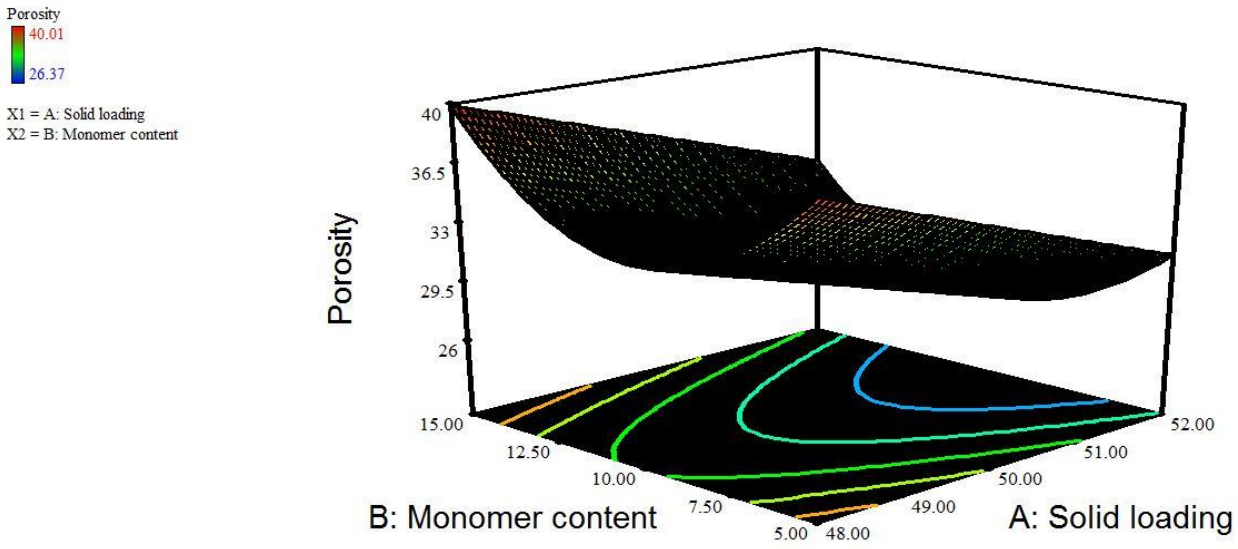

Figure 4.30. Effect of monomer content and solid loading on porosity

Porosity of ceramic composites mainly depends on solid loading, monomer ratio and monomer content. Solid loading has a negative impact on the porosity whereas monomer ratio and monomer content have optimal influence. The maximum porosity is obtained at 48% solid loading. Porosity decreases with increase of solid loading. Solid loading has more influence on density improvement in ceramic composites. The distance between the particles and shrinkage is less as the solid loading increases.

4.6.3. Modeling of Dielectric constant

ANOVA for response surface model of dielectric constant is shown in Table 4.4.

Table 4.4 ANOVA for response surface model of dielectric constant

Source	Sum of Squares	Df	Mean Square	F Value	p-value Prob > F	
Model	4.70679	6	0.78447	853.284	< 0.0001	Significant
A-Solid loading	0.2738	1	0.2738	297.82	< 0.0001	
B-Monomer content	0.08402	1	0.08402	91.3872	< 0.0001	
AB	0.1225	1	0.1225	133.247	< 0.0001	
A^2	0.07162	1	0.07162	77.9052	0.0001	
B^2	2.06159	1	2.06159	2242.44	< 0.0001	
AB^2	0.16333	1	0.16333	177.662	< 0.0001	
Residual	0.00552	6	0.00092			
Lack of Fit	0.00552	2	0.00276			
Pure Error	0	4	0			
Cor Total	4.71231	12				

R-Squared: 0.998, Adj R-Squared=0.997, Pred R-Squared=0.972, Adequate Precision: 101.005, C.V.: 0.537

From ANOVA it is observed that A, B, AB, A^2 and B^2 are significant model terms. The regression model developed for dielectric constant is given in Eq. 4.3.

$$Dielectric\ constant = 5.9682 + 0.37 \times A - 0.1183 \times B + 0.175 \times A \times B + 0.161 \times A^2 - 0.8639 \times B^2 + 0.35 \times A \times B^2 \quad (4.3)$$

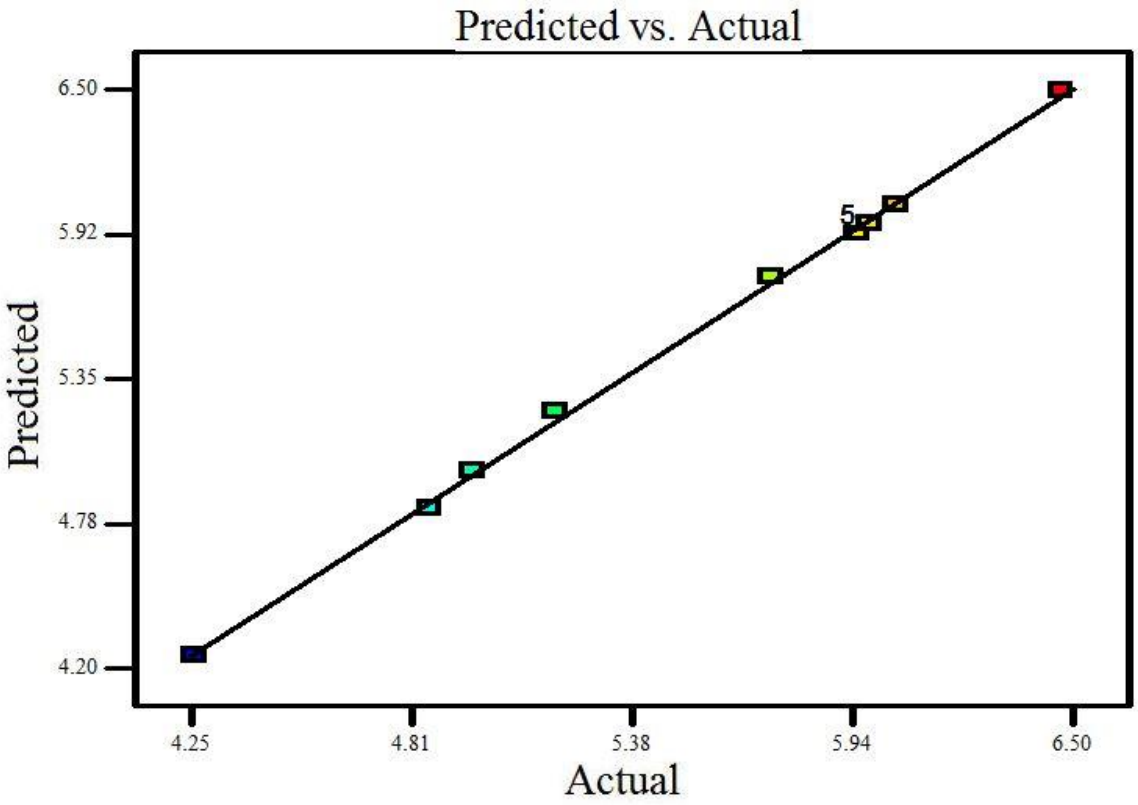

Figure 4.31. Predicted versus actual for dielectric constant

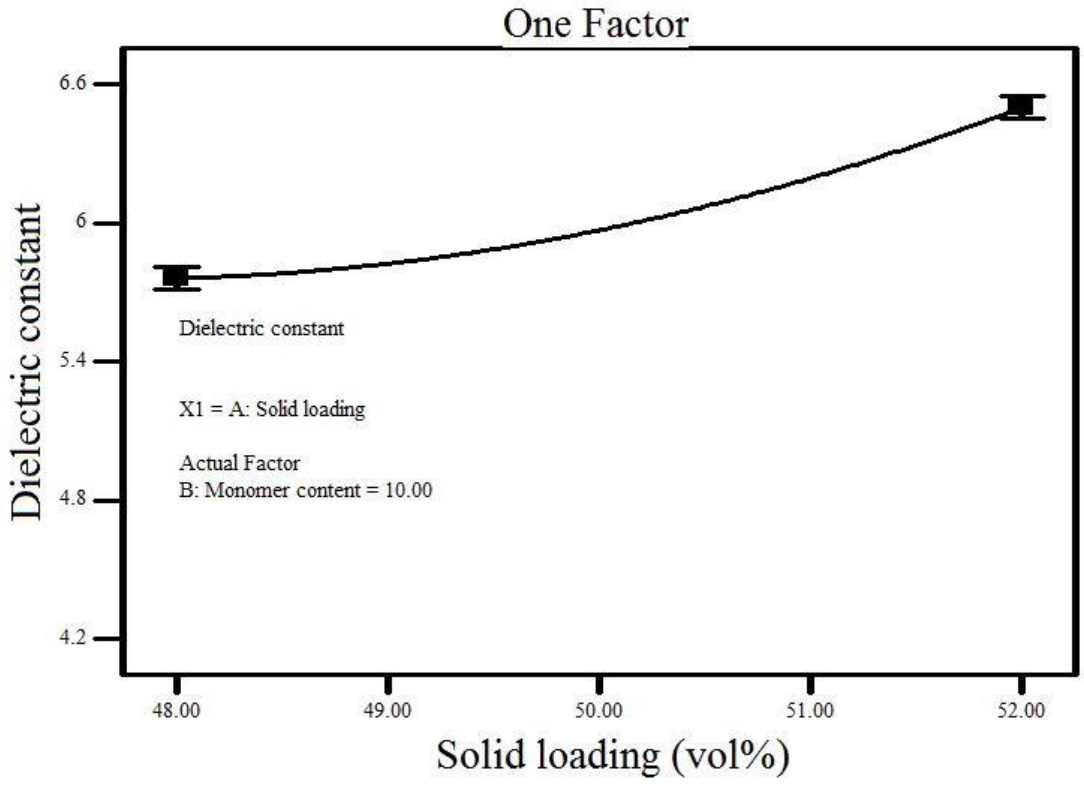

Figure 4.32. Effect of solid loading on dielectric constant

It is essential to know that the obtained model gives an adequate approximation to the actual system. Model acceptability can be ensured by drawing diagnostic figures like predicted versus experimental. Figure 4.31 represents the difference between experimentally measured values and predicted values for dielectric constant. The measured values were found relatively close to the straight line. The graphs backed by Adj. R^2 values for three responses were 0.998 which is near 1 indicating better compliance between observed and predicted values.

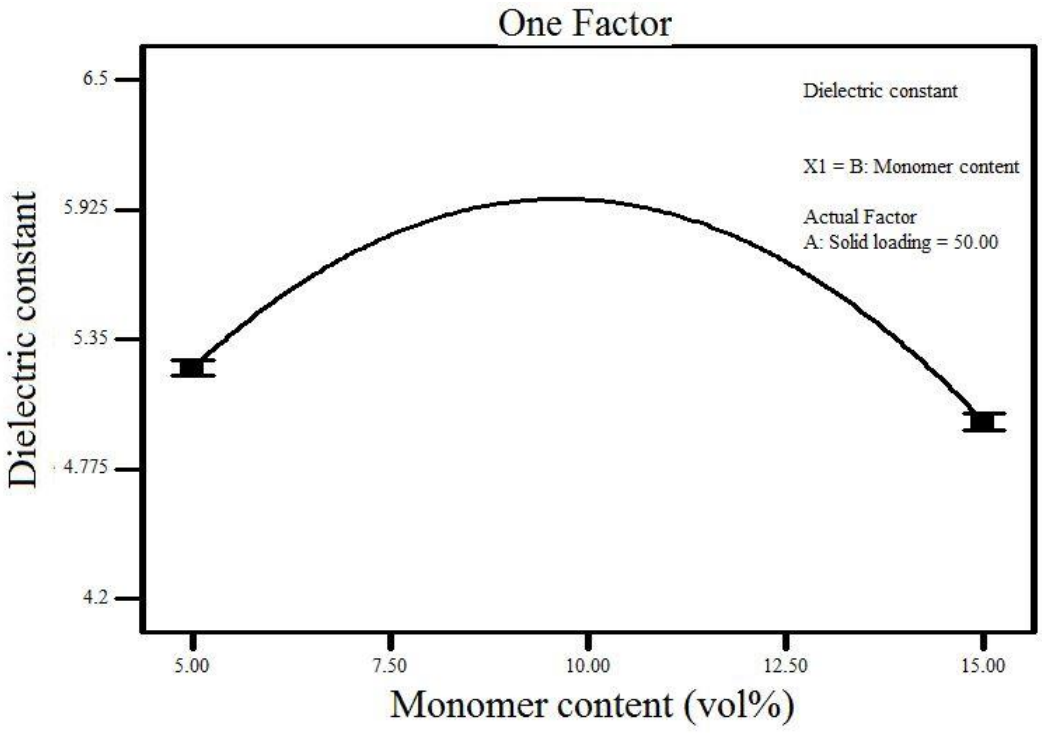

Figure 4.33. Effect of monomer content on dielectric constant

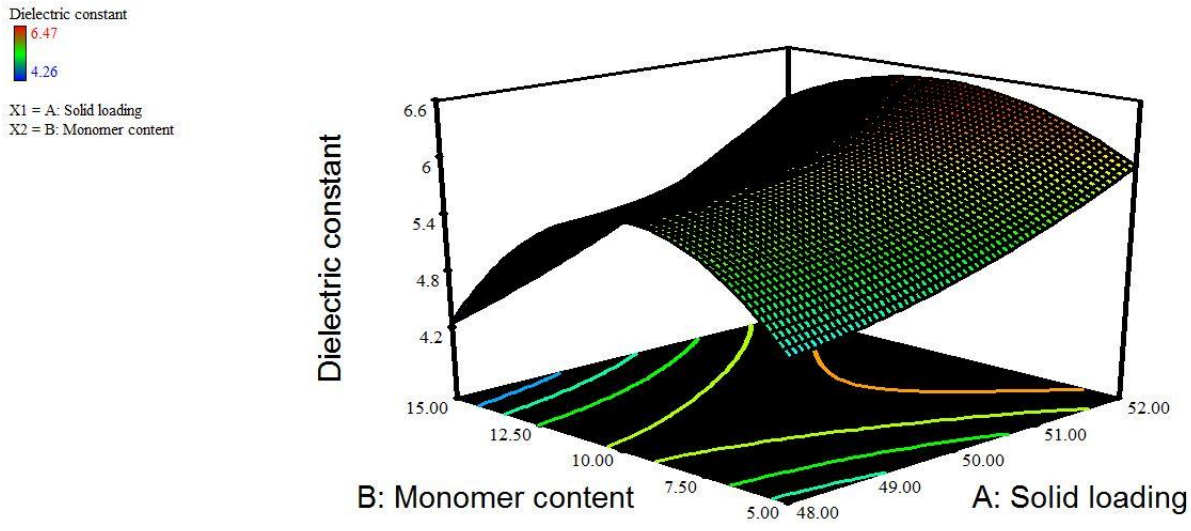

Figure 4.34. Effect of monomer content and solid loading on dielectric constant

Figures 4.32 and 4.33 show single factor effect and figure 4.34 show the interaction effect on dielectric constant. The dielectric constant of materials mainly depends on porosity. From the data, it is observed that the dielectric constant reduces with increase of porosity. Solid loading has positive impact on dielectric constant. The dielectric constant enhances up to a certain stage and then reduces as well as indicating an optimum limit with increase in MR and MC. The minimum dielectric constant is obtained by a combination of SiO_2–Si_3N_4–BN is 4.26 at a monomer content 15 wt%, monomer ratio of 10:1 and solid loading of 48%.

4.6.4 Multi Response Optimization

Multi objective optimization was performed on gelcasting process followed by mathematical modeling and analysis. The performance measures used for optimization modeling are flexural strength, porosity and dielectric constant with desirability approach implemented. The constraint for the optimization of the gelcasting process is shown in Table 4.5.

Table 4.5. Constraints and rules applied on process variables and responses

Constraints Name	Goal	Lower Limit	Upper Limit	Lower Weight	Upper Weight	Importance
Solid loading	is in range	48	52	1	1	3
Monomer content	is in range	5	15	1	1	3
Flexural Strength	maximize	46.7	98.27	1	1	3
Porosity	maximize	26.37	40.01	1	1	3
Dielectric constant	minimize	4.26	6.47	1	1	3

Alongside measurable approval and check of numerical models with regard to a solitary reaction, scientific models as far as multi objective optimization is concerned have additionally been affirmed by confirmation tests. Optimum settings of process variables were found by conducting optimization, maximizing flexural strength and porosity and minimizing dielectric constant. The optimal solutions are shown in Table 4.6. The optimum process parameters were found to be 48.63 vol% of solid loading, 10:1 of monomer ratio and 15 wt% of monomer content to meet the requirements of optimal responses. It is apparent from Table 4.7 that the actual (experimental) and predicted output values are match with each other,

which legitimizing ampleness of RSM based optimization and forecast of flexural strength, porosity and dielectric constant. The percentages of residuals for these responses are 2.889%, 6.875% and 5.196% individually. The ramp graphs for the optimization shown in Figure 4.35. The overall desirability value of the optimal factors obtained was 0.8568 and represented in Figure 4.36.

Table 4.6. Optimal solutions

S. No.	Solid loading	Monomer content	Flexural Strength	Porosity	Dielectric constant	Desirability	
1	48.63	15	71.8342	38.7984	4.44824	0.85688	Selected
2	48.68	15	72.2436	38.7046	4.46606	0.8568	
3	49.63	5.51	61.294	34.6228	5.29258	0.52082	

Table 4.7. Results of confirmation test

Dependent variables	Optimum input parameters			Predicted values	Actual values	Error (%)
	Solid loading (%)	Monomer ratio	Monomer content (wt%)			
	48.63	10:1	15			
Flexural strength (MPa)				71.834	69.817	-2.889
Porosity (%)				38.704	36.214	-6.875
Dielectric constant				4.4482	4.692	5.196

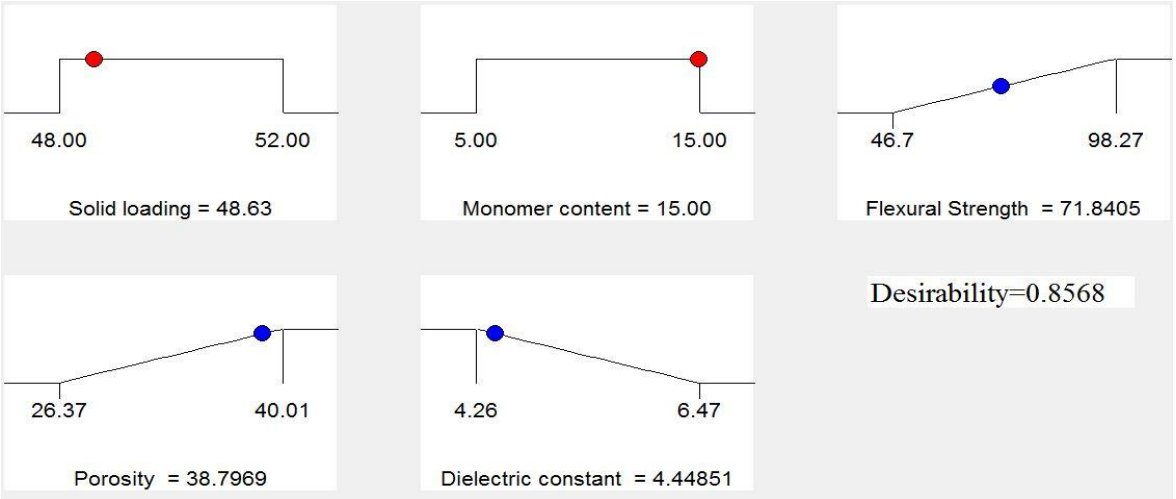

Figure 4.35. Ramp graphs for optimization

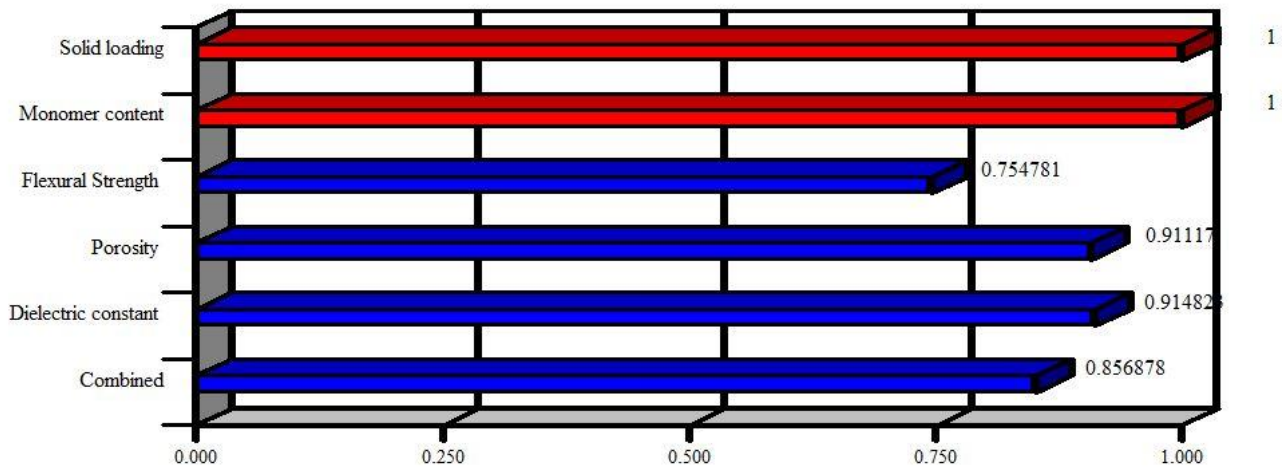

Figure 4.36. Bar chart of the optimization

Figure 4.37 shows EDAX image optimum process conditions. It contains Si, N, B and O representing major constituents of the ceramic composite. Figure 4.38 shows the SEM image of hybrid ceramic composite after applying the optimum conditions obtained from the desirability optimization through RSM. It is clear from the image that the ceramic obtained is denser and the particles are uniformly distributed.

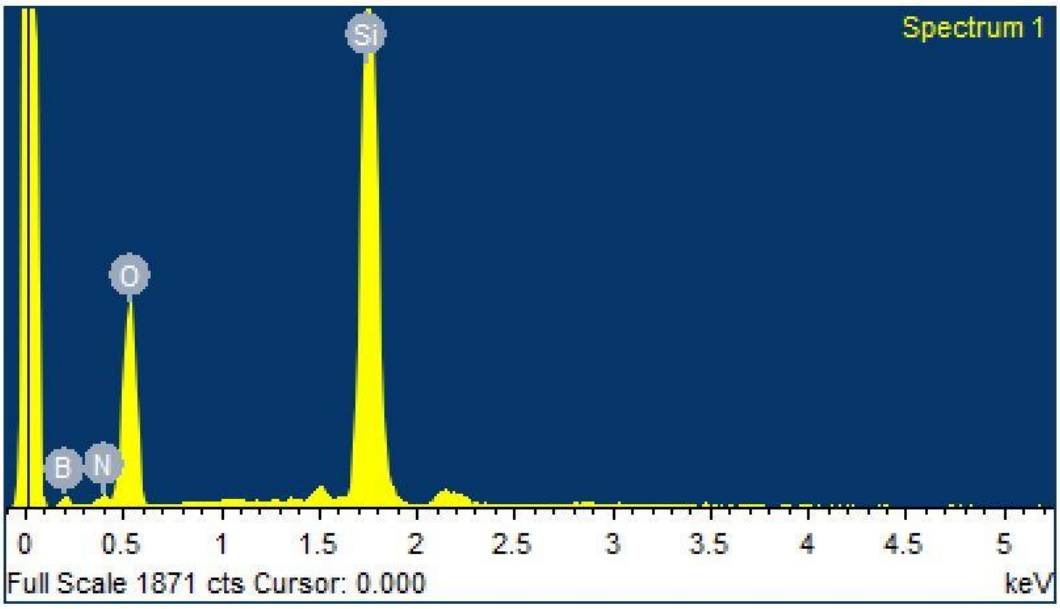

Figure 4.37. EDAX at optimum process conditions

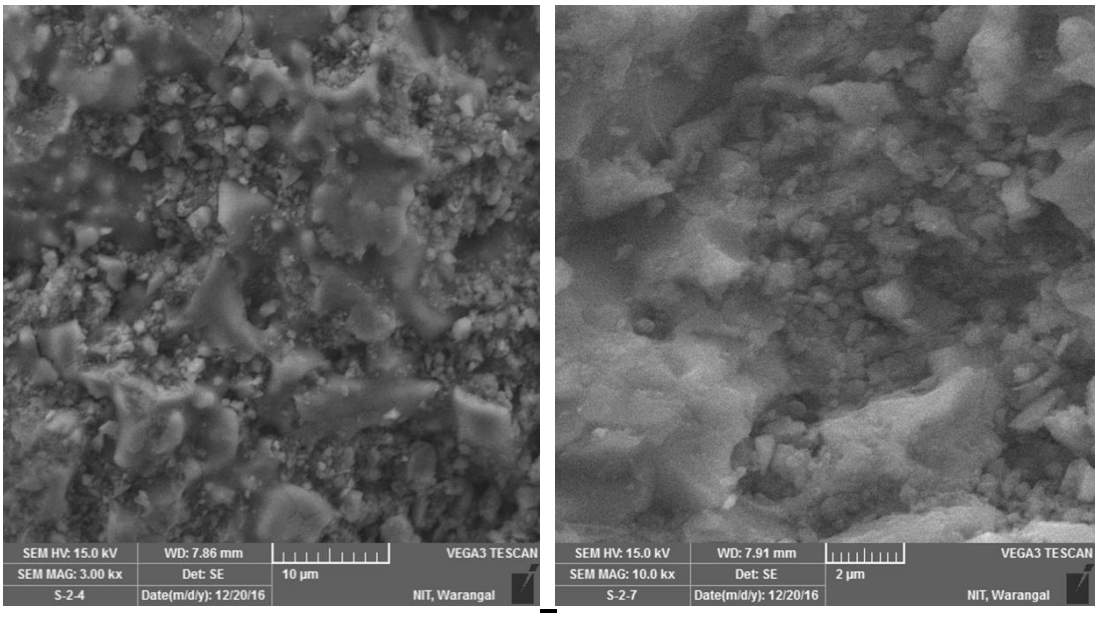

Figure 4.38. SEM images at optimum process conditions

4.7. Process modeling and optimization of SiO_2–Si_3N_4–Al_2O_3 ceramic Composite

The experimental design and test data is shown in Table 4.8.

Table 4.8. Experimental design and test data

Run	Solid loading (vol %): A	Ratio of monomers: B	Monomer content (wt %): C	Flexural Strength (MPa)	Porosity (%)	Dielectric Constant (30 MHz)
1	50	10	15	75.38	34.95	5.782
2	52	15	5	87.2	35.5	4.788
3	52	5	15	85.2	34.124	5.15
4	50	15	10	74.12	35.92	5.366
5	48	15	5	48.12	37.544	4.47
6	52	10	10	95.12	28.5	6.982
7	50	10	10	80.63	31.72	6.57
8	50	5	10	73.15	32.08	5.957
9	50	10	5	77.13	33.4	6.01
10	50	10	10	80.92	32.01	6.45
11	50	10	10	80.63	31.72	6.57
12	48	5	15	60.81	36.5	4.64

13	48	5	5	50.9	35.12	5.2
14	52	15	15	80.13	36.5	4.792
15	48	15	15	63.41	38.1	4.02
16	48	10	10	67.23	34.544	6.485
17	50	10	10	81.03	31.93	6.32
18	50	10	10	80.75	30.02	6.86
19	50	10	10	79.36	31.09	6.06
20	52	5	5	76.22	33.433	6.02

4.7.1. Modeling of flexural strength

ANOVA for response surface model of flexural strength is shown in Table 4.9.

Table 4.9. ANOVA for response surface model of flexural strength

Source	Sum of Squares	Df	Mean Square	F Value	p-value Prob > F	
Model	2582.45602	11	234.76873	1462.41642	< 0.0001	Significant
A-Solid loading	1779.556	1	1779.556	11085.17273	< 0.0001	significant
B-Monomer ratio	4.489	1	4.489	27.9627842	0.0007	significant
C-Monomer content	1.53125	1	1.53125	9.538430229	0.0149	significant
AB	4.6360125	1	4.6360125	28.87855136	0.0007	significant
AC	67.8030125	1	67.803013	422.3570965	< 0.0001	significant
BC	14.2311125	1	14.231113	88.64814607	< 0.0001	significant
A^2	0.17438409	1	0.1743841	1.086269704	0.3278	
B^2	146.073384	1	146.07338	909.9172457	< 0.0001	significant
C^2	59.9277841	1	59.927784	373.3008897	< 0.0001	significant
ABC	57.4056125	1	57.405613	357.5898316	< 0.0001	significant
B^2C	29.0873025	1	29.087303	181.1900117	< 0.0001	significant
Residual	1.28427841	8	0.1605348			
Lack of Fit	1.28427841	3	0.4280928			
Pure Error	0	5	0			
Cor Total	2583.7403	19				

R-Squared: 0.999, Adj R-Squared=0.998, Pred R-Squared=0.97, Adequate Precision: 149.417, C.V.: 0.535

From ANOVA it is observed that A, B, C, AB, BC, AC and $B^{2,}$ $C^{2}$and ABC are significant model terms. The regression model developed for flexural strength is given in Eq. 4.4.

$$Flexural\ strength\ (MPa) = 80.75 + 13.34 \times A + 0.067 \times B - 0.875 \times C + 0.761 \times A \times B - 2.91 \times A \times C - 1.33 \times B \times C + 0.252 \times A^2 - 7.29 \times B^2 - 4.67 \times C^2 - 2.68 \times A \times B \times C + 4.26 \times B^2 \times C \quad (4.4)$$

It is essential to know that the obtained model is giving an adequate approximation to the actual system. Model acceptability can be ensured by drawing diagnostic figures like predicted versus experimental. Figure 4.39 represents the difference between experimentally measured values and predicted values for flexural strength. The measured values were found relatively close to the straight line. The graphs backed by Adj. R^2 values for three responses were 0.998 which is near to 1 indicating a better compliance between observed and predicted values.

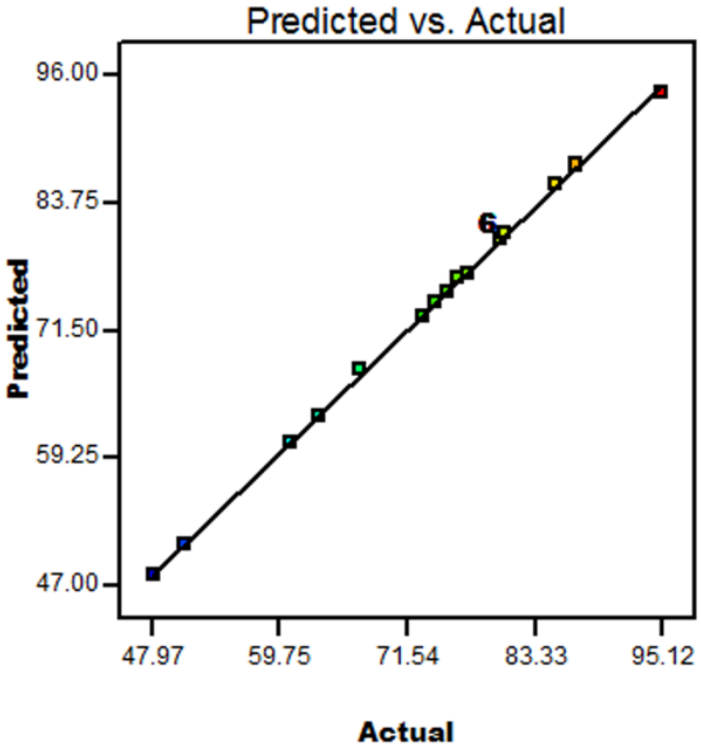

Figure 4.39. Predicted versus actual for flexural strength

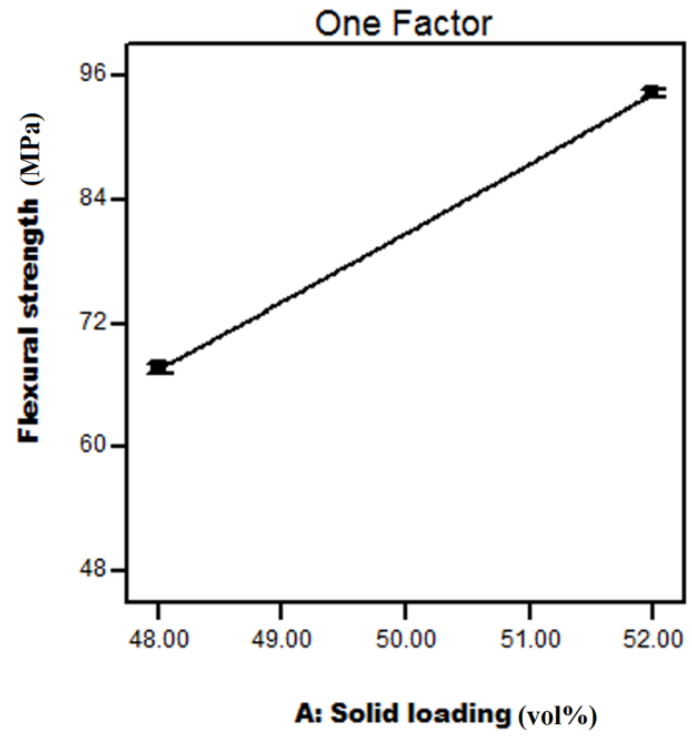

Figure 4.40. Effect of solid loading on flexural strength

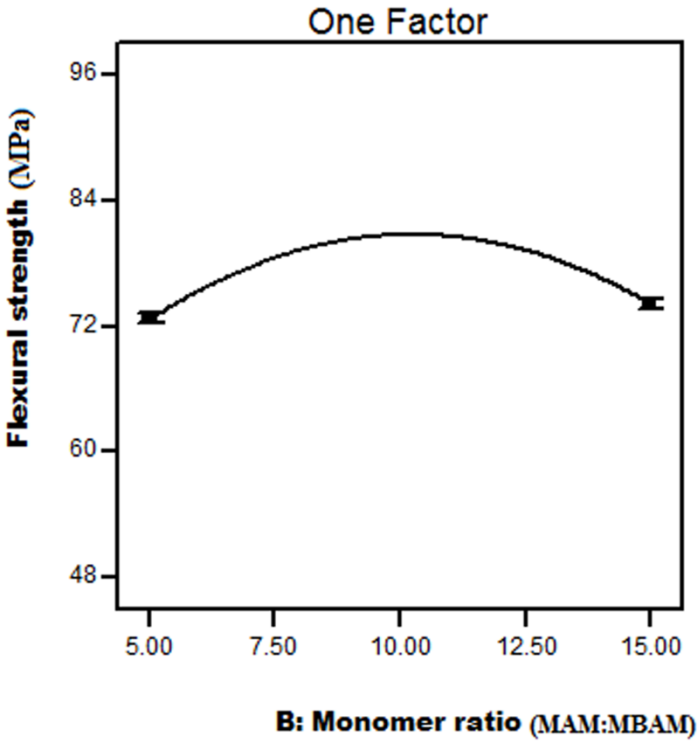

Figure 4.41. Effect of monomer ratio on flexural strength

Figure 4.40, 4.41 and 4.42 shows the single factor effect and Figure 4.43, 4.44 and 4.45 shows the interaction effect on flexural strength. It is observed that with increase in SL, there is enhancement in the density of fused silica ceramic composites which is favorable for the increase of flexural strength. However, the maximum flexural strength is obtained at 52%. The organic binder burnout plays a vital role in pore formations which affects the flexural strength of the sintered ceramics. If the MR is low, the flexural strength of dried samples remains low as the 3-dimensional network is too coarse which results in non-uniform distribution of SiO_2 particles, leading to decrease in flexural strength. Maximum flexural strength is obtained at 52 vol% SL, 10:1 MR and 10 wt% MC.

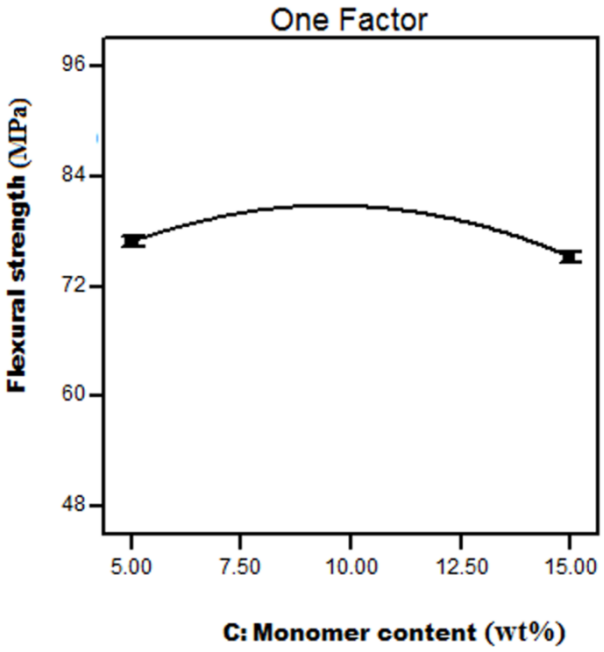

Figure 4.42. Effect of monomer content on flexural strength

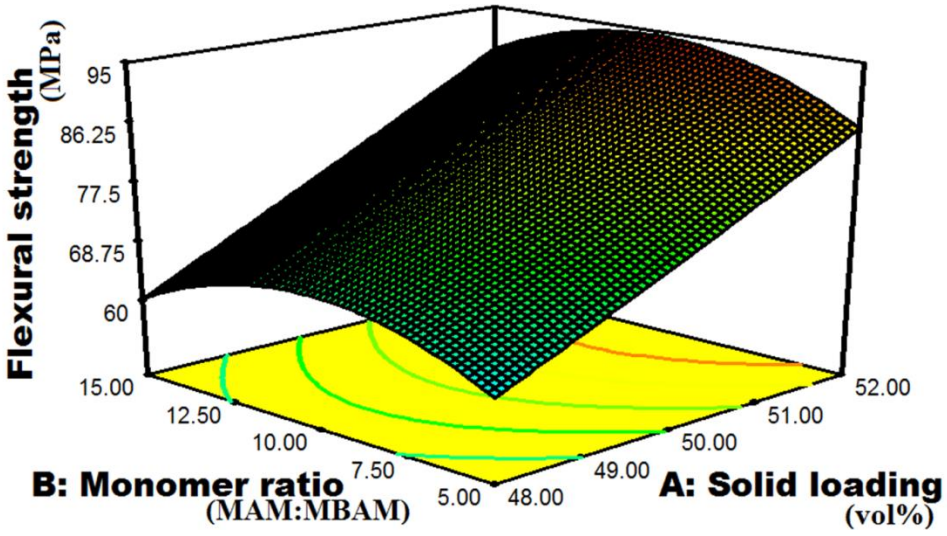

Figure 4.43. Effect of monomer ratio and solid loading on flexural strength

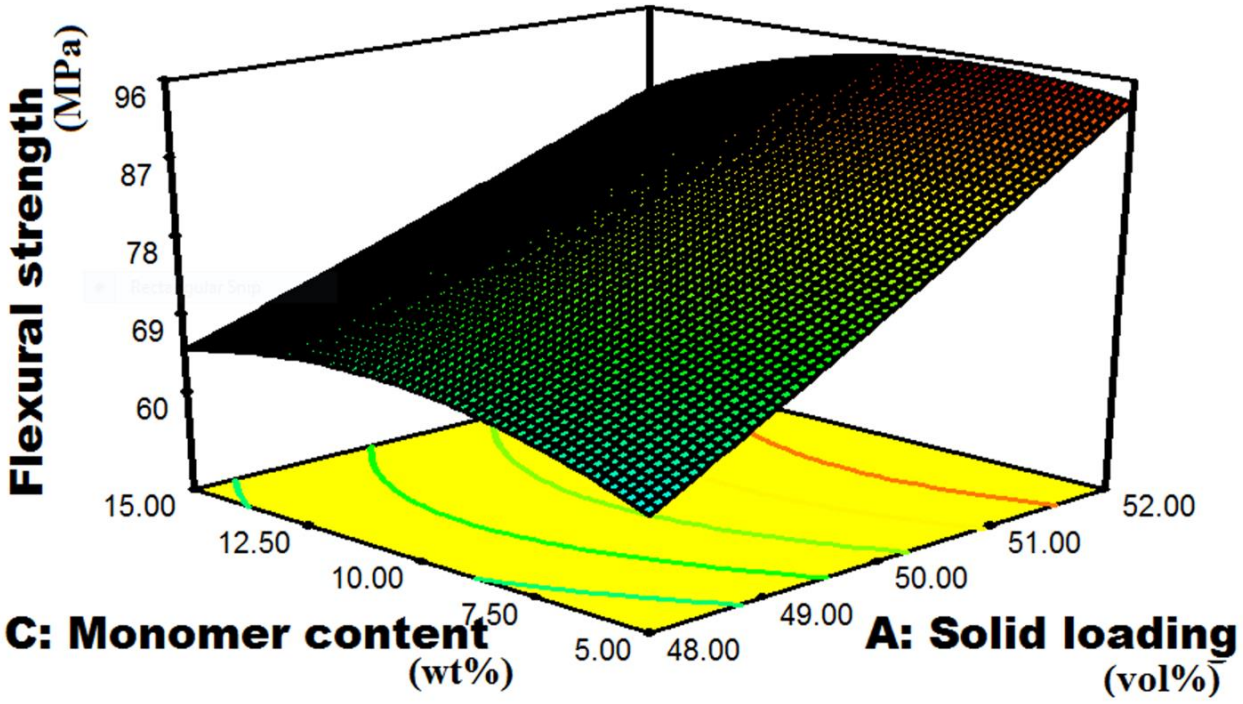

Figure 4.44. Effect of monomer content and solid loading on flexural strength

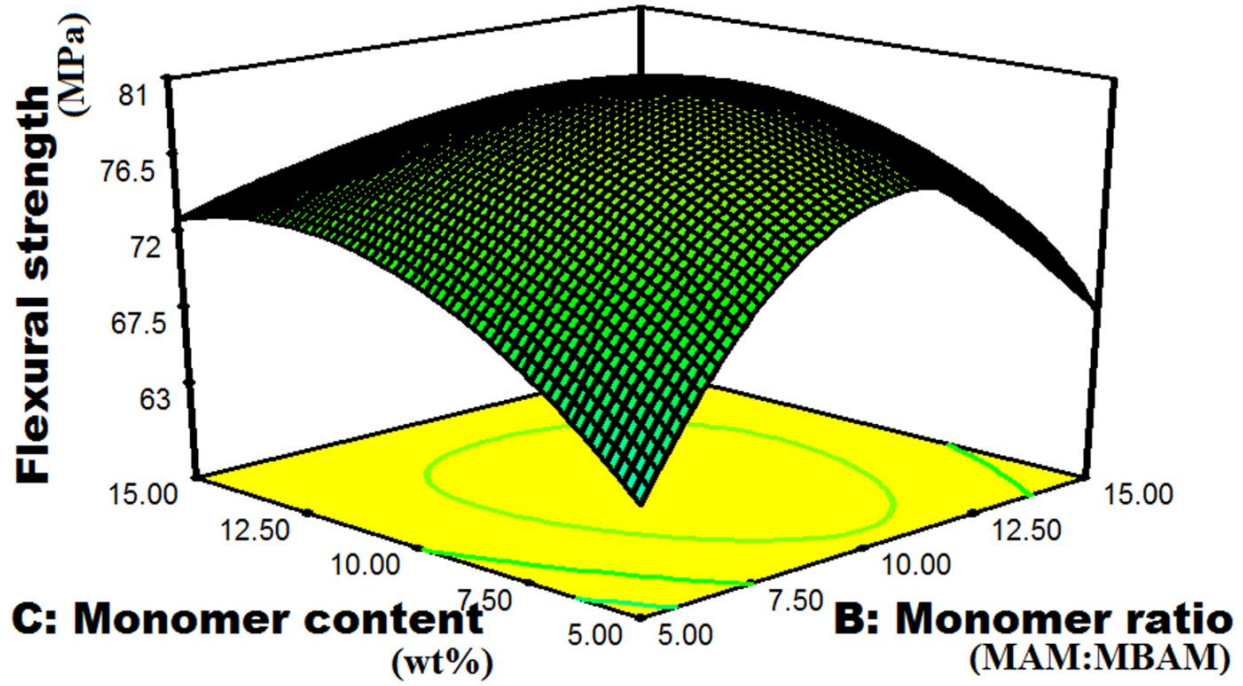

Figure 4.45. Effect of monomer content and monomer ratio on flexural strength

4.7.2. Modeling of porosity

ANOVA for response surface model of porosity is shown in Table 4.10.

Table 4.10. ANOVA for response surface model of porosity

Source	Sum of Squares	Df	Mean Square	F Value	p-value Prob > F	
Model	115.25071	12	9.604225902	290.0140245	< 0.0001	Significant
A-Solid loading	18.264968	1	18.264968	551.5381386	< 0.0001	Significant
B-Monomer ratio	7.3728	1	7.3728	222.6327683	< 0.0001	significant
C-Monomer content	1.20125	1	1.20125	36.27354776	0.0005	significant
AB	0.0219451	1	0.021945125	0.662666006	0.4424	
AC	0.0075031	1	0.007503125	0.226568127	0.6486	
BC	0.327405	1	0.327405006	9.886485835	0.0163	significant
A^2	0.0331531	1	0.033153125	1.001108398	0.3504	
B^2	12.511112	1	12.51111151	377.7918008	< 0.0001	significant
C^2	14.648299	1	14.64829901	442.3273869	< 0.0001	significant
AC^2	6.780699	1	6.780699025	204.7533901	< 0.0001	significant
B^2C	0.1655082	1	0.165508225	4.99776941	0.0605	
BC^2	1.1878362	1	1.187836225	35.86849868	0.0005	significant
Residual	0.2318149	7	0.033116419			
Lack of Fit	0.2318149	2	0.115907466			
Pure Error	0	5	0			
Cor Total	115.48253	19				

R-Squared: 0.997, Adj R-Squared=0.994, Pred R-Squared=0.8838, Adequate Precision: 67.149, C.V.: 0.5349

From ANOVA it is observed that A, B, C, BC, A^2, B^2, and C^2 are significant model terms. The regression model developed for porosity is given in Eq. 4.5.

$$Porosity\ (\%) = 31.78 - 3.02 \times A + 1.92 \times B + 0.775 \times C + 0.05 \times A \times B - 0.031 \times A \times C - 0.06 \times B \times C - 0.35 \times A^2 + 2.13 \times B^2 2.31 \times C^2 + 2.06 \times A \times C^2 - 0.32 \times B^2 \times C - 0.86 \times B \times C^2 \quad (4.5)$$

It is essential to know that the model obtained gives an adequate approximation to the actual system. Model acceptability can be ensured by drawing diagnostic figures like predicted versus experimental. Figure 4.46 represents the difference between experimentally

measured values and predicted values for porosity. The measured values were found relatively close to the straight line. The graphs backed by Adj. R^2 values for three responses were 0.994 which is near 1 indicating a better compliance between observed and predicted values.

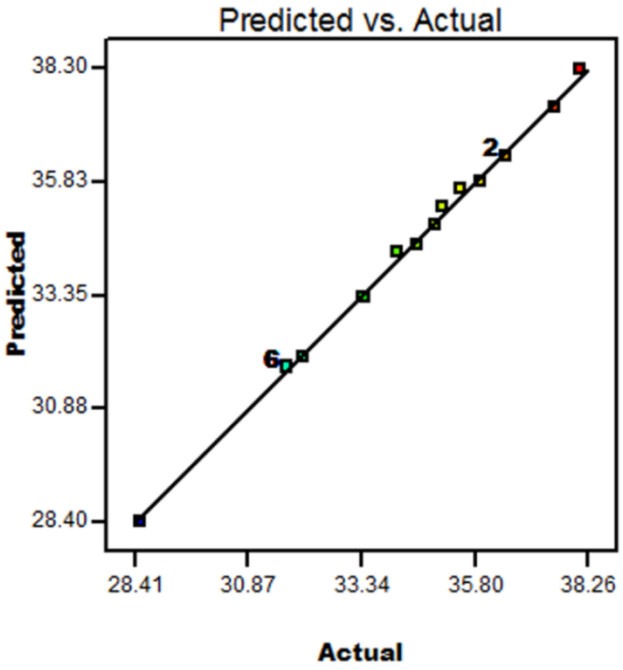

Figure 4.46. Predicted versus actual for porosity

Figures 4.47, 4.48 and 4.49 show single factor effect and figures 4.50, 4.51 and 4.52 show interaction effect on porosity.

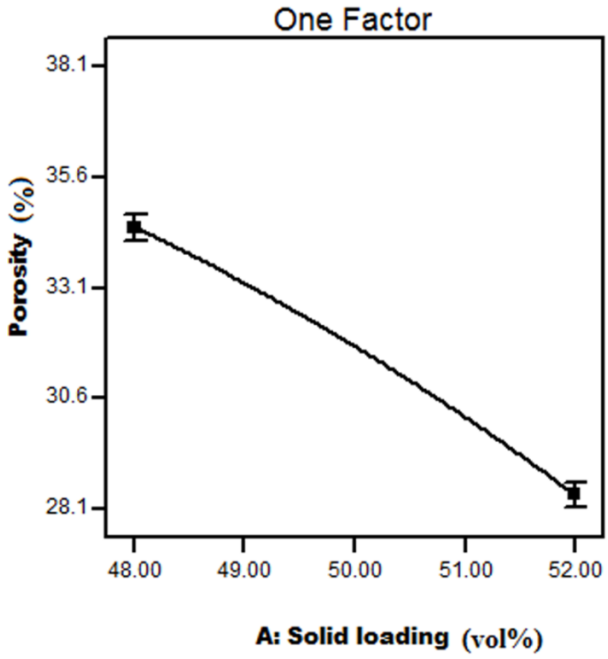

Figure 4.47. Effect of solid loading on porosity

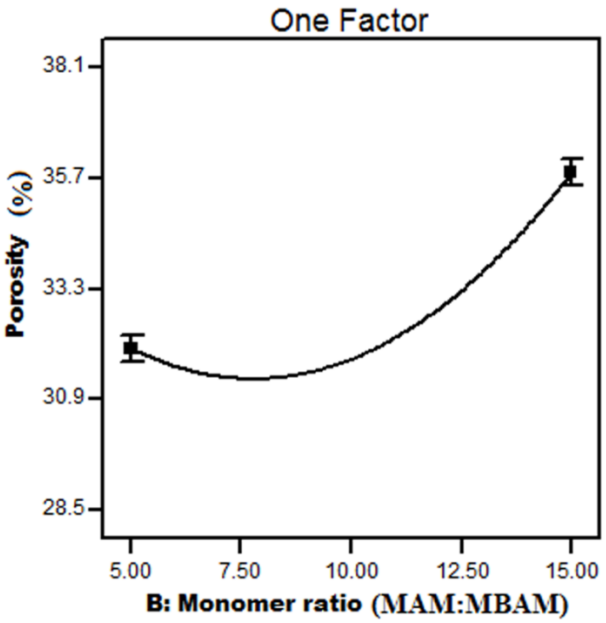

Figure 4.48. Effect of monomer ratio on porosity

Porosity of ceramic composites mainly depends on solid loading, monomer ratio and monomer content. Solid loading has negative impact on the porosity whereas monomer ratio and monomer content have an optimal point. The maximum porosity is obtained at 48% solid loading. Porosity decreases with increase of SL. SL has more influence on density improvement in ceramic composites. The distance between the particles and shrinkage is low as the solid loading increases.

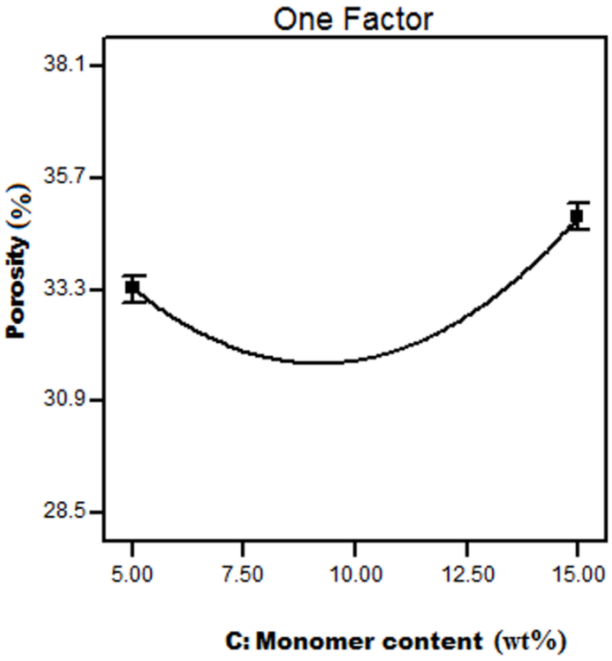

Figure 4.49. Effect of monomer content on porosity

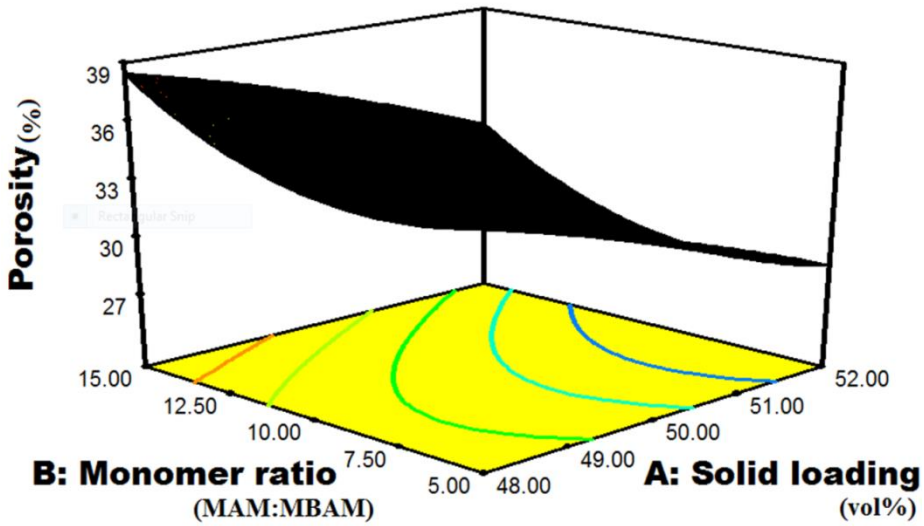

Figure 4.50. Effect of monomer ratio and solid loading on porosity

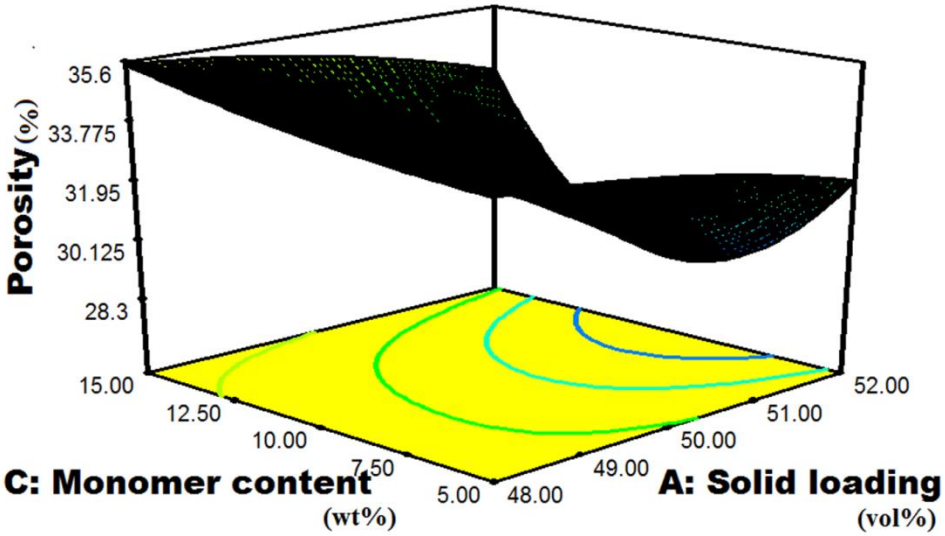

Figure 4.51. Effect of monomer content and solid loading on porosity

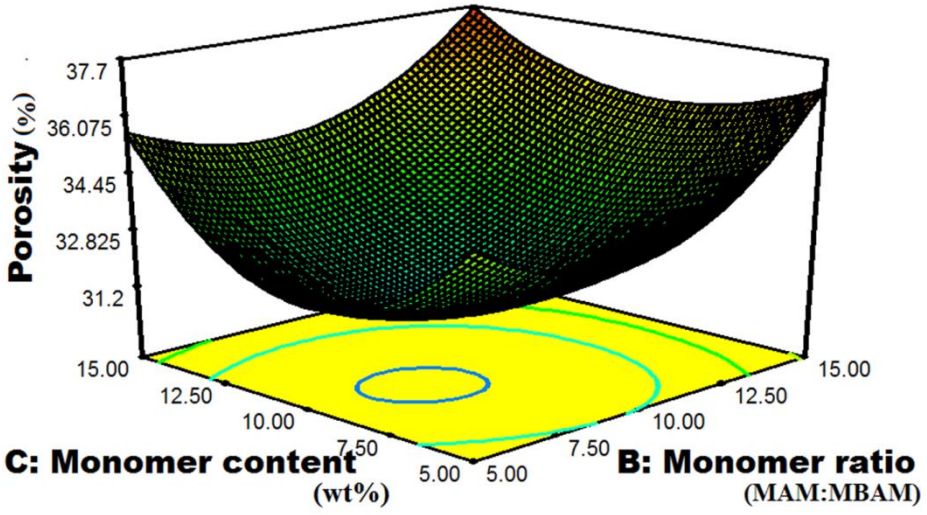

Figure 4.52. Effect of monomer content and monomer ratio on porosity

4.7.3. Modeling of Dielectric constant

ANOVA for response surface model of dielectric constant is shown in Table 4.11.

Table 4.11. ANOVA for response surface model of dielectric constant

Source	Sum of Squares	Df	Mean Square	F Value	p-value Prob > F	
Model	14.72598	10	1.4726	197.6118887	< 0.0001	significant
A-Solid loading	0.850889	1	0.85089	114.1830555	< 0.0001	significant
B-Monomer ratio	1.246796	1	1.2468	167.3109007	< 0.0001	significant
C-Monomer content	0.442682	1	0.44268	59.40462696	< 0.0001	significant
AB	0.0072	1	0.0072	0.966187242	0.3513	
AC	0.002592	1	0.00259	0.347827407	0.5699	
BC	0.121032	1	0.12103	16.24160754	0.0030	significant
A^2	0.012261	1	0.01226	1.645355419	0.2316	
B^2	2.778825	1	2.77883	372.8979722	< 0.0001	significant
C^2	1.633556	1	1.63356	219.2113063	< 0.0001	significant
ABC	0.072962	1	0.07296	9.79096577	0.0121	significant
Residual	0.067068	9	0.00745			
Lack of Fit	0.067068	4	0.01677			
Pure Error	0	5	0			
Cor Total	14.79305	19				

R-Squared: 0.995, Adj R-Squared=0.99, Pred R-Squared=0.8962, Adequate Precision: 45.038, C.V.: 1.50.

From ANOVA it is observed that A, B, C, BC, B^2, A^2 and ABC are significant model terms. The regression model developed for dielectric constant is given in Eq. 4.6.

$$Dielectric\ constant = 6.61 + 0.29 \times A - 0.35 \times B - 0.21 \times C - 0.03 \times A \times B + 0.018 \times A \times C + 0.123 \times B \times C + 0.067 \times A^2 - 1.001 \times B^2 - 0.771 \times C^2 + 0.095 \times A \times B \times C \quad (4.6)$$

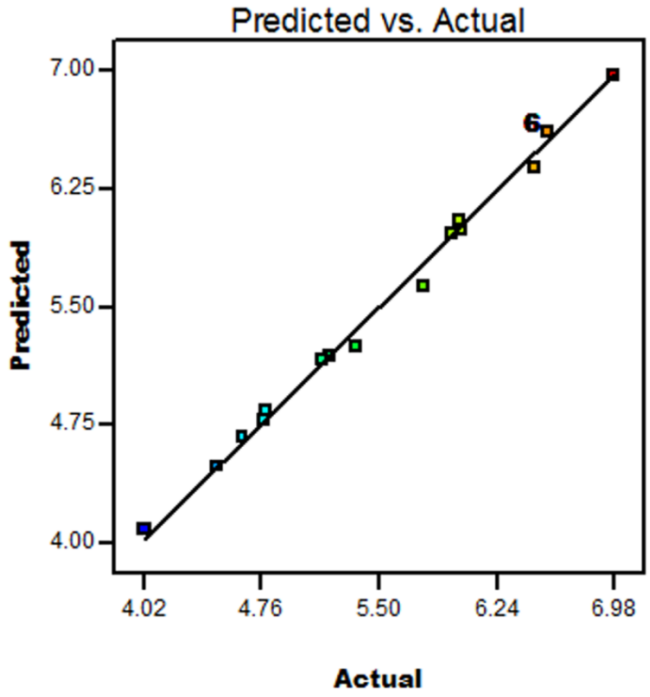

Figure 4.53. Predicted versus actual for dielectric constant

It is essential to know that the model obtained gives an adequate approximation to the actual system. Model acceptability can be ensured by drawing diagnostic figures like predicted versus experimental. Figure 4.53 represents the difference between experimentally measured values and predicted values for dielectric constant. The measured values were found relatively close to the straight line. The graphs backed by Adj. R^2 values for three responses were 0.99 which is near 1 indicating fine compliance between observed and predicted values.

Figures 4.54, 4.55 and 4.56 show the single factor effect and Figures 4.57, 4.58 and 4.59 show the interaction effect on dielectric constant. The dielectric constant of materials depends mainly on porosity. From the data, it is observed that the dielectric constant reduces with increase of porosity. SL has a positive impact on dielectric constant. The dielectric constant enhances up to a certain state and then reduces indicating an optimum limit with increase in MR and MC. The minimum dielectric constant is obtained by a combination of SiO_2–Si_3N_4–Al_2O_3 is 4.02 at 48 vol% solid loading, 15:1 monomer ratio and 15 wt% monomer content.

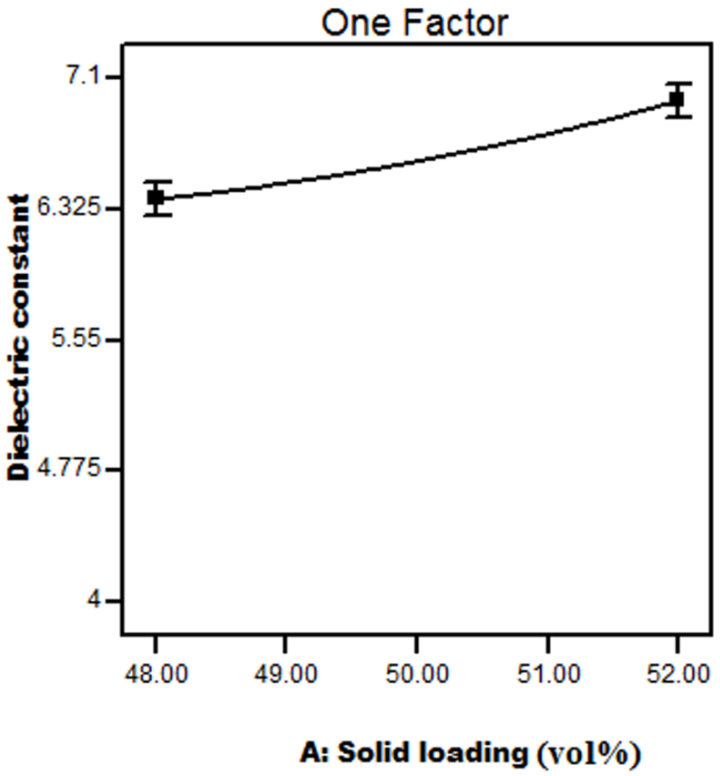

Figure 4.54. Effect of solid loading on dielectric constant

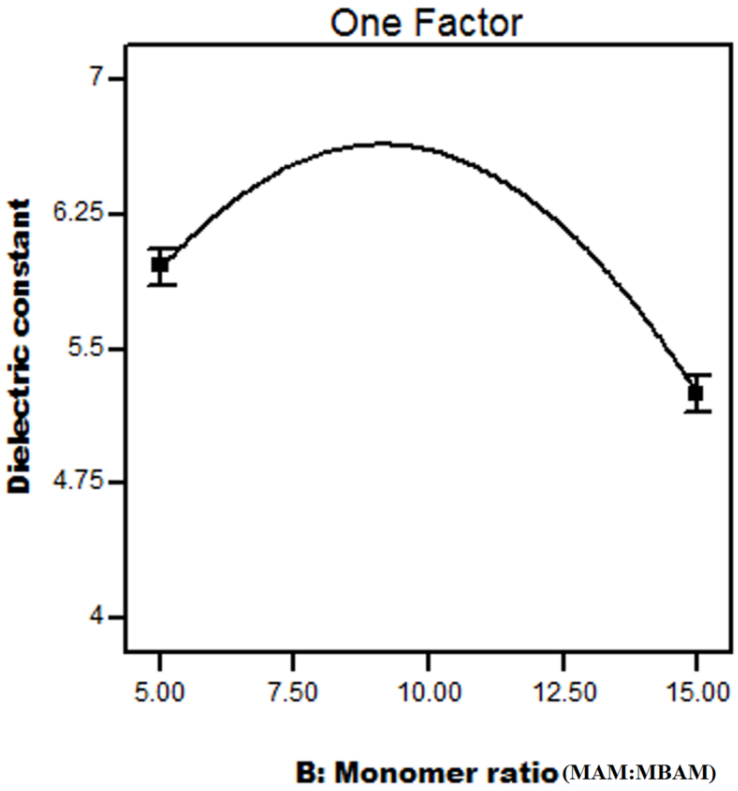

Figure 4.55. Effect of monomer ratio on dielectric constant

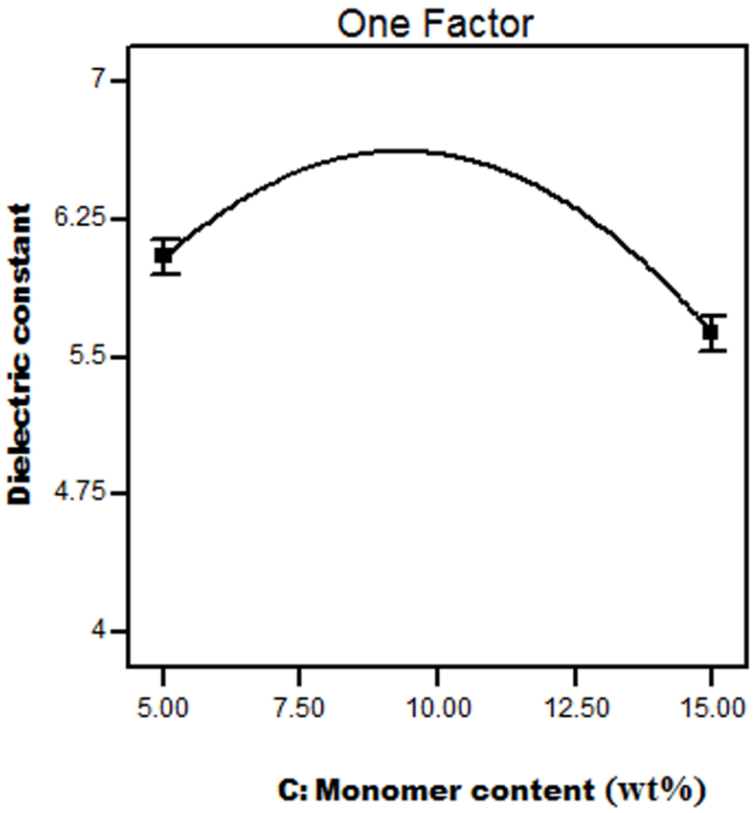

Figure 4.56. Effect of monomer content on dielectric constant

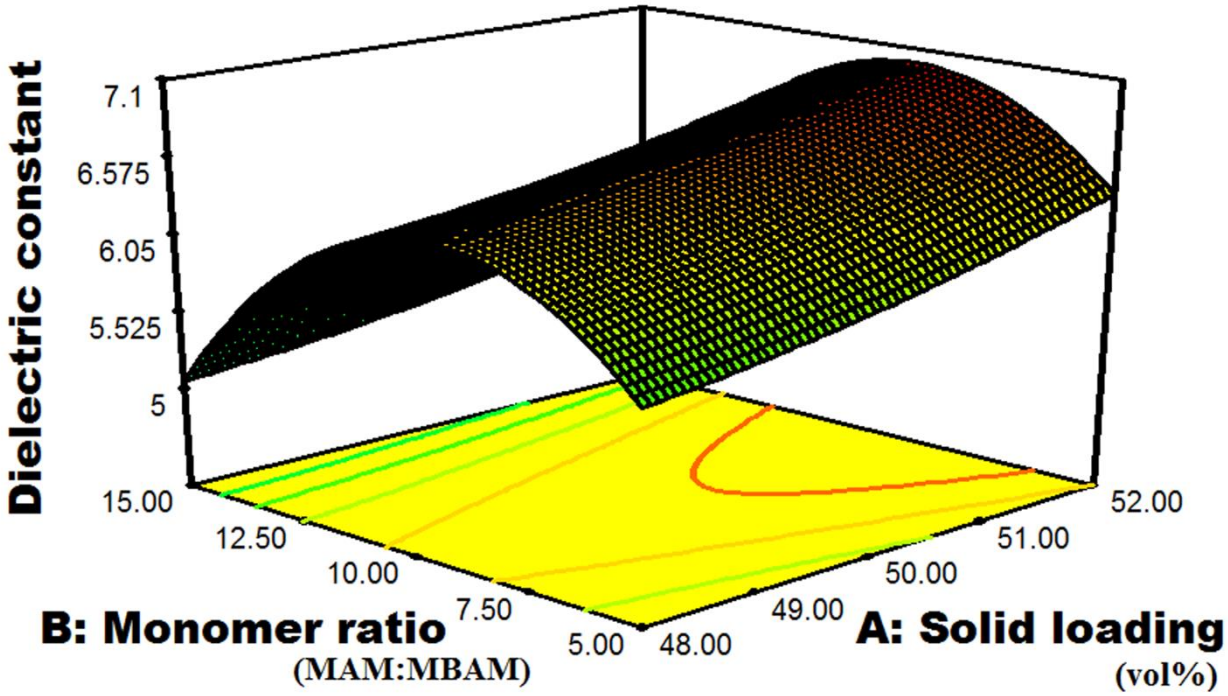

Figure 4.57. Effect of monomer ratio and solid loading on dielectric constant

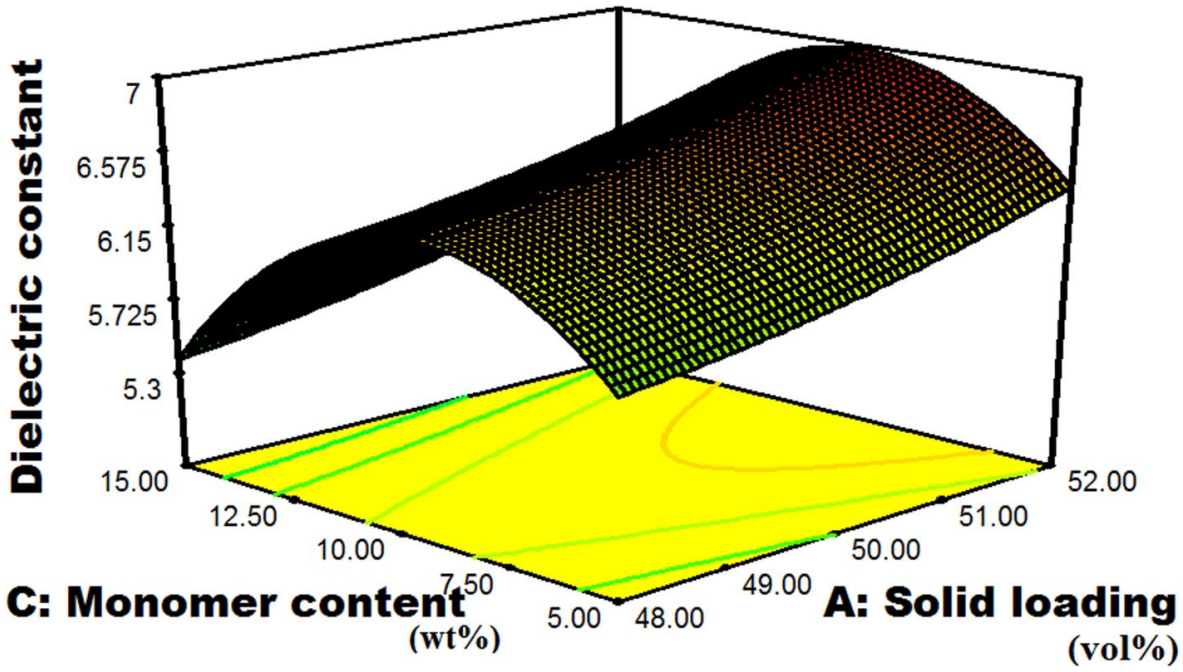

Figure 4.58. Effect of monomer content and solid loading on dielectric constant

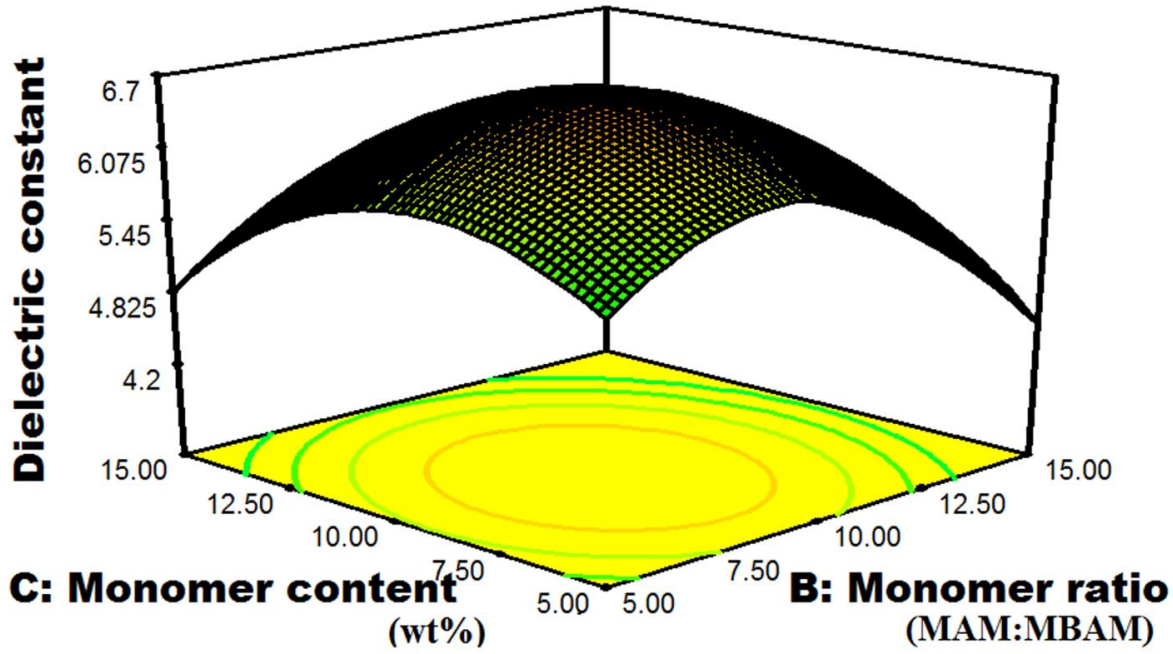

Figure 4.59. Effect of monomer content and monomer ratio on dielectric constant

4.7.4 Multi Response Optimization

Multi objective optimization has been conducted on gelcasting process followed by mathematical modeling and analysis. The performance measures used for optimization modeling are flexural strength, porosity and dielectric constant with desirability approach

implemented. The constraint for the optimization of the gelcasting process is shown in Table 4.12.

Table 4.12. Constraints and rules applied on process variables and responses

Name	Goal	Lower limit	Upper limit	Lower weight	Upper weight	Importance
A: Solid loading (vol %)	in range	48	52	1	1	3
B: Monomer ratio	in range	5:1	15:1	1	1	3
C: Monomer content (wt%)	in range	5	15	1	1	3
Flexural strength (MPa)	Maximize	48.12	95.12	1	1	3
Porosity (%)	Maximize	28.5	38.1	1	1	3
Dielectric constant	Minimize	4.02	6.982	1	1	3

Alongside measurable approval and check of numerical models regarding a solitary reaction, the scientific models as far as multi objective optimization is concerned have additionally been affirmed by confirmation tests. Optimum settings of process variables were found by conducting optimization, maximizing flexural strength and porosity and minimizing dielectric constant. The optimal solutions are shown in Table 4.13.

Table 4.13. Optimal solutions

Solid loading (%)	Monomer ratio (MAM:MBAM)	Monomer content (wt%)	Flexural strength (MPa)	Porosity (%)	Dielectric constant	Desirability	
52	15	5	87.338	35.664	4.781	0.7733	Selected
51.86	15	5.06	85.969	35.694	4.781	0.7653	
50.86	15	15	75.233	37.196	4.566	0.7525	
50.82	15	15	75.052	37.222	4.557	0.7525	
50.78	15	15	74.871	37.247	4.548	0.7524	
49.62	15	15	69.916	37.832	4.323	0.7396	
49.6	15	15	69.838	37.840	4.320	0.7392	
49.24	15	15	68.323	37.974	4.259	0.7305	
50.89	15	5	76.196	36.430	4.645	0.73010	
51.22	14.59	5	81.025	35.739	4.886	0.7201	

The optimum process parameters were found to be 52 vol% of solid loading, 15:1 of monomer ratio and 5 wt% of monomer content to meet the requirements of optimal responses. It is evident from Table 4.14 that the actual (experimental) and predicted output values are firmly aligned with each other, which legitimizes RSM based optimization and forecast of flexural strength, porosity and dielectric constant. The percentages of residuals for these responses are 6.523%, 3.362% and 0.104% individually. The ramp graphs for the optimization shown are in Figure 4.60. The overall desirability value of the optimal factors obtained was 0.7734 and represented in Figure 4.61.

Table 4.14. Results of confirmation test

Dependent variables	Optimum input parameters			Predicted values	Actual values	Error (%)
	Solid loading (%)	Monomer ratio	Monomer content (wt%)			
	52	15:1	5			
Flexural strength (MPa)				87.36	82.01	-6.523
Porosity (%)				35.66	34.5	-3.362
Dielectric constant				4.783	4.788	0.104

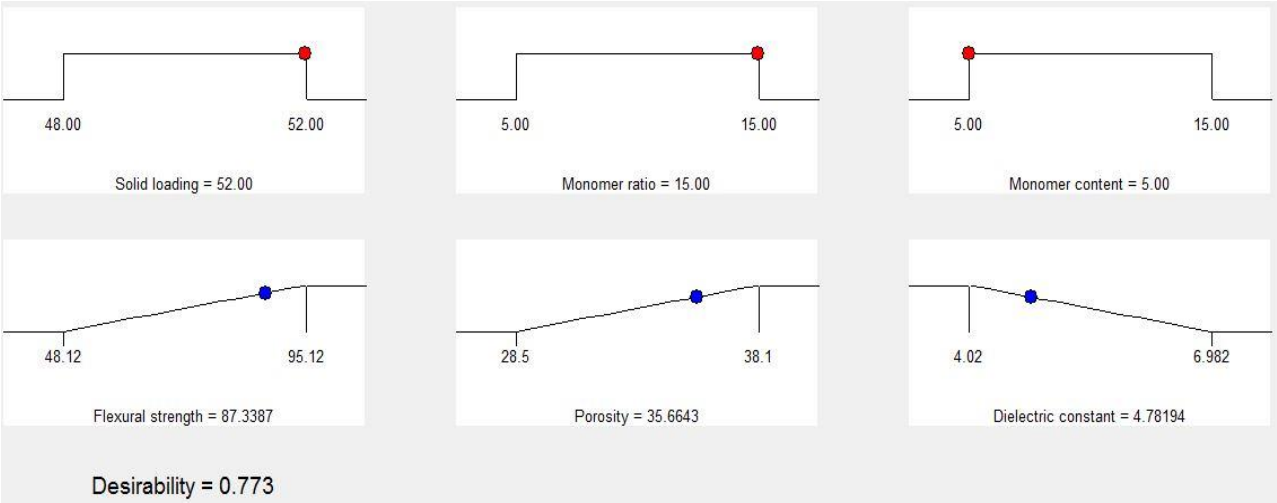

Figure 4.60. Ramp graphs for optimization

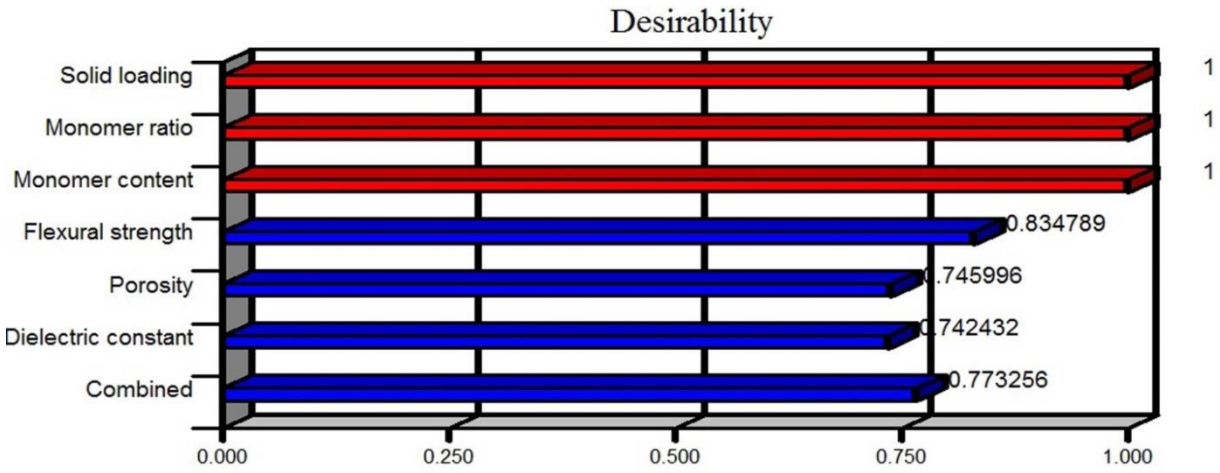

Figure 4.61. Bar chart of the optimization

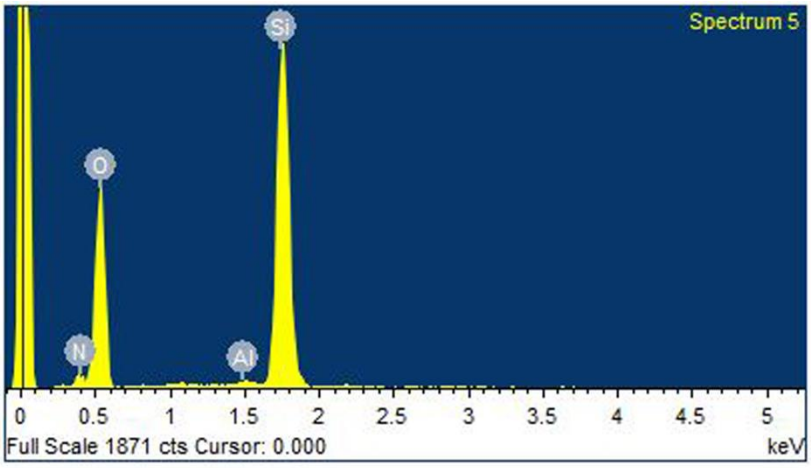

Figure 4.62. EDAX at optimum process conditions

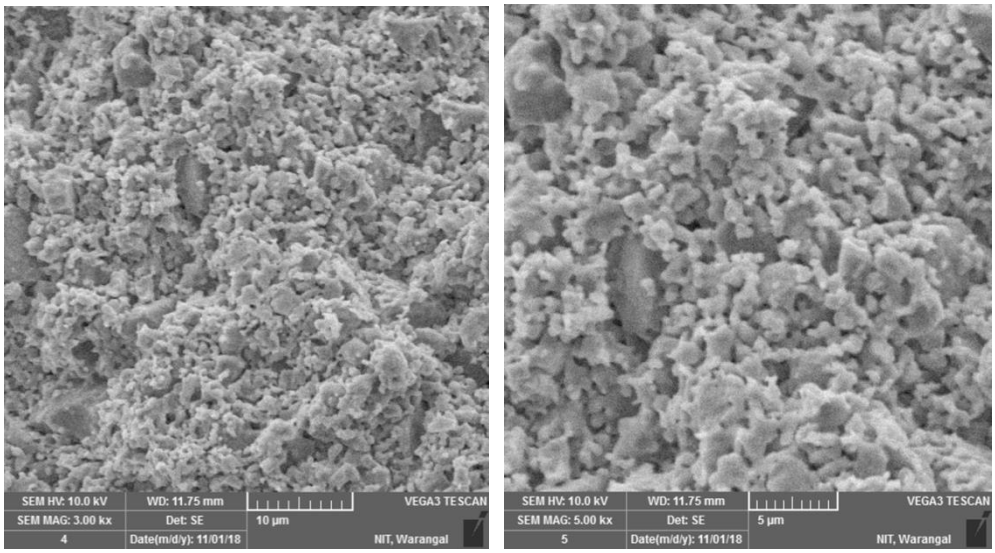

Figure 4.63. SEM images at optimum process conditions

Figure 4.62 shows EDAX image optimum process conditions. It contains Si, N, Al and O representing the major constituents of the ceramic composite. Figure 4.63 shows SEM image of the hybrid ceramic composite after applying optimum conditions obtained from the desirability optimization through RSM. It is clear from the image that the obtained ceramic is denser and the particles are uniformly distributed.

Summary

This chapter deals with the characterization of porous SiO_2–Si_3N_4–BN and SiO_2–Si_3N_4–Al_2O_3 ceramic composites by varying monomer content, the ratio of monomers and solid loading. The results of mechanical and dielectric constant of the sintered SiO_2–Si_3N_4–BN and SiO_2-Si_3N_4–Al_2O_3 ceramic composites were presented. Flexural strength enhances with solid loading because the density of sintered ceramic sample increases and the space between the particles decreases resulting in low shrinkage. Also flexural strength increases as the monomer content increases and reaches an optimal point and then decreases. The flexural strength of the sintered bodies is affected by the pores formed during organic binder burnout. If the monomer content is low, the flexural strength of green samples remains low as 3-dimesnsional network is very coarse resulting in non-uniform distribution of fused silica particles, which affects flexural strength. The monomer and cross linking agent can form macro molecular network to hold the ceramic particles together and furthermore it can assume an important role in the making of the pores during the fabrication of ceramic composites. The increased solid content could obviously decrease the porosity of the resultant porous material. Increase in the solid content decreases pore size. The increase of crosslinking agent makes the crosslink density of cross-linked polymer gels in green body increase, the distribution of ceramics particles very uniform, the drying shrinkage smaller, and thus increases the porosity of sintering body increases. This chapter also discussed the development of regression models for SiO_2–Si_3N_4–BN and SiO_2–Si_3N_4–Al_2O_3 ceramic composites and also the effects of process parameters on responses. The optimum process parameters were found to be 48.63 vol% of solid loading, 10:1 of monomer ratio and 15 wt% of monomer content to meet the requirements of optimal responses. Actual (experimental) and predicted output values are match with each other, which legitimizing ampleness of RSM based optimization and forecast of flexural strength, porosity and dielectric constant. The percentages of residuals for these responses are 2.889%, 6.875% and 5.196% individually for SiO_2–Si_3N_4–BN ceramics. The optimum process parameters were found to be 52 vol% of solid loading, 15:1 of monomer ratio and 5 wt% of monomer content to meet the requirements of optimal responses. Actual (experimental) and predicted output values are firmly aligned with each other, which legitimizes RSM based optimization and forecast of flexural strength, porosity and dielectric constant. The percentages of residuals for these responses are 6.523%, 3.362% and 0.104% individually for SiO_2–Si_3N_4–Al_2O_3 ceramics.

CHAPTER 5

SOLID PARTICLE EROSION

5.1. Introduction

This chapter deals with erosion studies of the pure silica, SiO_2–Si_3N_4–BN and SiO_2–Si_3N_4–Al_2O_3 ceramic composites. The variation of erosion rate with different impingement angles (30^o, 45^o, 60^o and 90^o) and impact velocities (86 m/sec, 101 m/sec and 148 m/sec) is studied. This chapter also deals with the surface roughness and morphology of eroded ceramic composites.

5.2. Erosion testing

The SEM micro graph of the used erodent is shown in Figure 5.1. It is observed that particles have angular shape with average particle size of 200 ± 20 μm.

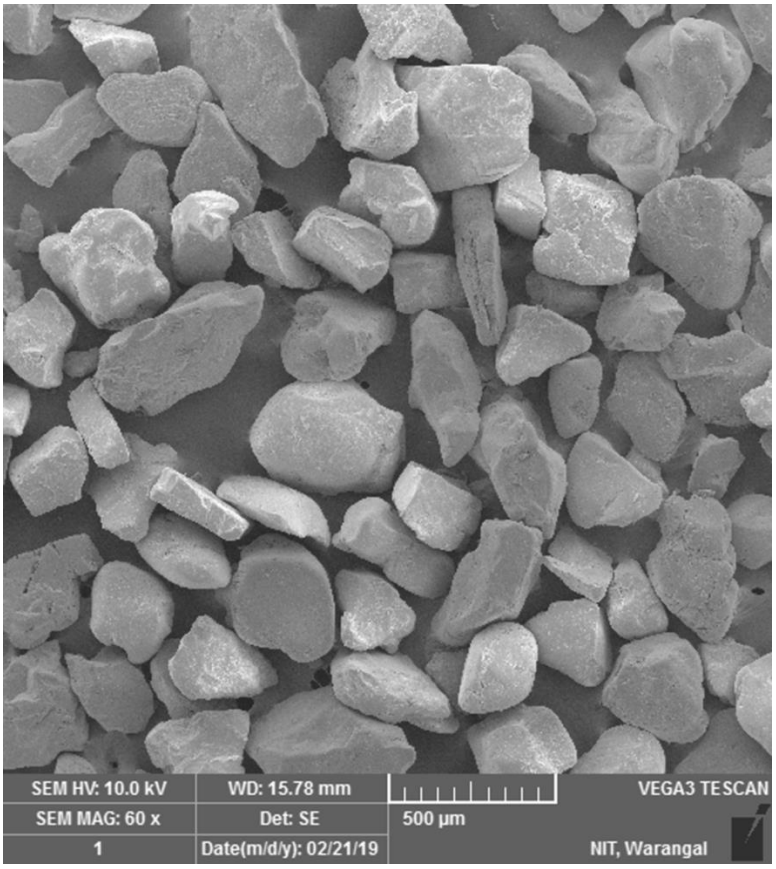

Figure 5.1. SEM micrograph of silica erodent particles

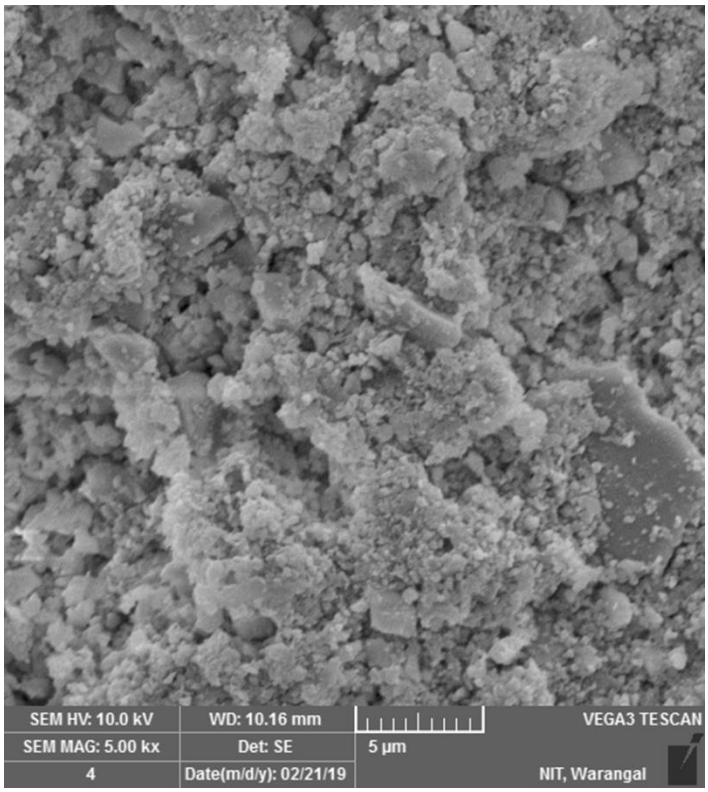

Figure 5.2. SEM image of pure fused silica

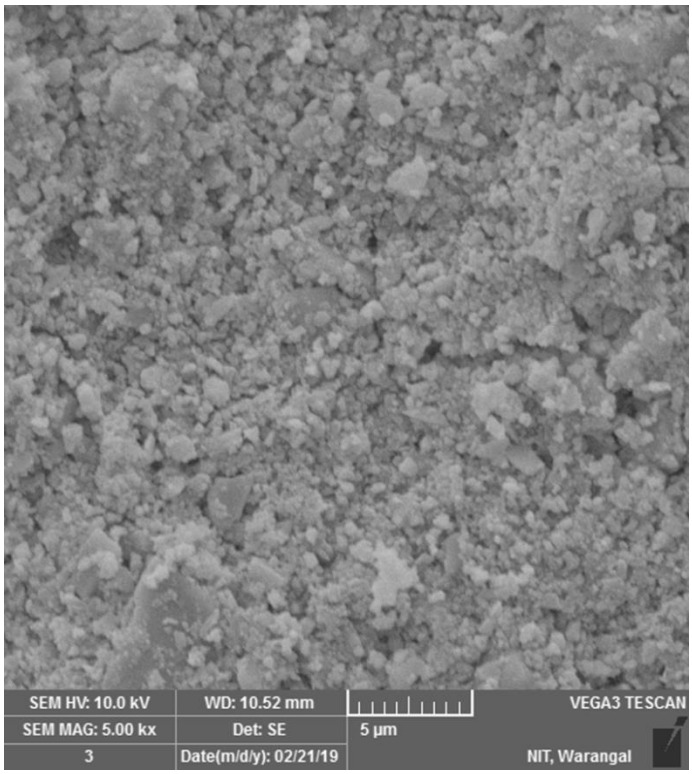

Figure 5.3. SEM image of SiO_2–Si_3N_4–BN

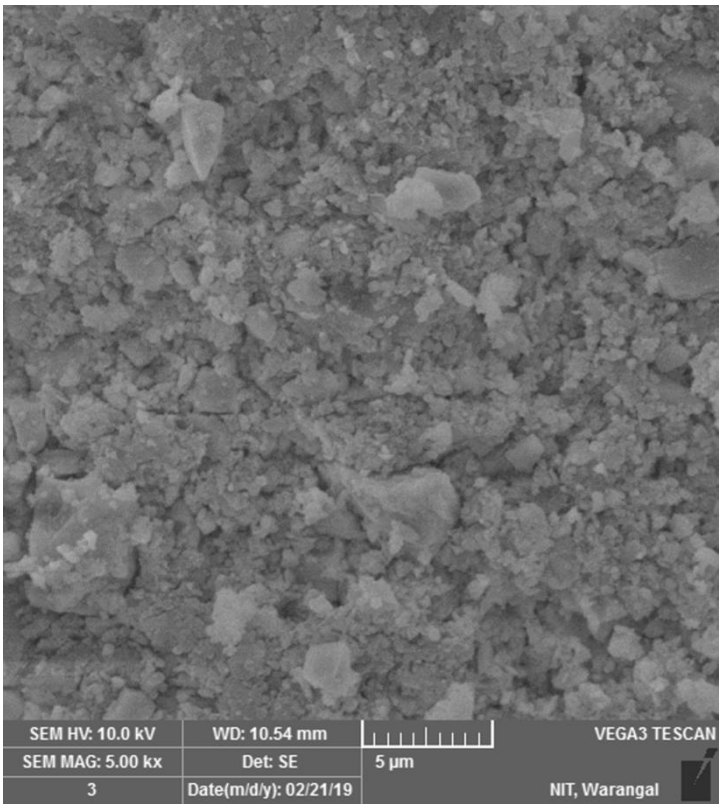

Figure 5.4. SEM image of SiO_2–Si_3N_4–Al_2O_3

The microstructure of pure silica, SiO_2–Si_3N_4–BN and SiO_2–Si_3N_4–Al_2O_3 ceramic specimens was observed using Scanning Electron Microscope (SEM) on polished and thermally etched surfaces presented in Figure 5.2, 5.3 and 5.4 respectively. The tested properties of fused silica ceramic samples are given in Table 5.1.

Table 5.1. Tested properties of fused silica ceramic composites

Ceramic composite	Solid loading (%)	Monomer ratio (MAM: MBAM)	Monomer content (wt%)	Flexural strength (MPa)	Porosity (%)	Dielectric constant	Hardness (HV)
Pure fused silica	52	10:1	10	43.2	38.01	4.214	482
Fused silica+ 5 wt% Si_3N_4+ 1 wt% BN	48.63	10:1	15	69.817	36.214	4.692	501
Fused silica+ 5 wt% Si_3N_4 + 1 wt% Al_2O_3	52	15:1	5	82.01	34.5	4.788	511

Fused silica ceramic composite specimens were polished to obtain fine surface finish. Then, samples were cleaned ultrasonically in alcohol and dried at 100 ± 5 °C for 2 to 4 h. Erosive wear experiment was performed at room temperature on erosion test rig as per ASTM G76 standard. The experimental conditions for the solid particle erosion test are presented in Table 5.2.

Table 5.2. Process parameters for erosion test

S. No.	Test conditions	
1	Erodent type	Silica sand
2	Sample size	20×20×5 mm^3
3	Erodent particle size (μm)	200±20
4	Erodent shape	Angular
5	Hardness of erodent (HV)	1420±50
6	Impact angles (α^o)	30, 45, 60 and 90
7	Impact velocity (m/sec)	86, 101 and 148
8	Feed rate of erodent (g/min)	2±0.02
9	Experimental temperature	Room Temperature (RT)
10	Standoff distance from Nozzle to sample (mm)	10±1

5.2.1 Effect of impingement angle and impact velocity on Erosion rate

Figure 5.5 shows the erosion rate of fused silica ceramic composites with respect to impingement angle and impact velocity. Erosive wear resistance depends on the properties of the target material, erodent type, size, test conditions, equipment, environment and set tribological system (Curkovic et al., 2011). The materials are mainly characterized as ductile and brittle based on erosive studies. The maximum erosion rate of ductile materials like metals occurs at low impact angles of 15^o–30^o, whereas for brittle materials such as ceramics, it happens at or near normal impingement angle i.e. 90^o. From Figure 5.5, it is found that erosion rate of all three fused silica ceramics increases with impingement angle and impact velocity. Higher erosion rate happened at normal impingement angle for all specimens. Moreover, erosion rate was more at higher impact velocities. It is evident that erosion rate is based on impingement angle and impact velocity of erodent particles. Solid erosive wear loss is higher for pure fused silica compared to combined ceramic composites. The order of

erosion rate is maximum for pure fused silica followed by SiO_2–Si_3N_4–BN and SiO_2–Si_3N_4–Al_2O_3 ceramics.

The flexural strength of pure fused silica ceramics is low compared to remaining ceramic composites, as evident from Table 5.1. Moreover, the erosion rate of SiO_2–Si_3N_4–Al_2O_3 ceramic composites is lower compared to SiO_2–Si_3N_4–BN ceramic for any given angle of impact and impingement velocity. The strength and hardness of SiO_2–Si_3N_4–Al_2O_3 ceramics is relatively more in comparison with SiO_2–Si_3N_4–BN ceramics.

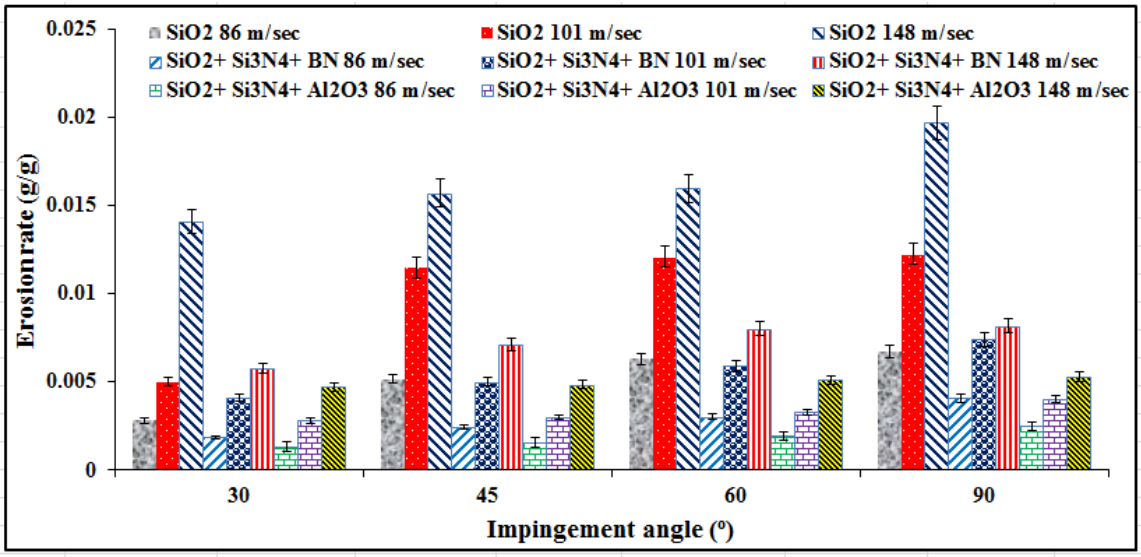

Figure 5.5. Erosion rate of ceramics with impingement angle at impact velocities 86 m/s, 101 m/s and 148 m/s

5.2.2 Effect of impingement angle on Surface roughness

Surface roughness values were measured before and after the erosion tests with impact angles of 30°, 60° and 90° respectively using Taylor Hobson profilometer. The selected range of measuring surface roughness values was obtained and presented based on weight loss results i.e. minimum wear rate (30° impact angle) and maximum wear rate (normal impact angle) at higher impingement velocity. The average surface roughness (Ra) values were obtained from these measurements. Variations of surface roughness with impact angle for different ceramics are shown in Figure 5.6. Surface roughness was more for eroded surfaces compared to un-eroded surfaces. It is observed that surface roughness is more at normal impingement compared to acute impact angle.

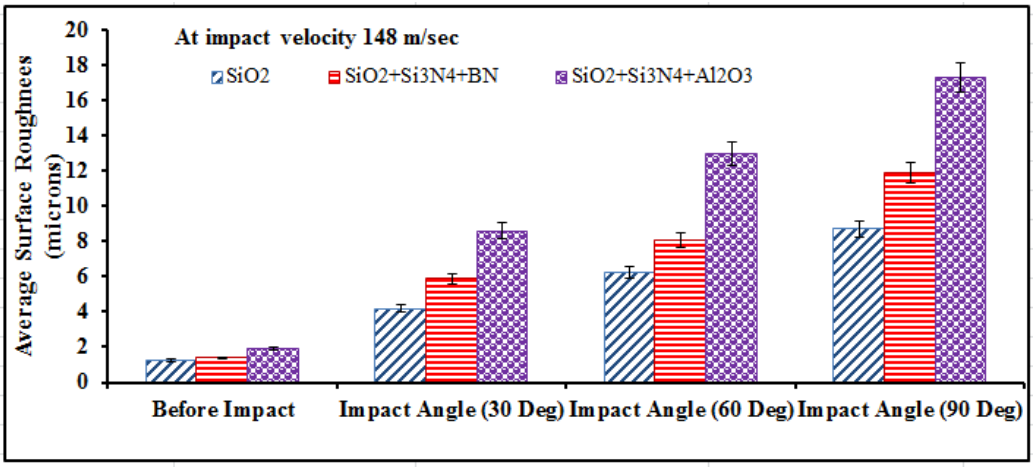

Figure 5.6. Surface roughness of ceramics at different impingement angle and at impact velocity of 148 m/s

The morphology of the surfaces after erosion test (at impingement angles 30^o and 90^o) at impact velocity 148 m/s are presented in Figure 5.7 to 5.12.

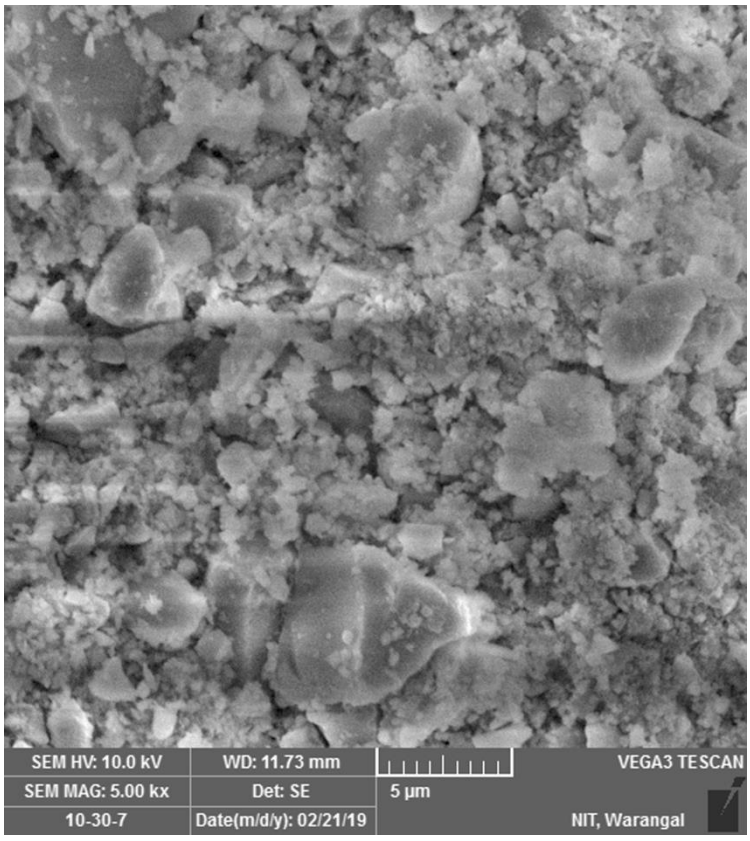

Figure 5.7. SEM micrograph of eroded surface of pure fused silica at 30^o impact angle

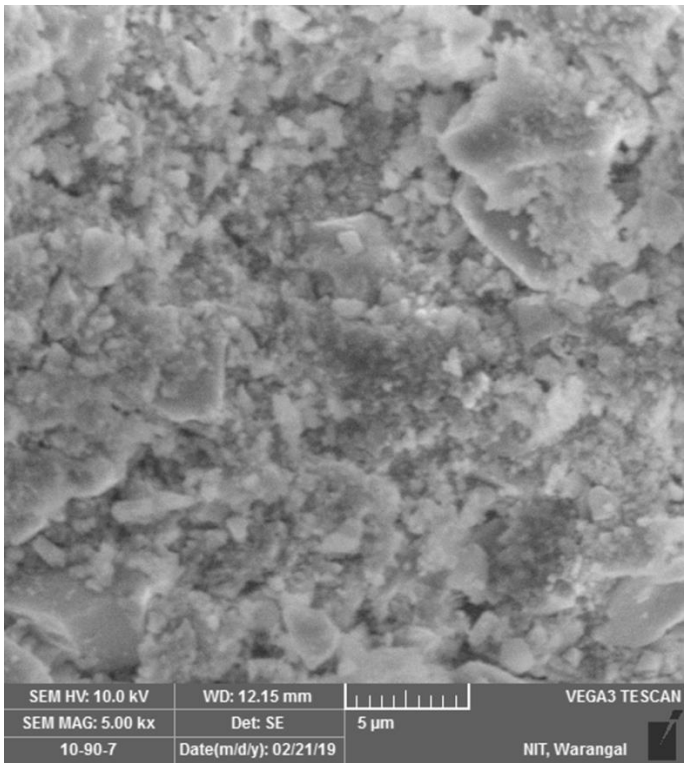

Figure 5.8. SEM micrograph of eroded surface of pure fused silica at 90^o impact angle

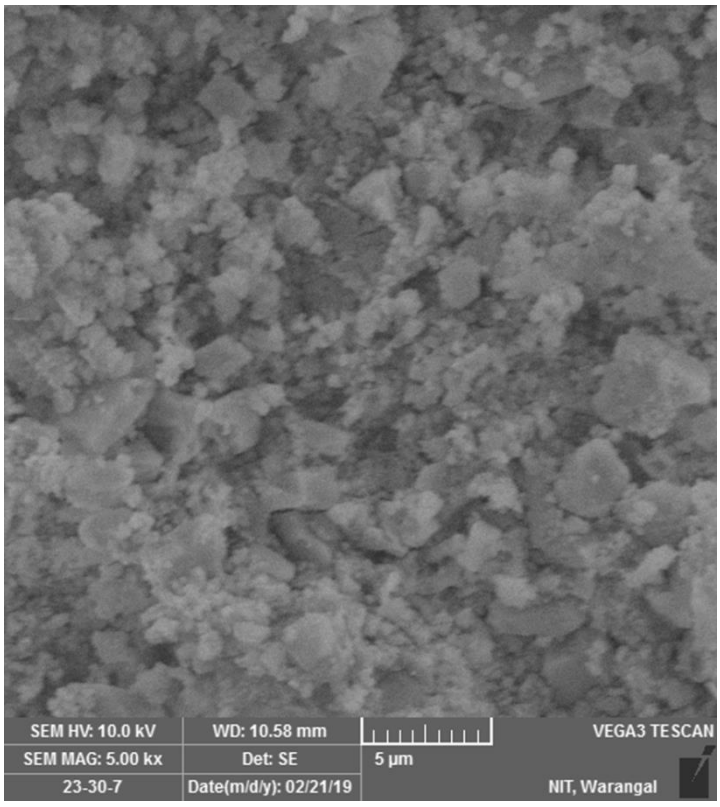

Figure 5.9. SEM micrograph of eroded surface of SiO_2–Si_3N_4–BN ceramic at 30^o impact angle

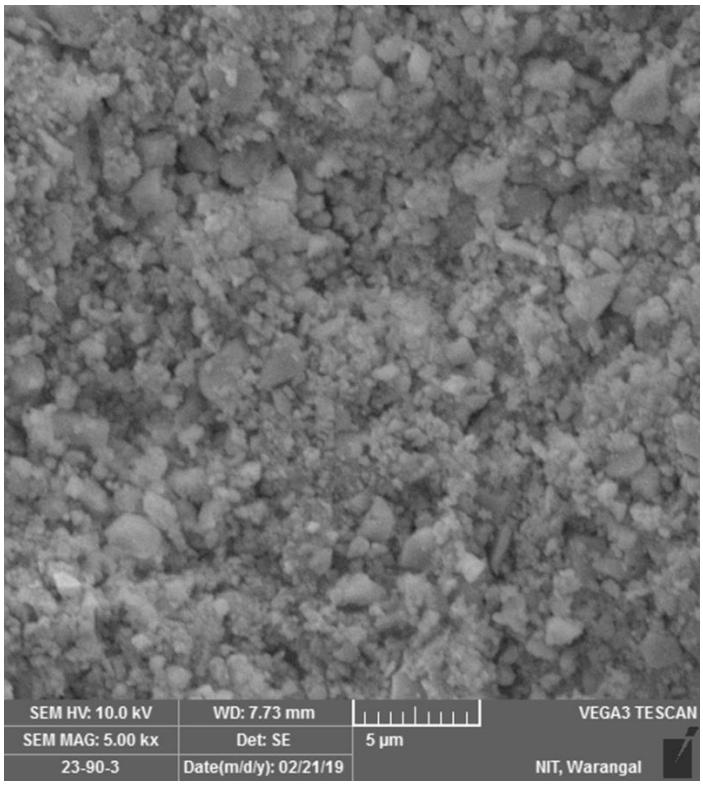

Figure 5.10. SEM micrograph of eroded surface of SiO_2–Si_3N_4–BN ceramic at 90^o impact angle

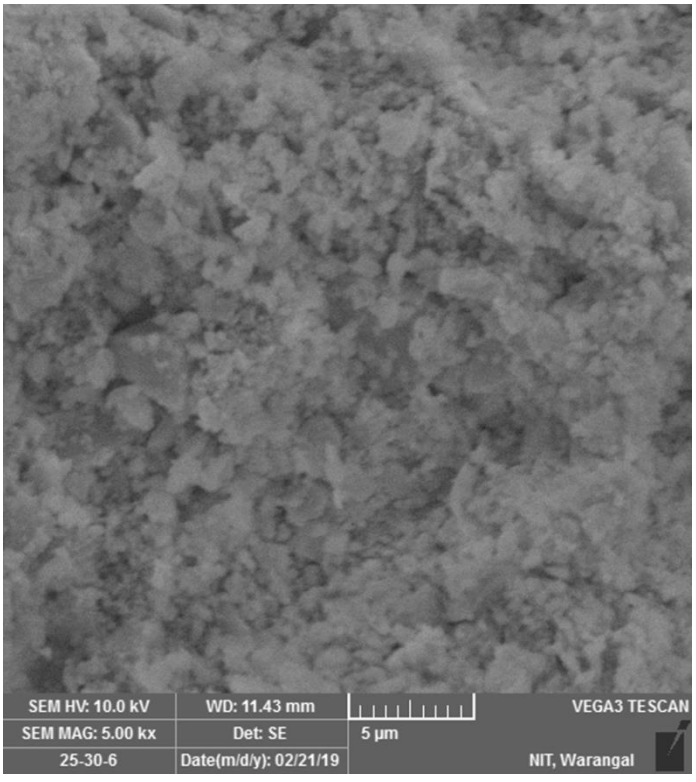

Figure 5.11. SEM micrograph of eroded surface of SiO_2–Si_3N_4–Al_2O_3 ceramic at 30^o impact angle

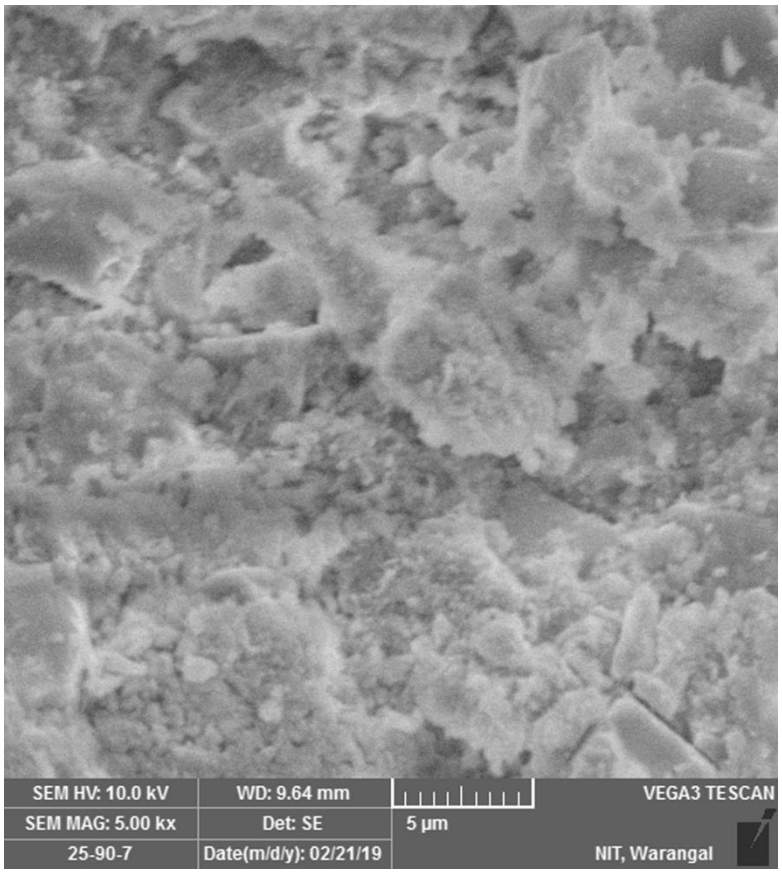

Figure 5.12. SEM micrograph of eroded surface of SiO_2–Si_3N_4–Al_2O_3 ceramic at 90^o impact angle

A comparison is drawn between the eroded specimen surface of silica ceramic composites at impingement angles of 30^o and 90^o at impact velocity 148 m/s. Grain ejection was prime material removal mechanism but it led to low plastic deformation when the impingement angle was close to normal impact; on the other hand, ploughing mechanism was dominant in the case of acute impingement angles. Ploughing mechanism is related to plastic smearing and removal of the surface material. The hardness of the ceramic material opposes plastic deformation, so that erosion rate is low at low impingement angles. At normal impact close to 90^o, the erosion rate is more because of low fracture toughness and hardness which results in cracks that grow to form a crack network across the grain boundaries. These findings are in agreement with previous studies on erosion mechanisms on ceramics [Curkovic et al., 2011 and Renjo et al., 2015). In order to analyze the damages and erosion mechanisms, the structure of the eroded surfaces of the specimen was examined by SEM.

It is reported that bulk materials like ceramics are indeed influenced by erosion mechanism i.e. ratio of particle hardness to target ceramic hardness (Hp/Ht). When the ratio

(Hp/Ht) is >1, wear mechanism essentially includes indentation induced fracture. For lower ratios, such cracking is curbed and material removal takes place by less critical microchipping mechanism. Table 5.3 shows the overall properties of ceramics.

Table 5.3. Overall properties of ceramics

Ceramic composite	Solid loading (%)	Monomer ratio (MAM:MBAM)	Monomer content (wt%)	Flexural strength (MPa)	Porosity (%)	Dielectric constant	Hardness (HV)	Erosion rate (g/g) (max)
Pure fused silica	52	10:01	10	43.2	38.01	4.214	482	0.0197
SiO_2–Si_3N_4–BN	48.63	10:01	15	69.817	36.214	4.692	501	0.0082
SiO_2–Si_3N_4–Al_2O_3	52	15:01	5	82.01	34.5	4.788	511	0.0053

Summary

This chapter presents the solid particle erosion studies of SiO_2, SiO_2–Si_3N_4–BN and SiO_2–Si_3N_4–Al_2O_3 ceramics with SiO_2 particles as erodent. This chapter discusses the effect of various impingement angles and impact velocities on erosion rate. Erosive wear resistance depends on the properties of the target material, erodent type, size, test conditions, equipment, environment and set tribological system. The maximum erosion rate of ductile materials like metals occurs at low impact angles of 15^o–30^o, whereas for brittle materials such as ceramics, it happens at or near normal impingement angle i.e. 90^o. Erosion rate of all three fused silica ceramics increases with impingement angle and impact velocity. Higher erosion rate happened at normal impingement angle for all specimens. Moreover, erosion rate was more at higher impact velocities. Solid erosive wear loss is higher for pure fused silica compared to combined ceramic composites. The order of erosion rate is maximum for pure fused silica followed by SiO_2–Si_3N_4–BN and SiO_2–Si_3N_4–Al_2O_3 ceramics.

This chapter also discusses the influence of acute and normal impingement angles on surface roughness and morphology of the SiO_2, SiO_2–Si_3N_4–BN and SiO_2–Si_3N_4–Al_2O_3 ceramics at with higher impact velocity. Surface roughness was more for eroded surfaces compared to un-eroded surfaces. Surface roughness is more at normal impingement compared to acute impact angle. The ascending order of surface roughness of ceramics is SiO_2, SiO_2–Si_3N_4–BN and SiO_2–Si_3N_4–Al_2O_3 respectively.

CHAPTER 6

MODELING AND OPTIMIZATION LASER ASSISTED MACHINING PROCESS

6.1. Introduction

This chapter deals with laser assisted machining of SiO_2–Si_3N_4–Al_2O_3 ceramic composite. This chapter also discusses the modeling of machining varying rotational speed, feed, depth of cut and laser power. The effect of input variables on responses such as surface roughness and material removal temperature was also studied. The optimal process variables for minimum surface roughness and minimum material removal temperature were studied using RSM coupled with desirability approach to optimize multiple responses. The predicted values for responses such as surface roughness and material removal temperature obtained from regression models were compared with experimental values was also presented in this chapter.

6.2. Process modeling and optimization of laser assisted machining

RSM is a statistical and numerical technique that is utilized for the design and optimization of engineering problems. It is mainly used to find an approximate mathematical model for estimating the future response and to find the process parameters that optimize the predicted model (Xiangli et al., 2008). The aim of the current experimental analysis is to find the optimum settings of interaction effects of the input process parameters (rotational speed, feed, depth of cut and laser power) that result in optimum responses for surface roughness and material removal temperature. Consequently RSM was decided for the present exploratory examination since it is perfect and a reasonable outline of multivariable measurable techniques. Analysis of Variance (ANOVA) was used for recommended and balanced models. The F-values were utilized to test the statistical immensity of recommended and changed models for ANOVA. It takes some effort to partition the variety in the trial information into parts. Every one of the terms in the condition was figured out and organized, using ANOVA table. There are parts of parameters which were proposed to assess the nature of scientific models and how ably they suit exploratory information like coefficient of

determination (R^2), adjusted coefficient of determination (Adj. R^2), coefficient of variation (C.V.), adequate precision and lack of fit (LOF) (Li et al., 2013). The experimental design and test data is shown in Table 6.1.

Table 6.1. Experimental design and test data

S. No.	Rotational Speed (RPM)	Feed (mm/rev)	Depth of cut (mm)	Power (W)	Surface Roughness (µm)	Material Removal Temperature (^oC)
1	500	0.05	0.2	500	2.13	647.4
2	600	0.075	0.1	400	1.46	433.2
3	400	0.05	0.2	500	2.17	648.5
4	400	0.075	0.1	400	1.3	452.2
5	500	0.05	0.2	500	2.13	647.4
6	600	0.025	0.1	400	1.74	434.2
7	500	0.05	0.2	500	2.13	647.4
8	500	0.05	0.2	500	2.13	647.5
9	400	0.025	0.3	400	1.35	444.3
10	600	0.025	0.3	400	1.76	468.3
11	600	0.075	0.1	600	1.51	801.7
12	400	0.075	0.3	400	1.95	476.4
13	400	0.075	0.3	600	1.61	813.9
14	500	0.05	0.2	500	2.13	647.4
15	600	0.025	0.3	600	1.91	824.6
16	500	0.05	0.3	500	2.1	679.6
17	500	0.05	0.2	600	2.04	802.04
18	600	0.05	0.2	500	2.03	677.2
19	400	0.025	0.1	600	1.54	804.7
20	400	0.075	0.1	600	1.57	798.67
21	600	0.025	0.1	600	1.54	790.3
22	500	0.05	0.2	500	2.13	648.21
23	600	0.075	0.3	600	2.61	820.4
24	500	0.05	0.1	500	2	637.25
25	400	0.025	0.1	400	1.1	434.9
26	500	0.025	0.2	500	1.96	644.92
27	500	0.075	0.2	500	2.2	649.2
28	600	0.075	0.3	400	1.98	456.9
29	400	0.025	0.3	600	1.77	817.3
30	500	0.05	0.2	400	1.8	637.31

6.2.1. Modeling of surface roughness

ANOVA for response surface model of surface roughness is shown in Table 6.2.

Table 6.2. ANOVA analysis for response surface model of surface roughness

Source	Sum of Squares	df	Mean Square	F Value	p-value Prob > F	
Model	3.027829942	17	0.178107644	11.96981924	< 0.0001	significant
A-Rotational Speed	0.364022222	1	0.364022222	17.74375434	<0.0012	
B-Feed	0.328355556	1	0.328355556	8.626203608	<0.0124	
C-Depth of cut	0.597688889	1	0.597688889	40.16800073	< 0.0001	
D-Power	0.800888889	1	0.800888889	10.28842047	<0.0005	
AB	0.000225	1	0.000225	0.015121245	0.9042	
AC	0.172225	1	0.172225	11.57447303	<0.0052	
AD	0.0016	1	0.0016	0.107528854	0.7486	
BC	0.1296	1	0.1296	8.709837161	<0.0121	
BD	0.0025	1	0.0025	0.168013834	0.6891	
CD	0.1521	1	0.1521	10.22196167	<0.0077	
A^2	0.008013477	1	0.008013477	0.53854999	0.4771	
B^2	0.014813477	1	0.014813477	0.995547619	0.3381	
C^2	0.028899841	1	0.028899841	1.942229204	0.1887	
D^2	0.143831659	1	0.143831659	9.666283378	0.0090	
ABC	0.065025	1	0.065025	4.370039826	0.0585	
ABD	0.0441	1	0.0441	2.963764034	0.1108	
ACD	0.005625	1	0.005625	0.378031127	0.5501	
Residual	0.178556725	12	0.014879727			
Lack of Fit	0.178556725	7	0.025508104			
Pure Error	0	5	0			
Cor Total	3.206386667	29				

R-Squared: 0.965, Adj R-Squared=0.944, Pred R-Squared=0.920, Adequate Precision: 15.769, C.V.: 7.579

From ANOVA it is observed that A, B, C, AC, BC, CD and D^2 are significant model terms. The regression model developed for surface roughness is given in Eq. 6.1.

$$Surface\ roughness\ (\mu m) = 1.8928 + 0.1211 \times A + 0.08445 \times B + 0.1822 \times C + 0.0922 \times D - 0.00375 \times A \times B + 0.0525 \times A \times C - 0.01 \times A \times D + 0.09 \times B \times C - 0.0125 \times B \times D + 0.01875 \times C \times D - 0.0556 \times A^2 - 0.0756 \times B^2 - 0.1056 \times C^2 - 0.2356 \times D^2 + 0.06375 \times A \times B \times C + 0.10375 \times A \times B \times D + 0.0975 \times A \times C \times D \quad (6.1)$$

It is essential to know that the model obtained gives an adequate approximation to the actual system. Model acceptability can be ensured by drawing diagnostic figures like predicted versus experimental. Figure 6.1 represents the difference between experimentally measured values and predicted values for surface roughness. The measured values were found relatively close to the straight line. The graphs backed by Adj. R^2 values for three responses were 0.944 which is near 1 indicating good compliance between observed and predicted values.

Figures 6.2, 6.3, 6.4 and 6.5 show the single factor effect and Figures 6.6, 6.7 and 6.8 show the interaction effect on surface roughness.

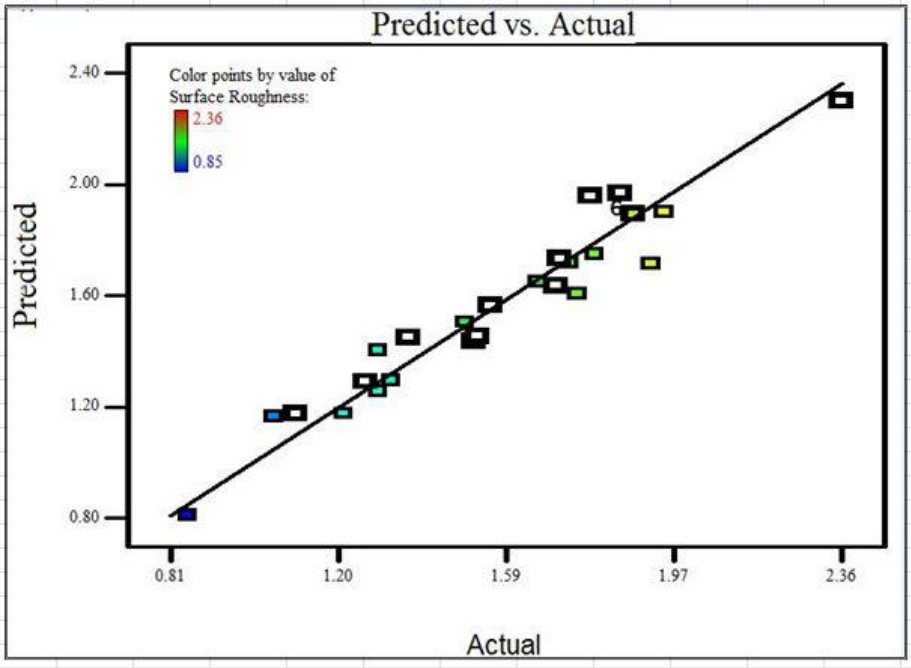

Figure 6.1. Predicted versus actual for roughness surface

The small amount of variation in surface roughness for the cases particularly with respect to variations in the feed and depth of cut suggests that the material removal mechanism is a hybrid of plastic deformation and brittle fracture, which is primarily affected by laser power and rotational speed. A low depth of cut and the feed rate process parameters are required in order to obtain a lower surface roughness during conventional machining. This meant that the same surface roughness was aimed to be obtained with laser assisted machining, where the depth of cut or the feed rate must be reduced in the conventional machining, leading to the material removal rate decrease. Therefore, the LAM technology could increase the removal rate of the material, improving the production efficiency and cost saving.

Contact between the cutting tool and the rotating workpiece leads to dynamic loading and an induced stress field within the material. During the cutting operation, strain energy accumulates within the workpiece and induced tensile stresses initiate crack sites. The cracks then propagate through material near the cutting tool, and, when they merge, chip fragments form and detach from the workpiece. Crack propagation is also promoted by a release of the strain energy built up in the workpiece, particularly from the compressive stresses, which can lead to micro-scale catastrophic failure away from the cutting tool and more chip fragments (brittle fracture chips).

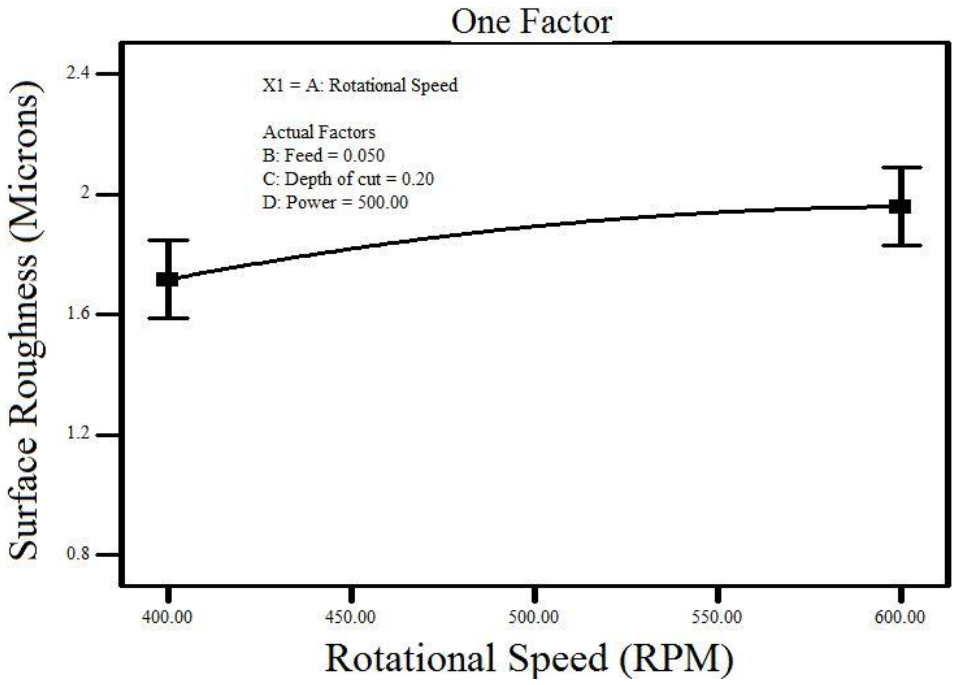

Figure 6.2. Effect of rotational speed on surface roughness

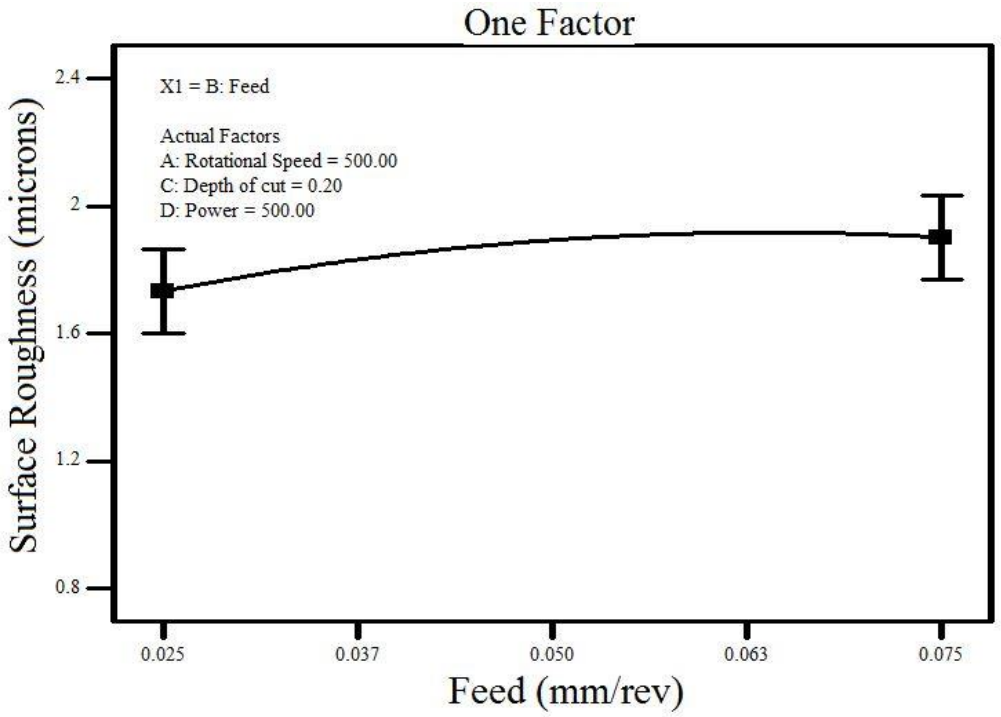

Figure 6.3. Effect of feed on surface roughness

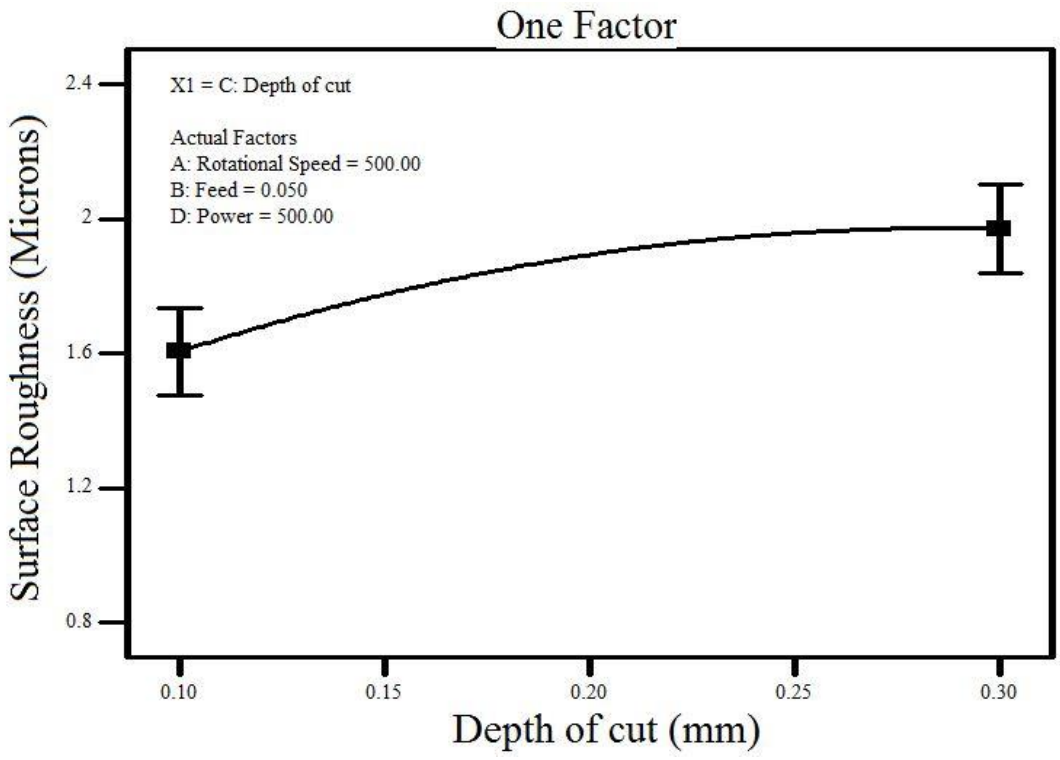

Figure 6.4. Effect of depth of cut on surface roughness

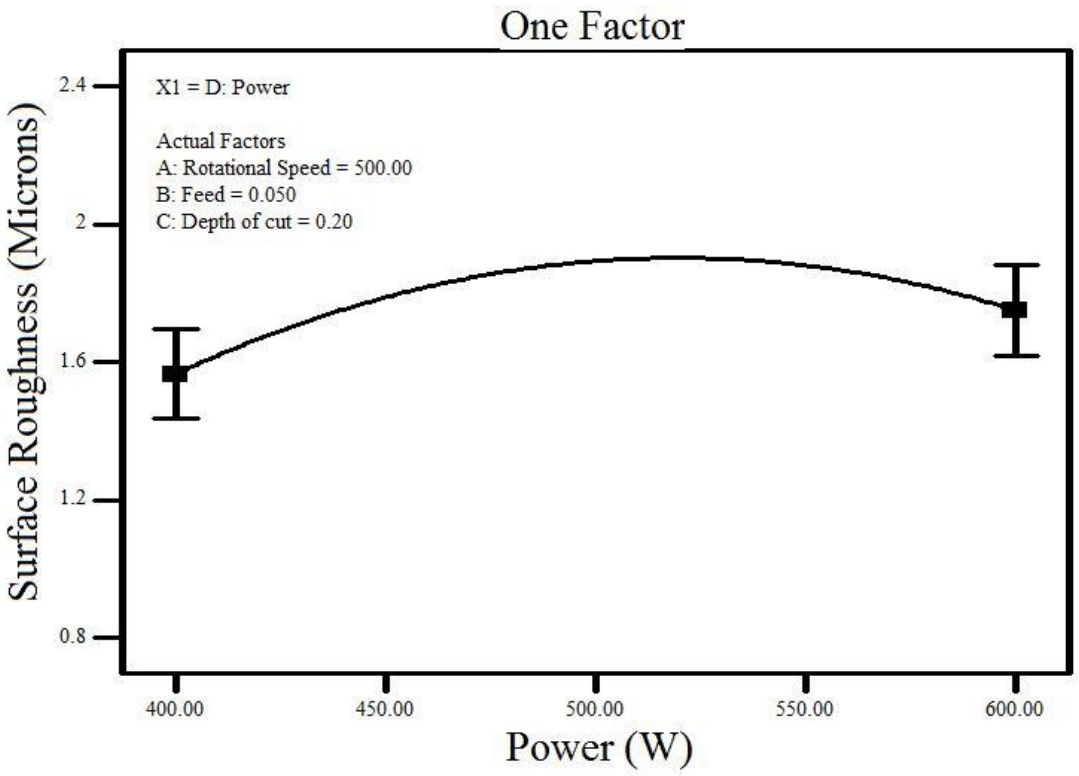

Figure 6.5. Effect of power on surface roughness

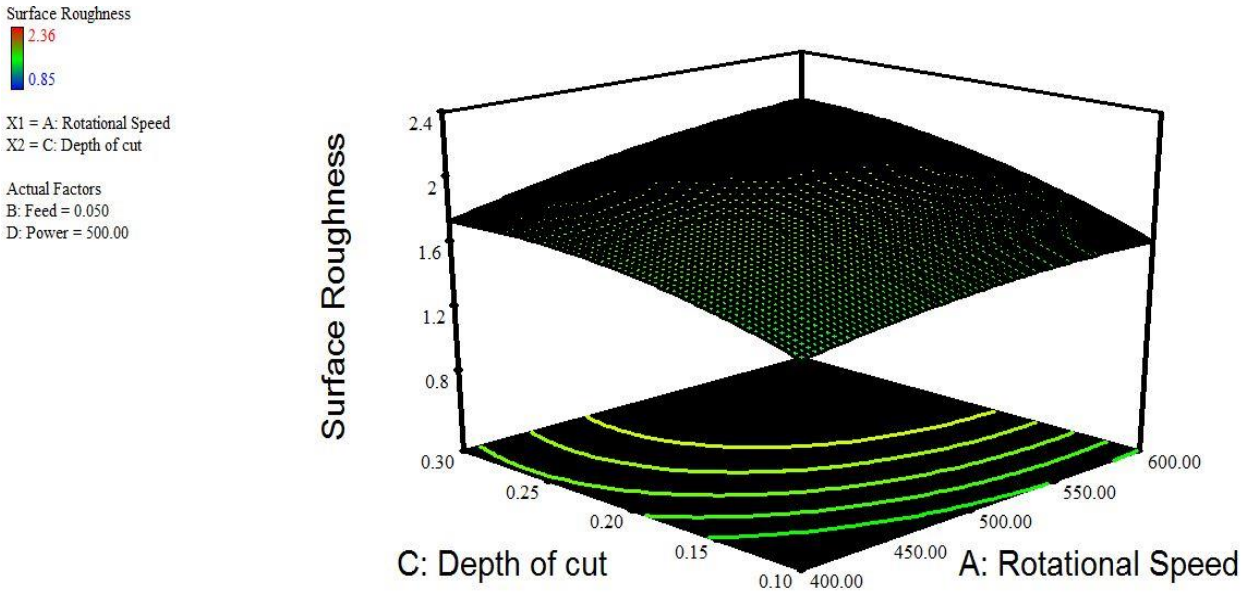

Figure 6.6. Effect of depth of cut and rotational speed on surface roughness

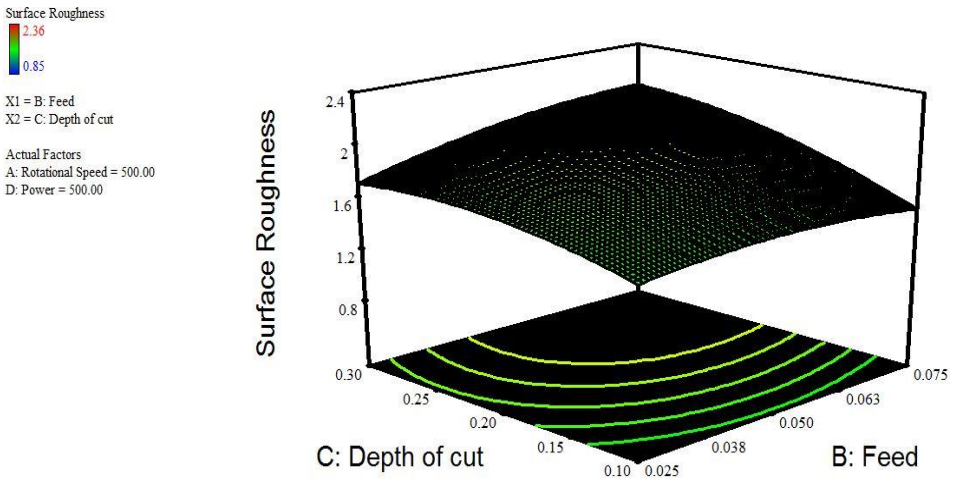

Figure 6.7. Effect of feed and depth of cut on surface roughness

One fundamental theory of machining is that as the rotational speed increases, surface roughness decreases because of increase in the nose radius of the tool insert. In laser assisted machining the opposite is observed because a small amount of vibration is sensed during cutting at higher rotational speeds which in turn increases surface roughness.

The relation between surface roughness and feed given in Eqn. 6.2

$$R_a = \frac{f^2}{32\,r} \tag{6.2}$$

Where R_a=surface roughness, f=feed, r = nose radius

As the feed increases, surface roughness increases which is evident from Eq. 6.3. Depth of cut has a positive effect on surface roughness. The more the depth of cut, more the surface roughness is achieved. The laser power softens the cutting zone better which reduces the hardness and strength of the workpiece material. Surface roughness increases as laser power increases. The reason may be that the molten pool softened by the laser is not completed removed by the cutting tool (Song et al., 2018 and 2019).

The machinability can be calculated as the percentage improvement in surface roughness, tool wear and cutting forces. In laser assisted machining, the percentage improvement in surface roughness, tool wear and cutting forces can be calculated when laser power changed from nonzero to a specific value. The surface roughness at speed 500 rpm, feed 0.025 mm/rev, depth of cut 0.1 mm and laser power 400 W is 1.74 µm. The surface roughness becomes 1.54 µm when the laser power is increased to 600 W at the same cutting conditions. The percentage improvement in surface roughness is 11.49.

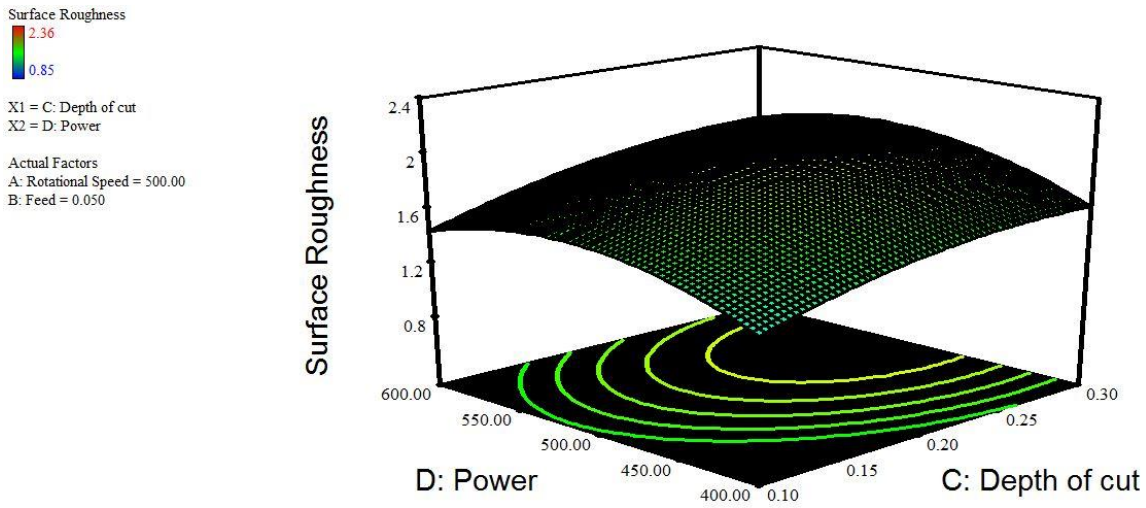

Figure 6.8. Effect of power and depth of cut on surface roughness

6.2.2. Modeling of material removal temperature

ANOVA for response surface model of material removal temperature is shown in Table 6.3.

Table 6.3. ANOVA analysis for response surface model of material removal temperature

Source	Sum of Squares	df	Mean Square	F Value	p-value Prob > F	
Model	5222.129	22	237.3694944	21.59737689	<0.0002	Significant
A-Rotational Speed	899.845	1	899.845	37.47226114	<0.0005	
B-Feed	393.6736	1	393.6736111	17.62164924	<0.0040	
C-Depth of cut	858.88	1	858.88	81.78578372	< 0.0001	
D-Power	1118.045	1	1118.045	9.830616993	<0.0065	
AB	126.5625	1	126.5625	11.51545618	<0.0115	
AC	152.5225	1	152.5225	13.87746106	<0.0074	
AD	19.8025	1	19.8025	1.801756611	0.2214	
BC	4.6225	1	4.6225	0.420584266	0.5373	
BD	7.0225	1	7.0225	0.638951435	0.4504	
CD	97.0225	1	97.0225	8.827720275	<0.0208	
A^2	307.6179	1	307.6178533	27.98901658	0.0011	
B^2	63.57829	1	63.57828517	5.784754228	0.0471	

C^2	107.6652	1	107.6651943	9.796059866	0.0166
D^2	137.8307	1	137.8307397	12.54071185	0.0095
ABC	117.7225	1	117.7225	10.71113711	0.0136
ABD	386.1225	1	386.1225	35.13186552	0.0006
ACD	0.0625	1	0.0625	0.005686645	0.9420
BCD	18.9225	1	18.9225	1.721688649	0.2309
A^2B	0.006944	1	0.006944444	0.000631849	0.9806
A^2C	8.82	1	8.82	0.802499346	0.4001
A^2D	15.08028	1	15.08027778	1.372098986	0.2798
AB^2	407.3669	1	407.3669444	37.06481935	0.0005
Residual	76.93464	7	10.99066316		
Lack of Fit	76.93464	2	38.46732105		
Pure Error	0	5	0		
Cor Total	5299.064	29			

R-Squared: 0.985, Adj R-Squared=0.939, Pred R-Squared=0.927, Adequate Precision: 15.252, C.V.: 2.170

From ANOVA it is observed that A, B, C, AB, AC, CD, A^2, B^2, C^2, D^2 and ABC are significant model terms. The regression model developed for material removal temperature is given in Eq. 6.3.

$$Material\ removal\ temperature\ (℃) = 149.676 \times A + 2.1 \times B + 21.2 \times C + 7.35 \times D - 2.8125 \times A \times B + 3.0875 \times A \times C + 1.1125 \times A \times D - 0.5375 \times B \times C - 2.4625 \times B \times D - 0.6625 \times C \times D + 10.8963 \times A^2 - 4.923 \times B^2 + 6.4463 \times C^2 - 7.293 \times D^2 - 2.7125 \times A \times B \times C + 4.912 \times A \times B \times D + 0.0625 \times A \times C \times D - 1.0875 \times B \times C \times D + 0.625 \times A^2 \times B - 10.4375 \times A^2 \times C + 2.9125 \times A^2 \times D - 15.137 \times A \times B^2 \quad (6.3)$$

It is essential to know that the model obtained is gives an adequate approximation to the actual system. Model acceptability can be ensured by drawing diagnostic figures like predicted versus experimental. Figure 6.9 represents the difference between experimentally measured values and predicted values for material removal temperature. The measured values were found relatively close to the straight line. The graphs backed by Adj. R^2 values for three responses were 0.939 which is near 1 indicating better compliance between observed and predicted values.

Figures 6.10, 6.11, 6.12 and 6.13 show the single factor effect and Figures 6.14, 6.15 and 6.16 show the interaction effect on material removal temperature.

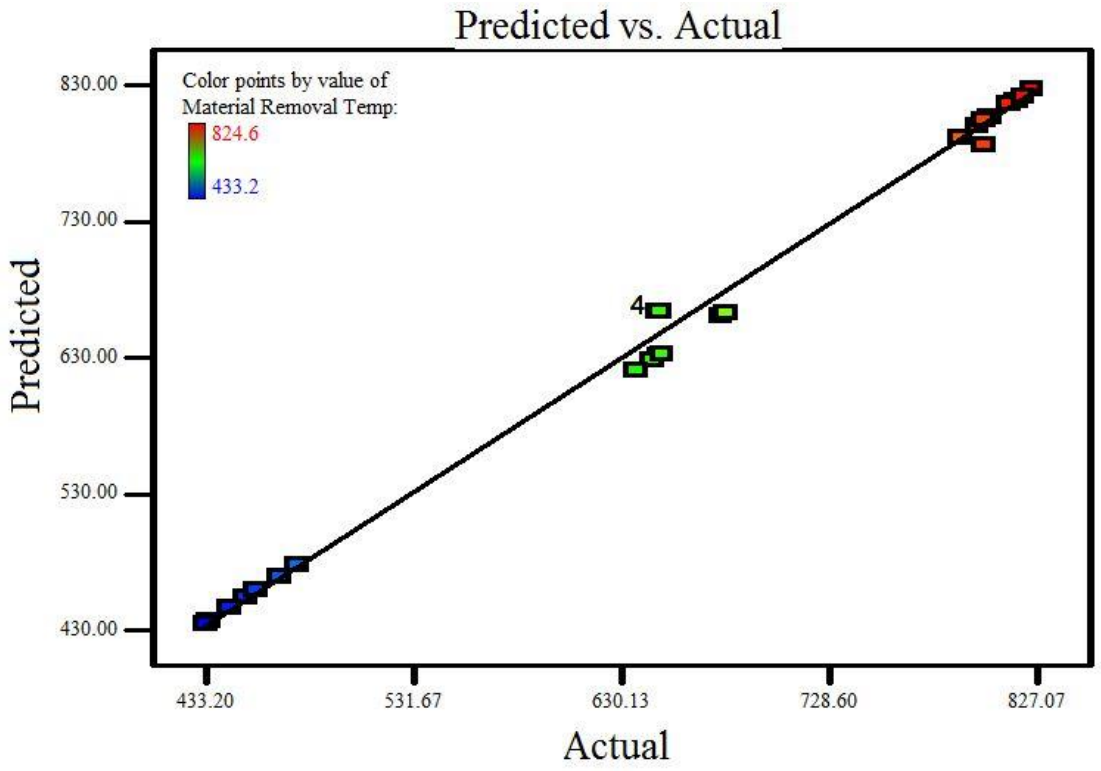

Figure 6.9. Predicted versus actual for material removal temperature

Viscosity of the ceramic boundary particles decreases as temperature increases, thereby enhancing plastic flow and postponing crack formation within the material, the chip quantity also increases as workpiece temperature rises. Since chip separation from the ceramics surface occurs through crack propagation along the shear zone, delayed break formation at the higher temperature should produce larger chips. Such chip formation is dominated by the intergranular fracture preceding the material's plastic flow, while the main fracture mechanism is transgranular fracture with negligible deformation at room temperature.

From the fundamental theories of machining, rotational speed plays an important role in material removal temperature of the machining process. The higher the rotational cutting speed, the faster the movement of the tool on the surface. Hence, more heat is generated by friction. When the cutting speed increases, there is little time available to dissipate the generated heat, which in turn increases the material removal temperature. Increase in feed and depth of cut increases material removal temperature. Higher depth of cut increases chip thickness. It is difficult to dissipate heat through large surface of the chip. There is very low

chance of dissipating temperature and hence material removal temperature increases. Laser power is sufficient to soften the hard surface of the workpiece material. The hardness and strength of the hard workpiece material reduce. Hence, there is little effect of rotational speed, feed and depth of cut on material removal temperature compared to laser power (Song et al., 2018 and 2019).

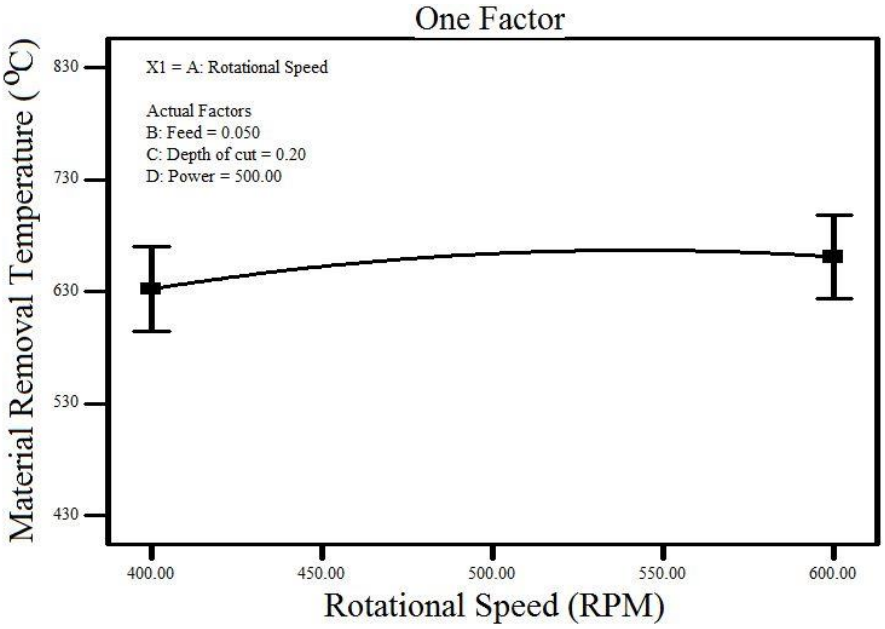

Figure 6.10. Effect of rotational speed on material removal temperature

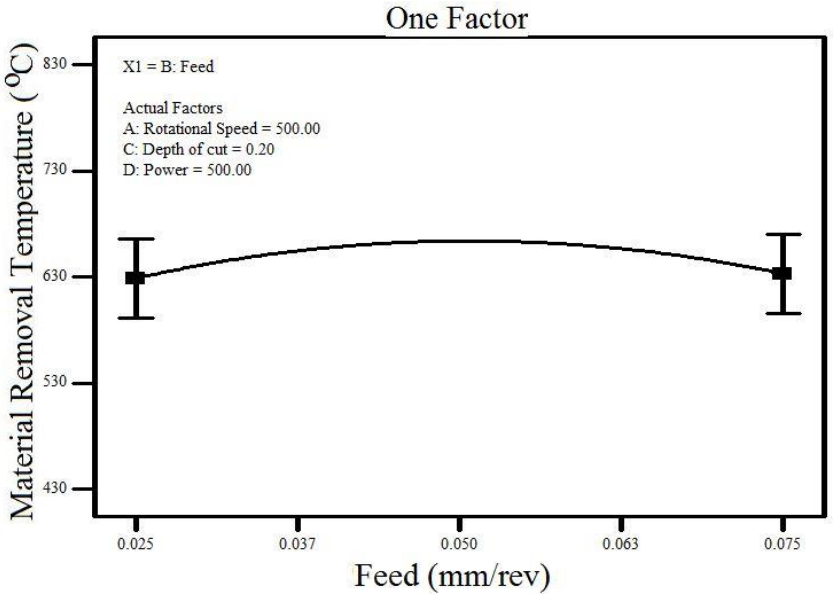

Figure 6.11. Effect of feed on material removal temperature

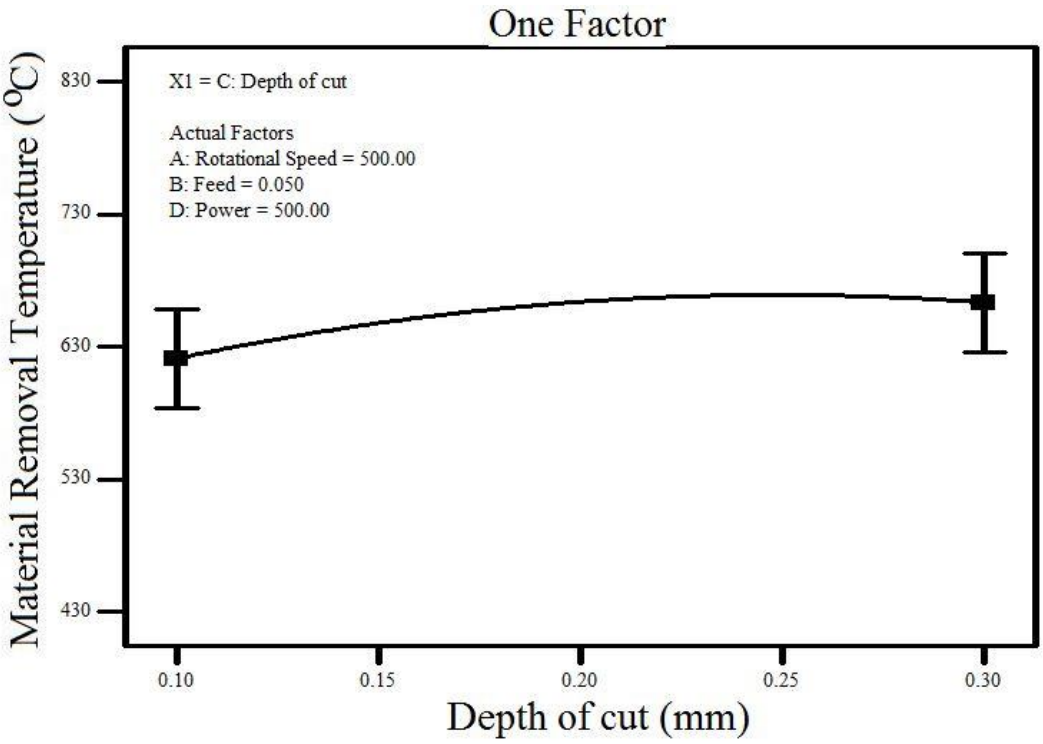

Figure 6.12. Effect of depth of cut on material removal temperature

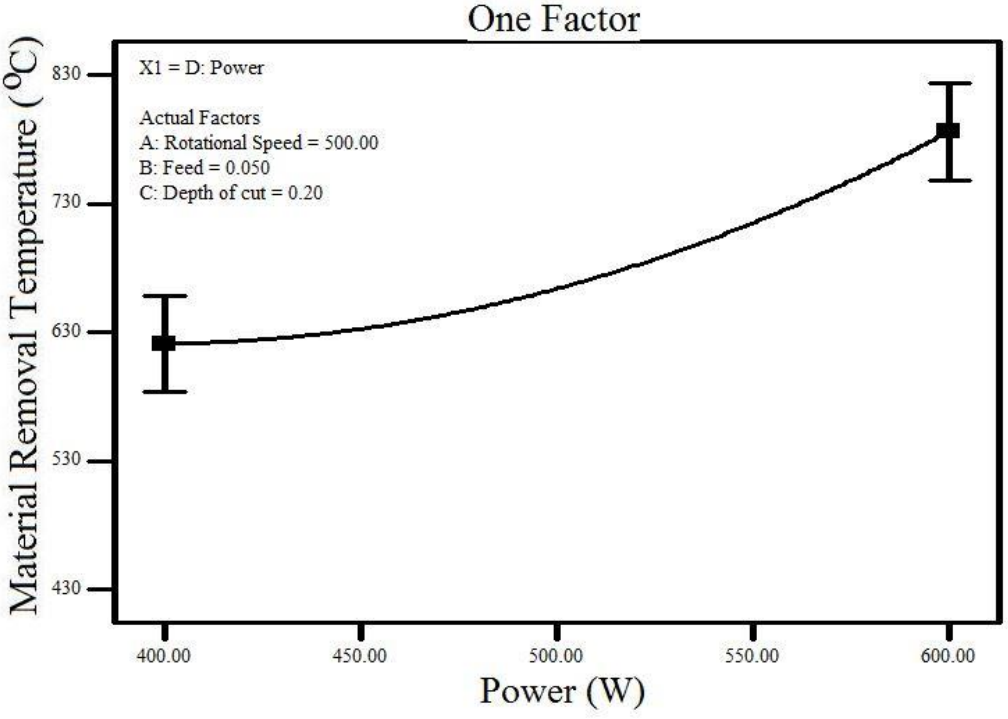

Figure 6.13. Effect of power on material removal temperature

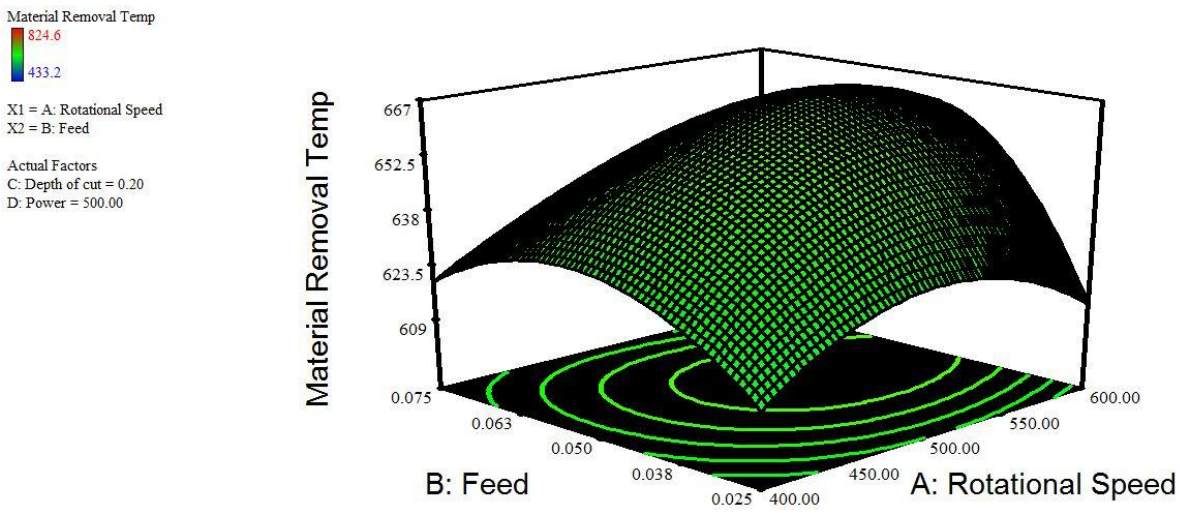

Figure 6.14. Effect of feed and rotational speed on material removal temperature

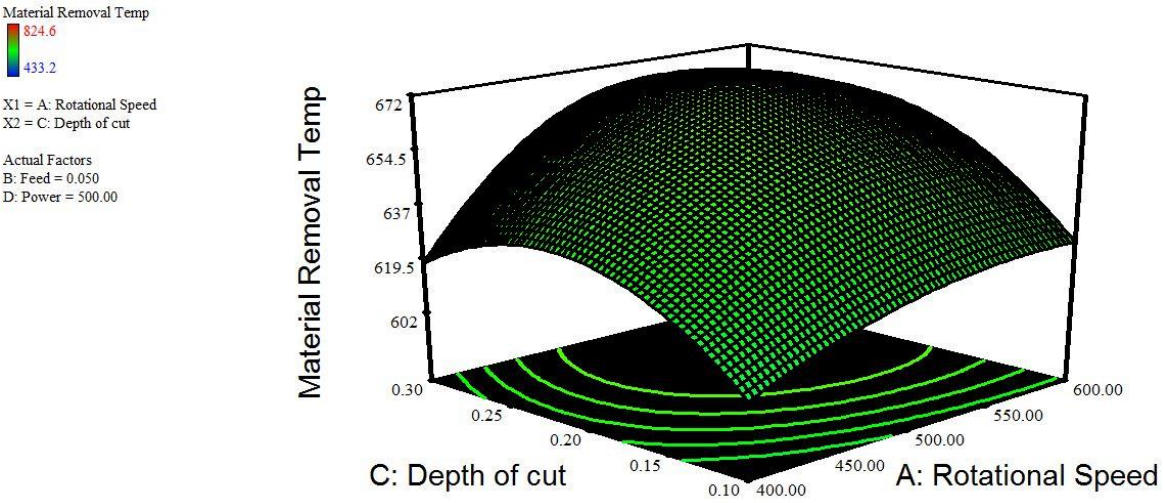

Figure 6.15. Effect of depth of cut and rotational speed on material removal temperature

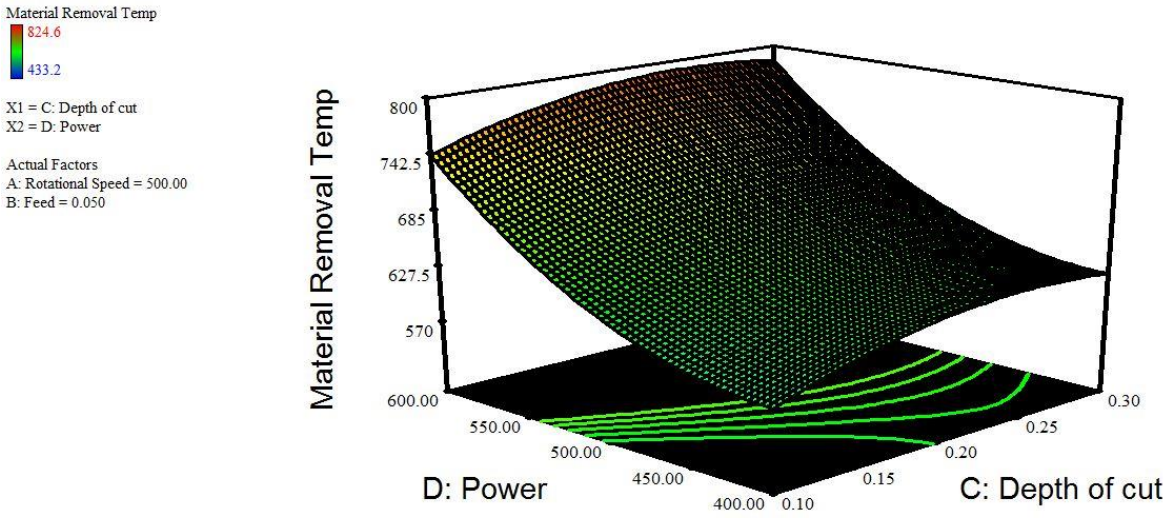

Figure 6.16. Effect of power and rotational speed on material removal temperature

6.2.3 Multi Response Optimization

Multi objective optimization has been conducted on laser assisted machining process followed by mathematical modeling and analysis. The performance measures used for the optimization modeling are surface roughness and material removal temperature with desirability approach implemented. The constraints for the optimization of the laser assisted machining process are shown in Table 6.4.

Table 6.4. Constraints and rules applied on process variables and responses

Constraints Name	Goal	Lower Limit	Upper Limit	Lower Weight	Upper Weight	Importance
Rotational Speed	is in range	400	600	1	1	3
Feed	is in range	0.025	0.075	1	1	3
Depth of cut	is in range	0.1	0.3	1	1	3
Power	is in range	400	600	1	1	3
Surface Roughness	Minimize	1.1	2.61	1	1	3
Material Removal Temperature	Minimize	433.2	824.6	1	1	3

Alongside measurable approval and check of numerical models regarding a solitary reaction, the scientific models as far as multi objective optimization is concerned have additionally been affirmed by confirmation tests. Optimum settings of process variables were found by checking for optimization, minimizing surface roughness and minimizing material removal temperature. The optimal solutions are shown in Table 6.5. The optimum process parameters were found to be 400 rpm rotational speed, 0.025 mm/rev feed, 0.1 mm depth of cut and 400 W laser power to meet the requirements of optimal responses. It is evident from Table 6.6 that the actual (experimental) and predicted output values are firmly aligning with each other, which legitimizes the ampleness of RSM based optimization and forecast of surface roughness and material removal temperature. The percentages of residuals for these responses are 4.371% and 0.867% respectively.

Table 6.5. Optimal solutions

Rotational Speed (RPM)	Feed (mm/rev)	Depth of cut (mm)	Power (W)	Surface Roughness (µm)	Material Removal Temperature (^oC)	Desirability	
400	0.025	0.1	400	1.07224545	437.96776	0.993891	Selected
400	0.034	0.1	400.27	1.17418145	450.95467	0.952754	
600	0.075	0.1	400.08	1.43307358	435.5892	0.88015	
400.03	0.025	0.3	400	1.42504318	446.88627	0.870229	
400	0.025	0.29	400	1.42631531	449.33848	0.866934	
400	0.025	0.3	400	1.43198909	447.73674	0.866698	
400	0.071	0.1	400	1.4109826	458.27437	0.86208	
600	0.075	0.1	407.11	1.46285952	442.50066	0.861187	
400	0.025	0.24	400	1.40361405	461.94539	0.860381	
401.07	0.065	0.1	400	1.39580311	464.70914	0.859867	

Table 6.6. Results of confirmation test

Dependent variables	Optimum input parameters				Predicted values	Actual values	Error (%)
	Speed (rpm)	Feed (mm/rev)	Depth of cut (mm)	Power (W)			
	400	0.025	0.1	400			
Surface Roughness (µm)					1.072	1.121	4.371
Material Removal Temp (^oC)					437.967	434.2	-0.867

The ramp graphs for the optimization shown in Figure 6.17. The overall desirability value of the optimal factors obtained was 0.994 and represented in Figure 6.18.

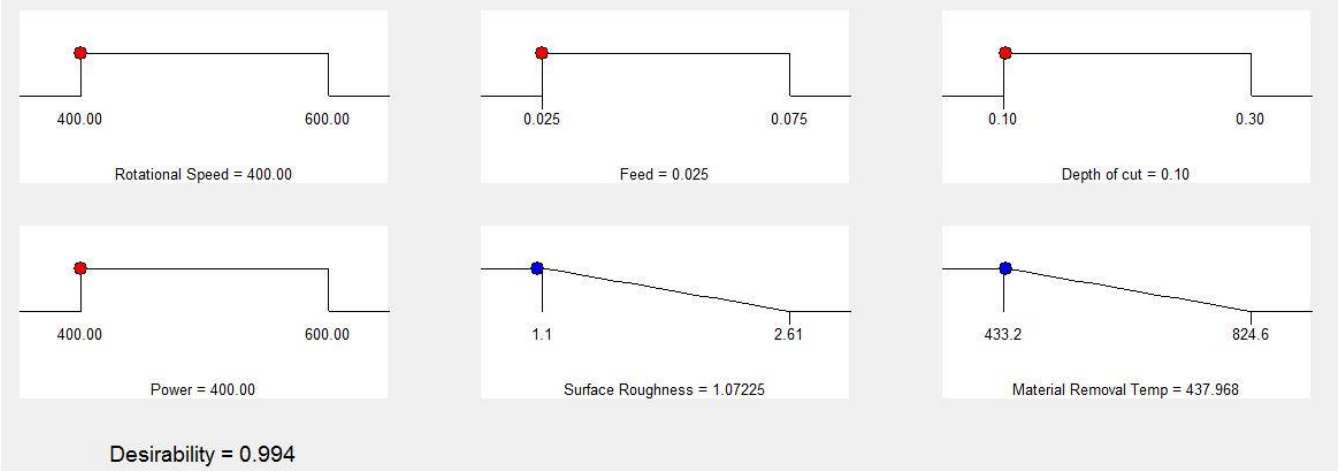

Figure 6.17. Ramp graphs for optimization

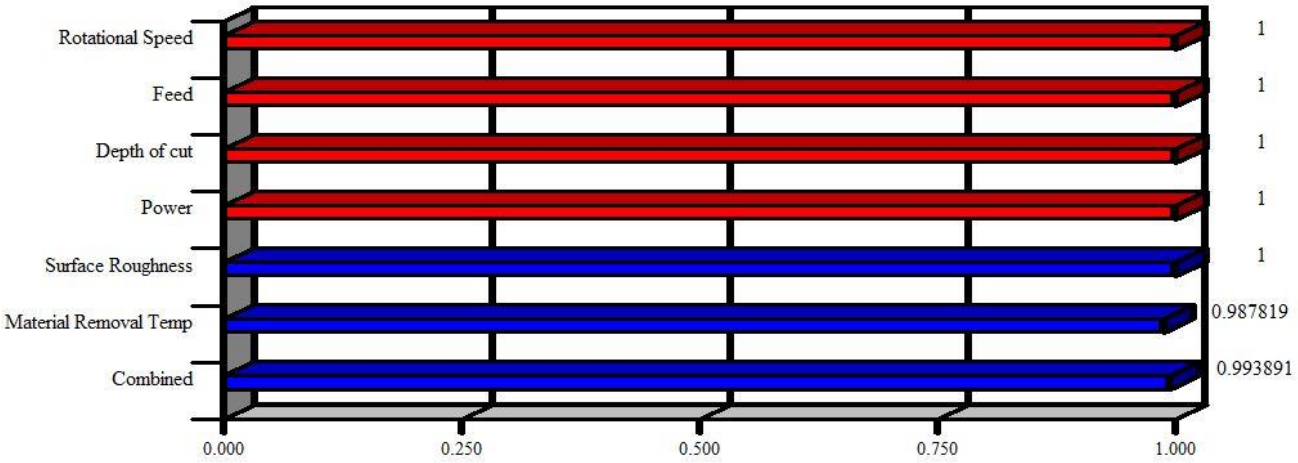

Figure 6.18. Bar chart of the optimization

Figure 6.19 shows unmachined ceramic composite and 6.20 shows machined at ceramic composite at optimum conditions. From the figures it is observed that in machined ceramic the grains are broken and scratches are occurred.

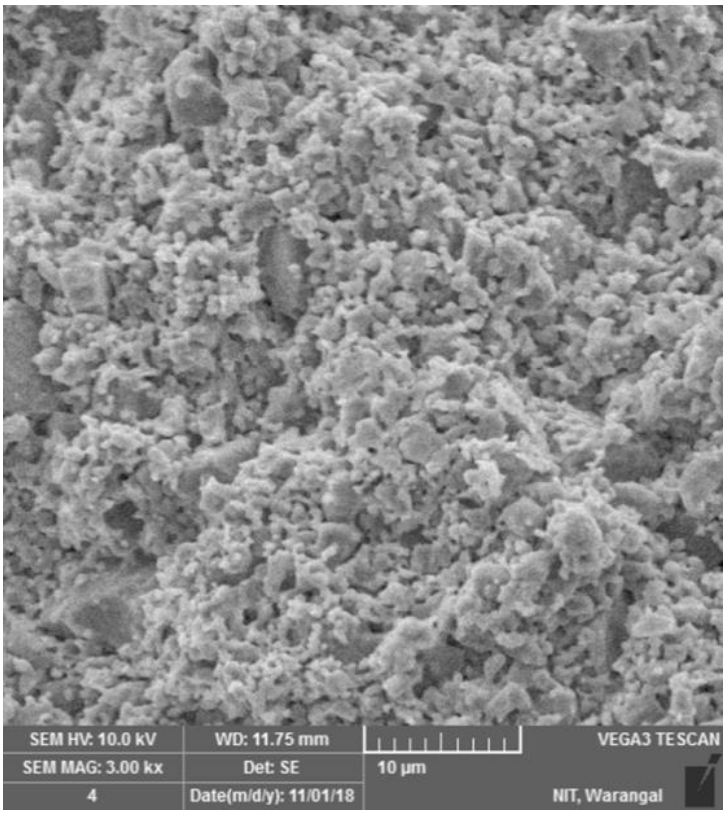

Figure 6.19. Unmachined ceramic composite

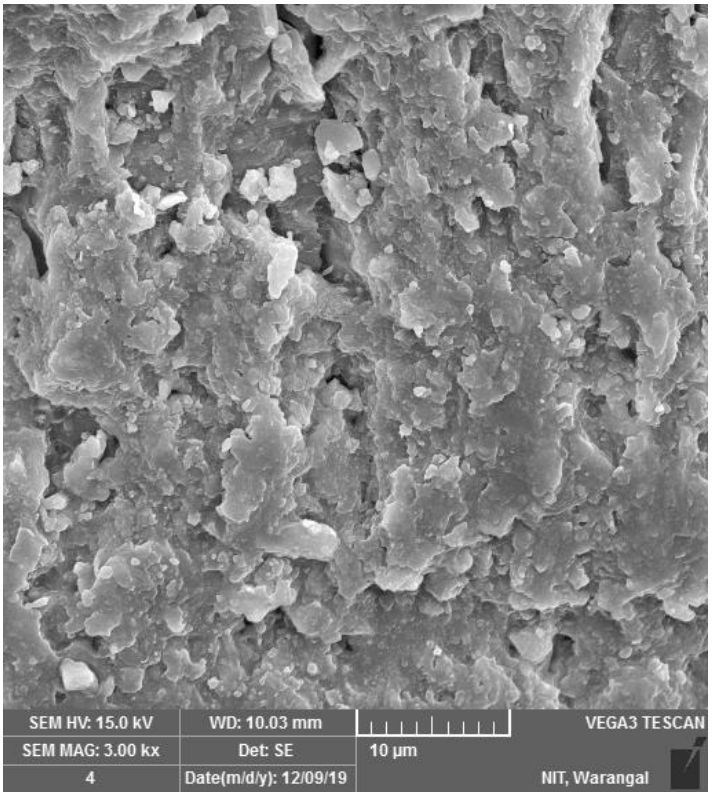

Figure 6.20. Machined ceramic composite at optimum conditions

Summary

This chapter deals with laser assisted machining of SiO_2–Si_3N_4–Al_2O_3 ceramic composite performed by the experimental plan obtained by RSM with a face centered central composite 6 points at the center. It studies the influence of process parameters on responses by developing regression models. Rotational speed increases, surface roughness decreases because of increase in the nose radius of the tool insert. In laser assisted machining the opposite is observed because a small amount of vibration is sensed during cutting at higher rotational speeds which in turn increases surface roughness. As the feed increases, surface roughness increases. Depth of cut has a positive effect on surface roughness. The more the depth of cut, more the surface roughness is achieved. The laser power softens the cutting zone better which reduces the hardness and strength of the workpiece material. Rotational speed plays an important role in material removal temperature of the machining process. The higher the rotational cutting speed, the faster the movement of the tool on the surface. Hence, more heat is generated by friction. When the cutting speed increases, there is little time available to dissipate the generated heat, which in turn increases the material removal temperature. Increase in feed and depth of cut increases material removal temperature. Higher depth of cut increases chip thickness. It is difficult to dissipate heat through large surface of the chip. There is very low chance of dissipating temperature and hence material removal temperature increases. Laser power is sufficient to soften the hard surface of the workpiece material.

This chapter also presents the multi response optimization of laser assisted machining of SiO_2–Si_3N_4–Al_2O_3 ceramic composite. The optimum process parameters were found to be 400 rpm rotational speed, 0.025 mm/rev feed, 0.1 mm depth of cut and 400 W laser power to meet the requirements of optimal responses. Actual (experimental) and predicted output values are firmly aligning with each other, which legitimizes the ampleness of RSM based optimization and forecast of surface roughness and material removal temperature. The percentages of residuals for these responses are 4.371% and 0.867% respectively.

CHAPTER 7

CONCLUSIONS

7.1. Conclusions

Fused silica based ceramic composites such as SiO_2–Si_3N_4–BN and SiO_2–Si_3N_4–Al_2O_3 have been successfully fabricated using gelcasting, a near net shape method. In this work, RSM models were developed for the prediction of flexural strength, porosity and dielectric constant of ceramics. Later, a multi objective problem was formulated to obtain optimum parameter combinations for maximization of both flexural strength, porosity and minimization of dielectric constant to find multiple sets of optimal solutions for ease of use by a ceramic processing engineer to save time, effort and cost. Also, the study saw laser assisted machining for ceramic and developed regression models. The following conclusions can be drawn from critical observations of results obtained.

- Flexural strength, porosity and dielectric constant of ceramic samples SiO_2, SiO_2–Si_3N_4–BN and SiO_2–Si_3N_4–Al_2O_3 were measured and it was found that obtained properties are within the limit of literature available. Pure SiO_2 has low strength compared to the SiO_2–Si_3N_4–BN and SiO_2–Si_3N_4–Al_2O_3 ceramic composite. Dielectric constant of as SiO_2–Si_3N_4–BN and SiO_2–Si_3N_4–Al_2O_3 ceramic composite is more compared to SiO_2 ceramic. The regression models for flexural strength, porosity and dielectric constant are developed and the influence of process variables on the responses is evaluated. The optimal process variables for maximum flexural strength, maximum porosity and minimum dielectric constant were studied using RSM coupled with desirability approach to optimize multiple responses. The predicted values for responses such as flexural strength, porosity and dielectric constant obtained from mathematical models were compared with experimental values for SiO_2–Si_3N_4–BN and SiO_2–Si_3N_4–Al_2O_3 ceramics. The optimum process parameters obtained for SiO_2–Si_3N_4–BN ceramic shown below.

Dependent variables	Optimum input parameters			Predicted values	Actual values	Error (%)
	Solid loading (%)	Monomer ratio	Monomer content (wt%)			
	48.63	10:1	15			
Flexural strength (MPa)				71.834	69.817	-2.889
Porosity (%)				38.704	36.214	-6.875
Dielectric constant				4.4482	4.692	5.196

The optimum process parameters obtained for SiO_2–Si_3N_4–Al_2O_3 ceramic shown below.

Dependent variables	Optimum input parameters			Predicted values	Actual values	Error (%)
	Solid loading (%)	Monomer ratio	Monomer content (wt%)			
	52	15:1	5			
Flexural strength (MPa)				87.36	82.01	-6.523
Porosity (%)				35.66	34.5	-3.362
Dielectric constant				4.783	4.788	0.104

- Hence, it is evident that predicted models are in line with experimental values. ANOVA also confirms that the models obtained were accurate. Hence, the predicted models developed from RSM can be used to evaluate the performance of ceramics. It is evident from the results that SiO_2 ceramics can be used for lower range missile applications and SiO_2–Si_3N_4–BN and SiO_2–Si_3N_4–Al_2O_3 ceramics for medium range missile applications.
- The erosive wear rate of fused silica ceramics is a function of composition of ceramic, impact velocity and impingement angle. It is examined in general that erosion rate enhances with impact velocity and impingement angle. It was found that higher erosion rate occurs at

near normal impingement angle i.e. 90^o. Erosion rate is maximum for pure fused silica ceramic compared with silica based ceramic composites. This may be attributed to the influence of hardness of ceramics. Morphology of the eroded surface is mainly based on the size and shape of erodent particles. The average surface roughness of eroded ceramics is more compared to un-eroded surfaces. Moreover, surface roughness increases from acute impingement angles to normal impingement angles. The ascending order of surface roughness of ceramics is as follows.

(i) SiO_2 (ii) SiO_2–Si_3N_4–BN and (iii) SiO_2–Si_3N_4–Al_2O_3

- Laser assisted machining was performed on SiO_2–Si_3N_4–Al_2O_3 ceramic. Rotational speed, feed, depth of cut and laser power were process variables, while surface roughness and material removal temperature were responses. The regression models for surface roughness and material removal temperature were developed and the influence of process variables on responses was evaluated. The optimal process variables for minimum surface roughness and minimum material removal temperature were studied using RSM coupled with desirability approach to optimize multiple responses. The predicted values for responses such as surface roughness and material removal temperature obtained from mathematical models were compared with experimental values of laser assisted machining of SiO_2–Si_3N_4–Al_2O_3 ceramic. The optimum machining parameters obtained for SiO_2–Si_3N_4–Al_2O_3 ceramic shown below.

Dependent variables	Optimum input parameters				Predicted values	Actual values	Error (%)
	Speed (rpm)	Feed (mm/rev)	Depth of cut (mm)	Power (W)			
	400	0.025	0.1	400			
Surface Roughness (µm)					1.072	1.121	4.371
Material Removal Temp (^{o}C)					437.967	434.2	-0.867

- Hence, it is evident that the predicted models are in line with experimental values. ANOVA also confirms that the models obtained were accurate. Hence, the predicted models developed from RSM can be used to evaluate the laser machining process.

7.2. Future scope

The results of the present work recommend research that may be contemplated in future for prospective researchers:

- Processing of fused SiO_2 based ceramics composites like SiO_2, SiO_2–Si_3N_4–BN and SiO_2–Si_3N_4–Al_2O_3 through gelcasting technique has been developed in the current study and there is a scope for further investigations by considering BN and Si_3N_4 as base ceramics.
- Low toxic monomers like 2-hydoxyethyl methacrylate (HEMA) and N, N'-dimethylacrylamide (DMAA) etc can be used in further studies.
- Only Silica (SiO_2) was used as erodent in solid particle erosion test of fused silica based ceramic composites. In future, Alumina (Al_2O_3), Silicon carbide (SiC), Tungsten carbide (TiC), Garnets etc. can be used as erodent particles.
- Laser assisted machining was performed on SiO_2–Si_3N_4–Al_2O_3 composite. Further, different types of ceramic composites and metal matrix composites can be processed through laser assisted machining.
- In this study only RSM was used for process optimization; furthermore Multi gene genetic programming and genetic algorithms etc. can also be implemented.

REFERENCES

1. Groover, M. P. (2007), "Fundamentals of modern manufacturing: materials processes, and systems", John Wiley & Sons.
2. Barsoum, M., and Barsoum, M. W. (2002), "Fundamentals of ceramics", CRC press.
3. Attili, N. K., and RamaKrishna, C. S. (2015), "Experimental Investigation and Analysis of Mechanical Properties of Chopped Strand Mat-E Glass Fiber Polyester Resin & Silica Powder Composite", *Journal of Machinery Manufacturing and Automation*, 4(1), 1-9.
4. Suzdaltsev, E. I. (2015), "Radio-transparent ceramics: yesterday, today, tomorrow", *Refract. Ind. Ceram.*, 55, 377-390.
5. Ganesh, I. (2011), "Development of β-SiAlON based ceramics for radome applications", *Process. Appl. Ceram.*, 5(3), 113-138.
6. Rice, R. W. (2002), "Ceramic fabrication technology", (Vol. 20). CRC Press.
7. Graule, T.J., Gauckler, L. J. and Baader F. H. (1995), "Direct coagulation casting- a new green shaping technique, Part1: Processing principles", *Ceramics charting the future*, 1601-1608.
8. Graule, T. J., Baader, E. H. and Gauckler, L. J.(1994), "Shaping of ceramic green compacts direct from suspensions by enzyme catalyzed reactions", *Scientific forum*, 6, 317-323.
9. Moreno, R., Moya, J. S. and Requena J. (1991), "Slip Casting of Zircon by Using an Organic Surfactant", *Ceram. Int.*, 17, 37-40.
10. Tari, G., Ferreira, J. M. F., Fonseca, A.T. and Lyckfeldt, O. (1998), "Influence of particle size distribution on colloidal processing of alumina", *J. Eur. Ceram. Soc.*, 18, 249-253.
11. Hotza, D. and Greil, P. (1995), "Review: aqueous tape casting of ceramic powders", *Mat. Sci. Eng. A.*, 202, 206-217.
12. Sofie, S. W. and Dogan, F. (2001), "Freeze Casting of Aqueous Alumina Slurries with Glycerol", *J. Am. Ceram. Soc.*, 84 [7], 1459–64.
13. Fukasawa, T. and Ando, M. (2001), "Synthesis of Porous Ceramics with Complex Pore Structure by Freeze-Dry Processing", *J. Am. Ceram. Soc.*, 84 [1], 230–32.

14. Fukasawa, T., Deng, Z.Y., Ando, M., OHJI, T. and Goto, Y. (2001), "Pore structure of porous ceramics synthesized from water-based slurry by freeze-dry process", Journal of Materials Science, 36, 2523 – 2527.
15. Kang, H.W., Tabata, Y. and Ikada, Y. (1999), "Fabrication of porous gelatin scaffolds for tissue engineering", *Biomaterials*, 20, 1339-1344.
16. Rak, Z. S. (2000), "Advanced Forming Techniques in Ceramics", Polish Ceramics conference, 1-18.
17. Kosmac, T., Novak, S. and Sajko, M. (1997), " Hydrolysis Assisted Solidification (HAS): A New Setting Concept for Ceramic Net Shaping", *J. Eur. Ceram. Soc*., 17, 427-432..
18. Nahass, P., Pober, R.L., Rhine, W.E., Robbins, W. L. and Bowen. H.K. (1992), "Prediction and Explanation of Aging Shrinkage in Tape-Cast Ceramic Green Sheets", *J. Am. Ceram. Soc.*, 75 [9], 2373-78.
19. Rahaman, M. N. (2017), "Ceramic processing and sintering", CRC press.
20. Young, A.C., Ornatete, O.O., Janney, M.A. and Menchhofer, P.A. (1991), "Gelcasting of Alumina", *J. Am. Cerarn. Soc*., 74 [3], 1612-18.
21. Ornatete, O.O., Janney, M.A and Nunn, S. D. (1997), "Gelcasting: From Laboratory Development toward Industrial Production", *J. Eur. Ceram. Soc*., 17, 407-413.
22. Janney, M.A., Ornatete, O.O., Walls, C.A., Nunn, S. D., Ogle, R.J. and Westmoreland, G. (1998*)*, "Development of Low-Toxicity Gelcasting Systems", *J. Am. Ceram. Soc*., 81 [3], 581–91.
23. Morissette, S.L. and Lewis, J.A. (2000), "Solid Freeform Fabrication of Aqueous Alumina–Poly (vinyl alcohol) Gelcasting Suspensions", *J. Am. Ceram. Soc*., 83 [10], 2409–16.
24. Cai, K., Huang, Y. and Yang, J.L. (2003), "Gelcasting of alumina with low-toxicity HEMA system", *J. Inorg. Mater*., 18(2), 343-347.
25. Huha, M. A. and Lewis, J.A. (2000), "Polymer Effects on the Chemorheological and Drying Behavior of Alumina–Poly (vinyl alcohol) Gelcasting Suspensions", *J. Am. Ceram. Soc*., 83 [8], 1957–63.
26. Zhou, L., Huang, Y and Xie, Z. (2000), "Gelcasting of concentrated aqueous silicon carbide suspension", *J. Eur. Ceram. Soc*., 20, 85-90.
27. Li, C., Han, Q., Guan, Y. and Zhang, Y. (2014), "Thermal gelation of chitosan in an aqueous alkali–urea solution", *Soft Matter*, 10, 8245–8253.

28. Chen, Y., Xie, Z., Yang, J. and Huang, Y. (1999), "Alumina Casting Based on Gelation of Gelatine", *J. Eur. Ceram. Soc*., 19, 271-275.
29. Colonetti, V.C., Sanches, M.F., de Souza, V.C., Fernandes, C.P., Hotza, D. and Quadri, M.G.N. (2018), "Cellular ceramics obtained by a combination of direct foaming of soybean oil emulsified alumina suspensions with gel consolidation using gelatin", *Ceram. Int*., 44, 2436-2445.
30. Sanches, M.F., Vitorino, N., Freitas, C., Abrantes, J.C.C., Frade, J.R., Neto, J.B.R. and Hotza, D. (2015), "Cellular ceramics by gelatin gelcasting of emulsified suspensions with sunflower oil", *J. Eur. Ceram. Soc*., 35, 2577-2585.
31. Hammel, E.C., Campa, J.A., Armbrister, C.E., Scheiner, M.V. and Okoli, O.I. (2017), "Influence of osmotic drying with an aqueous poly (ethylene glycol) liquid desiccant on alumina objects gelcast with gelatin", *Ceram. Int*., 43, 16443-16450.
32. Lombardi, M., Naglieri, V., Tulliani, J.M., and Montanaro, L. (2009), "Gelcasting of dense and porous ceramics by using a natural gelatine", *J. Porous. Mater*., 16, 393–400.
33. Santacruz, I., Nieto, M.I., and Moreno, R. (2005), "Alumina bodies with near-to-theoretical density by aqueous gelcasting using concentrated agarose solutions" *Ceram. Int*., 31, 439-445.
34. Zhang, J.Y. and Feng, Y.E. (2010), "Effect of agarose content on microstructures and mechanical properties of porous silicon nitride ceramics produced by gelcasting", *Zhejiang Univ-Sci A (Appl Phys & Eng)*, 11(10), 771-775.
35. Adolfssonw, E. (2006), "Gelcasting of Zirconia Using Agarose", *J. Am. Ceram. Soc*., 89 [6], 1897–1902.
36. Tulliani, J.M., Lombardi, M., Palmero, P., Fornabaio, M. and Gibson, L.J. (2013), "Development and mechanical characterization of novel ceramic foams fabricated by gel-casting", *J. Eur. Ceram. Soc*., 33, 1567-1576.
37. Olhero, S.M., Tari, G., Coimbra, M.A. and Ferreira, J.M.F. (2000), "Synergy of polysaccharide mixtures in gelcasting of alumina", *J. Eur. Ceram. Soc*., 20, 423-429.
38. Xu, J., Zhang, Y., Gan, K., Zhang, X., Qu, Y., Ma, N., and Yang, J. (2015), "A novel gelcasting of alumina suspension using curdlan gelation", *Ceram. Int*., 41, 10520-10525.

39. He, X., Sub, B., Zhouc, X., Yanga, J., Zhaoa, B., Wanga, X., Yanga, G., Tanga, Z. and Qiua H. (2011), "Gelcasting of Alumina Ceramics Using an Egg White Protein Binder System", *Ceramics – Silikaty*, 55 (1), 1-7.
40. Nayak, J.P. and Bera, J. (2012), "Bioactive Porous Silica Ceramics Prepared using Rice Husk Ash by Gelcasting Method", *Advanced Materials Research*, 548, 12-16.
41. Wan,W., Yang, J. and Qiu, T. (2014), "Study on Gelcasting of Fused Silica Glass Using
Glutinous Rice Flour as Binder", *Int. J. Appl. Glass*., 5 [4] 401–409.
42. Chandradass, J., Kim, K.H., Bae, D.S., Prasad, K., Balachandar, G., Divya, S.A. and Balasubramanian, M. (2009), "Starch consolidation of alumina: Fabrication and mechanical properties", *J. Eur. Ceram. Soc*., 29, 2219-2224.
43. Li, Y., Guo, Z., Hao, J. and Ren, S. (2008), "Gelcasting of metal powders in nontoxic cellulose ethers system", *J. Mater*., 208, 457–462.
44. Guo X. (2011), "Gel casting of high strength ceramics", Diploma work No. 75/2011 at Department of Materials and Manufacturing Technology, Chalmers University of Technology, Goteborg, Sweden.
45. Curkovic, L., Kumic, I. and Grilec, K. (2011), "Solid particle erosion behaviour of high purity alumina ceramics", *Ceram. Int*., 37, 29-35.
46. Choi, H.J., Han, D.H., Park, D.S., Kim, H.D., Han, B.D., Lim, D.S. and Kim, I.S. (2003), "Erosion characteristics of silicon nitride ceramics", *Ceram. Int*., 29, 713-719.
47. Wang, X., Fang, M., Zhang, L.C., Ding, H., Liu, Y.G., Huang, Z., Huang, S. and Yang, J. (2013), "Solid particle erosion of alumina ceramics at elevated temperature", *Mater. Chem. Phys*., 139, 765-769.
48. Liu, C. and Sun, J. (2010), "Erosion behaviour of B_4C-based ceramic composites", *Ceram. Int*., 36, 1297-1302.
49. Murugesh, L. and Scattergood, R.O. (1991), "Effect of erodent properties on the erosion of alumina", *J. Mater. Sci.*, 26, 5456-5466.
50. Srinivasan, S. and Scattergood, R.O. (1988), "Effect of Erodent Hardness on Erosion of Brittle Materials", *Wear*, 128,139 – 152.
51. Shipway, P.H. and Hutchings, I.M. (1996), "The role of particle properties in the erosion of brittle materials", *Wear,* 193, 105-113.
52. Zhou, J. and Bahadur, S. (1991), "The effect of material composition and operational variables on the erosion of alumina ceramics", *Wear,* 150, 343-354.

53. S. Lathabai, S. and Pender, D.C. (1995), "Microstructural influence in slurry erosion of ceramics", *Wear*, 189, 122-135.
54. Xiong, F., Manory, R.R., Ward, L. and Terheci, M. (1997), "Effect of Grain Size and Test Configuration on the Wear Behavior of Alumina", *J. Am. Ceram. Soc*., 80 [5], 1310–12.
55. Hussainova, I. (2001), "Some aspects of solid particle erosion of cermets", *Tribol. Int*., 34, 89–93.
56. Celotta, D.W., Qureshi, U.A., Stepanov, E.V., Goulet, D.P., Hunter, J., Buckberry, C.H. , Hill, R., Sherikar, S.V., Torbati, M.M. and Wood, R.J.K. (2007), "Sand erosion testing of novel compositions of hard ceramics", *Wear*, 263, 278-283.
57. Hussainova, I. (2003), "Effect of microstructure on the erosive wear of titanium carbide-based cermets", *Wear*, 255, 121–128
58. Germain, G., Santo, P. D. and Lebrun, J.L. (2011), "Comprehension of chip formation in laser assisted machining", Int. J. Mach. Tool. Manu., 51, 230–238.
59. Dutta, M.J. and Indranil, M. (2013), "Laser assisted fabrication of materials", Springer Series in Materials Science, Volume 161, ISBN 978-3-642-28358-1, Springer-Verlag Berlin Heidelberg.
60. Sun, S., Brandt, M. and Mo, J. (2013), "Current progresses of laser assisted machining of aerospace materials for enhancing tool life", *Advanced Materials Research*, 690693, 3359-3364.
61. Jeon, Y., Park, H.W. and Lee, C.M. (2013), "Current Research Trends in External Energy Assisted Machining", *Int. J. Precis. Eng. Man*., 14 (2), 337-342.
62. Kim, D.H. and Lee, C.M. (2013), "Development of a one-axis manipulator for laser-assisted machining", *J. Cent. South Univ*., 20, 378–384.
63. Armitage, K., Masood, S. and Brandt, M. (2006), "An investigation on laser assisted machining of hard to wear materials", Proceedings of the 2nd Pacific International Conference on Applications of Lasers and Optics, PICALO, Melbourne, Australia.
64. Chang, C.W. and Kuo, C.P. (2007), "Evaluation of surface roughness in laser-assisted machining of aluminum oxide ceramics with Taguchi method", *Int. J. Mach. Tool. Manu*., 47, 141–147.
65. Kuar, A.S., Doloi, B. and Bhattacharyya, B. (2006), "Modelling and analysis of pulsed Nd:YAG laser machining characteristics during micro-drilling of zirconia (ZrO_2)", *Int. J. Mach. Tool. Manu*., 46, 1301–1310.

66. Melkote, S., Kumar, M,. Hashimoto, F. and Lahoti, G. (2009), "Laser assisted micro-milling of hard-to-machine materials", *J. Manuf. Process,* 58(1): 45–48.
67. Rozzi, J.C., Pfefferkorn, F.E., Incropera, F.P. and Shin, Y.C. (2000), "Transient, three-dimensional heat transfer model for the laser assisted machining of silicon nitride: 1 Comparison of predictions with measured surface temperature histories", *Int. J. Heat. Mass. Tran*., 43(8), 1409–1424.
68. Rozzi, J.C., Pfefferkorn, F.E., Shin, Y.C. and Incropera, F.P. (2000), "Experimental Evaluation of the Laser Assisted Machining of Silicon Nitride Ceramics", *Transactions of ASME*, 122, 666-670.
69. Mun, S.D. (2010), "Micro Machining of High-Hardness Materials Using Magnetic Abrasive Grains" *Int. J. Precis. Eng. Man*., 11 (5), 763-770.
70. Dandekar, C. R., Shin, Y. C. and Barnes, J. (2010), "Machinability improvement of titanium alloy (Ti–6Al–4V) via LAM and hybrid machining", *Int. J. Mach. Tool. Manu*., 50, 174–182.
71. Anderson, M., Patwa, R. and Shin, Y.C. (2006), "Laser-assisted machining of Inconel 718 with an economic analysis", *Int. J. Mach. Tool. Manu*., 46, 1879–1891.
72. Skvarenina, S. and Shin, Y.C. (2006), "Laser-assisted machining of compacted graphite iron", *Int. J. Mach. Tool. Manu*., 46, 7–17.
73. Rebro, P.A., Incropera, F.P. and Shin, Y.C. (2002), "Laser-Assisted Machining of Reaction Sintered Mullite Ceramics", *Transactions of ASME*, 124, 875-885.
74. Lei, S., Shin, Y.C. and Incropera, F.P. (2000), "Deformation mechanisms and constitutive modeling for silicon nitride undergoing laser-assisted machining" *Int. J. Mach. Tool. Manu*., 40, 2213–2233.
75. Lei, S., Shin, Y.C. and Incropera, F.P. (2001), "Experimental Investigation of Thermo-Mechanical Characteristics in Laser-Assisted Machining of Silicon Nitride Ceramics", *Transactions of ASME*, 123, 639-646.
76. Kim, J.D., Lee, S.J. and Suh, J. (2011), "Characteristics of laser assisted machining for silicon nitride ceramic according to machining parameters", *J. Mech. Sci. Technol*., 25 (4), 995~1001.
77. Ding, H. and Shin, Y.C. (2013), "Improvement of machinability of Waspaloy via laser-assisted machining", *Int. J. Adv. Manuf. Technol*., 64, 475–486.

78. Dandekar, C.R. and Shin, Y.C. (2013), "Experimental evaluation of laser-assisted machining of silicon carbide particle-reinforced aluminum matrix composites", *Int. J. Adv. Manuf. Technol.* 66, 1603–1610.
79. Rashid, R. A. R., Sun, S., Wang, G. and Dargusch, M. S. (2013), "Experimental Investigation of Laser Assisted Machining of AZ91 Magnesium Alloy", *Int. J. Precis. Eng. Man.*, 14 (7), 1263-1265.
80. Anderson, M. C. and Shin, Y. C. (2006), "Laser-assisted machining of an austenitic stainless steel: P550", *P. I. Mech. Eng. B. J. Eng. Manuf.*, 220, 2055-2067.
81. Dumitrescu, P., Koshy, P., Stenekes, J. and Elbestawi, M.A. (2006), "High-power diode laser assisted hard turning of AISI D2 tool steel", *Int. J. Mach. Tool. Manu.*, 46, 2009–2016.
82. Shokrani, A., Dhokia, V. and Newman, S.T. (2012), "Environmentally conscious machining of difficult-to-machine materials with regard to cutting fluids", *Int. J. Mach. Tool. Manu.*, 57, 83–101.
83. Sun, S., Brandt, M. and Dargusch, M.S. (2009), "Characteristics of cutting forces and chip formation in machining of titanium alloys", *Int. J. Mach. Tool. Manu.*, 49, 561–568.
84. Bermingham, M.J., Kirsch, J., Sun, S., Palanisamy, S. and Dargusch, M.S. (2011), "New observations on tool life, cutting forces and chip morphology in cryogenic machining Ti-6Al-4V", *Int. J. Mach. Tool. Manu.*, 51, 500–511.
85. Dandekar, C.R. and Shin, Y.C. (2010), "Laser-Assisted Machining of a Fiber Reinforced Metal Matrix Composite", *J. Manuf. Sci. E-T. ASME.*, 132, 061004-8.
86. Wang, Y., Yang, L.J. and Wang, N.J. (2002), "An investigation of laser assisted machining of Al_2O_3 particle reinforced aluminum matrix composite", *J. Mater. Process. Technol.*, 129, 268-272.
87. Jeon, Y. and Lee, C.M. (2012), "Current Research Trend on Laser Assisted Machining", *Int. J. Precis. Eng. Man.*, 13 (2), 311-317.
88. Li, J., Peng, J., Guo, S. and Zhang, L. (2013), "Application of response surface methodology (RSM) for optimization of the sintering process of preparation calcia partially stabilized zirconia (CaO-PSZ) using natural baddeleyite", *J. Alloys. Compd.*, 574, 504–511.

89. Sktani, Z.D.I, Rejab, N.A., Ratnam, M.M. and Ahmad, Z.A. (2018), "Fabrication of tougher ZTA ceramics with sustainable high hardness through (RSM) optimisation", *Int. J. Refract. Met. H.*, 74, 78–86.
90. Baradeswaran, A., Vettivel, S.C., Perumal, A.E, Selvakumar, N. and Issac, R.F. (2014), "Experimental investigation on mechanical behaviour, modelling and optimization of wear parameters of B_4C and graphite reinforced aluminium hybrid composites", *Mater. Design*., 63, 620–632.
91. Rao, R.V., (2011), "Advanced Modeling and Optimization of Manufacturing Processes", Springer Series in Advanced Manufacturing, Springer-Verlag London Limited 2011.
92. Mia, M. (2018), "Mathematical modeling and optimization of MQL assisted end milling characteristics based on RSM and Taguchi method", *Measurement*, 121, 249–260.
93. Mohamed, O.A., Masood, S.H. and Bhowmik, J.L. (2016), "Mathematical modeling and FDM process parameters optimization using response surface methodology based on Q-optimal design", *Appl. Math. Model*., 40, 10052–10073.
94. ChittaranjanDas, V. (2016), "Response surface Methodology and Desirability Approach to Optimize EDM Parameters", Int. J. Hybrid Inf. Technol., 9, No.4, 393-406.
95. Yang, X., Li, B., Zhang, C., Wang, S., Liu, K. and Zou, C. (2016), "Fabrication and properties of porous silicon nitride wave transparent ceramics via gelcasting and pressureless sintering", *Mat. Sci. Eng. A*., 663, 174-180.
96. Zou, C., Zhang, C., Li, B., Wang, S., and Cao, F. (2016), "Microstructure and properties of porous silicon nitride ceramics prepared by gelcasting and pressureless sintering", *Mater. Design*., 44, 114–118.
97. Wang, S., Yang, Z., Duan, X., Jia, D., Cui, W., Sun, B. and Zhou, Y. (2013), "Effects of pore size on microstructure, mechanical and dielectric properties of gelcasting BN/Si_3N_4 ceramics with spherical shaped pore structures", *J. Alloys. Compd*., 581, 46–51.
98. Duan, L., Rui, Z.C., Li, B., Cao, F., Wang, S., Bei, Y. and kun, L. (2012), "Effects of oxidation treatment on properties of SiO2f/SiO2-BN composites", *J. Cent. South. Univ*., 19, 30−35.

99. Duan, X., Jia, D., Deng, J., Yang, Z. and Zhou, Y. (2012), "Mechanical and dielectric properties of gelcasted Si3N4 porous ceramics using CaHPO4 as an additive", *Ceram. Int.,* 38, 4363-4367.

100. Wang, S., Jia, D., Yang, Z., Duan, X., Tian, Z. and Zhou, Y. (2013), "Effect of BN content on microstructures, mechanical and dielectric properties of porous BN/Si_3N_4 composite ceramics prepared by gel casting", *Ceram. Int.,* 39, 4231-4237.

101. Wang, H., Yu, J., Zhang, J. and Zhang, D. (2010), "Preparation and properties of pressureless-sintered porous Si_3N_4", *J. Mater. Sci.,* 45, 3671–3676.

102. Li, Y., Chen, F., Li, L., Zhang, W., Yu, H., Shan, Y., Shen, Q. and Jiang, H. (2010), "Gas Pressure Sintering of Arbitrary Porous Silicon Nitride Ceramics with High Mechanical Strength", *J. Am. Ceram. Soc.,* 93 [6], 1565–1568.

103. Yu, J., Wang, H., Zhang, J., Zhang, D. and Yan, Y. (2010), "Gelcasting preparation of porous silicon nitride ceramics by adjusting the content of monomers", *Sol-Gel. Sci. Technol.,* 53, 515–523.

104. Yu, L.Z., Ran, G. H., Xi, Z. M. and Qin, H. X. (2008), "Preparation of aluminum borate whisker reinforced aluminum phosphate wave-transparent materials", *Chinese Science Bulletin*, 53 [19], 3073-3076.

105. Ganesh, I., Thiyagarajan, N., Jana, D. C., Mahajan, Y.R. and Sundararajan, G. (2008), "Aqueous Gelcasting Process for β-$Si_4Al_2O_2N_6$ Ceramics", *J. Am. Ceram. Soc.,* 91 [9], 3121–3124.

106. Zhou, L., Huang, Y., Xie, Z., Zimmermann, A. and Aldinger, F. (2002), "Preparation of Si3N4 ceramics with high strength and high reliability via a processing strategy", *J. Eur. Ceram. Soc.*, 22, 1347-1355.

107. Glide, G., Patel, P., Hubbard, C., Pothier, B., Hynes, T., Croft, W. and Wells, J. (1997), "SiON low dielectric constant ceramic nanocomposites", U.S. Patent No. 5,677,252.

108. Wan, W., Yang, J., Zeng, J., Yao, L. and Qiu, T. (2014), "Effect of solid loading on gelcasting of silica ceramics using DMAA", *Ceram. Int.,* 40, 1735-1740.

109. Wan, W., Huang, C., Yang, J., Zeng, J., Yao, L. and Qiu, T. (2014), "Effect of Sintering Temperature on the Properties of Fused Silica Ceramics Prepared by Gelcasting", *J. Electron. Mater.,* 43 [7], 2566-2572.

110. Wan, W., Yang, J. and Qiu, T. (2014), "Study on Gelcasting of Fused Silica Glass Using Glutinous Rice Flour as Binder", *Int. J. Appl. Glass. Sci*., 5 [4], 401–409.

111. Wan, W., Yang, J., Zeng, J. and Qiu, T. (2013), "Gelcasting of fused silica glass using a low-toxicity monomer DMAA", *J. Non-Cryst. Solids.,* 379, 229–234.

112. Manivannan, R., Kumar, A., and Subrahmanyam, Ch. (2013), "Aqueous Gelcasting of Fused Silica Using Colloidal Silica Binder", *J. Am. Ceram. Soc*., 96 [8], 2432–2436.

113. Mao, X., Wang, S. and Shimai, S. (2006), "Preparation of Porous Silica Ceramics with Low Dielectric Constant", *Chinese. J. Aeronaut.,* 19, S239-S243.

114. Zhang, Y. and Cheng, Y.B. (2006), "Use of HEMA in Gelcasting of Ceramics: A Case Study on Fused Silica", *J. Am. Ceram. Soc*., 89 [9], 2933–2935.

115. Lin, S., Ye, F., Ma, J., Ding, J., Yang, C. and Dong, S. (2016), "Fabrication of multilayer electronic magnetic window material by Si_2N_2O decomposition", *Mater Design.,* 97, 51–55.

116. Zou, C., Zhang, C., Li, B., Cao, F., and Wang, S. (2012), "Improved properties and microstructure of porous silicon nitride/silicon oxide composites prepared by sol–gel route", *Mat. Sci. Eng. A*., 556, 648-652.

117. Ganesh, I. and Sundararajan, G. (2010), "Hydrolysis-Induced Aqueous Gelcasting of β-SiAlON–SiO_2 Ceramic Composites: The Effect of AlN Additive", *J. Am. Ceram. Soc.,* 93 [10], 3180–3189.

118. Li, X., Yin, X., Zhang, L., Cheng, L., and Qi, Y. (2009), "Mechanical and dielectric properties of porous Si_3N_4–SiO_2 composite ceramics", *Mat. Sci. Eng. A*., 500(1-2), 63-69.

119. Jia, D.C., Zhou, Y. and Lei, T.C. (2003), "Ambient and elevated temperature mechanical properties of hot-pressed fused silica matrix composite", *J. Eur. Ceram. Soc*., 23, 801-808.

120. Du, M., Bi, J. Q., Wang, W. L., Sun, X. L., and Long, N. N. (2011), "Microstructure and properties of SiO_2 matrix reinforced by BN nanotubes and nanoparticles", *J. Alloys. Compd.,* 509(41), 9996-10002.

121. Jia, D., Zhou, L., Yang, Z., Duan, X., and Zhou, Y. (2011), "Effect of preforming process and starting fused SiO_2 particle size on microstructure and mechanical properties of pressurelessly sintered BNp/SiO_2 ceramic composites", *J. Am. Ceram. Soc.,* 94(10), 3552-3560.

122. Zhai, H. Z., Cai, H. N., Yang, X. Z., Li, J. B., Guo, G. F., and Cao, C. B. (2007), "Preparation and properties of BN-SiO2 composite ceramics", *Key. Eng. Mater*., 336, 1426-1428.

123. Wen, G., Wu, G. L., Lei, T. Q., Zhou, Y., and Guo, Z. X. (2000), "Co-enhanced SiO2-BN ceramics for high-temperature dielectric applications", *J. Eur. Ceram. Soc*., 20 (12), 1923-1928.

124. Dong, W., Wang, C. A., Yu, L., and Ouyang, S. X. (2012), "Preparation and Properties of Porous Si_3N_4/SiO_2/BN Composite Ceramics", *Key. Eng. Mater*., 512, 828-831.

125. Long, N. N., Bi, J. Q., Wang, W. L., Du, M., and Bai, Y. J. (2012), "Mechanical properties and microstructure of porous BN–SiO_2–Si_3N_4 composite ceramics", *Ceram. Int.*, 38(3), 2381-2387.

126. Han, J. C., Sun, Y. B., and Zhang, Y. M. (2010), "Dielectric properties in GHz range of porous Si_3N_4–BN–SiO_2 ceramics with considerable flexural strength prepared by low temperature sintering in air", *J. Mater. Sci. Technol*., 26(8), 996-1000.

127. Zhang, W. R., Wang, C. H., Li, L., Liu, J., and Chen, W. (2008), "Si_3N_4–BN–SiO_2 based microwave-transparent materials", *Key. Eng. Mater*., 368, 913-916.

128. Jiang, Y. G., Zhang, C. R., Cao, F., Wang, S. Q., Hu, H. F., and Qi, G. J. (2007), "Fabrication of High Performance 2.5 D SiO_{2f}/Si_3N_4-BN Composites for High-temperature Application", *Adv. Eng. Mater.*, 9(1-2), 114-116.

129. Jiang, Y. G., Zhang, C. R., Cao, F., Wang, S. Q., Hu, H. F., and Qi, G. J. (2007), "Moisture behavior and effects on the mechanical properties and the microstructures of SiO_{2f}/Si_3N_4-BN amorphous composites", *J. Non-Cryst. Solids.*, 353(22-23), 2301-2305.

130. Wan, W., Yang, J., Feng, Y., Bu, W., and Qiu, T. (2016), "Effect of trace alumina on mechanical, dielectric, and ablation properties of fused silica ceramics", *J. Alloys. Compd.*, 675, 64-72.

131. Wan, W., Feng, Y., Yang, J., Bu, W., and Qiu, T. (2016), "Microstructure, mechanical and high-temperature dielectric properties of zirconia-reinforced fused silica ceramics", *Ceram. Int.*, 42(5), 6436-6443.

132. Bermingham, M. J., Palanisamy, S., and Dargusch, M. S. (2012), "Understanding the tool wear mechanism during thermally assisted machining Ti-6Al-4V", *Int. J. Mach. Tool. Manu.*, 62, 76-87.

133. Rashid, R. R., Sun, S., Wang, G., and Dargusch, M. S. (2012), "An investigation of cutting forces and cutting temperatures during laser-assisted machining of the Ti–6Cr–5Mo–5V–4Al beta titanium alloy", *Int. J. Mach. Tool. Manu.*, 63, 58-69.

134. Rashid, R. R., Sun, S., Wang, G., and Dargusch, M. S. (2012), "The effect of laser power on the machinability of the Ti-6Cr-5Mo-5V-4Al beta titanium alloy during laser assisted machining", *Int. J. Mach. Tool. Manu.*, 63, 41-43.

135. Attia, H., Tavakoli, S., Vargas, R., and Thomson, V. (2010), "Laser-assisted high-speed finish turning of superalloy Inconel 718 under dry conditions", *CIRP annals*, 59(1), 83-88.

136. Germain, G., Lebrun, J. L., Braham-Bouchnak, T., Bellett, D., and Auger, S. (2008), "Laser-assisted machining of Inconel 718 with carbide and ceramic inserts", International journal of material forming, 1(1), 523-526. *Int. J. Mater. Form.*, 1, 523–526.

137. Chang, C. W., and Kuo, C. P. (2007), "Evaluation of surface roughness in laser-assisted machining of aluminum oxide ceramics with Taguchi method", *Int. J. Mach. Tool. Manu.*, 47(1), 141-147.

138. Pfefferkorn, F. E., Shin, Y. C., Tian, Y., and Incropera, F. P. (2004), "Laser-assisted machining of magnesia-partially-stabilized zirconia", *J. Manuf. Sci. Eng.*, 126(1), 42-51.

139. Kim, J. D., Lee, S. J., and Suh, J. (2011), "Characteristics of laser assisted machining for silicon nitride ceramic according to machining parameters", *J. Mech. Sci. Technol*., 25(4), 995-1001.

140. Masood, S. H., Armitage, K., and Brandt, M. (2011), "An experimental study of laser-assisted machining of hard-to-wear white cast iron", *Int. J. Mach. Tool. Manu*., 51(6), 450-456.

141. Ding, H., and Shin, Y. C. (2010), "Laser-assisted machining of hardened steel parts with surface integrity analysis", *Int. J. Mach. Tool. Manu*., 50(1), 106-114.

142. Dandekar, C. R., and Shin, Y. C. (2010), "Laser-assisted machining of a fiber reinforced metal matrix composite", *J. Manuf. Sci. E-T. ASME.*, 132(6), 061004-8.

143. Wang, Y., Yang, L.J. and Wang, N.J. (2002), "An investigation of laser assisted machining of Al_2O_3 particle reinforced aluminum matrix composite", *J. Mater. Process. Technol*., 129, 268-272.

144. Barnes, S., Morgan, R., and Skeen, A. (2003), "Effect of laser pre-treatment on the machining performance of aluminum/SiC MMC", *J. Eng. Mater. Technol*., 125(4), 378-384.

145. Sharma, S. K., Kumar, B. V. M., Lim, K. Y., Kim, Y. W., and Nath, S. K. (2014), "Erosion behavior of SiC–WC composites", *Ceram. Int.*, 40(5), 6829-6839.

146. Amirthan, G., Udayakumar, A., Prasad, V. B., and Balasubramanian, M. (2010), "Solid particle erosion studies on biomorphic Si/SiC ceramic composites" *Wear*, 268(1-2), 145-152.

147. Zhang, Y., Cheng, Y. B., and Lathabai, S. (2000), "Erosion of alumina ceramics by air-and water-suspended garnet particles", *Wear*, 240(1-2), 40-51.

148. Gopi, K. R., Nagarajan, R., Rao, S. S., and Mandal, S. (2008), "Erosion model on alumina ceramics: A retrospection, validation and refinement", *Wear*, 264(3-4), 211-218.

149. Renjo, M. M., Ćurković, L., and Grilec, K. (2015), "Erosion resistance of slip cast composite Al2O3-ZrO2 ceramics", *Procedia Engineering*, 100, 1133-1140.

150. Xiangli, F., Wei, W., Chen, Y., Jin, W., and Xu, N. (2008), "Optimization of preparation conditions for polydimethylsiloxane (PDMS)/ceramic composite pervaporation membranes using response surface methodology", *J. Membrane. Sci.*, 311(1-2), 23-33.

151. Li, J., Peng, J., Guo, S., and Zhang, L. (2013), "Application of response surface methodology (RSM) for optimization of sintering process for the preparation of magnesia partially stabilized zirconia (Mg-PSZ) using natural baddeleyite as starting material", *Ceram. Int.*, 39(1), 197-202.

152. Song, C., Li, X., Wang, L., and Shi, W. (2016), "Fabrication, characterization and response surface method (RSM) optimization for tetracycline photodegration by $Bi_{3.84}W_{0.16}O_{6.24}$-graphene oxide (BWO-GO)", *Scientific reports*, 6, 37466, 1-12.

153. Song, H., Ren, G., Dan, J., Li, J., Xiao, J. and Xu, J. (2019), "Experimental Study of the Cutting Force During Laser-Assisted Machining of Fused Silica Based on Artificial Neural Network and Response Surface Methodology", *Silicon*, 11, 1903–1916.

154. Song, H., Dan, J., Li, J., Du, J., Xiao, J. and Xu, J. (2019), "Experimental study on the cutting force during laser assisted machining of fused silica based on the Taguchi method and response surface methodology", *J. Manuf. Process.*, 38, 9-20.